DELTA
Annual Report 2023

Dortmund
1. December 2023

Edited by C. Sternemann, M. Paulus,
D. Lützenkirchen-Hecht (2023)

November 2023

Preface

Dear readers, dear colleagues,

we are at the end of a year 2023 characterized by energy-saving measures, which have also left its mark on the operation of DELTA. The available beam time for the users had to be significantly reduced this year, which all employees and scientists involved endeavored to compensate for as best they could, with a high level of personal commitment and motivation. Accordingly, an impressive number of contributions to the annual report 2023 (reporting period October 2022 to October 2023) have been submitted by the users. 12 reports are dedicated to instrumentation, 31 reports on X-ray scattering and 11 to X-ray spectroscopies, respectively, which reflects that all the different instruments and endstations were intensively used in the past twelve months. As in the years before, many users have mailed-in their samples, and the DELTA staff and the beamline scientists did their best to get the external users satisfied. Furthermore, the shut-down periods were effectively used to install new experimental setups, in particular new instrumentation for X-ray diffraction at beamline BL8 that has proven its functionality during the last weeks of DELTA operation in October and November.

The contributions included in this annual report all have a high quality, and reflect a broad spectrum of scientific activities. DELTA appears to bring together scientists and scientific activities from various disciplines such as engineering, physics, chemistry, biology and geology, dealing with both, fundamental and applied research questions.

After almost more than 10 years of service, Ralph Wagner from Wuppertal University had to leave the editorial team – we wish him all the best for his future activities. Michael Paulus from TU Dortmund took over starting with this annual report. We take the opportunity to thank the involved technicians, engineers and scientists of the machine group for running the DELTA machine, as well as we acknowledge the financial support by the funding agencies and the local government. Furthermore, the success of DELTA would not be possible without the manifold contributions from the universities and research institutions, in particular the TU Dortmund.

Christian Sternemann, Michael Paulus & Dirk Lützenkirchen-Hecht

Contents:

Instrumentation

Energy Consumption at DELTA

S. Khan, C. Mai
Zentrum für Synchrotronstrahlung (DELTA), Technische Universität Dortmund

The rising cost of energy necessitated a drastic reduction of the energy consumption at DELTA, resulting in a cut of accelerator operation by 50% in 2023 and exploring possible ways to use less power during machine operation and also in shutdown periods.

Data of the electrical, thermal, and cooling energy consumption at DELTA are available since July 2021 with a sampling period of 15 minutes. Figure 1 shows data until the 25th of October 2023 sorted by user operation (blue), accelerator physics (red), and shutdown weeks (black). Raw data of electric power versus time are shown in Fig. 1 (a), while (b-d) display the power averaged from Tuesday 00:00 until Thursday 24:00 to emphasize the effect of full-day accelerator operation. Electric power (b) will be discussed below. Thermal power (c) naturally peaks during the winter period and was significantly lower in winter 2022/2023 than before. Cooling power has its maximum in summer and reached similar peak values as before, while the total consumption in 2023 was much lower since very little accelerator operation took place after spring.

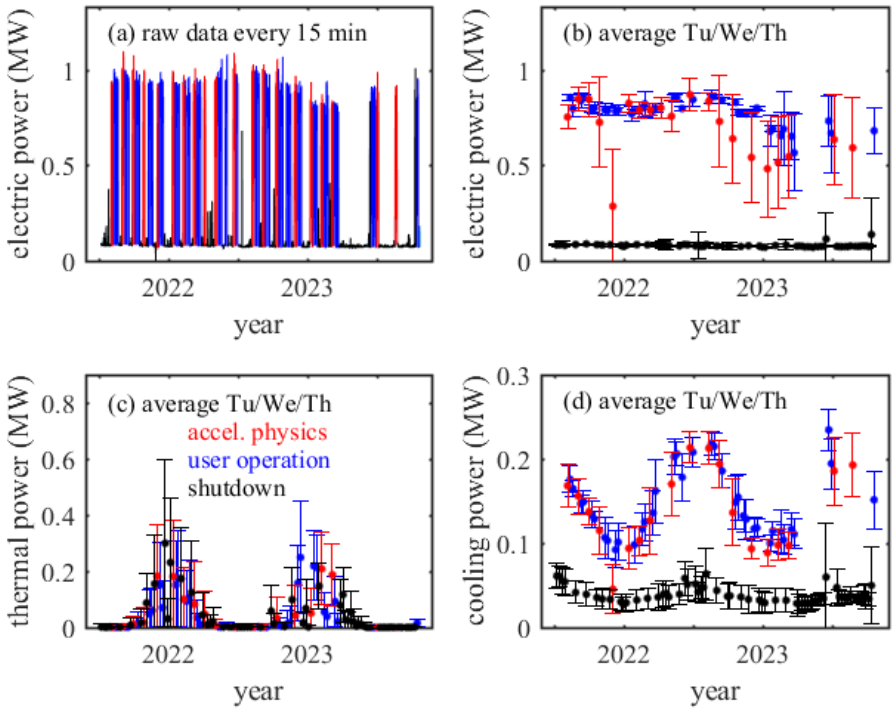

Figure 1: Power consumption from July 2021 to October 2023: (a) Electric power recorded every 15 minutes. (b) Electric power averaged from Tu 00:00 to Th 24:00 with error bars showing the root-mean-square fluctuation of the 15-minute values. (c) Thermal power and (d) cooling power averaged over the same period. Red: Accelerator studies. Blue: User operation. Black: Shutdown weeks.

The electric power consumption during user operation (Fig. 1 (b), blue symbols) has a slight maximum in summer due to the operation of cooling systems for radiofrequency (RF) components and magnets. Since the beginning of 2023, the RF power was reduced by operating only one 500-MHz resonator, which is fed by a solid-state amplifier while the other klystron-powered resonator was switch off. With good progress in reactivating vacuum pumps and improved magnet alignment, the beam lifetime is still excellent with values around 25 hours.

Single-resonator operation is possible as long as the recently installed superconducting wiggler is operated at a reduced magnetic field of 5 T, which is presently the case because the delivery of vacuum components (new dipole chamber, tapers, and absorbers) required for 7-T operation was delayed.

Furthermore, a “sleeping mode” configuration was developed reducing RF power and magnet current during every predictable interruption exceeding one hour while avoiding intolerable thermal changes. This is particularly useful during accelerator studies with varying beam requirements leading to large variations in weekly power consumption (see Fig. 1 (b), red symbols).

The evolution of electric power during accelerator operation is again shown in Fig. 2 (top right). Some components of the accelerator complex cannot be switched off during shutdown periods, e.g., the compressors keeping the superconducting wiggler under liquid helium and IT hardware. Nevertheless, also the power consumption during shutdown periods has steadily decreased by about 10% (see Fig. 2, top left), partly by identifying additional accelerator components that can safely be turned off and possibly also an increased energy saving awareness. In the two shutdown weeks with increased mean power, the accelerator complex had to be operated for a day in order to fix problems in view of the upcoming user weeks.

Finally, the bottom part of Fig. 2 shows the total power consumption in the period for which data are available. After March 2023, the slope of the graph is significantly lower and the electric energy used until the 25th of October is only 46.7% of the consumption in 2022 (see dashed lines). Since these energy saving measures were necessary, the user call for the second half of 2023 had to be cancelled and less time was available for thesis research using synchrotron radiation as well as for accelerator physics. Another well-known drawback is that infrequent operating makes a complex machine more prone to failure and unstable operation. Given these unfavorable circumstances, the operation of DELTA in 2023 was still excellent.

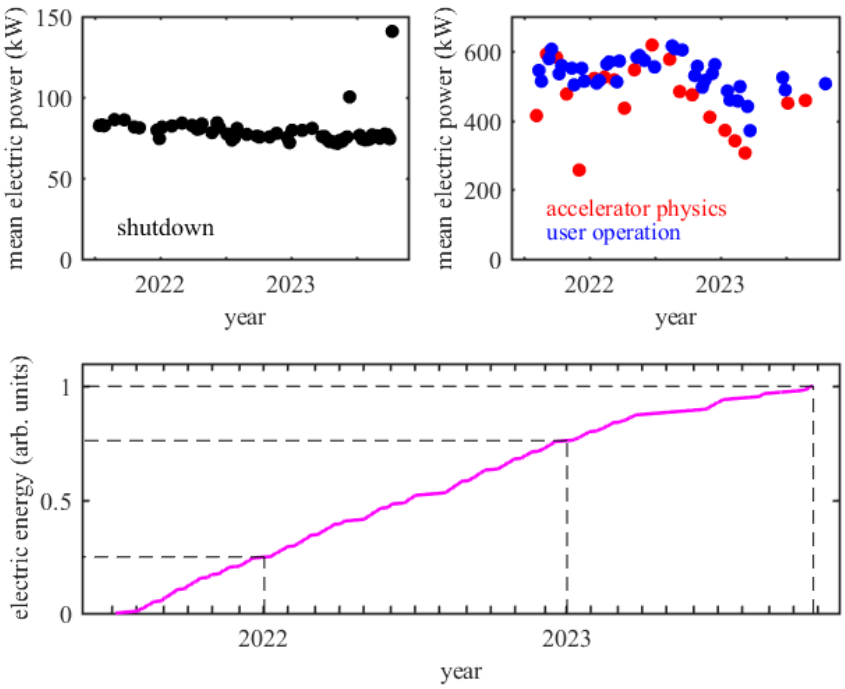

Figure 2: Top: Evolution of averaged electric power during shutdown periods (left) and during user operation as well as accelerator studies (right). Bottom: Total consumption of electric energy between summer 2021 and the 25th of October 2023.

DELTA Radiofrequency Systems

P. Hartmann, V. Kniss, A. Leinweber and the DELTA team
Zentrum für Synchrotronstrahlung (DELTA), Technische Universität Dortmund

Linear Accelerator and Booster Synchrotron (BoDo): The radiofrequency (RF) systems of the linear accelerator and the booster have worked flawlessly over the past year. The reduction in parking power of the booster three-cell cavity reported in last year's annual report did not cause any trouble. An upgrade of the BoDo low-level RF (LLRF) system is being prepared. The BoDo LLRF is on the critical path of accelerator operation. It consists of more than 40 years old components and needs an upgrade. In order to test the function of a modern LLRF, a test stand made of spare parts is currently being set up.

Storage Ring: The DELTA storage ring RF system performed well within the last year. The ring is equipped with one EU-type RF resonator fed with power from a high-efficiency semiconductor amplifier and a DORIS-type resonator, which is powered by a klystron tube. During regular operation, both cavities are operated. Initial attempts to reduce the energy consumption of the RF system by reducing the power in both cavities, reported in last year's annual report, were only partially successful. In contrast to a semiconductor amplifier, a klystron tube is similar in power consumption to class-A amplifiers in low-power electronics: Since a constant DC current inside the tube is modulated, the line power consumption of the klystron is independent of its AC output power. For this reason, operation of the storage ring with just one cavity was started in January 2023. The klystron amplifier is switched off and the missing RF power is provided by the more energy-efficient solid-state amplifier of the EU-type cavity. The lifetime of the beam was adjusted by reducing the RF power such that the number of daily injections was not increased. In this way, the power consumption of DELTA during beam operation could be reduced by 100 kW. However, his operating mode is only possible as long as the superconducting wiggler (SCW) is not operated at its maximum field strength of 7 T. Figure 1 shows that more than 12% of the DELTA line power was saved during beam operation this way ever since.

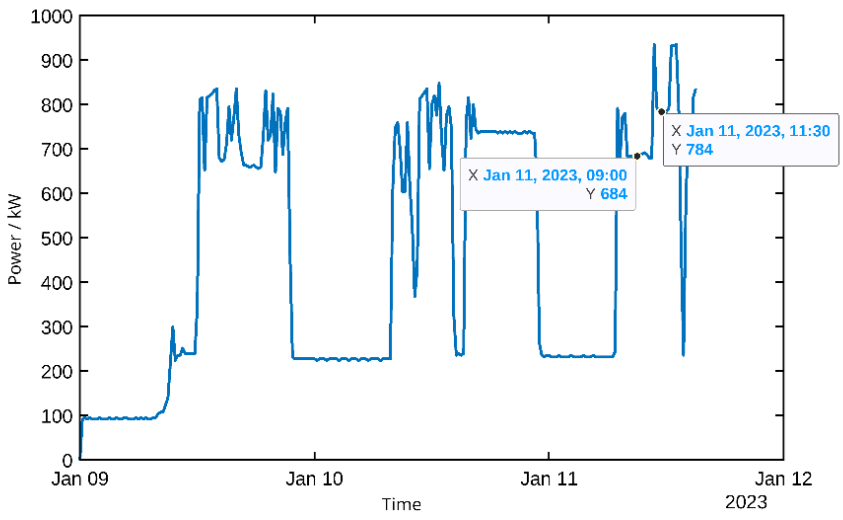

Figure 1: Power consumption of DELTA versus time during accelerator operation. Two labels show the amount of power with the klystron amplifier switched off (left) and on (right). Courtesy C. Mai.

RECENT STATUS OF MACHINE-LEARNING-BASED APPLICATIONS

D. Schirmer, S. Khan, A. Radha Krishnan
Zentrum für Synchrotronstrahlung (DELTA), Technische Universität Dortmund

Introduction: Accelerator facilities are equipped with highly complex control systems with several thousand parameters, some of which must be regulated with high accuracy and within small time scales. Today, artificial intelligence (AI) methods, in particular machine learning (ML) algorithms, support the automatic control, monitoring and diagnosis of accelerator operation. Due to its high availability for accelerator physics studies, the electron storage ring facility DELTA offers an excellent test environment for the development innovative AI-based control and optimization methods. The applications cover a wide range of tasks. The following ML projects have been implemented so far [1]:

- Self-regulating trajectory correction of the stored electron beam [2].
- Feedback systems to control the working points (betatron tunes) and chromaticity values of the storage ring [3-5].
- Optimization of the electron transfer rate from the booster synchrotron (BoDo) to the storage ring (injection optimization) [5-8].
- Spectral analysis of CHG (Coherent Harmonic Generation) radiation [9].

This year, due to reduced machine operating time, ML studies focused mainly on injection optimization and the analysis of CHG spectra.

Injection optimization: At the DELTA storage ring facility, all magnets as well as the radiofrequency power of the booster synchrotron (BoDo) cavity are software-controlled to cyclically ramp up and down. Each of these energy ramp cycles takes about 7 seconds, whereby the electron energy is increased from 90 MeV to 1.5 GeV. Depending on the injection efficiency and the stored beam current in BoDo, typically 150 to 200 ramp cycles are required to reach the maximum beam current of 130 mA in the storage ring. To minimize injection times, optimizing the injection efficiency from BoDo to the storage ring is crucial. Figure 1 shows a typical injection sequence.

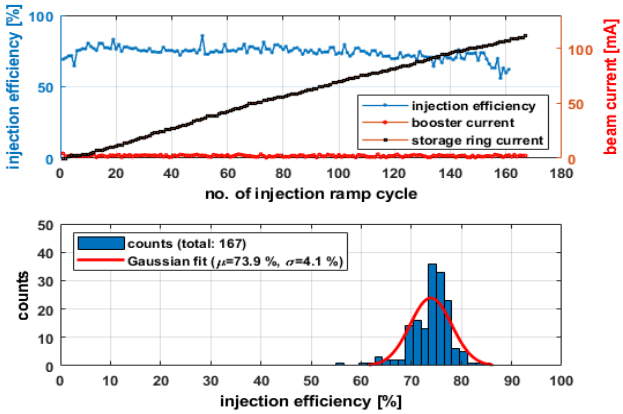

Figure 1: Example of a standard injection sequence at DELTA. Here, 167 booster injection ramp cycles were needed to fill the storage ring from 0 mA up to 111 mA. The averaged injection efficiency is 73.9 % ± 4.1 %. The average booster current amounts to 2.14 mA ± 0.74 mA.

During injection, a variety of parameters must be manually adjusted such as the strength of transfer channel magnets and trigger timings for pulsed injection and extraction elements. Innovative ML concepts were tested to automate this process and improve electron transfer

rates. In two consecutive studies [6,7], initially 13 and later up to 18 injection parameters were slightly varied to identify the corresponding impact on injection efficiency. The measurements served as labeled data for supervised learning of different injection prediction models. In addition to neural networks (NNs), decision trees (DTs) and Gaussian Process Regressors (GPR) were employed as prediction models. Heuristic (e.g., simulated annealing) and statistical (e.g., Bayesian optimization) algorithms utilized these ML-based surrogate models to improve settings between each injection cycle. This process resulted in significant improvements in injection efficiency for both the GPR- and NN-based models within a few injection cycles. Some current examples are shown in Fig. 2. Decision trees were found to be ineffective in this area. Recent results are summarized in [8].

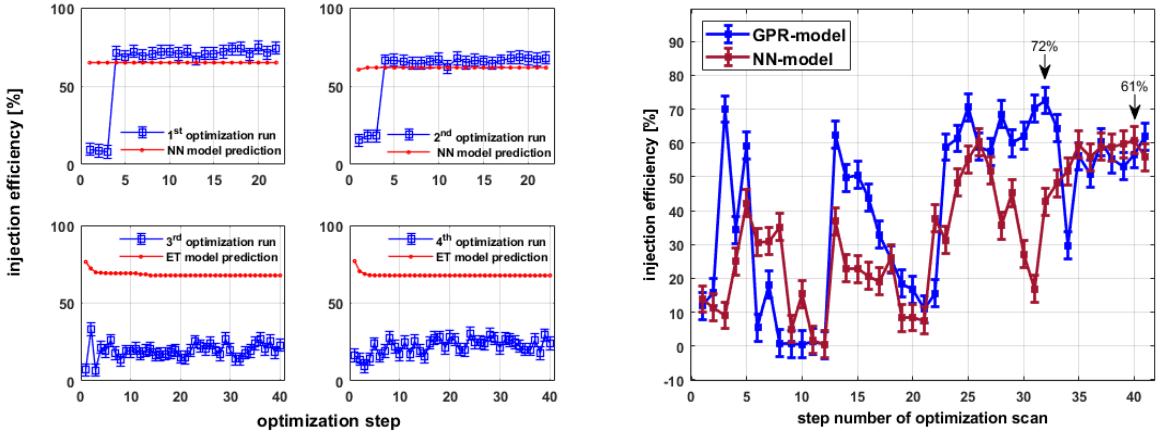

Figure 2: Left: Four examples of injection efficiency optimization runs using neural networks (top: 1st and 2nd run) and Extra Trees (bottom: 3rd and 4th run) as surrogate models. The red lines indicate the prediction of the relating ML-trained model for each optimization step which corresponds to one injection ramp cycle. Right: Injection efficiency optimization scans using Bayesian optimization and applying a Gaussian Process Regressor (GPR) as a surrogate injection model (blue) in comparison to an NN-trained model (red).

References

[1] D. Schirmer, S. Khan, A. Radha Krishnan, *Summary report on machine learning-based applications at the synchrotron light source DELTA*, Proc. of ICALEPCS 2023, Cape Town, South Africa, TUPDP020.

[2] D Schirmer, *A machine learning approach to electron orbit control at the 1.5 GeV synchrotron light source DELTA*, J. Phys.: Conf. Ser. 2420, 012069 (2023).

[3] D. Schirmer, "*Machine learning applied to automated tunes control at the 1.5 GeV synchrotron light source DELTA*", Proc. of IPAC 2021, Campinas, Brazil, pp. 3379-3382.

[4] D. Schirmer, A. Althaus, T. Schüngel, *Machine learning methods for chromaticity control at the 1.5 GeV synchrotron light source DELTA*, Proc. of IPAC 2022, Bangkok, Thailand, pp. 1141-1144.

[5] D. Schirmer, A. Althaus, S. Hüser, S. Khan, T. Schüngel, *Machine learning projects at the 1.5 GeV synchrotron light source DELTA*, Proc. of ICALEPCS 2021, Shanghai, China, pp. 631-635.

[6] S. Hüser, "*Implementierung neuartiger Optimierungsalgorithmen an der Speicherringsanlage DELTA*", Diploma Thesis, TU Dortmund, May 2022.

[7] T. Schüngel, *Development of a Container-Based Work Environment for an Automated Optimization of the Sextupole Settings and Injection Efficiency using Machine-Learning at the Storage Ring DELTA*, Master's Thesis, TU Dortmund University, August 2022.

[8] D. Schirmer, A. Althaus, S. Hüser, S. Khan, T. Schüngel, *Machine learning-based optimization of storage ring injection efficiency*, Proc. of IPAC 2023, Venice, Italy, WEPA106.

[9] A. Radha Krishnan, B. Büsing, A. Held, H. Kaiser, S. Khan, C. Mai, Z. Usfoor, V. Vijayan, *Investigation of spectro-temporal properties of CHG radiation at DELTA*, Proc. of IPAC 2022, Bangkok, Thailand, pp. 1423-1144.

Beam Diagnostics for the New Superconducting Wiggler

P. Hartmann
Zentrum für Synchrotronstrahlung (DELTA), Technische Universität Dortmund

A new superconducting wiggler (SCW) has been installed in the DELTA storage ring [1]. Its internal vacuum chamber profile is adapted to the DELTA beam pipe via two tapers, which are attached upstream and downstream to the SCW. Both tapers contain beam position monitors (BPM) which consist of an arrangement of four detectors (buttons) embedded in the beam chamber. The electron beam circulating in the storage ring induces voltages with an amplitude depending on the distance between the beam and the respective button. The position of the electron beam at the location of the BPM is determined by calculating the horizontal and vertical asymmetry of the signals generates in the four BPM buttons. For example, in the horizontal plane

$$A_x = \frac{(U_{\mathrm{TR}} + U_{\mathrm{BR}}) - (U_{\mathrm{TL}} + U_{\mathrm{BL}})}{U_{\mathrm{TR}} + U_{\mathrm{BR}} + U_{\mathrm{TL}} + U_{\mathrm{BL}}} \qquad \begin{array}{l} \mathrm{T/B} \equiv \text{top/bottom} \\ \mathrm{L/R} \equiv \text{left/right} \end{array}$$

Although the buttons are welded into the steel chamber with high precision by the manufacturer, there is an individual and constant attenuation of the signal strength for each button, e.g., due to slight positioning errors or contact resistances, which lead to systematic errors of the measured beam position. These deviations are taken into account by correction factors a_i for the voltages $\tilde{U}_i$ generated in the buttons:

$$U_i = a_i \cdot \tilde{U}_i .$$

The correction factors are measured experimentally and result in constant offsets added to the measured beam position. The measurement method is described in [2]. The results are:

	horizontal offset (mm)	vertical offset (mm)
upstream taper	0.067	0.314
downstream taper	0.200	0.167

If the position of the beam deviates from the center of the chamber, the asymmetries A_x or A_y are different from zero. These asymmetries are then multiplied by proportionality factors k_x and k_y, the so-called gradient of the BPM, in order to finally obtain the beam position

$$x = k_x \cdot A_x \qquad \text{and} \qquad y = k_y \cdot A_y .$$

The proportionality factors k_x and k_y depend on the arrangement and spacing of the buttons and must be determined experimentally. For this purpose, a thin metal wire is stretched through the taper parallel to the beam direction and can be moved horizontally and vertically at both ends using four micrometer screws. A pulse generator generating a pulse of 20 V amplitude with a duration of approx. 2 ns (FWHM) is connected to the wire. At the transition point from the pulse generator (coaxial output, 50 Ω) to the wire, most of the pulse charge is reflected due to a jump in impedance. Since the impedance of the wire is large but not infinite, a small part of

the pulse charge moves on through the wire and induces an easily measurable voltage in the buttons. The buttons are connected to a four-channel oscilloscope which averages the pulse amplitudes over several signals. Due to the identical button geometry (see Fig. 1) and the very good agreement of two individual measurements, the error-weighted mean values are used for both BPMs, resulting in k_x = 16.7 mm and k_y = 20.9 mm.

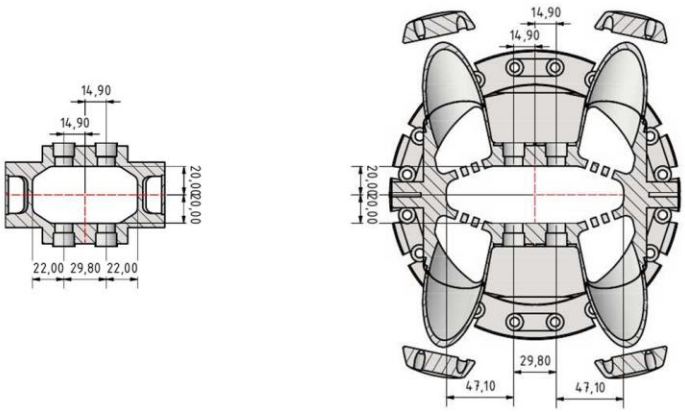

Figure 1: Drawings of the upstream (left) and downstream (right) taper with four BPM buttons at the center (courtesy T. Schulte-Eickhoff, DELTA).

References

[1] G. Schmidt et al., *Installation and Conditioning of the 7-T Superconducting Wiggler at DELTA*, DELTA Annual Report 2020, p. 15.

[2] A. Jankowiak, *Kalibration der DELTA-Strahllagemonitore*, Diplomarbeit, Universität Dortmund (1994).

Single-Electron Operation of the DELTA Storage Ring

S. Khan[1], C. Mai[1], A. Radha Krishnan[1], W. Salah[2], Z. Usfoor[1], V. Vijayan[1]
[1] Zentrum für Synchrotronstrahlung (DELTA), Technische Universität Dortmund
[2] The Hashemite University, Zarqa, Jordan

Single-electron operation of storage rings has been performed at several facilities in the past. Already in the 1960s, distinguished visitors of AdA in Frascati/Italy, the worldwide first e^+e^- collider, were shown that synchrotron light from one electron was visible to the naked eye [1]. The stochastic nature of synchrotron radiation photons from a single electron was studied at VEPP-2 and VEPP-3 in Novosibirsk/Russia [2]. At BESSY and MLS in Berlin/Germany, single electrons are used by the Physikalisch-Technische Bundesanstalt (PTB) for metrology purposes [3], and recently, the motion of single electrons was tracked at the experimental storage ring IOTA of Fermilab in Batavia/USA [4]. Compared to traditional accelerator physics, single-electron operation opens up new opportunities in beam diagnostics and to study the quantum nature of synchrotron radiation.

The knowledge of beam properties, such as the beam size or energy distribution, is usually deduced from the assumed dynamics of single particles under the influence of electromagnetic fields in a storage ring as well as the interaction of particles with the residual gas and among themselves. These assumptions can only be tested by tracking single and few particles. While the experimental study of single hadrons would be difficult, photons emitted by electrons in a dipole magnet or undulator can be easily detected using, e.g., a photomultiplier (PMT) or an avalanche photodiode (APD). Classical electrodynamics describes synchrotron radiation quantitatively rather well as an electromagnetic wave [5], but does not explain the stochastic emission of quanta by individual electrons. The statistical properties of photons provide additional information beyond the classical treatment.

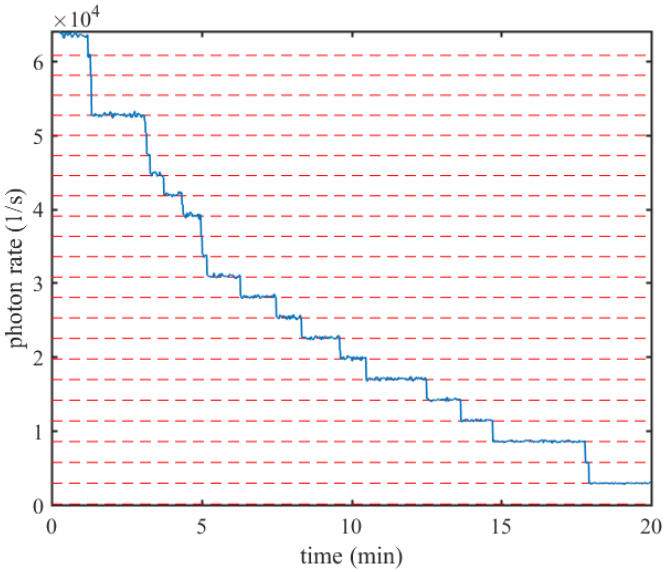

Figure 1: Evolution of the rate of synchrotron radiation photons from a single electron passing the undulator U250 while the electron beam is scraped. Each step corresponds to the loss of one electron.

Since February 2023, the DELTA storage ring has been repeatedly operated with a single or a small number of electrons at an energy of 1.5 GeV. With a revolution time of 384 ns, the "beam" current of one electron is 0.42 pA, while a typical current of 100 mA corresponds to 240 billion electrons circulating in the ring. The mean lifetime of a single electron cannot be

determined in practice, but with radiation desorption and collective effects being absent, it is definitely higher than the typical beam lifetime, which is presently around 30 hours. At beamline BL 4, single photons from the undulator U250 are counted using a PMT [6] connected to a digital oscilloscope sampling the signal every 10 ns over a period of 1 s.

To produce a single-electron beam, a low current is first injected into the storage ring. Given the usual beam lifetime, it would take several weeks until only a single electron is left. Thus, an obstacle (a so-called scraper) is moved close to the beam in order to increase the loss rate. As shown in Fig. 1, the loss of each electron corresponds to a step in the photon counting rate. Retracting the obstacle at the right moment leaves the desired number of electrons in the ring. The steps in Fig. 1 are not equal: While the difference between 21 and 20 electrons is 2700 photons/s, more than 2800 photons/s are detected from the last electron. This is because the photomultiplier does not distinguish between one and several simultaneous photons, the probability of which reduces with decreasing number of electrons. The background from dark counts and residual light is a few 10 photons/s.

The setup was first tested with a moderate single-bunch current and a strongly attenuated beam of synchrotron radiation. Figure 2 demonstrates the good agreement of the measured data with a Poisson distribution and the expected time interval between successive photons. Synchrotron radiation from a single electron was studied under different conditions, and the analysis of the measurements is in progress.

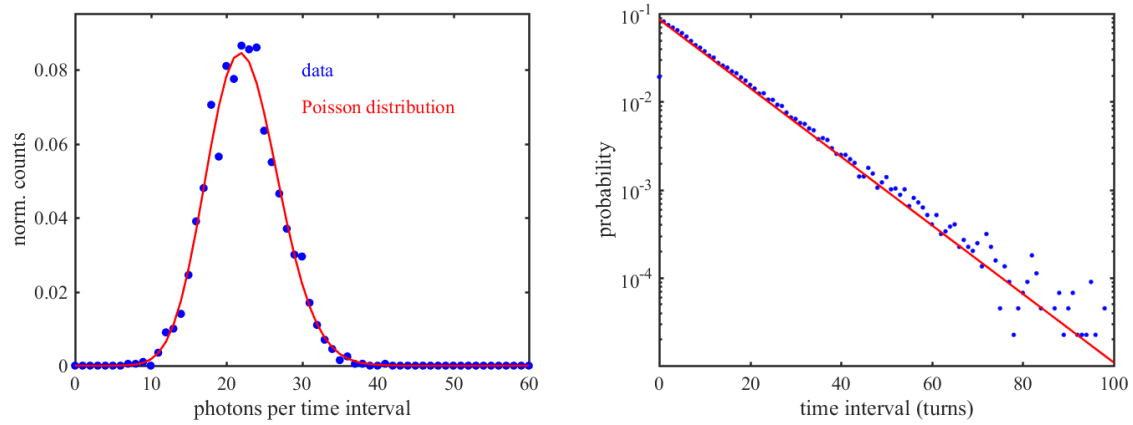

Figure 2: Left: Poisson distribution of synchrotron radiation photons counted in equal time intervals. Right: Measured probability of detecting two successive photons as function of the time interval between them.

References

[1] C. Bernardini, *AdA: the first electron-positron collider*, Phys. Perspect. 6 (2004), p. 156.

[2] I. V. Pinayev et al., *A study of the influence of the stochastic process on the synchrotron oscillations of a single electron circulated in the VEPP-3 storage ring*, Nucl. Instrum. Methods A 375 (1996), p. 71.

[3] R. Klein et al., *Operation of the Metrology Light Source as a primary radiation source standard*, Phys. Rev. ST – Accel. Beams 11, p. 110701 (2008).

[4] I. Lobach et al., *Single electron in a storage ring: a probe into the fundamental properties of synchrotron radiation and a powerful diagnostic tool*, Journal of Instrumentation 17, P02014 (2022).

[5] J. D. Jackson, *Classical Electrodynamics (3rd Edition)*, John Wiley & Sons (1998).

[6] Hamamatsu photon counting head H11870-01.

Space-Charge-Enhanced Energy Modulation at Free-Electron Lasers

S. Khan
Zentrum für Synchrotronstrahlung (DELTA), Technische Universität Dortmund

As an external activity, an experimental investigation [1-3] of the effect of longitudinal space charge (LSC) at FERMI, a free-electron laser (FEL) user facility at *Elettra Sincrotrone Trieste* in Italy [4] was conducted. In this context, a new method to enhance an initially small laser-induced energy modulation is proposed.

Seeding of FELs with laser pulses improves the longitudinal coherence of the FEL output and reduces pulse-to-pulse fluctuations of pulse energy, arrival time, and central wavelength compared to self-amplified spontaneous emission (SASE). In the high-gain harmonic generation (HGHG) scheme [5], the interaction with a laser pulse in a first undulator ("modulator") creates a sinusoidal modulation of the electron energy, which is converted to periodic microbunches in a dispersive section ("chicane") – see Fig. 1 (a). Lasing takes place in a second undulator ("radiator") tuned to a harmonic of the initial seed laser wavelength.

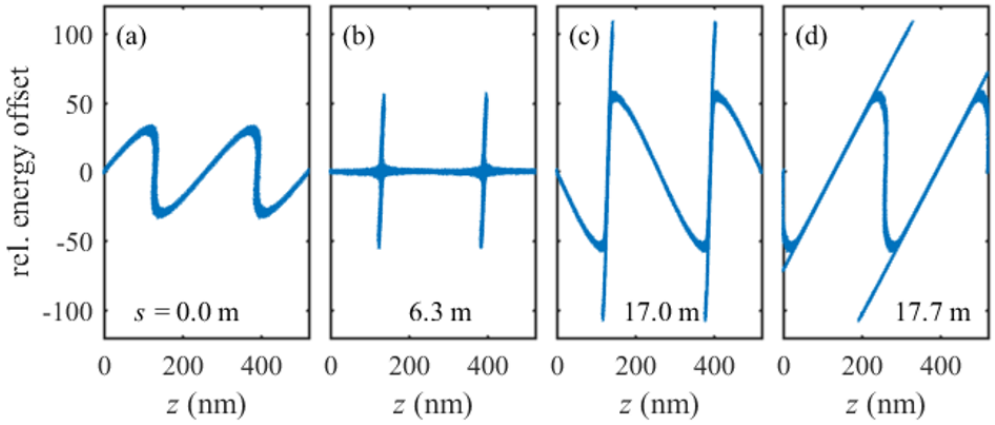

Figure 1: Phase-space distribution of electrons (energy offset versus longitudinal position) after laser-induced energy modulation and a dispersive section (a), after additional drift under the influence of longitudinal space charge (b,c), and after a second dispersive section (d).

If the chicane is followed by a drift section, LSC causes a debunching effect, i.e., it broadens the microbunches, thus reducing their bunching factor. On the other hand, it also flattens the correlated energy spread of the electrons between the microbunches (Fig. 1 (b)), which may be advantageous for harmonic generation [6].

If the drift section is long enough, the correlated energy spread rises again with opposite sign (Fig. 1 (c)), which can be used to create new microbunches in a second chicane (Fig. 1 (d)). Simulation studies suggest that the bunching factor of the new microbunches may be larger than that of the original ones, as shown in Fig. 2 as function of the energy modulation amplitude.

Introducing a second chicane may recover the initial bunching factor after the debunching effect in a drift space. In addition, it may even increase the bunching factor when the initial energy modulation amplitude is small, e.g., in seeded FELs with high repetition rate, where the seed pulse energy is a limiting factor.

An experimental investigation of this yet unexplored regime, in which the correlated energy spread rises with opposite sign, is underway.

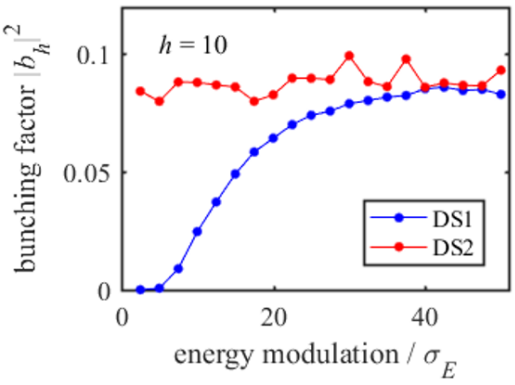

Figure 2: Squared bunching factor of the 10th seed harmonic as function of the laser-induced energy modulation amplitude, calculated directly after a first dispersive section (DS1, blue) and after a 17 m long drift space followed by a second dispersive section (DS2, red).

References

[1] S. Khan et al., *Evolution of microbunching in drift sections*, Proc. of the 40th International Free-Electron Laser Conference (FEL'22), Trieste, Italy, August 2022, paper MOP01.

[2] S. Khan et al., *FEL Microbunching in Drift Sections*, DELTA Annual Report 2022, pp. 21-23.

[3] S. Khan et al., *Space charge effects on density-modulated electron beams in drift spaces*, Proc. of the 14th International Particle Accelerator Conference (IPAC'23), Venice, Italy, May 2023, pp. 1835-1838.

[4] E. Allaria et al., *The FERMI free-electron lasers*, J. Synchrotron Radiation 22, pp. 485-491 (2015).

[5] L. H. Yu, *Generation of intense uv radiation by subharmonically seeded single-pass free-electron lasers*, Phys. Rev. A 44, pp. 5178-5193 (1991).

[6] E. Hemsing et al., *Correlated Energy-Spread Removal with Space Charge for High-Harmonic Generation*, Phys. Rev. Lett. 113, p. 134802 (2014).

Angular Streaking at 1030 nm – measurement of hundred-gigawatt attosecond pulses at European XFEL

L. Funke[1], S. Savio[1], L. Wülfing[1], N. Wieland[1], K. Dingel[4], T. Otto[2], R. Hindrikson[4], L. Marder[4], C. Passow[2], R. Boll[3], A. De Fanis[3], S. Dold[3], T. Mazza[3], D. Raiser[3], M. Meyer[3], T. Mullins[3], M. Ilchen[2,5], W. Helml[1]

[1] Zentrum für Synchrotronstrahlung (DELTA), Technische Universität Dortmund, Germany
[2] Deutsches Elektronen-Synchrotron DESY, Germany
[3] European XFEL GmbH, Schenefeld, Germany
[4] Universität Kassel, Germany
[5] Universität Hamburg, Germany

Introduction: Angular Streaking is a method for characterizing ultrashort X-ray pulses by overlapping the pulse with a circularly polarized IR laser pulse in a noble gas target. Photoelectron momenta are shifted in a characteristic way for a given spectro-temporal X-ray pulse structure. Measuring the photoelectron energy spectra with multiple time-of-flight spectrometers allows the reconstruction of pulse structures, up to a maximum duration of one optical cycle of the IR streaking laser. [1]

Experiment at European XFEL: A *Cookiebox*-type photoelectron spectrometer array (see Figure 1) was set up at the SQS instrument of European XFEL to characterize specially tuned sub-femtosecond soft X-ray FEL pulses. Originally, the proposal planned for a 3.6 µm streaking laser, corresponding to a maximum resolvable pulse duration of 12 fs. Due to technical difficulties, the wavelength was changed to 1030 nm, corresponding to 3.5 fs. In Figure 2, one exemplary shot of the measurement is shown, demonstrating that the special short-pulse mode of the machine provided pulses significantly shorter than the streaking window. The target gas was neon, irradiated with an FEL photon energy of 1010 eV. Due to the high repetition rate of the XFEL, in this case 576 kHz intra-train and 2400 Hz on average, millions of streaked shots were recorded, even though the stability of the partly-improvised laser setup was limited.

The measurements were analyzed ad-hoc using iterative and machine-learning [2] methods, providing near-realtime feedback with regards to a pulse duration to the machine scientists. In Figure 3, an iterative reconstruction of the spectrogram of the same shot as in Figure 2 is shown. An FWHM pulse duration on the order of 350 as is in agreement with this measurement.

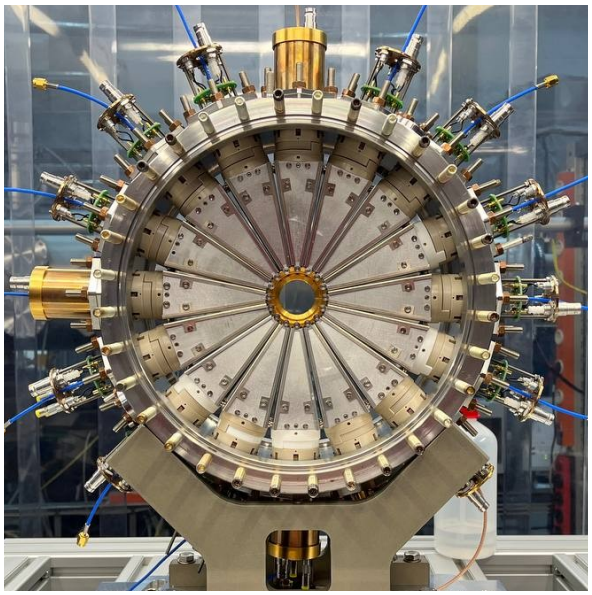

Figure 1: Array of 16 electron time-of-flight spectrometers (*Cookiebox*) used in the experiment. Each spectrometer consists of an electrostatic lens system for focusing and retardation (metallic wedges) and a microchannel plate detector assembly (inside insulating PEEK parts). Neon gas is injected through a gas nozzle (not shown) into the central area of the array.

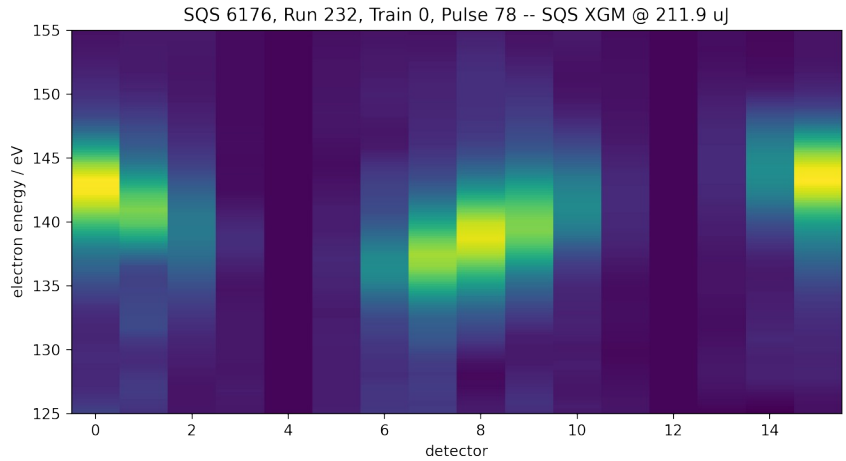

Figure 2: Angle-resolved photoelectron spectrum in a range of ±15 eV around the Neon 1s photoline for one shot with a *streaking kick* of approx. 8 eV. The clearly discernible sinusoidal modulation of electron energies along the 16 detection angles from 0 ° to 337.5 ° perpendicular to the X-ray propagation hints to a pulse duration of only a fraction of the optical cycle (sub-fs).

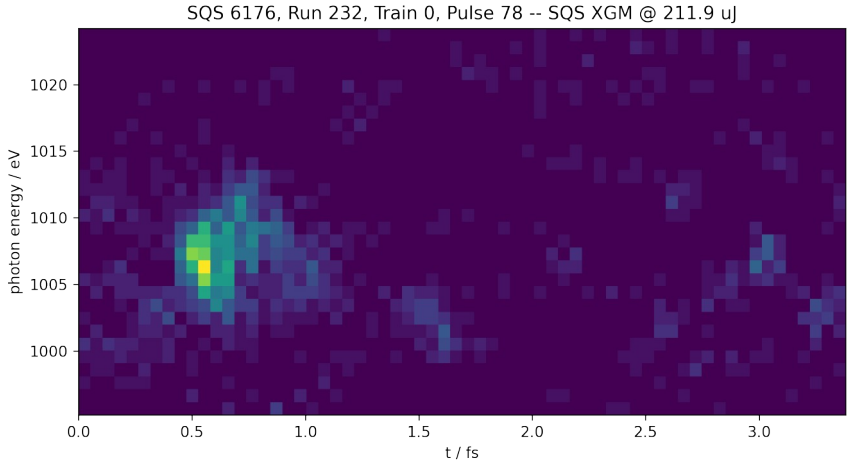

Figure 3: Reconstructed spectrogram of the shot in Figure 2 with the *Pacman* algorithm, iteratively subtracting the strongest contributing sinusoidal component. A pulse duration on the order of 350 as FWHM can be deduced. With an independently measured pulse energy of 212 µJ, this corresponds to a peak power of approx. 500 GW.

Conclusion: In the measurement, we found the most intense attosecond X-ray pulses at European XFEL, with pulse durations on the order of 300 as and a peak power of around 500 GW. The lower-than-planned streaking laser wavelength of 1030 nm turned out to be beneficial for characterizing the ultrashort pulses provided. In view of future experiments, this simplifies the experimental concept, as lower laser wavelengths can be produced readily (without use of an optical parametric amplifier) at more than sufficient intensities.

References

[1] Hartmann, N. et al. *Attosecond time–energy structure of X-ray free-electron laser pulses.* Nature Photonics 12, 215–220 (2018).

[2] Dingel, K. et al. *Artificial intelligence for online characterization of ultrashort X-ray free-electron laser pulses.* Sci Rep 12, 17809 (2022).

First prototype of a time-of-flight electron spectrometer designed for the SpeAR project

A. Held, L. Funke, D. Reinke, S. Savio, N. Wieland, L. Wülfing, W. Helml

Zentrum für Synchrotronstrahlung (DELTA), Technische Universität Dortmund

Introduction: In the BMBF project „SpeAR_XFEL", a detector to employ the technique angular streaking [1,2] is in development. Angular streaking enables a non-invasive measurement of x-ray pulse shapes with sub-fs resolution. To do so, a circularly polarized infrared laser pulse is brought to overlap with the x-ray pulse. With an infrared laser wavelength longer than the whole x-ray pulse, each longitudinal position of the x-ray pulse coincides with a different phase of the infrared laser pulse. In a gas target, photoelectrons generated by the x-ray photons interact with the infrared laser pulse resulting in an energy shift depending on the initial emission direction and the infrared laser phase. By measuring the photoelectron spectra in various different directions, the x-ray pulse shape imprinted in those spectra can be retrieved.

Figure 1: SpeAR vacuum chamber built by Just Vacuum and delivered to the European XFEL in Hamburg.

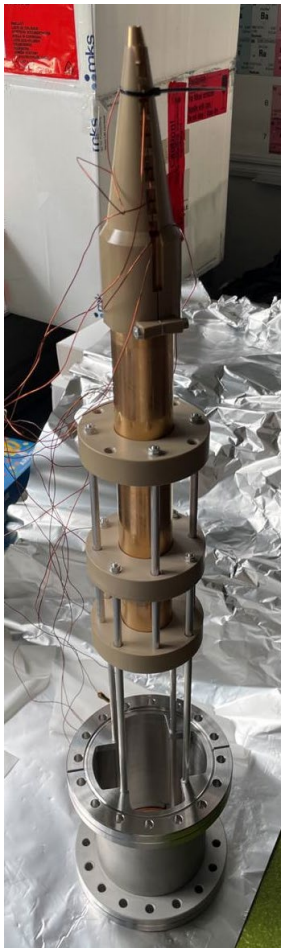

Figure 2: Prototype of the time-of-flight spectrometer designed for the SpeAR project

Progress: Recently, the vacuum chamber designed for the detector has been delivered (see Fig. 1). In its first interaction plane designated to angular streaking, it will be equipped with 16 electron time-of-flight detectors (eToF) for single-shot measurements of photoelectron spectra. In a second interaction plane, a liquid jet experiment will be implemented.

Additionally, a first prototype of the electron time-of-flight detector for angular streaking has been constructed (see Fig. 2). It consists of 6 electrodes and a drift tube made of copper which are held in position by a cone-shaped sleeve made of the vacuum-compatible polymer PEEK. This structure is fixed on custom-made CF100 flanges of a short full nipple by aluminum rods connected to PEEK rings holding the drift tube. At the end of the drift tube, an MCP assembly (Hamamatsu F9890-32) with a time resolution of 450 ps allows the measurement of the electron arrival times and, thus, their energies. Due to the interaction with the infrared laser pulse in angular streaking, the photoelectron spectra are broadened to several 10 eV. To optimize the transmission of electrons from the source point to the MCP for such a broad energy window, the voltages applied to the electrodes resulting in electrostatic lenses and the retardation voltage

applied to the drift tube to enhance the energy resolution are in thorough investigation via simulations [3].

Prototype Experiment: As a first experiment, the general ability of the prototype eToF to measure electron arrival times has been tested. In a temporary setup located just before the experimental chamber at beamline 5 at DELTA, electrons emitted by Argon were investigated. The monochromator of the beamline was set to 260 eV, such that an L-shell electron is emitted via photo emission. The created electron vacancy is then filled by an M-shell electron which results in the emission of another M-shell electron via the Auger-Meitner effect. The energy distribution of electrons emitted in this LMM transition is dominated by two peaks with 203.5 eV and 205.2 eV. The measured time traces for different retardation voltages are shown in Fig. 3. The time axis is shifted such that the so-called "prompt signal", scattered photons traveling with the speed of light directly to the MCP, is at t = 0. In the case without retardation, the arrival time of about 51.2 ns fits with the expected 53 ns given by the distance of 450 mm between interaction point and MCP, when including the 1.5 ns travel time of the prompt signal. When applying retardation voltages, the arrival time shift accordingly while also the number of electrons decreases. This is mostly caused by Earth' magnetic field affecting the trajectory of the low-energy electrons after the retardation. As an example, the radius of curvature of the trajectory of electrons retarded by 90 V is about 1 m in the Earth magnetic field.

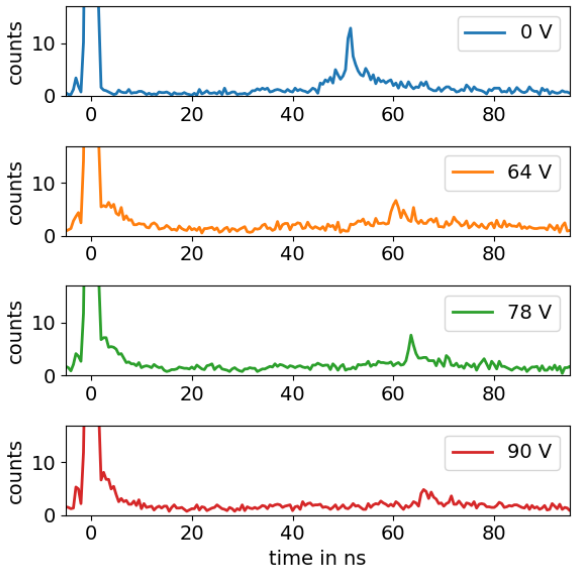

Figure 3:Time traces of LMM Auger-Meitner electrons with different retardation voltages measured with the prototype eToF.

Conclusion and outlook: The prototype eToF proofs the viability of the general concept of the design. The experimental data fits to the expected behavior although the influence of Earth' magnetic field limits the accessible retardation voltages. In the SpeAR vacuum chamber, a mu metal layer shields the inner volume from any outside magnetic field.

Currently, another revision of the eToF which includes minor improvements on the mechanical stability of the components is being designed.

References

[1] E. Constant, V. Taranukhin, A. Stolow, P. Corkum, Methods for the measurement of the duration of high-harmonic pulses. Phys. Rev. A. 56, 3870–3878 (1997).

[2] N. Hartmann et al., Attosecond time–energy structure of X-ray free-electron laser pulses. Nature Photonics 12, 215–220 (2018).

[3] N. Wieland, master's thesis, to be published

Measurement of the Threshold Behavior of Coherent THz Bursts During Low-Energy Operation of DELTA

C. Mai[1], B. Büsing[1], S. Khan[1], A. Radha Krishnan[1], W. Salah[1,2], Z. Usfoor[1], V. Vijayan[1]
[1] Zentrum für Synchrotronstrahlung (DELTA), Technische Universität Dortmund
[2] The Hashemite University, Zarqa, Jordan

Introduction: The emission of THz bursts at high single-bunch current was recently observed for the first time at DELTA. The effect, which was studied at many other facilities (ALS, ANKA, BESSY, MLS – see, e.g., [1]), could not be seen at the DELTA storage ring formerly because the bursting threshold at the nominal beam energy is too high (approx. 20 mA). Generally, the emission threshold of coherent THz bursting can be overcome if a single bunch with high charge is stored. Synchrotron radiation at wavelengths being longer than the emitting charge distribution is emitted coherently. In this case, the spectral power is proportional to the number of electrons squared.

THz Bursts: The coherent synchrotron radiation (CSR) impedance leads to a modulation of the longitudinal phase space distribution above a certain bunch current threshold, which gives rise to the formation of substructures in the longitudinal electron density causing the emission of CSR in the (sub-)THz regime [2]. The influence of a conductive vacuum chamber of height $2h$ on an electron bunch is modeled by the parallel-plates model [3,4]. The threshold bunch current

$$I_{\mathrm{b}}^{\mathrm{th}} = \gamma I_{\mathrm{A}} \sigma_{\delta}^{2} \alpha_{c} R^{-1/3} \sigma_{\mathrm{z},0}^{1/3} \left(0.5 + 0.12 R^{1/2} \sigma_{\mathrm{z},0} h^{-1/3}\right) \qquad (1)$$

with the Lorentz factor γ, the Alvén current $I_{\mathrm{A}} \approx 17$ kA, the relative energy spread σ_{δ}, the momentum compaction factor α_c, the bending radius R and the natural bunch length $\sigma_{\mathrm{z},0}$, describes the single-bunch current above which coherent THz emission can be observed.

Measurement of the Bursting Threshold: The DELTA storage ring is designed for operation at different beam energies up to 1.5 GeV. Recently, after injection at full energy, the beam energy was ramped down to energies between 1.0 GeV and 1.2 GeV. In this regime, the bursting threshold is overcome and coherent THz signals were observed with a Schottky-barrier detector. The emission of THz bursts occurs in different modes which are depicted in Fig. 1. Emission in quasi-continuous mode is observed as well as emission in bursts being separated by several thousand turns (see Fig. 1, right). A more detailed analysis of the bursting behavior is possible in frequency domain: The spectrogram shown in Fig. 2 is calculated by Fourier transformation for different bunch currents.

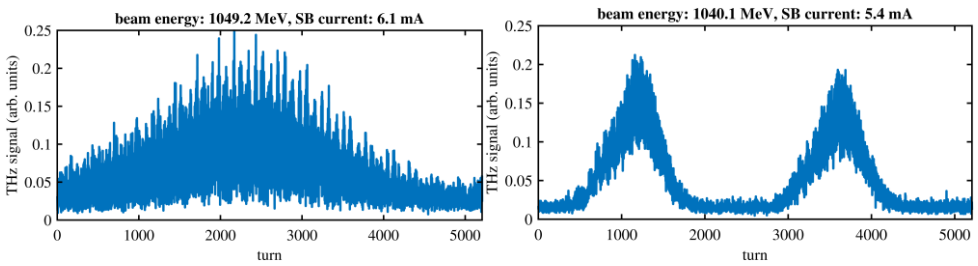

Figure 1: Examples of different THz-bursting regimes. Depending on beam energy and beam current, the coherent emission is observable during each turn (left) or in repetitive bursts (right).

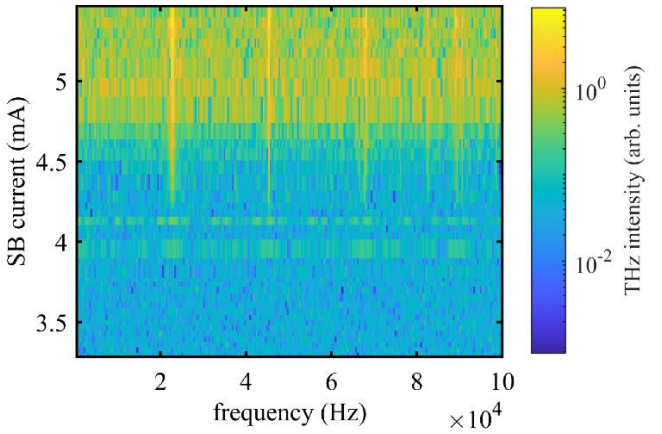

Figure 2: Spectrograms of THz signals as function of the single-bunch current at a beam energy of E = 1.0 GeV (see text for details).

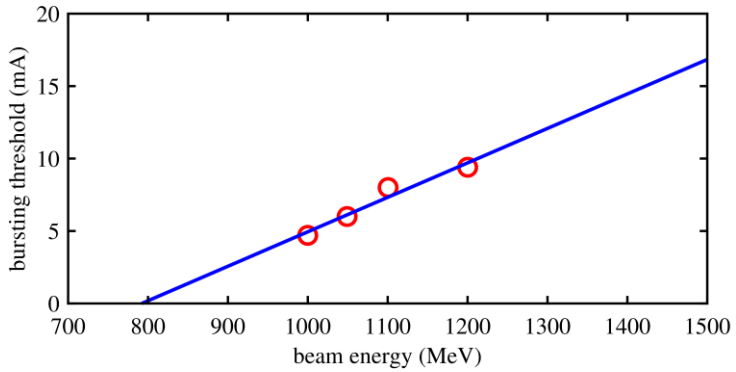

Figure 3: Measurement (red) of the bursting threshold as function of the beam energy and extrapolation to the nominal beam energy of 1.5 GeV.

Typically, at a beam energy of 1.0 GeV, the threshold is about 4.8 mA. Bursts at a frequency of 22.8 kHz and harmonics thereof have a lower threshold of about 4.2 mA. These frequencies are equal to (harmonics of) the synchrotron oscillation frequency [4].

A measurement of the threshold outside the synchrotron oscillation harmonics as function of the beam energy is shown in Fig. 3, which agrees with a linear relation as suggested by Eq. 1. Extrapolating the data to the standard beam energy of 1.5 GeV shows that here the threshold current is about 17 mA – near the practical limit of a single-bunch current at DELTA. The observed THz bursts offer another way to generate short pulses at DELTA, where the high repetition rate of 2.6 MHz is of special interest. Further studies are in progress.

References

[1] M. Ries et al, *THz bursting thresholds measured at the metrology light source*, Proc. of IPAC'12, New Orleans, Louisiana, USA, p. 3030.

[2] G. Stupakov, S. Heifets, *Beam Instability and microbunching due to coherent synchrotron radiation*, Phys. Rev. ST Accel. Beams, p. 054402 (2002).

[3] J. Murphy, S. Krinsky, R. Gluckstern, *Longitudinal wakefield for an electron moving on a circular orbit*, Part. Accel., p. 9 (1997).

[4] M. Brosi et al., *Fast Mapping of terahertz bursting thresholds and characteristics at synchrotron light sources*, Phys. Rev. Accel. Beams 19, p. 110701 (2016).

X-ray diffraction at beamline BL8 of DELTA

Michael Paulus[1,*], Georg Jülicher[1], Thorsten Witt[1], Lena Friedrich[1], Eric Schneider[1], Ralph Wagner,[2] Dirk Lützenkirchen-Hecht[2], Christian Sternemann[1]

[1]Fakultät Physik/DELTA, Technische Universität Dortmund, 44221 Dortmund, Germany
[2]Fakultät für Mathematik und Naturwissenschaften, Bergische Universität Wuppertal, 42097 Wuppertal, Germany.

[*]michael.paulus@tu-dortmund.de

The beamline BL8 of the DELTA synchrotron radiation source, served by the new superconducting wiggler (SCW), is dedicated to material science experiments using X-ray absorption spectroscopy [1, 2]. By a collaborative effort of Bergische Universität Wuppertal and Technische Universität Dortmund, the capabilities of the beamline were extended to applications in the field of wide angle X-ray scattering. A corresponding setup was implemented, commissioned and tested in June 2023 and is available for user experiments since October 2023.

The main component of the setup is a MAR345 image plate detector that is mounted on a Huber xyz-translation stage attached to a support table. This table is fixed behind the diffractometer that is permanently installed at the beamline. The translations allow a detector movement in x, horizontal translation perpendicular to the beam, and z, translation parallel to the beam, of about ±25 mm to align the beam stop and to vary the detector-to-sample distance slightly which is nominally set to 440 mm. The height of the detector can be adjusted using the y-translation in a range +10 mm and -40 mm with respect to the beam position. Hence, the detector can be used in symmetric and asymmetric mode thereby adjusting the achievable wave vector range accordingly. A variety of 3D-printed beam stops of different size equipped with a lead beam catcher is available. The exposure is controlled via a fast shutter system. Both detector and a fast shutter system are controlled via a separate computer accessible at the BL8 control desk. The samples are mounted in the sample stage of the diffractometer and can be adjusted by motorized translational and rotational stages. Currently, the incident energy can be set between 14 keV and 25 keV utilizing the Si (311) double crystal monochromator with a beam size of about 1x1 mm^2 or smaller controlled by a slit system in front of the ionization chamber which measures the incident photon flux. The sample can be aligned with a PIN diode to be mounted between sample and detector. Various sample environments are available such as a Linkam temperature stage, an Anton Paar heating unit and a nitrogen cryostream cooler. The setup is shown in figure 1 a) and the sample stage with installed Linkam heater/cooler in figure 1 b). In a next stage the installation of a vacuum beam path is planned in order to reduce the air scattering significantly, particularly when working at lower incident energies.

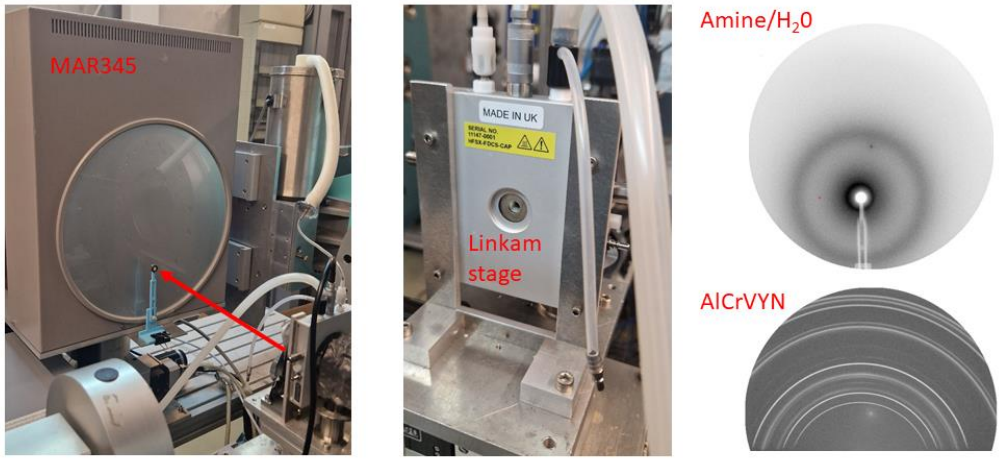

Figure 1: Left: MAR345 detector with beam stop (left) and Linkam temperature stage mounted on the diffractometer sample support (bottom, right) – the beam path of the direct beam is indicated as red arrow. Center: Linkam stage used for temperature dependent X-ray diffraction measurements of amine/water mixtures. Right: MAR images of a water-amine solution (top) and an AlCrVYN coating on a WC-Co support (bottom) measured in transmission and reflection geometry, respectively.

In the following we show selected examples of X-ray diffraction studies carried out so far at BL8 covering investigations of changes in structure formation in amine-water solutions with temperature and of structure modification of AlCrVYN layers on WC-Co substrates during annealing measured.

Hexylamine-water solutions with different water content were studied using wide angle X-ray scattering. These self-associating liquid mixtures show, depending on water content, a strong enhancement of the so-called structure factor pre-peak which can be likewise observed e.g. in branched and linear monohydroxy alcohols [4]. This pre-peak provides information about the formation of transient supramolecular structures in the liquids mediated by hydrogen bonding and

constraint by the alkyl tail of the alcohols/amines. The liquids were filled into capillaries of 1.5 mm diameter and mounted in the Linkam temperature controller. The diffraction patterns were measured using 14 keV incident radiation and a beam size of 1x1 mm^2 with an exposure time of 300 s. The calibrated and integrated diffraction images are presented in figure 2 (left) for pure hexylamine at room temperature and for a hexylamine solution with 20vol% water at temperatures of 30°C, 50°C and 80°C. A pre-peak appears for the pure amine at wave-vector transfer q of about 4 nm^{-1}. This pre-peak is much weaker compared to the corresponding linear alcohol hexanol due to the stronger tendency of the OH group to form hydrogen bonds compared to the amino group. However, the situation changes drastically if water is added. The pre-peak increases and moves to smaller q-values indicating the formation of larger hydrogen-bonded clusters in the presence of water showing a peculiar temperature dependency potentially related to changes in cluster number density. In a next step, these observations will be analyzed and interpreted in terms of transient cluster formation using molecular dynamics simulations of such mixtures.
Functional coatings that feature exceptional high temperature resistance are of utmost relevance for industrial manufacture processes. In this example, AlCrVYN coatings deposited on a WC-Co substrate via combined high power impulse magnetron sputtering (HiPIMS) and direct-current magnetron sputtering (dcMS) were investigated using X-ray diffraction in surface scattering geometry. The incident energy was 20 keV and a beam size of 1.0x0.2 mm^2 (hxv) was used. The angle of incidence was set to 4°. For each sample the MAR345 detector was exposed for 300s. Figure 2 (right) shows the diffraction patterns of two AlCrVYN coatings, one produced using AlCrVY targets (type-1) and the other with separated AlCrY and V targets (type-2) during the HiPIMS/dcMS process. The results show different abundance of CrN and Cr_2N in the coating owing to the variation in target composition.
Both examples demonstrate the versatile capabilities of the new setup available at beamline BL8 to perform wide angle X-ray scattering experiments on crystalline, liquid and amorphous systems at various thermodynamic conditions.

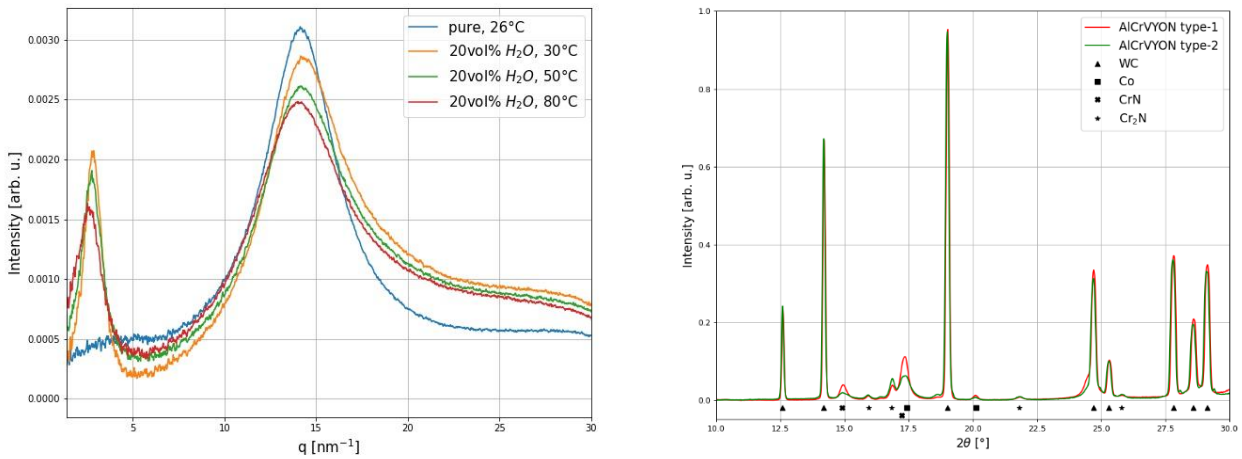

Figure 2: Left: Integrated X-ray diffraction patterns of hexylamine and hexylamine-water solution with 20vol% water. We note the appearance of a pronounced scattering pre-peak when water is added showing a distinct temperature dependency. Right: Integrated X-ray diffraction patters of AlCrVYN coatings on WC-Co produced using different combination of sputter targets during the HiPIMS/dcMS process indicating different abundance of CrN compared to Cr_2N.

References

[1] D. Lützenkirchen-Hecht, R. Wagner, U. Haake, A. Watenphul, R. Frahm, *The materials science X-ray beamline BL8 at the DELTA storage ring*, Journal of Synchrotron Radiation 16, 264 (2009).
[2] R. Frahm, R. Wagner, A. Herdt, D. Lützenkirchen-Hecht, *XAS at the materials science X-ray beamline BL8 at the DELTA storage ring*, Journal of Physics: Conference Series 190, 012040 (2009).
[3] W. Tillmann, D. Kokalj, D. Stangier, M. Paulus, C. Sternemann, M. Tolan, *Investigation on the oxidation behavior of AlCrVxN thin films by means of synchrotron radiation and influence on the high temperature friction*, Applied Surface Science, 427, 511 (2018).
[4] J. Bolle, S.P. Bierwirth, M. Požar, A. Perera, M. Paulus, P. Münzner, C. Albers, S. Dogan, M. Elbers, R. Sakrowski, G. Surmeier, R. Böhmer, M. Tolan, and C. Sternemann, *Isomeric effects in structure formation and dielectric dynamics of different octanols*, Physical Chemistry Chemical Physics 23, 24211 (2021).

Acknowledgments

We thank the DELTA machine group for providing synchrotron radiation and acknowledge F. Ontrup, N.F. Lopes Dias and W. Tillman (Fakultät Maschinenbau, TU Dortmund) for lending AlCrVYN samples for the test experiments. L. Friedrich and C. Sternemann acknowledge the BMBF for funding via DAAD in the scope of the French-German collaboration PROCOPE 2024-2025 (Project-ID 57704875) *Analysis of the molecular coherence in the self-assembly process: experiment and theory*. This work was performed using the radiation supplied by the SCW funded via DFG under INST 212/330-1.

Quick scanning X-ray absorption spectroscopy at DELTA beamline 10

D. Lützenkirchen-Hecht, S. Paripsa, L. Voss, F. Braun, F. Eckelt

Bergische Universität Wuppertal – Fakultät für Mathematik und Naturwissenschaften, Gauß-Str. 20, 42097 Wuppertal, Germany.

Time-resolved X-ray absorption spectroscopy (quick-EXAFS) is a valuable tool to study chemical reactions [1], electrochemical processes such as corrosion [2] or battery charge and discharge [3], and surface phenomena such as thin film growth [4]. EXAFS in general contains short-range order structural information on the vicinity of the X-ray absorbing atom and can thus be applied to crystalline, disordered and amorphous materials, and even liquids can be investigated, offering unique opportunities for in-situ studies accordingly [5]. While conventional EXAFS experiments consist of the step-wise measurement of the absorption around the absorption edge of a selected element for some few seconds for each data-point, in the quick-scanning mode, the spectrum is recorded on-the-fly, while the monochromator Bragg angle is continuously moved, and each datapoint is integrated for some milliseconds only [6]. Thanks to the photon flux available at the superconducting wiggler at DELTA beamline 10, the stable mechanics of the channel-cut monochromator installed there and the short distance to the wiggler source [7], we conducted first quick-scanning EXAFS measurement employing the continuous scan option included in the SPEC beamline software package [8].

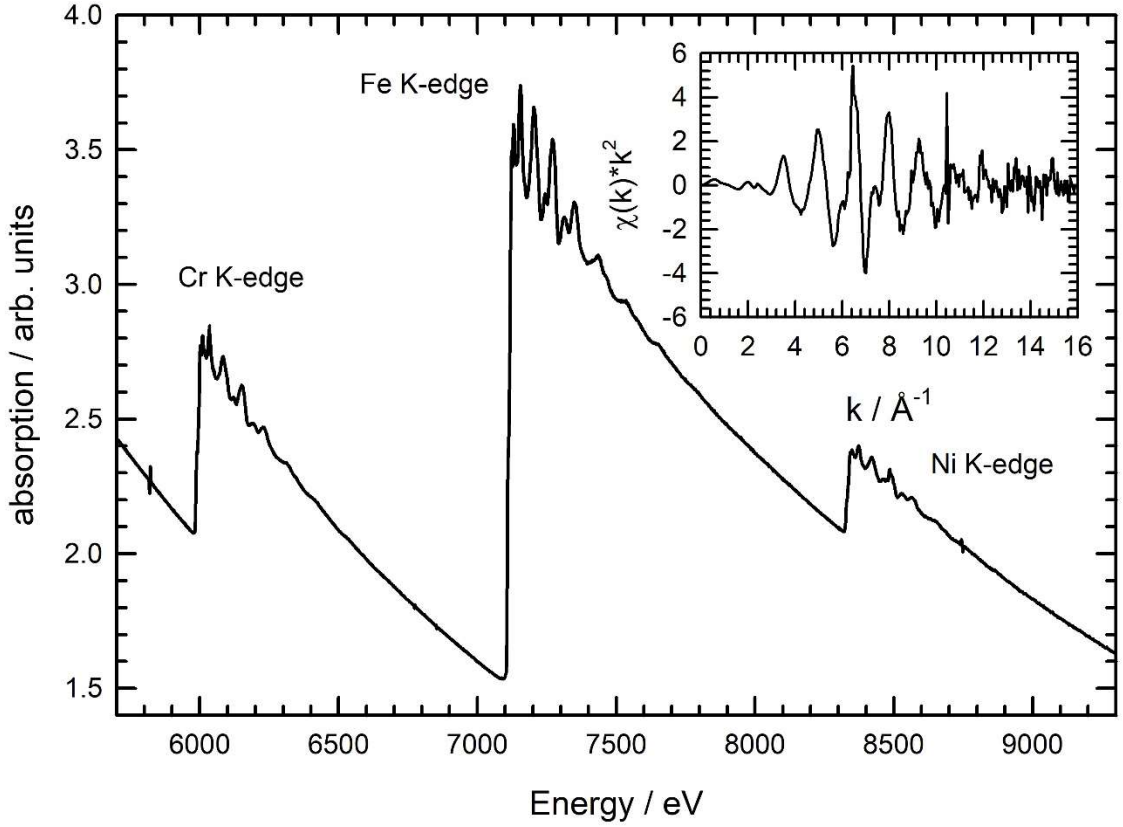

Fig. 1: Quick-scanning EXAFS measurement of a steel sample in transmission mode at room temperature. A total time of 128 s was spent for the measurement of the Cr, Fe and Ni K-edges. In the insert, the k^2-weighted EXAFS fine structures $\chi(k)*k^2$ extracted at the Ni K-edge are shown.

The experiments presented here make use of N_2- and Ar-filled ionization chambers for the measurements of the incident and transmitted X-ray intensities. As a representative sample, we have

used a stainless steel foil, with about 20% Cr, 70% Fe and 10 % Ni. In Fig. 1, a raw spectrum covering the entire range of the Cr, Fe and Ni K-edges spanning over a scan range of 3600 eV (ca. 2500 data points) measured within 128 seconds (i.e. ca. 30 eV/s) is shown. The data quality is excellent, as can be deduced from the extracted, k^3-weighted EXAFS fine structure oscillations $k^2*\chi(k)$ at the Ni K-edge, i.e. the edge of the element with the smallest concentration, are shown. Besides a crystal glitch at about 10.5 $Å^{-1}$, that can also be recognized in the raw absorption spectrum at a photon energy of about 8700 eV, the data are of a quality suited for a detailed analysis even up to 15 $Å^{-1}$.

In Fig. 2, the XANES measured at the Fe K-edge, as well as the $k^3*\chi(k)$ calculated from the fine structure oscillations at the Fe K-edge are presented. For this concentrated element, the edge region data were collected in about 1.5 s only, with excellent signal to noise ratio, and the EXAFS, detected in ca. 40 s, provide clear and almost noise-free fine structure oscillations up to 16 $Å^{-1}$. The obtained results are promising for future applications of the Quick-EXAFS technique at DELTA beamline 10.

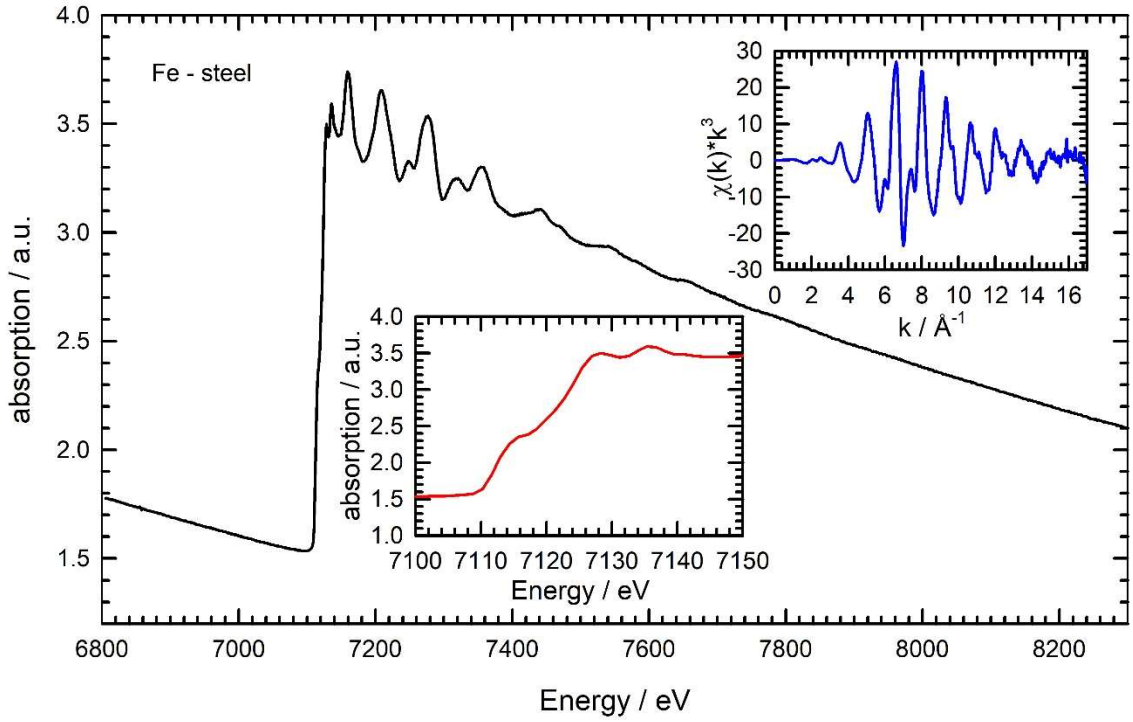

Fig. 2: Fe K-edge of a steel sample measured within 40 s. In the inset, the XANES, measured within ca. 1.5 seconds, revealing clear signatures of the fcc-structure and the calculated, almost noise-free EXAFS oscillations $\chi(k)*k^3$ extracted at the Fe K-edge are provided.

Acknowledgements:

The authors like to thank the DELTA machine group for the delivery of a high-quality beam.

References:

[1] F. Eckelt, P. Rothweiler, L. Voss, et al., Materials 15 (2022) 8186.
[2] D. Lützenkirchen-Hecht, R. Frahm, J. Phys. Chem. B 105 (2001) 9988.
[3] G. Aquilanti, M. Giorgetti, R. Dominko, et al., J. Phys. D: Appl. Phys. 50 (2017) 074001
[4] D. Lützenkirchen-Hecht, J. Stötzel, J. Just, et al., Phys. Stat. Sol. a 219 (2022) 2100514.
[5] D.C. Koningsberger, R. Prins (Eds.): X-Ray Absorption, Principles, Applications, Techniques of EXAFS, SEXAFS and XANES, John Wiley & Sons, New York (1988).
[6] R. Frahm, Nucl. Instrum. Methods Phys. Res. A 270 (1988) 578.
[7] D. Lützenkirchen-Hecht, R. Wagner, S. Szillat, et al., J. Synchrotron Rad. 21 (2014) 819.
[8] Certified Scientific Software, www.certif.com

A high-pressure/high-temperature cell for interface-sensitive X-ray scattering experiments of supercritical fluids

Mike Moron, Susanne Dogan-Surmeier, Marc Moron, Nicola Thiering, Christian Sternemann, Michael Paulus, and Julia Nase

Fakultät Physik/DELTA, TU Dortmund, 44221 Dortmund, Germany

A supercritical fluid (SCF) is a fluid that is above its critical pressure p_{crit} and its critical temperature T_{crit}. At the critical point, there are no longer differences in density or viscosity between the gaseous and liquid phases. This leads to SCFs having similar densities and solvent properties to liquids while having the viscosity of a gas. Understanding the properties of fluids below and above the critical point at solid interfaces is essential to optimise processes in numerous applications, such as heterogeneous catalysis or the oxidation of industrial sludge in supercritical water. However, studying SCFs at interfaces poses technical challenges for a suitable sample environment, as the critical points of many fluids, for example water ($T_{\mathrm{crit}} = 374\,°\mathrm{C}$, $p_{\mathrm{crit}} = 221\,\mathrm{bar}$) or ethanol ($T_{\mathrm{crit}} = 243\,°\mathrm{C}$, $p_{\mathrm{crit}} = 64\,\mathrm{bar}$), are at high pressures and temperatures.

Therefore, in cooperation with the company Dieckers GmbH & Co. KG and SITEC-Sieber Engineering AG, a sample cell was designed and manufactured for the investigation of solid-liquid, solid-gas and solid-SCF interfaces. The sample cell withstands pressures of up to 1000 bar at temperatures up to 500 °C thus enabling the interface-sensitive analysis of a variety of SCFs. A sectional view of the sample cell is shown in Figure 1 a).

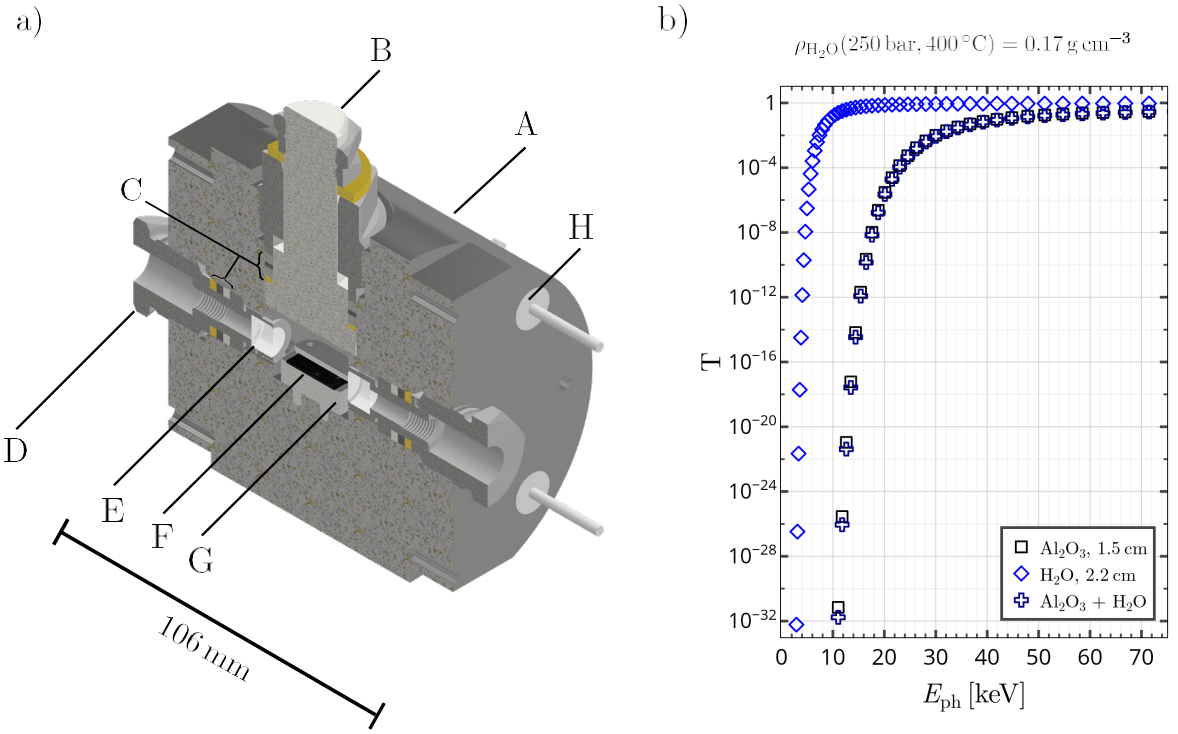

Figure 1: a) Sectional view of the sample cell: A: Incoloy steel body; B: Sealing plug; C: Bridgman type sealings; D: Window unit with E: Sapphire window ($d = 7.5$ mm); F: Sample in G: Sample holder; H: Heating cartridge. b) X-ray transmission T [Henke et al., 1993; Chantler, C. T. et al., 2009] of sapphire windows and of a supercritical water phase at 250 bar and 400 °C ($\rho_{H_2O} = 0.17\,\mathrm{g \cdot cm^{-3}}$) [Lemmon et al., 2023].

The sample cell essentially consists of a cylindrical steel body (A) with a height and a diameter of $H = 106\,\mathrm{mm}$ and $D = 104\,\mathrm{mm}$, respectively. The cell body has three drill holes that hold two, for high photon energy X-rays, transparent window units (D) and a sealing plug (B). Each window unit holds a 7.5 mm thick sapphire window (E). The X-ray transmission of the sapphire

windows and of a supercritical water phase ($\rho_{H_2O}(250\,\text{bar}, 400\,°\text{C} = 0.17\,\text{g}\cdot\text{cm}^{-3})$) are shown in Figure 1 b). For photon energies E_{ph} above 20 keV the transmission of the sapphire windows is above 1×10^{-5}. If a high-density phase, e. g. supercritical water inside the sample cell is present, the transmission of this phase has also to be considered. The sealing plug allows the sample, e. g. a silica substrate, to be placed in the sample volume. The sample (F) is in a holder (G), which is fixed and aligned with two pins in holes in the base of the sample volume. There are two holding jaws above the sample to prevent it from slipping. The sealing plug and the window units have Bridgman type sealing systems (C), that ensure leak tightness in the whole pressure and temperature range. The sample cell can be heated by four heating cartridges (H). The temperature inside the sample cell is measured by a type K thermocouple, which is connected to the sample cell using one of the two $1/4''$-high-pressure-ports (not shown in Figure 1 a)). The thermocouple is connected to a temperature control unit (Eurotherm 3508), so that the heating power can be regulated to reach the target temperature and keep it constant. A temperature stability of up to 0.1 °C can be achieved. For the investigation of solid-liquid or solid-gas interfaces, a liquid can be pumped inside the sample volume via a $1/4''$-high-pressure-port using a hand spindle pump or gas from a gas bottle can be introduced to the sample volume. For the investigation of the solid-SCF interface a liquid, for example water, can be filled into the cell, which is then sealed. If the volume of water is suitably selected, the critical point can be reached by increasing the temperature. Due to the large temperature and pressure range that can be covered with the sample cell, a variety of supercritical systems can be analysed by interface-sensitive X-ray scattering techniques with high photon energy X-ray radiation above 20 keV, as provided by e. g. beamline BL9 at DELTA. The results of these investigations can contribute to a better understanding of the properties of SCFs at interfaces.

References

[Chantler, C. T. et al. 2009]: Chantler, C. T., Olsen, K., Dragoset, R. A., Chang, J., Kishore, A. R., Kotochigova, S. A., and Zucker, D. S. (2009). "X-Ray Form Factor, Attenuation, and Scattering Tables". In: *NIST*.

[Henke et al. 1993]: Henke, B.L., E.M. Gullikson, and J.C. Davis (1993). "X-ray interactions: photoabsorption, scattering, transmission, and reflection at E=50-30000 eV, Z=1-92". In: 54.2, pp. 181–342.

[Lemmon et al. 2023]: Lemmon, Eric W., Ian H. Bell, Marcia L. Huber, and Marc O. McLinden (2023). "Thermophysical Properties of Fluid Systems". In: *NIST Chemistry WebBook, NIST Standard Reference Database*. Ed. by P. J. Linstrom and W. G. Mallard. 69th ed. Gaithersburg MD.

Soft X-ray Spectroscopy

Evolution of monolayer antimony at different temperatures on Ag(110)

S. Hilgers[1,2,*], J. A. Hochhaus[1,2], U. Berges[1,2], and C. Westphal[1,2]

[1] Department of Physics - TU Dortmund University, Otto-Hahn-Str. 4a, 44227 Dortmund
[2] DELTA - TU Dortmund University, Maria-Goeppert-Mayer-Str. 2, 44227 Dortmund
[*] corresponding author: stefanie.hilgers@tu-dortmund.de

In recent years, the study of two-dimensional (2D) materials has drawn the attention of research due to their extraordinary properties. Especially graphene has gained widespread recognition as a prominent 2D material, characterized by its atomically flat honeycomb arrangement of carbon atoms. However, graphene's lack of a bandgap limits its potential for future electronic applications. If we step down the periodic table within the fourth main group, we observe a bandgap increase for 2D-materials like silicene and germanene. This bandgap increase is based on sp^2/sp^3-mixed hybridisation and the so-called buckling [1], which describes that the atoms are not longer arranged in an atomically flat structure, but in a corrugated honeycomb arrangement. Therefore, the structure of 2D-materials determines their electronic properties and is the focus of our investigations.

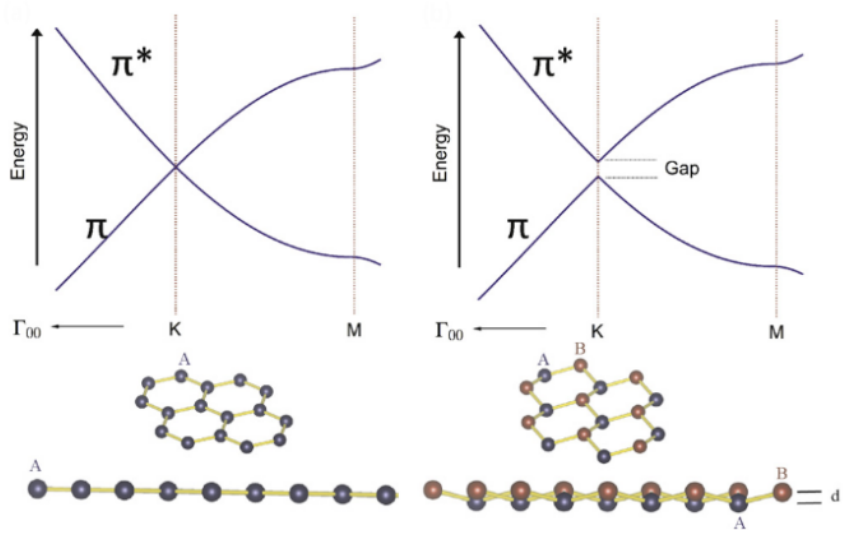

(a) Comparison of the band structure for a flat and buckeld 2D-material [1]

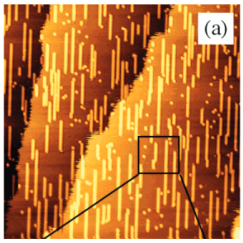

(b) Si on Ag(110) [2]

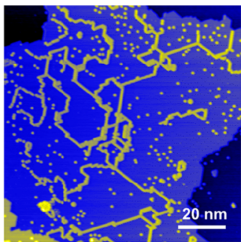

(c) Sb on Ag(111) [3]

Fig. 1: Schematic account of the band structure of 2D materials, as well as STM images of Si- and Sb-nanowires.

A defined current flow direction is essential for future electronic applications, therefore 1D-materials, by structurally determining the possible direction of charge transport, are also of great interest in addition to 2D-materials. Furthermore, not only two-dimensional counterparts of materials from the fourth main group are experimentally known. There are also some one-dimensional structures that have been realized experimentally too, for example silicon nanowires, as shown in 1b [2].
Nevertheless, besides the elements of the fourth main group in low dimensional arrangements, the elements of the fifth main group form low-dimensional structures, too. For example, Sun et al. were able to prepare antimony nanowires on an Ag(111) surface, as indicated in figure 1c [3]. However, these wires are not aligned, which raises the question of whether the Ag(110) surface is more suitable for the growth of nanowires due to its row-like arrangement.

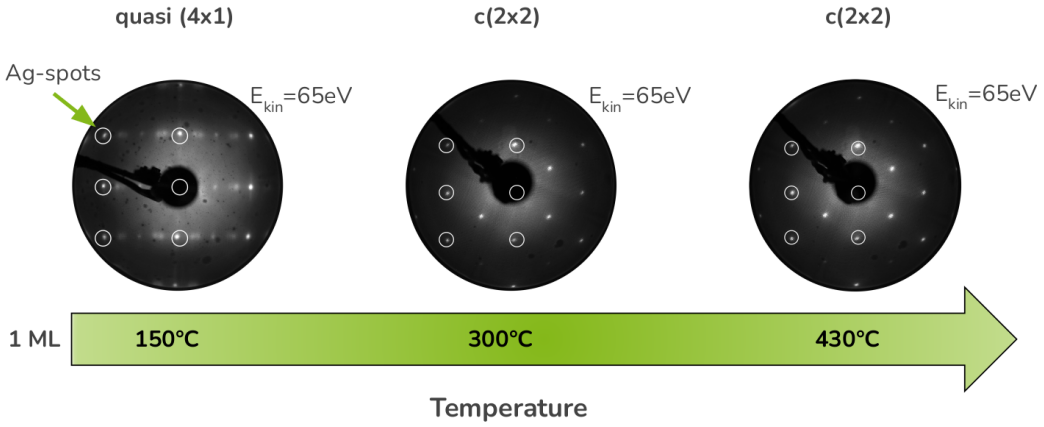

Fig. 2: Structural phase diagram of one monolayer antimony on Ag(110) in dependency of different heating temperatures.

In our analysis, we focus on the structural and chemical investigation of antimony monolayers on the Ag(110) surface at room temperature. Therefore, we use low-energy electron diffraction (LEED) and photoelectron spectroscopy (XPS) as surface sensitive methods. The preparation and measurements are carried out at an UHV-endstation with a base pressure of $p \leq 1 \times 10^{-10}$ mbar at beamline 11 at DELTA.

In figure 2, an overview of the structural arrangements for 1 ML antimony on the Ag(110) surface is given by LEED-patterns. Structurally different phases are observed as a function of the heating temperature. A quasi (4×1)-reconstruction is observed, after heating the sample to 150 °C. Additional heating to 300 °C results in a $c(2 \times 2)$-reconstruction, while further heating to 430 °C does not reveal any differences in the periodicity, as observed by LEED. In order to determine the chemical composition of the observed reconstructions, and to find out whether all observed $c(2 \times 2)$-reconstructions observed for heating at 300 °C and above are all identical, these phases are examined by means of XPS.

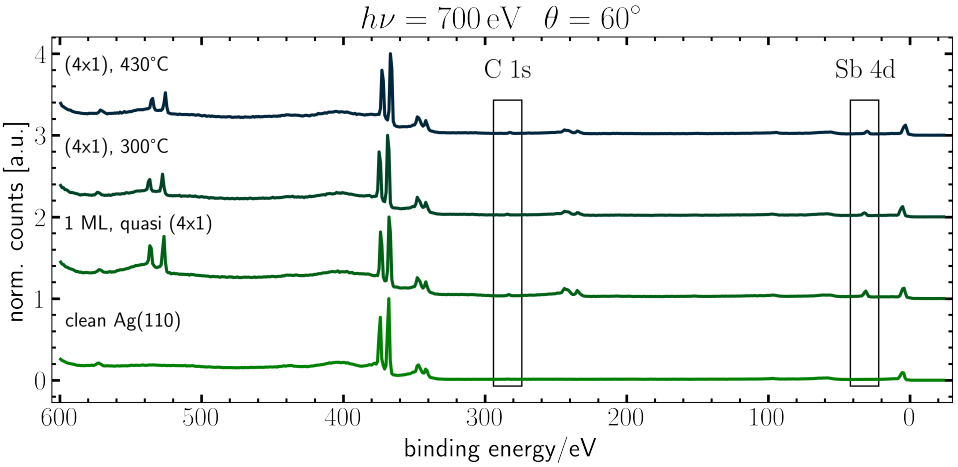

Fig. 3: XPS-survey spectra of the presented antimony phases and additionally of the clean Ag(110) surface, all recorded for an angle of $\theta = 60°$ with respect to the surface normal. No evidence of residual oxygen or carbon contamination was found for all phases. Nevertheless, the spectra differ in the amount of antimony on the Ag(110) sample, which could be explained by desorption of antimony during the heating process.

In figure 3 the XPS-survey spectra indicate that all phases were prepared with high quality, because no evidence of carbon or oxygen residuals were found. In this context, it is important to note that these surveys were recorded under a 60° emission angle, making them highly surface-sensitive.

For a detailed investigation of the Antimony's chemical environment we examine the high-resolution spectra of the Sb4d- and the Ag3d-signal, which are shown in figure 4. For the (4×1)-phase we can identify three components in the Sb-signal. By comparing spectra recorded at normal emission to spectra taken at a polar-angle of $\theta = 60°$ it is evident that atoms to component *CompC* are located upmost at the surface while atoms to *CompA* and *CompB* are located below the surface.

After heating this phase to 300 °C, the structure underwent a transformation, resulting in a $c(2 \times 2)$-reconstruction, as confirmed by LEED. In addition, the high-resolution XPS-spectra in figure 4b also indicates a change of the chemical composition. More precisely, *CompA* of the Sb-signal increases, while the other two components decrease. Also, the second component of the Ag-signal, which is assigned to *Comp1* decreases.

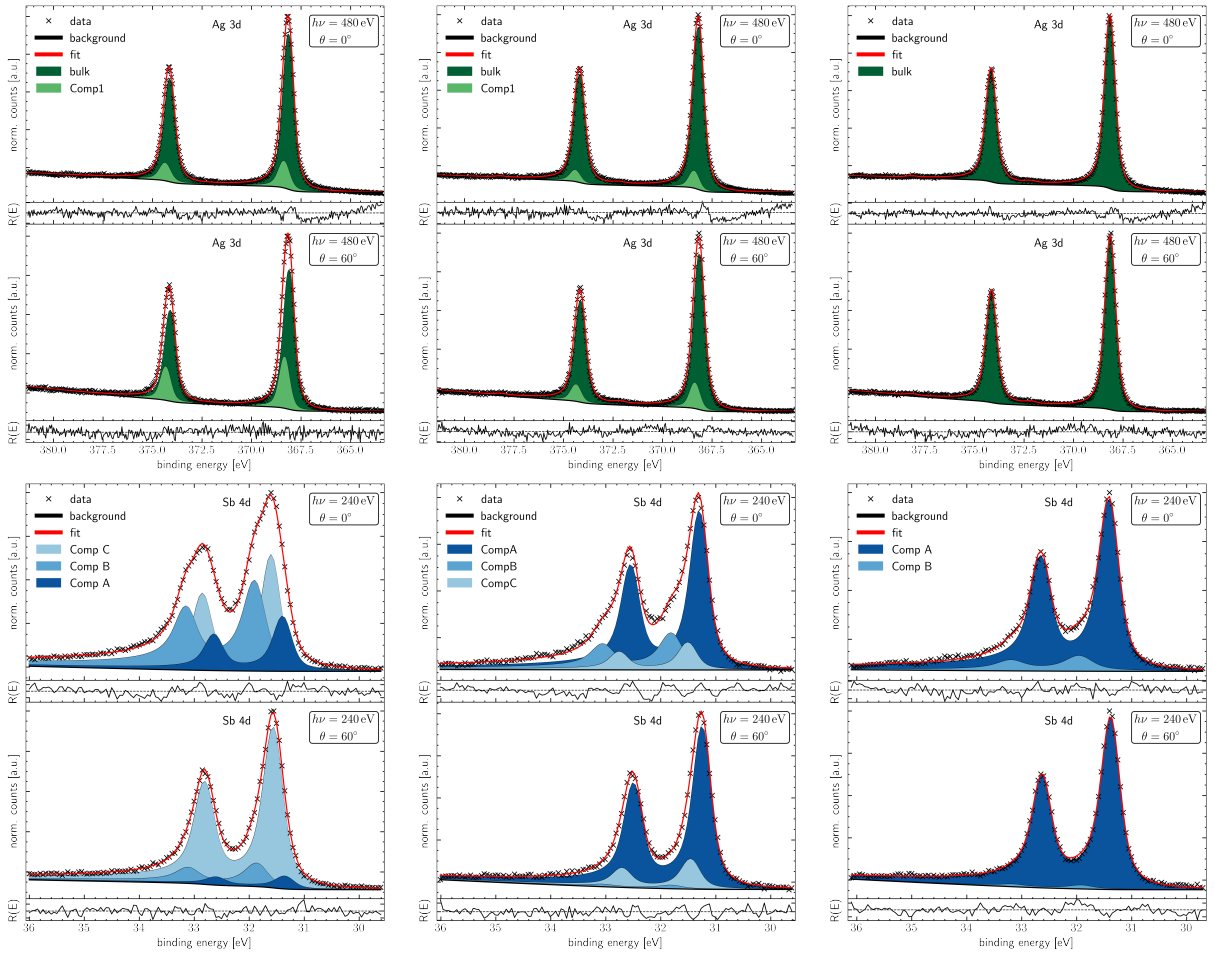

(a) (4×1); 150 °C **(b)** $c(2 \times 2)$; 300 °C **(c)** $c(2 \times 2)$; 430 °C

Fig. 4: High-resolution spectra of all three presented antimony phases. The upper spectra show the Ag3d-signal and the lower ones the Sb4d-signal. **a)** spectra of the (4×1)-phase annealed up to 150 °C; **b)** spectra of the $c(2 \times 2)$-phase annealed up to 300 °C; **c)** spectra of the $c(2 \times 2)$-phase annealed up to 430 °C.

After further heating to 430 °C, no difference in LEED can be observed. However, analysis of the XPS-spectra reveals the presence of two distinct phases. As depicted in figure 4c, the spectra are dominated by *CompA*, while *CompC* is not longer present. Additionally, we observe the signal decrease of the Sb-component *CompC* with the Ag-component *Comp1*. Consequently, we conclude that these components are related to each other. Furthermore, these components can be assigned to the (4×1)-structure, as the loss of this component is accompanied by the disappearance of the (4×1)-structure in LEED.
For a further insight into the Sb/Ag(110) system, the phases as a function of layer-thickness have already been investigated by XPS. Nevertheless, the recorded data need to be analyzed and put into the context to the already presented results.

References

[1] J. Avila, P. D. Padova, S. Cho, I. Colambo, S. Lorcy, C. Quaresima, P. Vogt, A. Resta, G. L. Lay, and M. C. Asensio, J.Phys.: Condens. Matter **25**, 262001 (2013).

[2] P. De Padova, Q. Claudio, P. Perfetti, B. Olivieri, C. Leandri, B. Aufray, S. Vizzini, and G. L. Lay, Nano Lett. **8**, 271 (2008).

[3] S. Sun, T. Yang, Y. Z. Luo, J. Gou, Y. Huang, C. Gu, Z. Ma, X. Lian, S. Duan, A. T. S. Wee, M. Lai, J. L. Zhang, J. Y. Ping, and W. Chen, J. Phys. Chem. Lett. **11**, 8976 (2020).

X-ray Scattering

Pressure-induced deswelling of silica-PNIPAm core-shell particles

Nele Striker[1], Florian Schulz[2], Michael Paulus[3], and Felix Lehmkühler[1]

[1]Deutsches Elektronen-Synchrotron DESY, Hamburg, Germany
[2]Institute of Nanostructure and Solid State Physics, University of Hamburg, Hamburg, Germany
[3]Fakultät Physik/DELTA, TU Dortmund, Dortmund, Germany

Stimuli responsive cross-linked microgel particles offer a plethora of useful applications in technical [1] as well as medical [2] fields. Most of the macrocells react to an external stimulus like temperature or pH. A prominent example is poly (N-isopropylacrylamide) (PNIPAm) which has a lower critical solution temperature (LCST) in water around 32°C leading to a coil-to-globule transition [1,3]. This volume phase transition manifests itself as a rapid decrease of the particle's radius at the LCST. Due to the sharp phase transition and its soft interface pNiPAm microgels have been used in many different fields such as model systems to study the specific phase behavior of soft colloids [4]. A still open question, however, is its structure and especially dynamics at high particle concentrations. Owing to high particle density in these dispersions, particle-particle interactions will affect the structure and dynamics which is crucial for technical applications.

In recent years, we have performed different studies on silica-PNIPAm core-shell systems. Using X-ray photon correlation spectroscopy (XPCS) and small-angle X-ray scattering (SAXS) we studied the structure and dynamics of this systems as function of temperature and particle concentration [5,6], as well as the role of co-solutes [7]. Here, the silica core is the main scattering object in the X-ray scattering experiments. Our results are summarized in Fig. 1 showing a phase diagram of the colloidal system. At low temperature, we found repulsive liquid and glass states. With increasing temperature, the particles deswell and become attractive, supporting the formation of a gel phase.

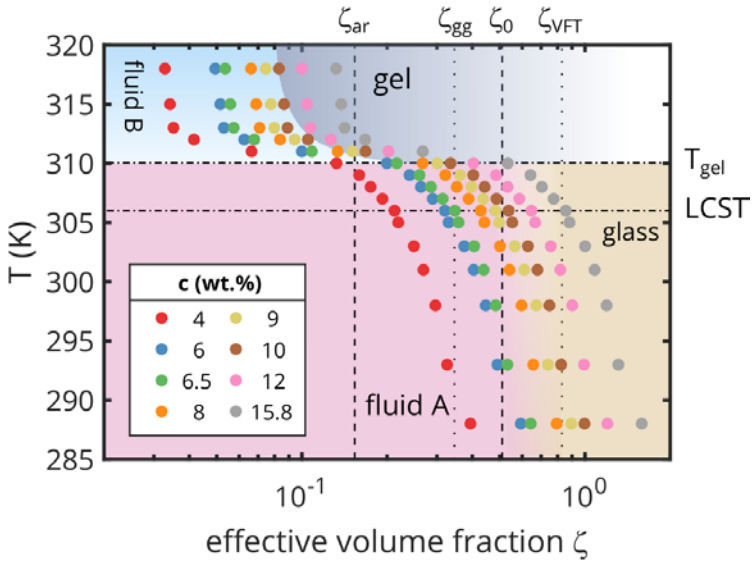

Figure 1: Phase diagram of colloidal silica-PNIPAm particles. Reprinted figure with permission from [6]. Copyright (2021) by the American Physical Society.

Besides temperature, PNIPAm is known the show a response on hydrostatic pressure. Therefore, we performed pressure-dependent studies on the same particle system. The sample system consisted of silica particles with a radius of 50 nm and a pnipam shell with a temperature-dependent thickness of about 100 nm at room temperature and 10 nm above 40 °C. The pressure-dependent SAXS measurements on silica-PNIPAm core-shell particles were carried out at the BL2 beamline at the DELTA synchrotron radiation source in Dortmund [8]. The photon energy was 12 keV and the beam cross-section 0.5 x 0.5 mm^2. A hydrostatic pressure of up to 4 kbar was generated using a special pressure cell [9]. The measurement time per pressure step was 250 s and the distance between the sample and the MAR345

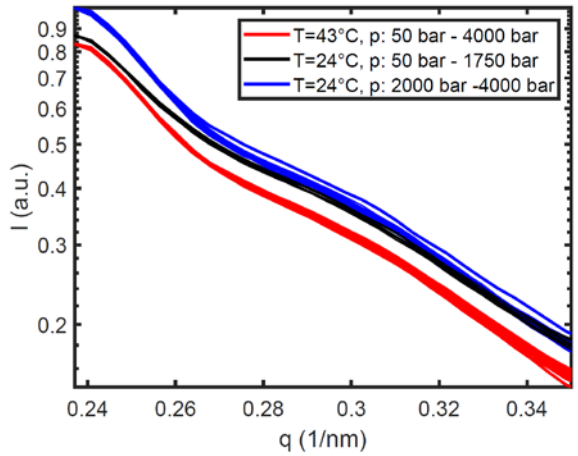

Figure 2: Pressure-dependent SAXS data of silica PNIPAm particles measured at 24°C and 45°C.

detector was 1500 mm. The samples temperature was controlled by a heat exchanger connected to the pressure cell via water pipes. The measurements were carried out in 250 bar steps at a temperature of 24°C and 45°C. A silver behenate sample was used for the calibration of the setup. To determine the scattering background, corresponding pressure-dependent measurements were carried out on water, which were subtracted from the sample data. Figure 1 shows two pressure series taken at 24°C and 45°C. The 45°C series was shifted downwards by a constant factor. While the measurements at elevated temperature show no pressure dependence, the series of measurements at 24°C can be divided into two different pressure ranges. While the high- pressure range of the data between 2000 bar and 4000 bar shows a similar course to the measurements at 45°C, the low- pressure range between 50 bar and 1750 bar shows a reduction of the scattering intensity at small wave vector transfers q, which suggests a more repulsive interaction between the particles compared to the other measurements.

Afterwards, we performed pressure-dependent XPCS experiments at P10 of PETRA III on the same sample system. Correlation functions g_2 are shown for different pressures in Fig. 3. At 2000 bar we observe a slow-down of the dynamics by more than one order of magnitude. This is similar to the behavior at high temperatures where the sample system was found to form a colloidal gel, and is in line with the SAXS results discussed above. Further analysis of structure and dynamics is currently ongoing.

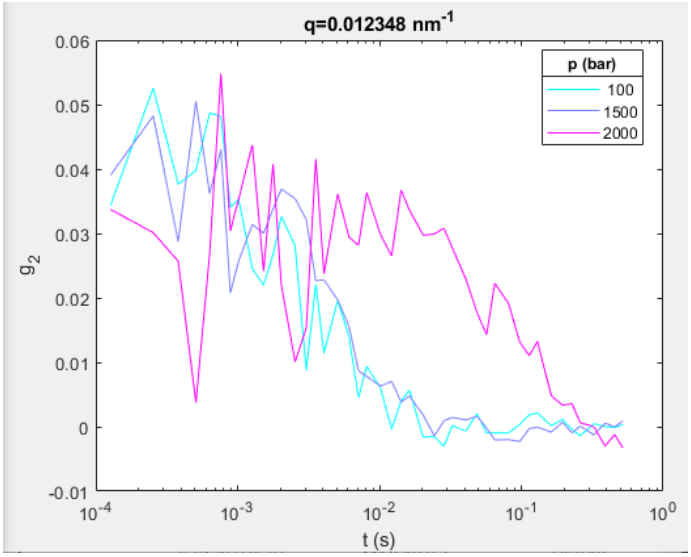

Figure 3: XPCS results. Correlation functions g2 at q=0.0123 nm-1 and three pressures as indicated.

References

[1] M. Das et al. Annu. Rev. Mater. Res. 36, 117 (2006).
[2] Y. Guan et al. Soft Matter 7, 6375 (2011).
[3] C. Lian et al. J. Col. Int. Sci. 406, 148 (2013).
[4] P.S. Mohanty et al. J. Phys. Chem B 112, 14692 (2008). T. Eckert et al. J. Chem. Phys. 129, 124902 (2008). M. Karg et al. Langmuir 35, 6231 (2019).
[5] F. Lehmkühler et al. IUCrJ 5, 801 (2018). L. Frenzel et al. J. Phys. Chem. Lett. 10, 5231 (2019); L. Frenzel et al. Soft Matter 16, 2864 (2020).
[6] L. Frenzel et al. Phys. Rev. E 104, L012602 (2021). Doi:10.1103/PhysRevE.104.L012602.
[7] L. Frenzel et al. ChemPhysChem 21, 1318 (2020).
[8] M. Dargasz et al. Journal of Physics: Conference Series 2380, 012031 (2022).
[9] C. Krywka et al. ChemPhysChem 9, 2809 (2008).

Investigation of the interaction of hyaluronan and albumin at high hydrostatic pressures

D.C.F. Wieland[1], Jaqueline Savelkouls[2], Felix Lehmkühler[3], Michael Paulus[2]

[1]Helmholtz-Zentrum hereon (Außenstelle am DESY), Institute for Metallic Biomaterials, Notkestr.85, 22607 Hamburg, Germany

[2]Fakultät Physik/DELTA, TU Dortmund, 44221 Dortmund, Germany

[3]Deutsches Elektronen-Synchrotron (Photon Science), Notkestr. 85, 22607 Hamburg, Germany

The origin for the exceptional good lubrication properties in articular joints stems from the self-organization of the constituents in synovial fluid (SF) and at the surface of the cartilage [1]. The components of the SF account for different load and shear conditions by re-structuring and thereby provide extremely low friction coefficients under low and high pressures up to several tens of MPa [2]. The friction coefficients found are the lowest in nature and have not been reproduced by technical systems yet [3]. The components in the SF are mainly hyaluronic acid (HA), phospholipids, albumin and proteoglycans (aggrecan and lubricin) [2,3]. Every of these components is known to reduce friction on its own, but up to now, little is known about the self-assembly and synergistic effects of the components which lead to the extraordinary lubricating properties of the SF. Thus, it is of high relevance to investigate the impact of different factors like composition and parameters like pressure on the interactions and formed structure. Hyaluronic acid is an unbranched polysaccharide having carboxylate groups and, thus, being charged at distinct solution conditions. Consequently, it is able to form different associate structures with the other constituents of the synovial fluid. In order to better understand the mechanisms, we have investigated the structure of HA at different concentrations and solution conditions. In the next step, we checked the influence of pressure on the structure of human serum albumin (HSA) at near-physiological conditions (150 mM NaCl). Here we used two different albumins either with bound lipids and without to test the impact on the interaction.

We performed SAXS measurement at the beamline BL9 with a photon energy of 12 keV and a distance of 1500 mm. A MAR345 image plate detector was used to collect the scattered data. We could acquire a q-range from 0.25 to 3 nm^{-1}. HA was measured in MilliQ water (resistivity 18.8MΩ) with different concentrations. HA was purchased from Creative PEG Works, having a molecular weight of 250k. Further measurements were done in 200 mM NaCl (Sigma-Aldrich, Germany). For the investigation of formed associate structures, we used two different HSA bought from Sigma Aldrich either with fatty acids (A8763) and without fatty acids (A3782).

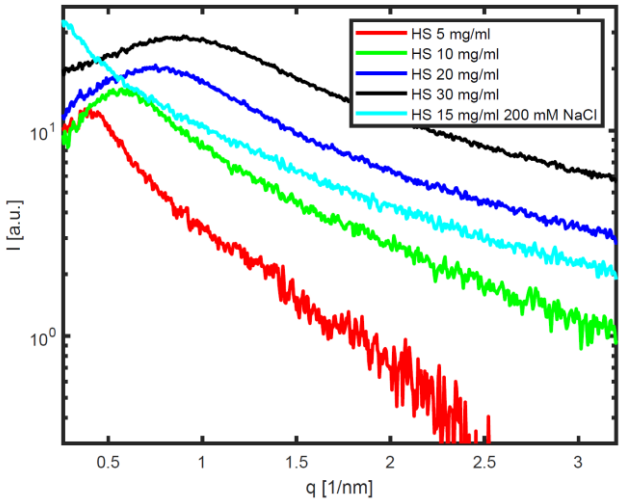

Figure 1: SAXS data for different HS concentrations and with the addition of 200 mM NaCl.

Figure 1 shows the SAXS curves of HA having a MW of 250 K at different concentrations up to 30 mg/mL. The SAXS curves show a peak which changes its position towards higher q values with an increase in concentration. This observation can be explained by the fact that at this solution condition, the carboxylate group is deprotonated and HA is charged [4]. Thus, a repulsive interaction between the change exists becoming apparent in the formation of a structure factor (polyelectrolyte peak) [4,5]. The shift in the

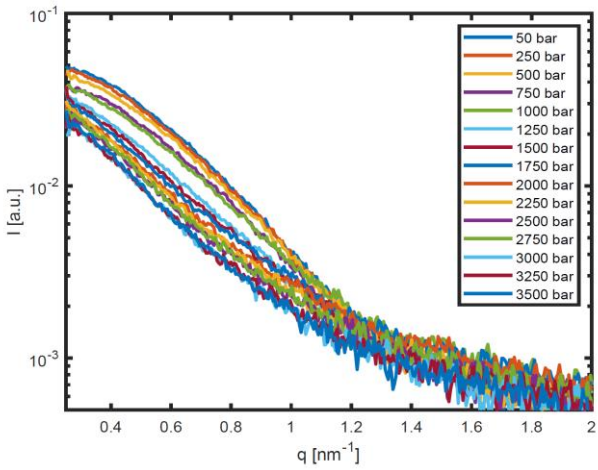

Figure 3:pressure dependent SAXS data from fatty acid free HSA

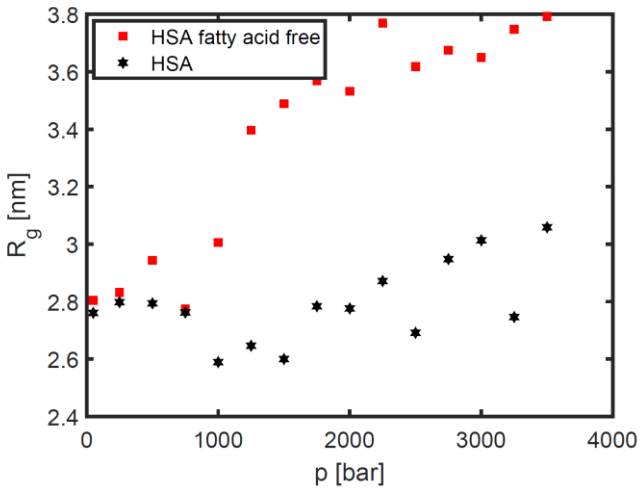

Figure 3: Pressure-dependent gyration radius of the two HSA samples examined. The gyration radii were determined by a Guinier analysis of the SAXS data at low q values.

position of this polyelectrolyte peak is caused by the increase in the concentration and, thus, a smaller distance between the HA chains. Changing the solution conditions to meet more physiological conditions (addition of NaCl) the polyelectrolyte peak vanishes and decay can be seen. Now, the charge of the HA chain is completely screened at this condition suppressing the repulsive interaction. Here HA just behaves like a random coil [5].

In the next step, we tested the effect of pressure on different types of albumin. Figure 2 shows the pressure dependent SAXS data of fatty acid free HSA while figure 3 the evaluated radius of gyration from the SAXS curves. By comparing HSA with and without fatty acids, we see that HSA with fatty acid is more stable against pressure, whereas the albumin without fatty acid shows a strong increase in the R_g around 1.25 kbar which is an indication for denaturation. This clearly demonstrates that fatty acid stabilize the protein.

In summary, we have tested the effect of pressure on HA and HSA. We could observe that HA shows strong inter and intra-chain interactions as the polyelectrolyte peak is visible at no salt conditions. By adding 200 mM NaCl we can see that this electrostatic interaction is completely screened. HSA without fatty acids exhibit a denaturation by pressure increase above 1250 bar. Lipids can increase the stability allowing the structure to be stable up to 3000 bar.

Acknowledgment

We thank the DELTA team for providing synchrotron radiation.

References
[1] A.R.C. Jones et al. Binding and localization of recombinant lubricin to articular cartilage surfaces. Journal of Orthopaedic Research 25, 283-292 (2007) (10.1002/jor.20325).
[2] S. Lee et al. Sweet, hairy, soft, and slippery. Science 319, 575-576 (2008) (10.1126/science.1153273).
[3] C. Liu et al. Hyaluronan and phospholipids in boundary lubrication. Soft Matter 8, 10241-10244 (2012) (10.1039/C2SM26615F).
[4] Camara CI et al. Hyaluronic Acid-Dexamethasone Nanoparticles for Local Adjunct Therapy of Lung Inflammation. International journal of molecular sciences., 22, 10480 (2021)
[5] M. Villetti et al. SAXS from polyelectrolyte solutions under shear: Xanthan and Na-hyaluronate examples. Macromolecules 33, 9418-9422 (2000)

Observation of Pressure-Induced Phase Transitions in Flexible Metal-Organic Frameworks by Powder X-ray Diffraction on Beamline BL9

Mariia Maliuta[1], Joohan Nam[2], Pascal Kolodzeiski[3], Vitaly Romaka[1], Samuel J. Baxter[4], Jack D. Evans[5], Leila Abylgazina[1], Wenlong Xue[3], Eunji Jin[1], Michael Paulus[6], Christian Sternemann[6], Stefan Kaskel[1], Sebastian Henke[3], Irena Senkovska[1], Wonyoung Choe[2] and Andreas Schneemann[1,*]

[1]Anorganische Chemie I, Technische Universität Dresden, Bergstr. 66, 01069 Dresden, Germany.
[2]Department of Chemistry, Ulsan National Institute of Science and Technology, 50 UNIST, Ulsan 44919, Republic of Korea.
[3]Anorganische Chemie, Fakultät für Chemie und Chemische Biologie, Technische Universität Dortmund, Otto-Hahn-Straße 6, 44227 Dortmund, Germany.
[4]School of Chemistry and Biochemistry, Georgia Institute of Technology, Atlanta, GA 30332, USA.
[5]Department of Chemistry, The University of Adelaide, Adelaide3800, Australia.
[6]Fakultät Physik/DELTA, Technische Universität Dortmund, Maria-Goeppert-Mayer Str. 2, 44221 Dortmund, Germany.
E-Mail: Andreas.Schneemann@tu-dresden.de

I - Crystal Size Dependent Response to Hydrostatic Pressure in DUT-8

The influence of the particle size on the mechanical response of the flexible metal-organic framework DUT-8(Cu) ($Cu_2(ndc)_2(dabco)$ with ndc^{2-} = 2,6-naphthalenedicarboxylate and dabco = diazabicyclo[2.2.2]octane) was analysed using a hydraulic pressure jump cell for in-situ powder X-ray diffraction experiments. Interestingly, for the material featuring macrosized crystals a phase transition from an open pore state to a much denser, closed pore state can be observed when the pressure is gradually increased, while for submicron sized crystals the material is significantly stiffer and the material remains in the open pore state over the entire applied pressure range. Furthermore, extraction of the cell parameters by Pawley Refinements also allowed the determination of the bulk modulus. Interestingly, the small particles showed a higher bulk modulus and hence a higher stiffness, which is also reflected in their phase transition behavior (see Figure 1).

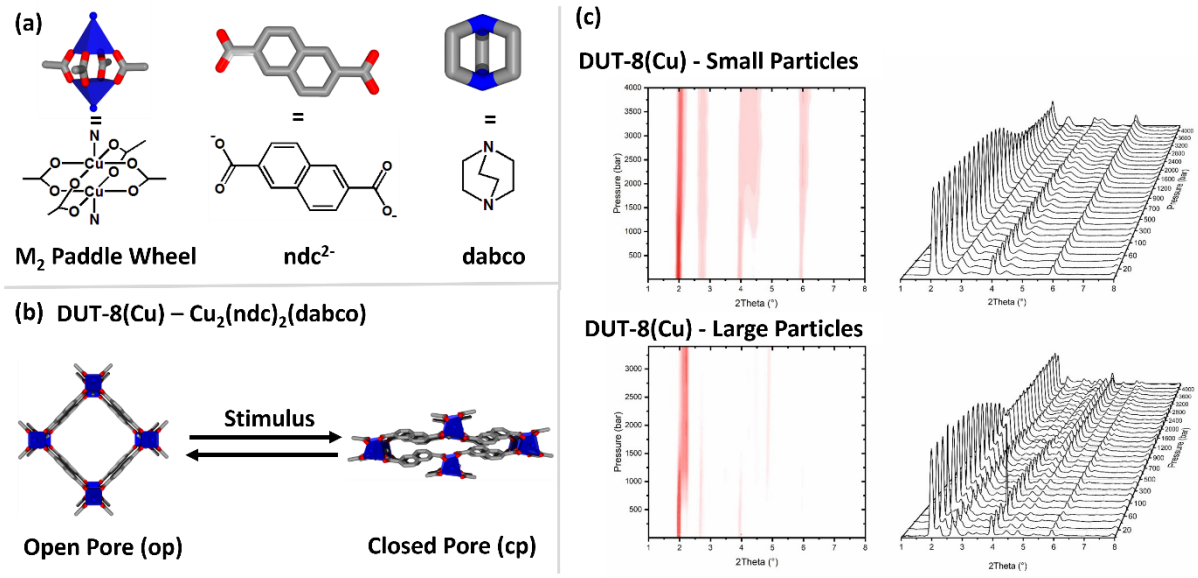

Figure 1. (a) Building blocks of DUT-8(Cu) and (b) graphical depiction of the phase transition from the open pore to the closed pore phase occurring upon hydrostatic pressure. Carbon is represented in grey, oxygen in red, and nitrogen in blue. Blue polyhedral represent the coordination environment around Cu. Hydrogens are omitted for clarity. (c) Contour plot and waterfall diagram of the pressure dependent powder X-ray diffraction patterns of small and large particles of DUT-8(Cu).

M. Maliuta, P. Kolodzeiski, V. Romaka, S. J. Baxter, J.D. Evans, L. Abylgazina, W. Xue, M. Paulus, C. Sternemann, S. Kaskel, S. Henke, I. Senkovska, and A. Schneemann, **2023**, *in preparation*

II - Anisotropic Compression of a Flexible Zeolititc Imidazolate Framework

Using variable-pressure synchrotron powder X-ray diffraction technique, we successfully demonstrated high-pressure mechanics of flexible zeolitic imidazolate framework (ZIF) with **gis** topology (0 to 0.4 GPa, total 29 pts). All the data profiles were refined by Le Bail method, and we demonstrated the anisotropic compression of gis-ZIF along *c* direction, with anisotropic linear compressibility. To analyze the anisotropic mechanics in detail, we conducted Rietveld refinement for 5 pts from 0 to 0.4 GPa, with 0.1 GPa interval. In the series of data, all R_{wp} values are under 0.05. We have revealed that the origin of this high-pressure mechanics is unique selective deformation within the ZIF structure, and we are trying to link this phenomenon to gas adoption property (see Figure 2).

J. Nam, E. Jin, A. Schneemann, W. Choe, et. al. *Manuscript in Preparation*

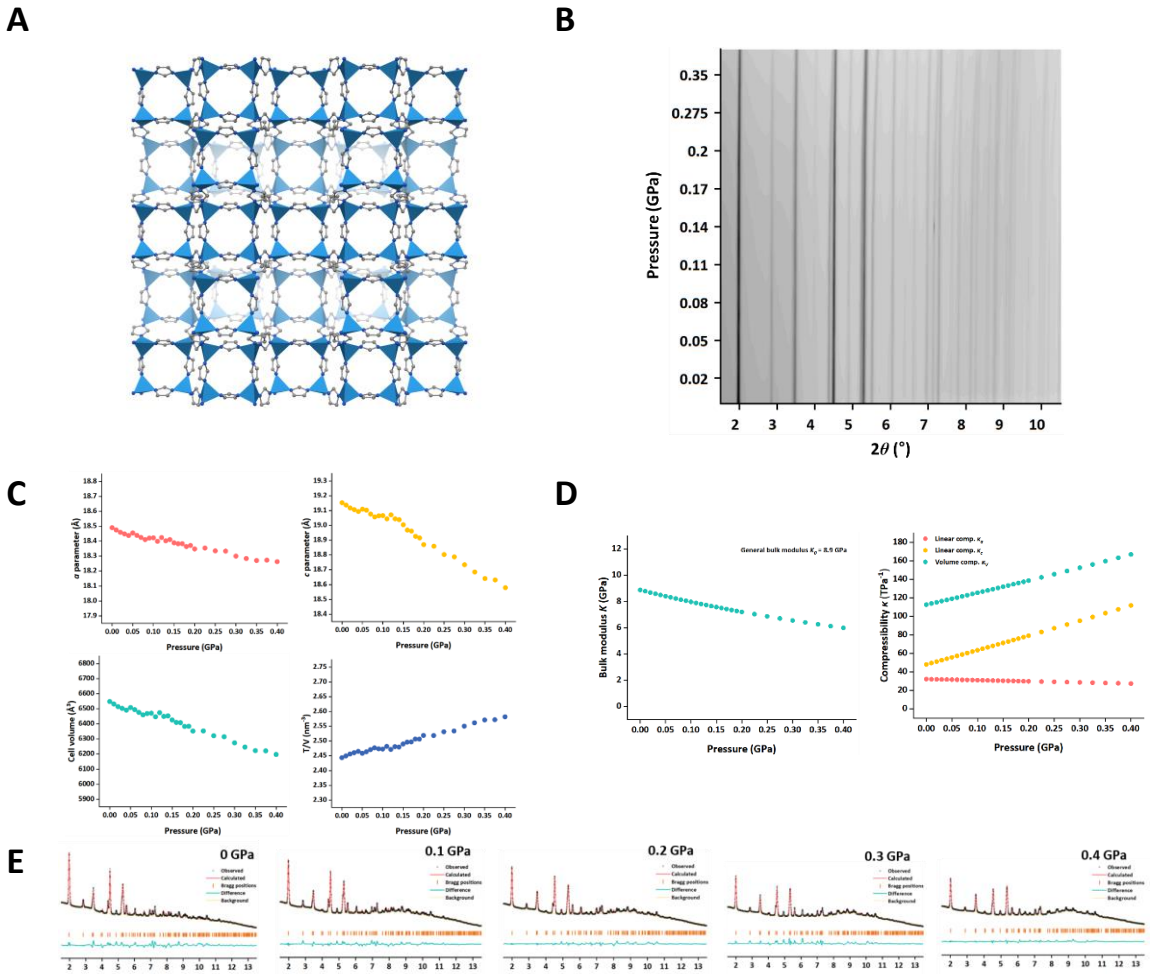

P (GPa)	0	0.1	0.2	0.3	0.4
a (Å)	18.4829(7)	18.4343(12)	18.360(4)	18.302(3)	18.2655(17)
c (Å)	19.1456(15)	19.079(3)	18.884(8)	18.737(6)	18.589(3)
V (Å^3)	6540.4(6)	6483.5(10)	6366(3)	6276(2)	6201.7(14)
R_{wp}	**0.04706**	**0.03626**	**0.03026**	**0.04819**	**0.02464**
R_p	**0.03046**	**0.02521**	**0.01972**	**0.03050**	**0.01758**
R_{exp}	**0.03848**	**0.03827**	**0.03988**	**0.04130**	**0.04325**
χ^2	1.22293	0.94752	0.75882	1.16677	0.56971

Figure 2. Structure and high-pressure mechanics of gis-ZIF. (A) Single-crystal structure of tetragonal **gis**-ZIF and its (B) high-pressure PXRD profile. (C) Crystallographic unit cell information fitted by Le Bail method and (D) derived mechanical properties. (E) Parameters and related profiles of gis-ZIF structures under high-pressure, refined by Rietveld method.

The influence of temperature on gas adsorption on solid supported lipid multilayers

Jaqueline Savelkouls[1*], Michelle Dargasz[2], Susanne Dogan-Surmeier[1], Marvin Kowalski[2], Mike Moron[1], Nicola Thiering[1], Gordon Scholz[1], Eric Schneider[1], Christian Sternemann[1] and Michael Paulus[1]

[1]Technische Universität Dortmund, Fakultät Physik / DELTA, 44227 Dortmund, Germany
[2]Universität Siegen, Department Physik, 57072 Siegen, Germany

*jaqueline.savelkouls@tu-dortmund.de

A lipid bilayer is the fundamental component of cell membranes which separate the intracellular and extracellular domains and regulate the exchange of substances between two domains in all living organisms [1]. Solid-supported lipid systems consisting of multiple lipid bilayers are well established as biomimetic models to study various biological processes at membranes [2]. In our case, we want to analyze *in situ* structural changes in the lipid systems under the influence of temperature both in air and in presence of the substances perfluoropropane (CAS number: 76-19-7) and sevoflurane (CAS number: 28523-86-6). Both gases are relevant for medical applications, i.e. perfluoropropane is used in ultrasound diagnostics and sevoflurane as an anaesthetic [3,4].

For our measurements, we prepared multilayers consisting of the zwitterionic phospholipid 1,2-dimyristoyl-sn-glycero-3-phosphocholine (DMPC) (CAS number: 18194-24-6) and spin-coated them onto (10x18) mm^2 hydrophilised silicon wafers [5,6]. The generated solid-supported lipid multilayers are placed in a DHS1100 heating cell from the company Anton-Paar (Graz, Austria) installed at the six-circle diffractometer of beamline BL9 [7-9]. The Anton-Paar cell has a heating plate to increase the temperature and connections for flushing with gas. We used this setup to investigate structural changes of the lipid multilayers with X-ray reflectivity (XRR) measurements. The XRR data were collected using a PILATUS 100k area detector (Dectris, Baden-Dättwil, Switzerland) at an incident photon energy of 27 keV with a beamsize at the sample position of (1.0 x 0.1) mm^2 (h x v) up to wave vector transfers of q_z = 0.7 Å^{-1}.

At first, the DMPC multilayers were measured in air as a function of temperature. All measurements were taken above 25 °C, so the lipid systems are in the fluid L_α phase [10]. Figure 1a) shows the corresponding Fresnel-normalized reflectivities of the solid-supported DMPC multilayer for selected temperatures. The first, dark purple XRR curve represents the reference measurement at 25°C. The corresponding fit function, which was determined using the program LSFIT [11] is drawn in red. Figure 1c) shows the corresponding electron density profile and a schematic of the system. The resulting reflectivities have sharp Bragg reflections up to the fourth diffraction order in the initial state. These reflections are caused by the highly ordered bilayers which are arranged in periodic planes parallel to the substrate. The reference sample consists of 10 bilayers with a respective thickness of $d_\mathrm{B} = 52$ Å, whereby the head group is $d_\mathrm{h} = 9.39$ Å and the tail group $d_\mathrm{t} = 15.37$ Å. We observe also a lipid monolayer at the interface between the lipid film and air, which can be recognized by the minimum of the XRR curve at the high q_z-tail of the first Bragg reflex. The total layer thickness of the multilayer ($D = 588.2$ Å) results from the parameters of the Gaussian fit to the first Bragg reflex (see figure 1b)) applying the Scherrer formula. Because of the complexity of modelling any changes in individual layers of a multilayer, the data are discussed below only in terms of the positions and amplitudes of the Bragg reflections as well as the disappearance of the minimum.

As the temperature increases, it is noticeable that the positions of the Bragg reflections shift towards larger q_z-values and have a larger width but a lower amplitude (refer to Figure 1b)). The intensities of the Bragg reflections decrease at 90°C, which disappear at even higher temperatures. The oscillations between the Bragg reflections weaken at high temperatures too. Above a temperature of 90°C, the disappearance of the minimum after the first Bragg reflection may indicate structural changes to the terminal monolayer. Furthermore, the layer thicknesses of the individual bilayers are reduced by approximately $d_{\mathrm{B,dif}} \approx 12$ Å, resulting in a total thickness loss of $D_\mathrm{dif} \approx 120$ Å. Finally, at 110°C, only a thickness of $D = 431.96$ Å is observed for the entire multilayer. Consequently, the reduction in bilayer thickness approximately corresponds to the reduction in the total thickness of the multilayer. Moreover, the temperature-related effects are reversible, so the multilayer system returns to its initial state as the temperature decreases and the negative peak arises again. These observations

imply that high temperatures cause a disorder in the system, which is resolved by cooling. An influence of radiation damage can be ruled out.

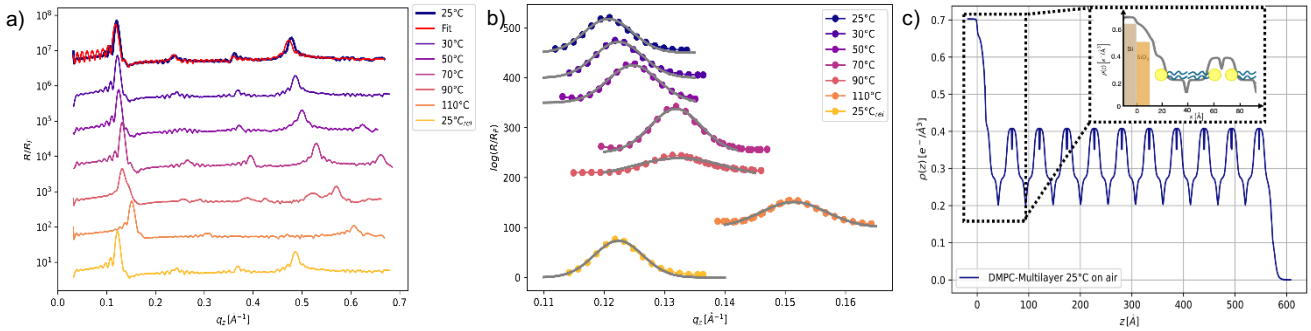

Figure 1: a) Fresnel-normalized XRR curves, shifted vertically for clarity, of solid- supported DMPC multilayers on previously hydrophilised silicon/silicon dioxide wafers collected at different temperatures at air. The red solid line symbolizes the fit function. b) The first order Bragg maxima and the fitted Gaussian curves (grey solid lines) c) Electron density profile of the reference measurement. The inset shows a zoom on the first 100 Å of the profile.

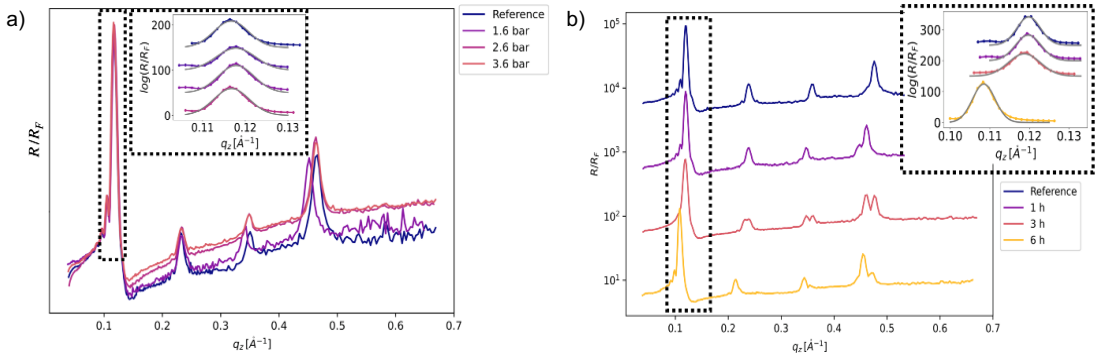

Figure 2: Fresnel-normalised XRR curves of solid supported DMPC multilayers under a perfluoropropane atmosphere and the corresponding first order Bragg maxima in the inset plot. a) As a function of gas pressure. b) As a function of flow time.

Compared to the reference measurements in air, DMPC multilayers were also analyzed under a perfluoropropane atmosphere. Figure 2a) shows the Fresnel-normalized XRR curves at different gas pressures and figure 2b) for different flow times. As can be seen from the XRR curves, the Bragg reflexes do not shift significantly at different gas pressures, which indicates that no structural changes affect the entire multilayer. In the measurements with a perfluoropropane flow over several hours, it is noticeable that the first Bragg reflection shifts towards smaller q_z-values. Consequently, the total layer thickness of the system increases, which could indicate a swelling of the bilayers in the multilayer. In addition, it can be seen that the 3rd- and 4th- order reflexes form double peaks over time. This indicates the formation of two different multilayer systems with different bilayer thicknesses. In all measurements, the gas perfluoropropane had no influence on the minimum assigned to the lipid top-layer.
In summary, the temperature has a much larger influence on the structural changes of the lipid system than the gas atmosphere. Perfluoropropane induces a swelling of parts of the lipid membranes after several hours. Nevertheless, the analysis and final interpretation of the XRR data are in progress.

References

[1] Werner Mäntele. „*Biophysik*“. Bd. 1. Ulmer (2012), pp. 56–97 **[2]** Ulrike Mennicke et. al.; “Structure and interaction potentials in solid-supported lipid membranes studied by x-ray reflectivity at varied osmotic pressure”, in: The European Physical Journal E 20.2 (2006), pp. 221–230. **[3]** Yi Lin et al.; “Evaluation of perfluoropropane (C3F8)-filled chitosan polyacrylic acid nanobubbles for ultrasound imaging of sentinel lymph nodes and tumors” in: Biomater. Sci., 10 (2022), pp.6447-6459 **[4]** Larsen R.; “Inhalationsanästhesie” in: *Anästhesie und Intensivmedizin für die Fachpflege*, (2016), pp.139–151 **[5]** U. Mennicke et al., “*Preparation of Solid-Supported Lipid Bilayers by Spin-Coating*“, in: Langmuir, (2002), pp. 8172–8177. **[6]** Benedikt Nowak et al., “Solid-supported lipid multilayers under high hydrostatic pressure”, in: Langmuir 32.11 (2016), pp. 2638–2643. **[7]** https://www.anton-paar.com/de-de/produkte/details/heizzusatz-fuer-vierkreis-goniometer-dhs-1100/ **[8]** F.J. Wirkert et al.;*” X-ray reflectivity measurements of liquid/solid interfaces under high hydrostatic pressure*”, in: Journal of Synchrotron Radiation 21, 76 (2014) **[9]** Michael Paulus et al.,*“An access to buried interfaces: the X-ray reflectivity set-up of BL9 at DELTA”*, in: Journal of Synchrotron Radiation, (2007), pp.60-605 **[10]** Ruthven N.A.H. Lewis et al.; “Calorimetric and spectroscopic studies of the phase behavior and organization of lipid bilayer model membranes composed of binary mixtures of dimyristoylphosphatidylcholine and dimyristoylphosphatidylglycerol”, in: Biochimica et Biophysica Acta (BBA) – Biomembranes 1668, 2 (2005), pp.203-214 **[11]** O.H. Seeck, *LSFit: Available on request from the author. Software for X-ray and neutron reflectivity calculation.* 1999.

Acknowledgments We thank the DELTA machine group for providing synchrotron radiation.

DELTA Report

Temperature induced nanostructuration of semiconducting polymers

Maximilian Stremel and Souren Grigorian, University of Siegen
Christophe Sinturel, University of Orléans

Organic semiconductors have the potential to drastically reduce the manufacturing costs of various smart applications. From a more scientific point of view, it is known that the electronic performance of the polymer layers is related to the properties of the semicrystalline structure (size and orientation of the crystalline structure with respect to the surfaces and interfaces). In thin films, this can be tuned by many experimental parameters during deposition and post-treatment, and by the composition of the blends. It is generally accepted that increasing the crystallinity of the semi-crystalline thin films leads to an increase in mobility [1]. However, recent studies have shown that surrounding matrix and interfacial regions (i.e. interphase between crystalline and amorphous and/or between phase-separated domains) can strongly influence the electronic performance [2]. The exact nature of these regions and their interconnectivity is not fully understood, and there are currently few first attempts to address this issue at advanced synchrotron radiation facilities [3-4]. A particular advantage here is the use of in situ characterisation, where the microstructure of the mixtures could be observed in detail using GIXD.

Semiconducting polymers (SPs) blended with insulating polymers (both of which are immiscible) are the most promising candidates for future electronics. Tuning the orientational and structural properties could be an elegant way to achieve superior device performance of novel type or functional materials and blends. Here, identifying the process of nanostructuration and phase separation progression of the crystalline domains could lead to new material properties. In the current study we identify the link between the blend morphology and the crystallization/orientation of the SP, during the nanostructuration process (upon heating), using AFM observations and in situ GIXD.

We characterise different compositions of thin solid polymer films (100 to 200 nm) from room temperature to 200°C and reveal the changes in ordering and crystallization in SP under confinement, caused by confinement strength, interfacial energy and competition between ordering and crystallization.

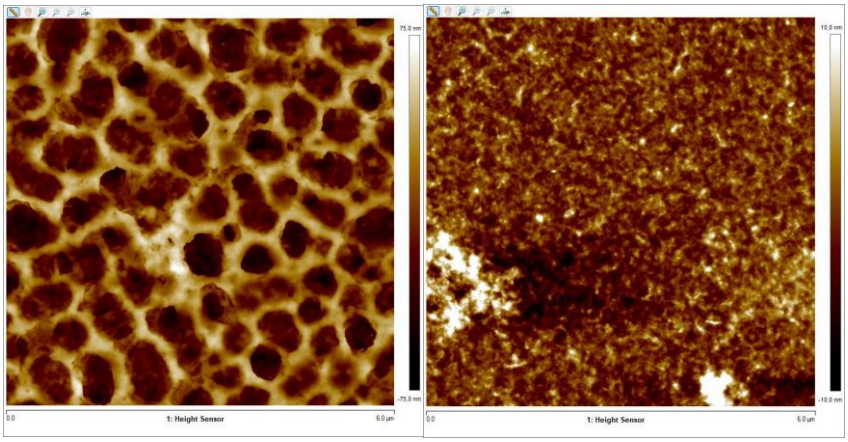

Figure 1 AFM images of 70 % (left) and pure P3HT (right), after annealing at T = 150 °C under N_2 atmosphere, PLA was removed with Acetic acid.

To determine any effects of thermal annealing, the films were examined in their as-spun state (Figure 1). By selectively removing the PLA with acetic acid, a clearer, unmasked appearance was observed. After annealing, the visual characteristics were compared to the as-spun state. This arrangement can be further tuned by adding immiscible insulating polymers (creating phase separation or interconnected fibrillar morphology).

In particular, the phenomenon that occurs when the systems are confined to nanoscale domains is still unknown and will form the core of this proposal. In order to identify the relationship between the blend morphology and the crystallisation/orientation of the semiconducting polymer, the in situ GIXD technique was used during the process of blend nanostructuring (upon heating).

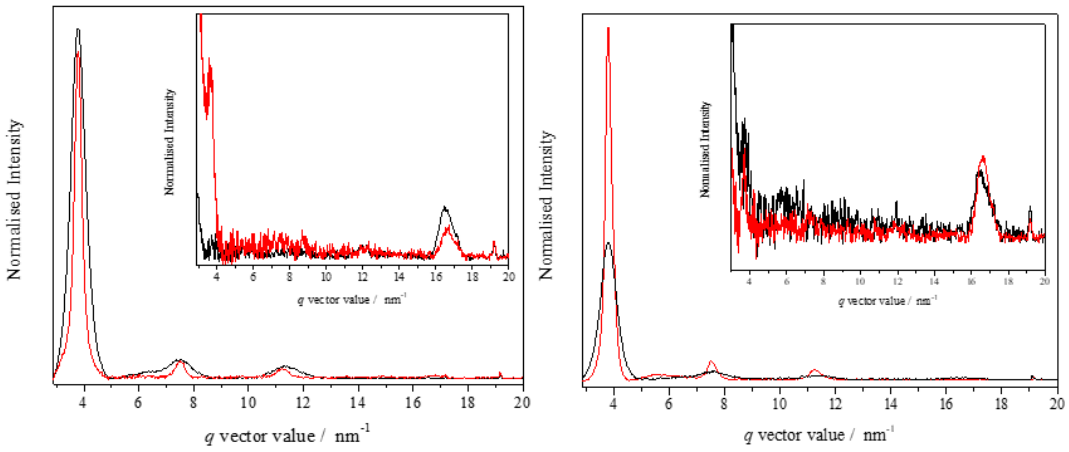

Figure 2 Integrated out-of-plane and in-plane (small insert) line profiles, 70 % (left) and pure P3HT (right), as spun at RT in black and after annealing at T = 150 °C under N_2 atmosphere / RT in red.

GIXD line profiles for pristine P3HT and blended with PLA are shown in Figure 2. These line profiles show different behaviour for the pure P3HT and the blended thin film upon annealing. For the pure P3HT, annealing significantly improves the crystallinity, especially for the (h00) series. In contrast, for the blend side chains associated lamellae are moderately improved. Interestingly, an opposite trend is observed for the pi-pi conjugation: moderate changes for the pristine film and stronger modifications for the blend. These results are promising in terms of carefully adjusting the blend ratio between P3HT and PLA to further improve the performance of OFETs.

References

[1]. J. Freudenberg et al. Immobilization Strategies for Organic Semiconducting Conjugated Polymers. Chemical Reviews 2018, 118 (11), 5598
[2]. R. Hildner et al. π-Conjugated Donor Polymers: Structure Formation and Morphology in Solution, Bulk and Photovoltaic Blends. Advanced Energy Materials 2017, 7 (16), 1700314
[3]. L. Grodd et. al. Local scale structural changes of working OFET devices. Nanoscale 2020, 12, 2434
[4]. C. Sinturel et al. Structural Transitions in Asymmetric Poly(styrene)-block- Poly(lactide) Thin Films Induced by Solvent Vapor Exposure ACS applied materials & interfaces, 2014, 6, 12146

An X-ray diffraction study on lithium greases

Kevin Lehninger[1], Michael Paulus[1], Christian Sternemann[1], Metin Tolan[1], Patrick Degen[2]

[1]Fakultät Physik/DELTA, TU Dortmund University, 44221 Dortmund, Germany
[2]Carl Bechem GmbH, Weststraße 120, 58089 Hagen, Germany

Lubricating greases play an important role in everyday life. Their properties protect mechanical components from premature wear and friction reduction result in enormous energy savings. The greases are often used under extreme conditions, they remain operational at a wide range of temperatures and are exposed to extreme pressures of up to 10 kbar (1 GPa) in gearboxes, for example. Metal soaps are often used as thickeners in combination with mineral oils in industrially manufactured heavy-duty greases. These soaps consist of a metal ion and a monocarboxylic acid. In order to extend the pressure stability and the temperature range in which the grease can be used, lithium complex soaps are often applied. Here a short-chain dicaboxylic acid is used in addition to the monocarboxylic acids [1].

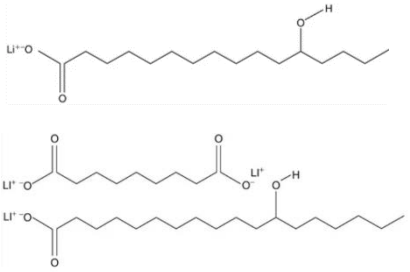

Figure 1: Top: Lithium soap, bottom: Lithium complex.

Beside other greases, the behaviour of lithium complex and lithium grease were investigated using small angle X-ray scattering (SAXS) in a high-pressure hydrostatic cell up to 4000 bar (0.4 GPa). The sample

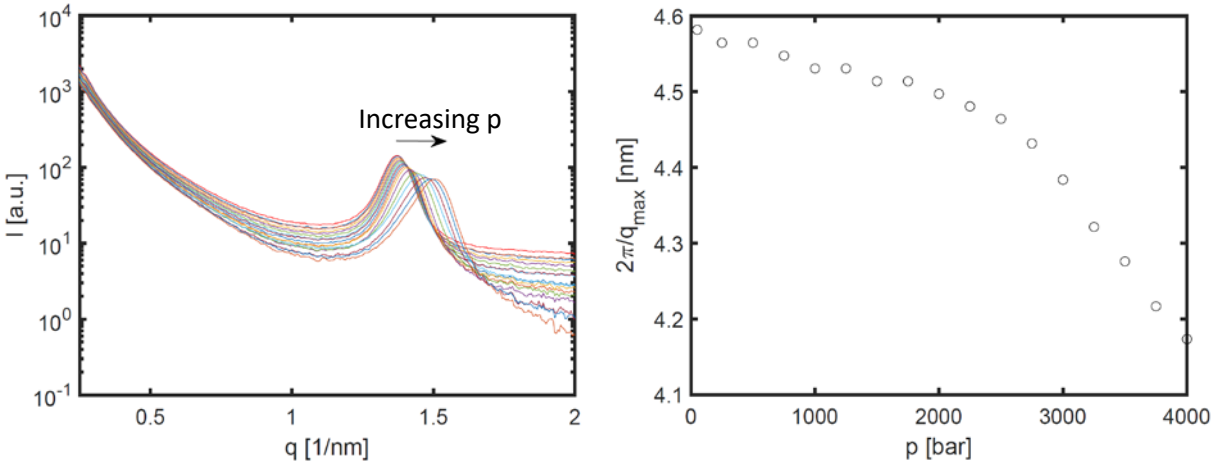

Figure 2: Left: Pressure-dependent SAXS data of a lithium grease. Right: The characteristic distance $2\pi/q_{max}$ resulting from the position of the Bragg reflection.

material was enclosed in a sample holder with two flexible polyimide foils fixed between two cylindrical diamond windows. The different samples were prepared and measured individually from 50 bar to 4000 bar in 250 bar steps. The measurements were carried out at beamline BL2 of DELTA [2]. The photon energy was 12 keV and a beam size of 0.5 x 0.5 mm^2 (h x v) was used. The scattered intensity was detected by a MAR345 image plate detector. A water sample was used for background subtraction. The setup was calibrated by a silverbehenate sample.

Figure 1 left shows a pressure dependent series recorded on lithium grease. A Bragg reflection can be clearly seen, which shifts to higher wave vector transfers with increasing pressure. It is obvious that the Bragg reflex is caused by the strongly asymmetric unit cell of the lipid-lithium soaps, of which the long side is determined by the chain length of the lipids. For example, unit cell sizes of lithium stearate in the order of 4.6 nm can be found in the literature for

lithiumhydroxystearate [3]. A closer look at the pressure behaviour shows that the position of the reflex does not shift linearly with the pressure, but that there is a stronger shift above 2500 bar. In figure 2 on the right-hand side, the pressure-dependent behaviour is plotted using the distance $d = 2*\pi/q_{max}$ where q_{max} is the pressure-dependent position of the Bragg reflex. This illustration clearly shows a change in the compressibility of the system above 2500 bar. Over the entire pressure range, d changes by 9.8%.

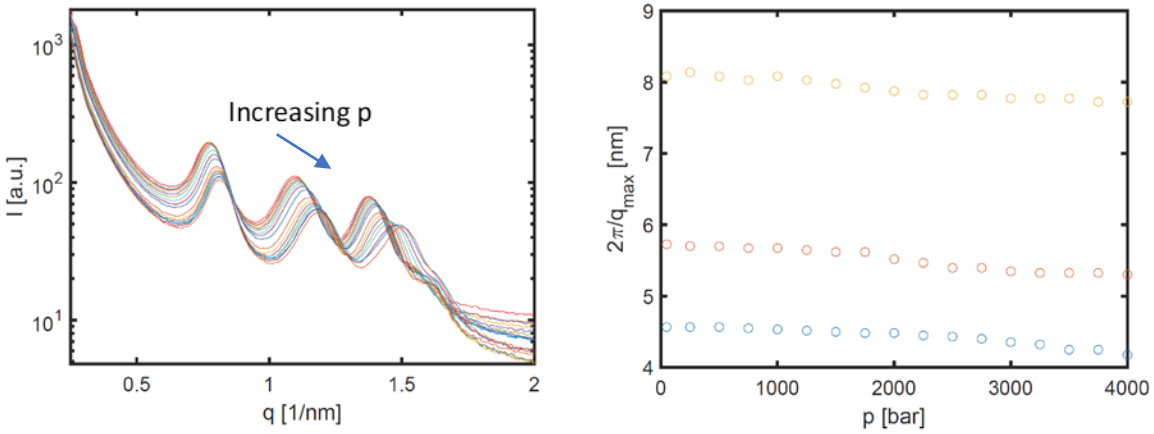

Figure 3: Left: Pressure-dependent SAXS data of a lithium complex grease. Right: The distance 2π/q resulting from the position of the Bragg reflections.

Figure 3 shows the pressure-dependent SAXS data of the lithium complex grease. The combination of at least two different fatty acids appears to result in a more complex elementary cell compared to the simple lithium soap, generating three strong Bragg reflections in the SAXS range. Here, too, there is an increasing shift towards larger wave vector transfers with increasing pressure, which indicates a compression of the elementary cell. Again, the positions of the Bragg reflections were evaluated and displayed in accordance with Figure 2. In contrast to the lithium grease, the compression in this case is relatively continuous over the entire pressure range and, at 4.7 %, 8.0 % and 9.3 % for the different Bragg reflections, is lower than in the first sample.

References

[1] W. Dresel (2014). Lubricating Greases. In: T. Mang (eds) Encyclopedia of Lubricants and Lubrication. Springer, Berlin, Heidelberg. https://doi.org/10.1007/978-3-642-22647-2_16 and Lithium Complex Greases, Industrial Lubrication and Tribology, September/October 1976.

[2] M. Dargasz, J. Bolle, A. Faulstich, E. Schneider, M. Kowalski, C. Sternemann, J. Savelkouls, B. Murphy, and M. Paulus, X-ray scattering at beamline BL2 of DELTA: Studies of lysozyme-lysozyme interaction in heavy water and structure formation in 1-hexanol, Journal of Physics: Conference Series 2380, 012031 (2022).

[3] M.J. Vold and R.D. Vold, A comparative study of the X-ray diffraction patterns and thermal transitions of metal soaps, Journal of the American Oil Chemists' Society volume 26, pages 520–525 (1949).

Acknowledgments

We thank the DELTA team for providing synchrotron radiation. This work was supported by the DFG via TO 169/21-1 and TI 343/190-1.

Investigating melting and glass formation of phenanthroline-modified zeolitic imidazolate frameworks with X-ray diffraction

Jan-Benedikt Weiß, Pascal Kolodzeiski, Sebastian Henke*

Anorganische Materialchemie, Fakultät für Chemie und Chemische Biologie, TU Dortmund

1. Scientific background

Metal-organic framework (MOF) glasses have attracted a lot of attention because they offer a unique combination of the intrinsic properties of glasses (e.g. absence of grain boundaries) and the high structural and functional variety of MOFs [1]. MOF glasses are accessible by melting and rapid cooling (i.e. melt-quenching) of certain crystalline MOFs, allowing processability in the liquid phase. Among MOFs, zeolitic imidazolate frameworks (ZIFs) are the most thoroughly investigated regarding their melting and glass-forming behaviour. ZIFs are composed of divalent metal cations (typically Zn^{2+} or Co^{2+}) which are tetrahedrally coordinated and interconnected by imidazolate linkers, forming two- or three-dimensional frameworks. Despite more than 250 crystalline ZIFs being reported in the literature, only ~10 ZIFs melt upon heating. Most of these meltable ZIFs exhibit a dense structure, leading to glasses with relatively low porosity [2]. Therefore, the structural and functional variety of ZIF glasses is yet limited.

Since the melting of MOFs is initiated by dissociation of the metal linker bond, a popular strategy to reduce the melting point is to weaken these bonds. Recently, our group has applied that strategy to ZIFs by using imidazolate linkers which are decorated with electron-withdrawing nitrile groups, leading to a significant weakening of the metal linker bond and a strong reduction of the melting point [3]. Inspired by our previous work on preparing new ZIF glasses based on this approach, we now developed an approach in which known crystalline ZIFs are mixed with the chelating ligand phenanthroline (phen). The concept evolves around the idea that phen coordinates to the tetrahedral nodes of the ZIFs at elevated temperature, leading to the formation of octahedral nodes (Fig. 1). These octahedral nodes exhibit weaker metal linker bonds in comparison to the tetrahedral nodes, leading to lower melting temperatures.

This approach was successfully applied to the meltable ZIF-62(M) ($M(im)_{1.7}(bim)_{0.3}$; M^{2+} = Zn^{2+} or Co^{2+}, im^- = imidazolate, bim^- = benzimidazolate) and the non-meltable and highly porous ZIF-12 ($Co(bim)_2$). Differential scanning calorimetry (DSC) reveals that heating and subsequent cooling of these phases to room temperature leads to the formation of monolithic glasses with glass transition temperatures of T_g = 206 °C for $(ZIF\text{-}62(Co))_{0.7}(phen)_{0.3}$ and T_g = 137 °C for $(ZIF\text{-}12)_{0.55}(phen)_{0.45}$. Combined analysis of the materials with far infrared spectroscopy (FIR) and density functional theory (DFT) calculations strongly suggest that phenanthroline coordinates to the metal nodes in the glassy state, suggesting the partial transformation of the tetrahedral metal nodes to octahedral ones.

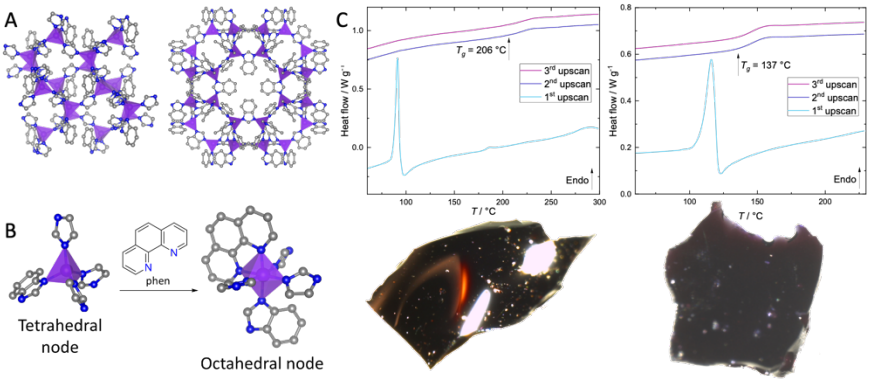

Figure 1. A: Crystal structures of ZIF-62 (left) and ZIF-12 (right). B: Illustration of the concept. C: DSC thermograms and images of monolithic glass shards obtained after the thermal cycling of $(ZIF\text{-}62)_{0.7}(phen)_{0.3}$ (left) and $(ZIF\text{-}12)_{0.55}(phen)_{0.45}$ (right). The strong endothermic signal on the 1st upscan corresponds to the melting of phen. The exothermic offset of this signal is associated to the coordination of phen to the tetrahedral Co^{2+} centers of the ZIFs. On the 2nd and 3rd upscans stable glass transitions are detected.

Our work reveals an innovative approach to preparing new ZIF glasses and manipulating the local coordination environment, expanding the so far limited structural and functional variety of ZIF glasses.

2. Experimental setup

In order to complete and extend our study, we collected variable temperature X-ray powder diffraction (VT-XRPD) data for the three above mentioned physical mixtures as well as physical mixtures containing various other modifiers. All samples were sealed in borosilicate capillaries and investigated in the temperature range from ambient temperature up to about 300 °C in steps of 25 to 50 °C (as appropriate) using the Anton Parr heating stage with a graphite dome. The sample temperature was determined by a temperature calibration of the setup using an external calibration with a thermocouple. After reaching about 300 °C, the samples were returned to 50 °C for another data collection to check whether the samples had maintained the non-crystalline state or if the sample showed recrystallisation.

3. Results

The physical mixtures containing phen all show a complete amorphization at elevated temperatures, as expected for a melting process. In agreement with the DSC results, the PXRD data show that phen melts after 100 °C and the reflections of the ZIF successively become less intense with increasing temperature. Two of the samples show minor recrystallisation upon subsequent cooling to 50 °C. The recrystallization can likely be suppressed by lowering the maximum temperature or increasing the cooling rate. No recrystallization is observed for $(ZIF\text{-}62(Co))_{0.7}(phen)_{0.3}$ indicating a high stability of the liquid phase.

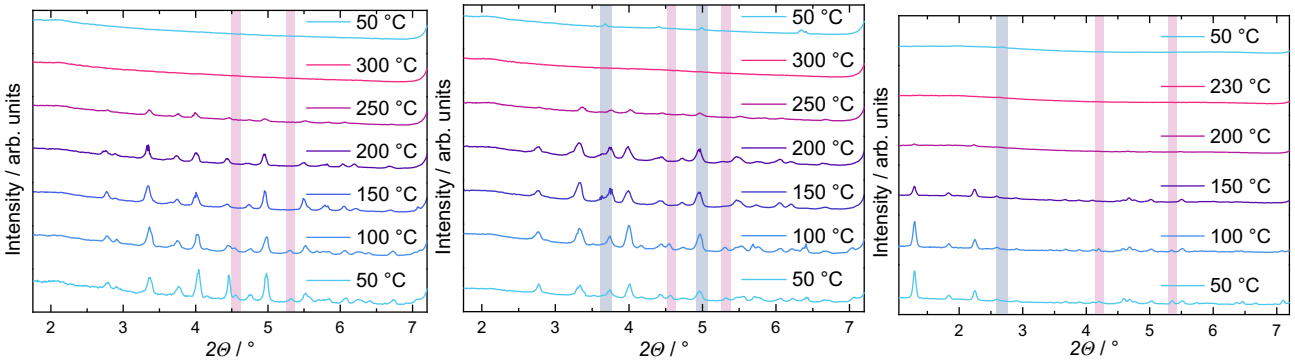

Figure 2. Variable temperature XRPD patterns of $(ZIF\text{-}62(Co))_{0.7}(phen)_{0.3}$, $(ZIF\text{-}62(Zn))_{0.7}(phen)_{0.3}$, and $(ZIF\text{-}12)_{0.55}(phen)_{0.45}$ (from left to right). Reflections corresponding to phen are highlighted in pink and reflections corresponding to recrystallized phases are highlighted in blue.

In summary, the data collected at BL9 enabled us to monitor the phase transitions of various physical mixtures of ZIFs and organic modifiers. The results clearly indicate a complete melting of the physical mixtures at elevated temperatures. Importantly, the data demonstrate the capability of organic chelating ligands like phenanthroline to induce or facilitate melting in various ZIFs.

The VT-XRPD data acquired during this beamtime are part of a manuscript which will be submitted for publication soon. The authors thank the DELTA group for the granted beamtime and the beamline scientists of BL9, C. Sternemann and M. Paulus, for their invaluable support during the experiments.

4. References

[1] N. Ma and S. Horike, *Metal–Organic Network-Forming Glasses*, Chem. Rev. **122**, 4163 (2022).

[2] L. Frentzel-Beyme, P. Kolodzeiski, J.-B. Weiß, A. Schneemann, and S. Henke, *Quantification of Gas-Accessible Microporosity in Metal-Organic Framework Glasses*, Nat. Commun. **13**, 7750 (2022).

[3] J. Song, L. Frentzel-Beyme, R. Pallach, P. Kolodzeiski, A. Koutsianos, W.-L. Xue, R. Schmid, and S. Henke, *Modulating Liquid–Liquid Transitions and Glass Formation in Zeolitic Imidazolate Frameworks by Decoration with Electron-Withdrawing Cyano Groups*, J. Am. Chem. Soc. **145**, 9273 (2023).

[4] R. Pallach, J. Keupp, K. Terlinden, L. Frentzel-Beyme, M. Kloß, A. Machalica, J. Kotschy, S. K. Vasa, P. A. Chater, C. Sternemann, M. T. Wharmby, R. Linser, R. Schmid and S. Henke, *Frustrated Flexibility in Metal-Organic Frameworks*, Nat. Commun. **12,** 4097 (2021).

[5] L. Frentzel-Beyme, M. Kloss, P. Kolodzeiski, R. Pallach and S. Henke, *Meltable Mixed-Linker Zeolitic Imidazolate Frameworks and Their Microporous Glasses - From Melting Point Engineering to Selective Hydrocarbon Sorption*, J. Am. Chem. Soc. **141**, 12362 (2019).

[6] L. Frentzel-Beyme, M. Kloß, R. Pallach, S. Salamon, H. Moldenhauer, J. Landers, H. Wende, J. Debus, and S. Henke, *Porous Purple Glass – a Cobalt Imidazolate Glass with Accessible Porosity from a Meltable Cobalt Imidazolate Framework*, J. Mater. Chem. A **7**, 985 (2019).

Phase dependent switching effect in phospholipid vesicles containing photo-sensitive azobenzene-glycolipids

Svenja Hövelmann[1,2,3], Rajendra Giri[1], Sonja Reinheimer[1], Michelle Dargaz[4], Michael Paulus[5], Bridget Murphy[1,3]

[1]Institute für experimentelle und angewandte Physik, Kiel University, Leibnizstr. 19, D-24118 Kiel, Germany,

[2]Deutsches Elektronen-Synchrotron DESY, Notkestraße 85, D-22607 Hamburg, Germany,

[3]Ruprecht Haensel Laboratory, Kiel University, D-24118 Kiel, Germany,

[4]Physikinstitut, Univeristät Gießen, 57072 Gießen,

[5]Zentrum für Synchrotronstrahlung, Technische Universität Dortmund, Maria-Goeppert-Mayer-Str. 2, D-44227 Dortmund, Deutschland

Experimental Report

1) Actual experiment

The aim of this experiment was to investigate the effect of photoswitchable azobenzene glycoconjugates (AZ) on the structure of phospholipid vesicles composed of dipalmitoyl phosphatidylcholine (DPPC) at different temperatures and ratios between AZ and DPPC. The small angle x-ray scattering (SAXS) measurements were carried out at BL2 (DELTA) at a photon energy of 12 keV using a MAR345 detector in a q-range between 0.25 and 3.10 nm^{-1} in the transmission geometry from glass capillaries. The vesicles were prepared freshly before each measurement by adding Milli-q water to the dried films of the binary mixture of DPPC and different AZ. This beamtime we focused on two AZ without any sugar in the headgroup. AZOL-C12 has twelve and AZOL-C16 has 16 carbon atoms in the alkyl chain in the tail group. For both AZ, multiple ratios between 2.5% and 100% AZ were measured at room temperature. For both molecules, a clear and reversible light induced switching effect was observed for percentages up to 20%. The samples were illuminated with LEDs of the wavelength 365 nm and 455 nm to switch the AZ molecules between their *trans* and *cis* isomer. For the AZOL-C16 mixtures up to 20% we identified a reversible switching between the lamellar phase for the *trans* isomer and the Pn3m bicontinuous phase for the *cis* isomer.

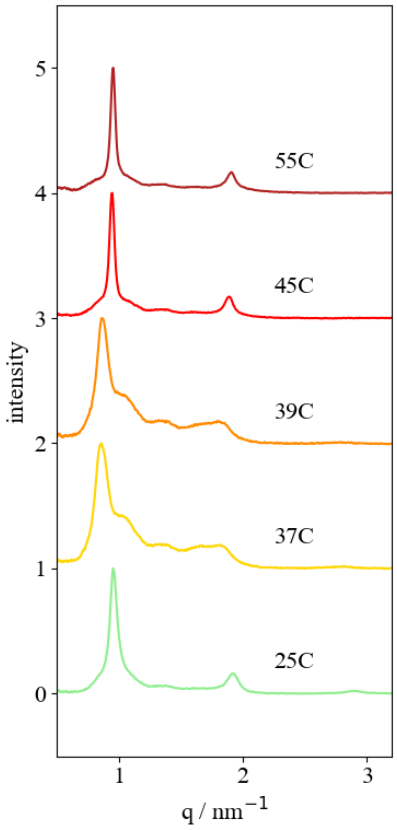

Figure 1 Data from the vesicles of binary mixture of DPPC and 10% AZOL in the trans state at different temperatures.

As the mixed vesicles with 10% and 20% AZOL-C12 and AZOL-C16, respectively, showed the clearest change in mesophase, temperature dependent measurements ranging from room temperature to 55°C were performed. This range covers the transition between gel phase and liquid crystalline phase. Figure 1 shows the SAXS data for AZOL-C16 with 10% at the different temperature in the *trans* configuration. Upon heating the sample under goes two phase transitions, from a lamellar to a bicontinuous cubic Pn3m and back to a lamellar structure.

2) Experimental equipment

During the beamtime two different sample setups were used.
The Lincolm stage was used as a sample holder for the temperature-controlled measurements in the range between room temperature and 55°C. In addition, a simple sample holder was used for *in-situ* illumination followed by measurements at room temperature. Our illumination device was mounted above the sample to allow direct illumination.

3) Achievement of aims

We successfully studied photoinduced reversible structural changes in binary mixed vesicles consisting of DPPC and photoswitchable glycoconjugates at different ratios. The main aim for this beamtime was to study the temperature dependent structure and phase of the vesicles and their change upon illumination. Upon heating, we found two phase transitions in the vesicle structure. These findings correspond to previous Differential Scanning Calorimetry measurements in which two phase temperatures were identified. Furthermore, we could observed at room temperature a change in the mesophase upon switching between *cis* and *trans* isomer but not for temperatures above the phase transition temperature.

The effect of doping nanoparticles on the temperature dependent behavior of micelle structure formation in NIPA

Özgül Öztürk[1], Gülsen Evingür[2], Christian Gutt[1]

[1]Department of Physics, University of Siegen, Walter-Flex-Str. 3, 57072 Siegen, Germany
[2]Department of Industrial Engineering, Piri Reis University, 34940 Tuzla/İstanbul, Turkey

Graphene oxide (GO) is a carbon-based material in two dimensions (2D) and has hydrophilic oxygenated functional groups (1). In parallel with developments from the basic scientific perspective, many applications of GO have been proposed. Thus, it can be used as a super capacitor, gas sensor, drug delivery system, and nano-electronic device, and presents the behavior of high strength, and thermal stability. Like GO, multiple wall carbon nanotubes (MWCNTs) have attracted enormous interest owing to their potential applications in field-emission devices, electronics, fibers, composites, sensors, detectors, capacitors, hydrogen storage media, and fuel cells, among others (2). Their high mechanical strength makes GO and MWCNT attractive materials for polymer reinforcement. The purpose of this study is to discuss the role of GO and MWCNT in the swelling and abrupt volume phase transition of Poly(N-isopropylacrylamide) (NIPA). NIPA is well known as a temperature-sensitive gel (2) which is chosen and studied for various technological applications. When the temperature increases, a transition is expected to occur in the morphological properties of NIPA-GO and NIPA-MWCNT between 33 and 40 °C as observed before for NIPA hydrogels (4).

NIPA-GO and NIPA-MWCNT composites were obtained by free radical copolymerization. Different weight percentages of crosslink agent Bissulfosuccinimidyl suberate (BIS) were added. The samples in glass capillaries were measured by using SAXS geometry with an energy of 12keV between a temperature range 22 to 45°C in 2°C steps. The temperature was increased by 0.29°C/min and 300s was waited at every step. Pure water sample using the same capillary was measured first to use for normalization.

Figure 1 shows the Porod plot of a NIPA with an amount of 20µL GO. There is a slight increase of intensity with temperature at low q region up to ~35°C which marks a temperature induced clustering enhancement. This results with more micelle like compact structures at large length scales. After 35°C, the scattering intensity decreases pointing out the loss of the temperature induced clustering. This is a common behavior observed for all NIPA-GO and NIPA-MWCNT samples.

The Porod and Kratky plots of NIPA samples with different amounts of GO and MWCNT at 33°C are seen respectively in Figure 3 and Figure 4. The peak around $q=3.8$ nm^{-1} is a parasitic effect related with Kapton. On the other hand, a definite change in the increase of scattering intensity with respect to change in the amount of GO and MWCNT exists at higher q values beyond the capability of the geometry used in this experiment. The upward deviation at high q region noticed at the Kratky plots indicates the swollen, less compact state of the samples. The measurements done with different BIS concentrations implies that the BIS amount does not have a pronounced effect on either the scattering intensity or the temperature dependence of the samples as detected for NIPA samples.

SAXS measurement of these GO and MWCNT doped NIPA samples, covering the higher q region seems promising as the signals of a peak in scattering intensity at higher q values worth a more detailed investigation.

References:

1. Akin Evingür G et.al, JOTCSA. 2016; 3(3): 463-478
2. Akin Evingür G et.al, Journal of Reinforced Plastics and Composites 33(13)
3. Dušek K, Editor, Springer Berlin Heidelberg; 1993. 110: 1- 26
4. Öztürk Ö et.al, DELTA Annual Report 2022, 59-60

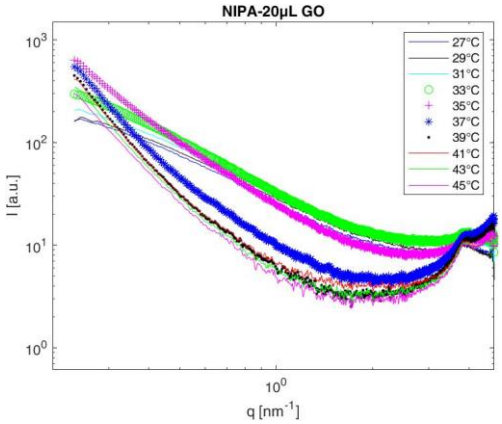

Figure 1. Porod plot of NIPA-20µL GO sample at different temperatures shows the typical behavior of both GO and MWCNT doped NIPA samples.

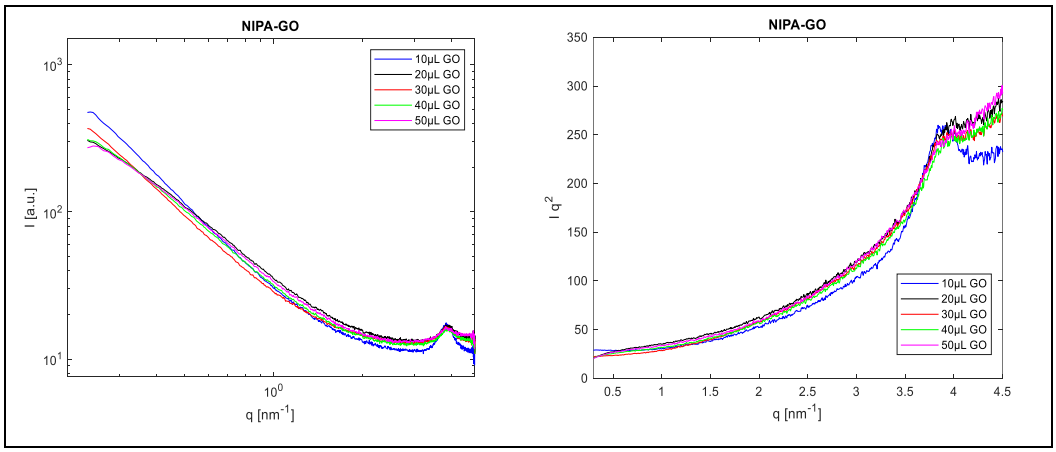

Figure 2. On the left; the Porod plot of samples with different GO concentrations at 33°C, on the right; the Kratky plot of the same samples are seen.

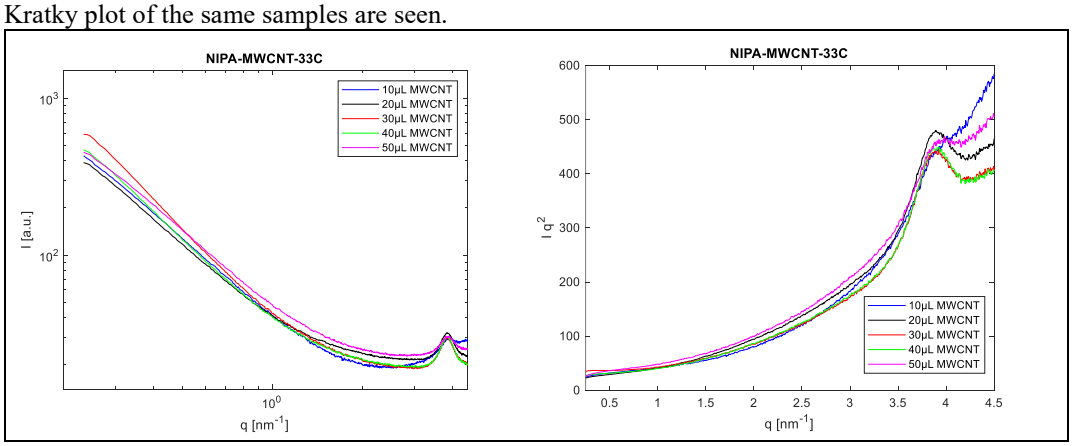

Figure 3. On the left; the Porod plot of samples with different MWCNT concentrations at 33°C, on the right; the Kratky plot of the same samples are seen.

Probing pre-hydrate structure in water-tetrahydrofuran mixtures

Robert Bauer[1], Jaqueline Savelkouls[2], Eric Schneider[2], Michael Paulus[2], Christian Sternemann[2], and Felix Lehmkühler[1]

[1]Deutsches Elektronen-Synchrotron DESY, Hamburg, Germany
[2]Fakultät Physik/DELTA, TU Dortmund, Dortmund, Germany

Clathrates commonly referred to as gas hydrates are cage-like water/ice structures that may form in the presence of guest molecules or atoms [1]. Hydrates are present in a variety of environments, from vast methane hydrate deposits on the ocean floor to potential occurrences of many different hydrates in the rings and on the moons of Saturn. The current climate crisis highlights uses of clathrates as possible filtration and storage media, and for sustained containment of methane and CO_2 under a warming ocean.

Interaction between water atoms and enclathrated guest contributes to the onset of gas hydrate formation. However, under appropriate conditions weakly interacting species also form clathrates, given the stochastic nature of the crystal nucleation process. Three clathrate structures are known to exist with two cubic structures referred to simply as structure SI and SII, and a hexagonal structure (SH) observed under high pressure. The constituent cages in these systems share the structure of small cages 5^{12}, i.e., the cage is formed by 12 pentagons with the O atom of the water molecules placed at the corners, with the largest cages varying by the number of hexagonal units $5^{12}6^2$ (SI), $5^{12}6^4$ (SII) and $5^{12}6^8$ (SH). The latter ones are formed by pentagons and hexagons, e.g. 12 pentagons and four hexagons in the case of $5^{12}6^4$. Given the variability in the structure formation, it is generally believed that a pre-hydrate structure forms before the onset of long-range order [2, 3, 4]. The onset of cage formation is influenced by the presence of a guest molecule as it is not observed in pure water. Thus, it is vital to better understand the nature of these precursor structures and to distinguish between the onset of differing clathrate structures. By now, computational simulations have examined the nucleation process in a variety of environmental conditions, and specific consideration is given to formation site and the number of cages [5]. In general, simulations converge into a picture of transient pre-hydrate structure that play a key role for the nucleation, see Fig. 1. However, a clear picture on the hydrate formation process, in particular from an experimental point of view, is still missing [6,7,8]. Does the hydrate form via a crystalline critical nucleus or does an amorphous critical nucleus exist so that an amorphous hydrate structure forms which then reaches the crystalline phase voa ripening/annealing?

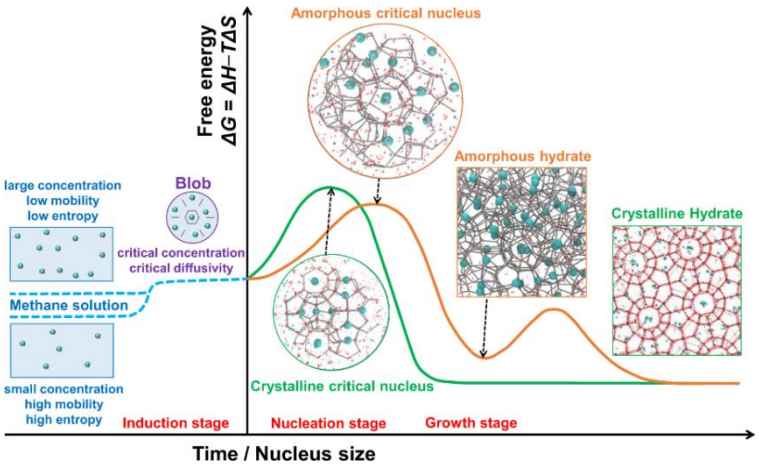

Figure 1: Proposed schematic for hydrate formation. Figure from [8] reproduced under CC-BY 4.0.

To shed light on this hydrate formation process, we investigated the structure of tetrahydrofuran (THF)-water mixture. THF and water form an SII hydrate at temperatures below 4°C and atmospheric pressure, thus hydrate formation is preferred over freezing to hexagonal ice. We performed X-ray diffraction measurements at BL9 that aim at probing the

onset of clathrate hydration shells in aqueous mixtures of water and guests by studying the kinetics of the formation process via analysis of pair-distribution functions (PDFs). THF-water mixtures with a THF wt.% between 0% and 30% in steps of 5% were used. Note that THF hydrate can form at minimum concentration of 9 wt.%, thus we covered both the hydrate stability and co-existence regime. The mixtures were filled to borosilicate capillaries with at diameter of 1.5 mm. The capillaries were place to the Linkam temperature stage of BL9. In order to cover a large q-range, we used an incident energy of 27 keV, resulting in a usable q-range of 5 to 65 nm^{-1} with the MAR345 image plate. Data were taken at temperatures below 295 K and 253 K, covering liquid and supercooled states. At the lower temperatures, Bragg reflections were observed, indicating crystallization of ice and/or hydrate.

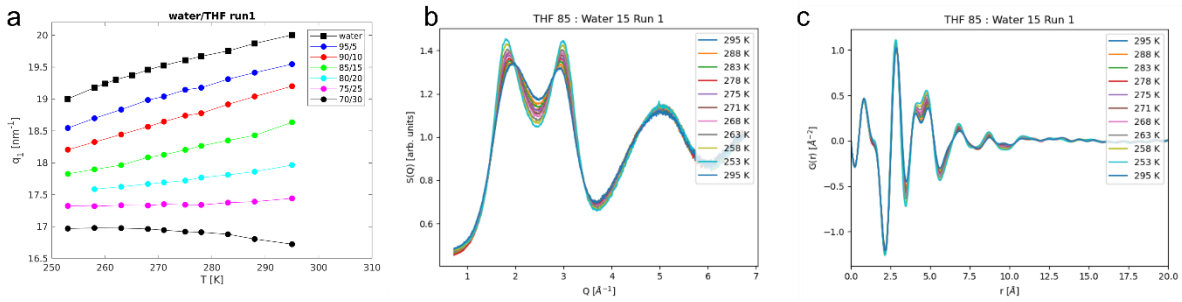

Figure 2: a) Position of the first peak of I(q) for different THF content and temperatures. b) Structure factor S(q) for 15 wt.% THF. c) G(r) from the data of panel b.

Selected results are shown in Fig. 2. The left panel (Fig. 2 a) shows the temperature dependence of the main peak in the I(q). The peak position decreases with increasing THF content and moves to smaller q while cooling for THF concentration above 25%. At 25% the peak is almost constant, while at higher concentration it grows. In general, for all concentrations the peak positions change towards around 17 nm^{-1}. This value is found as well for an ideal tetrahedral coordination in water [9], e.g. as reported for low-density amorphous ice. Fig. 2 b shows the extracted structure factors S(q) for one selected THF concentration and Fig. 2 c the corresponding pair distribution function (PDF) G(r). The most changes appear in the second coordination shell below 0.5 nm.

Note that the so-obtained data measures the time-averaged structure. As hydrate precursors are transient, we performed a femtosecond-PDF experiment at European XFEL on the THF hydrate process. The XFEL data is currently under analysis and will be compared to the DELTA data to find differences between ensemble-averaged and instantaneous structure.

References

[1] E.D. Sloan, *Nature* 426, 353-359 (2003).
[2] F. Lehmkühler, M. Paulus, C. Sternemann et al. *J. Am. Chem. Soc.* 131, 585 (2009).
[3] H. Conrad, F. Lehmkühler, C. Sternemann et al. *Phys. Rev. Lett.* 103, 218301 (2009).
[4] J. Liu et al. *Crystals* 9, 73 (2019).
[5] K.W. Hall, S. Sheelagh, and P.G. Kusalik, *PNAS* 113(43), 12041-12046 (2016).
[6] S. Liang et al., *Philosophical Transactions of the Royal Society A*, 377(2146), (2019).
[7] J.S. Tse, and D.D Klug, *Journal of Supramolecular Chemistry*, 2(4-5), 467-472 (2006).
[8] G. J. Guo, and Z. Zhang. *Communications Chemistry* 4(1), 102 (2021).
[9] D. Mariedahl et al. *J. Phys. Chem. B* 122, 7616-7624 (2018).

Unravelling the mechanical behaviour of zeolitic imidazolate frameworks with sod topology under cyclic high-pressure compression

Wenlong Xue and Sebastian Henke*

Anorganische Materialchemie – TU Dortmund, Otto-Hahn-Str. 6, 44227 Dortmund

Scientific context

Metal-organic frameworks (MOFs) have recently gained significant attention as a new type of porous material. These solids consist of inorganic nodes, either metal ions or clusters, linked with organic linkers via coordination bonds in an infinite array.[1] Due to their permanent porosity, MOFs have attracted attention for their potential uses in gas sorption, separation processes, and catalysis.[2] For industrial applications, it is vital to understand the fundamental mechanical properties of these functional materials. In this research, we pursued further investigations into the structural behaviour of a family of zeolitic imidazolate frameworks with the **sod** (i.e. sodalite) topology (*sod*-ZIFs) upon exposure to hydrostatic mechanical pressure (up to 4000 bar) using cyclic high-pressure powder X-ray diffraction (HP-PXRD)[3]. This study enhances our comprehension of the essential mechanical and structural characteristics of MOFs with **sod** topology when subjected to cyclic mechanical pressure; a critical factor for their application in catalysis and separation processes.

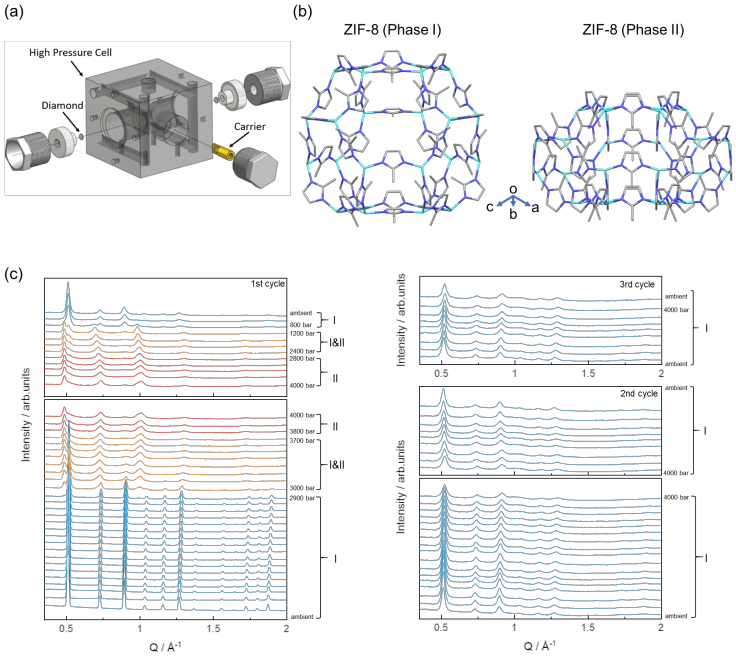

Fig. 1. (a) Schematic representation of the modified high-pressure X-ray reflectivity cell used for HP-PXRD measurements. (b) Structural models of the pristine ZIF-8 framework (phase I, left) and compressed ZIF-8 framework (phase II, right). Zn, C and N atoms are shown in cyan, grey, and blue, respective<ely. H atoms are omitted for clarity. (c) Cyclic HP-PXRD patterns of ZIF-8 shown as stacked plots, observing a reversible phase transition (phase I – phase II – phase I) in the first compression-decompression cycle and absence of the phase transition in two consecutive compression-decompression cylces.

We previously investigated the structural response of ZIF-8 ($Zn(mim)_2$, mim^- = 2-methylimidazolate) to hydrostatic mechanical pressure with HP-PXRD using the hydraulic pressure jump cell available at BL9 of DELTA (Fig. 1a). As shown in Fig. 1c, ZIF-8 harbours a series of fascinating pressure stimuli-responsive properties. We observed a drastic change in the PXRD patterns at p = 2600-2800 bar, discovering large volume structural flexibility in ZIF-8, similar to the previously reported pressure-responsive phase behaviour of ZIF-4 and ZIF-62[4]. By refinement of the PXRD pattern of ZIF-8 recorded at 4000 bar, we obtained a model of the compressed structure, which we named phase II (Fig. 1b). In contrast to the cubic phase I (space group $I\bar{4}3m$), phase II exhibits rhombohedral symmetry (space group $R3m$) and is about 45% denser. Importantly, the **sod** topology of the network, i.e. the connectivity pattern of the building units is identical in both phases of ZIF-8. Very surprisingly, ZIF-8 returns to phase I upon decompression, but does not transition back to phase II during repeated compression to 4000 bar. The non-repeatability of the phase transition of ZIF-8 may be associated with particle size and strain effects, leading to the 'work hardening' of the porous framework within the first compression-decompression cycle.

In order to extend our study and to get insights into the effect of the linker on the phase behaviour of *sod*-ZIFs, we further investigated the structural response of other *sod*-ZIFs, i.e., ZIF-65 ($Zn(nim^-)_2$, nim^- = 2-nitroimidazolate) and ZIF-90 ($Zn(fim^-)_2$, fim^- = 2-formylimidazolate). Furthermore, with the aim of investigating the particle size effect of the phase changes, we also performed cyclic HP-PXRD on nano-ZIF-8 (i.e. a ZIF-8 material composed of smaller nanoparticles and not micron-sized particles).

Experimental procedure

Powdered samples were filled into Kapton capillaries (1.0 mm diameter Kapton tube, bottom sealed with superglue) and silicone oil was added to the capillary as a non-penetrating pressure transmitting fluid (PTF). This non-penetrating PTF ensures the complete transmission of the hydrostatic pressure to the powdered sample. The thus prepared sample was introduced to the sample carrier (Fig. 1a), which was transferred into the high-pressure cell at BL9. The cell was tightly sealed and the pressure was cyclically increased/decreased stepwise from ambient to 4000 bar, whilst PXRD patterns were recorded at each pressure interval. A monochromatic X-ray beam of an energy of 27 keV was used.

Results

ZIF-65 and ZIF-90 with a larger substituent at the 2-position of imidazolate did not exhibit a phase transition in the range from ambient to 4000 bar (Fig. 2 left and middle). The larger nitro- and aldehyde-groups of these *sod*-ZIFs appear to increase the mechanical resistance of the frameworks thus hindering the transition to phase II. Strikingly, nano-ZIF-8 also did not undergo the phase transition to phase II upon compressing the material from ambient to 4000 bar. Only a decrease of the reflection intensities is observed (Fig. 2 right). We speculate that the smaller particle size hinders the phase transition due to smaller grain sizes and the larger grain boundary area.[5] We are currently in the process of analysing the collected data in detail. Besides refinement of the developed model structure of the high-pressure phase II, compressibilities and bulk moduli shall be extracted by profile fitting of the PXRD patterns of all materials studied. The latter might give valuable insights into changes in the mechanical materials' properties as a function of linker functionalization as well as compression cycle number.

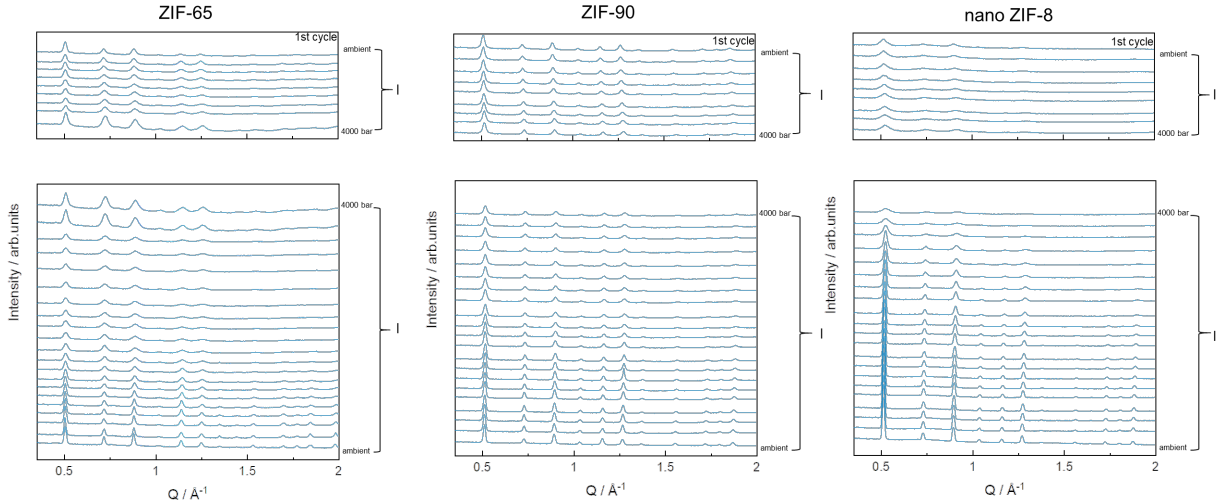

Fig. 2. HP-PXRD patterns of ZIF-65 (left), ZIF-90 (middle) and nano ZIF-8 (right) are shown as stacked plots. The bottom panels show the HP-PXRD patterns recorded during compression from ambient pressure to 4000 bar and the top panels show diffraction patterns collected during decompression from 4000 bar to ambient pressure.

BL9 enabled us to monitor the peculiar phase behaviour of *sod*-ZIFs under high mechanical pressure. We observe that the molecular structure and particle size of the *sod*-ZIFs play a key role in their response to high pressures, affecting their ability to undergo structural transformation or deformation. Detailed structural and mechanical property analyses are currently in progress. The HP-PXRD data acquired during this beamtime are part of a manuscript which will be submitted for publication once data analysis is completed. The authors thank the DELTA group for the granted beamtime and the beamline scientists of BL9, C. Sternemann and M. Paulus, for their invaluable support during the experiments.

References

[1] a) *Chem. Soc. Rev.* **2009**, *38*, 1213–1477; b) *Chem. Soc. Rev.* **2011**, *40*, 453–1152; c) *Chem. Rev.* **2012**, *112*, 673–1268.
[2] a) U. Mueller et al., *J. Mater. Chem.* **2006**, *16*, 626; b) A. U. Czaja, et al. *Chem. Soc. Rev.* **2009**, *38*, 1284.
[3] a) F.J. Wirkert et al., *J. Synchrotron Rad.* **2014**, *21*, 76–81; b) L. Frentzel-Beyme et al., *Adv. Funct. Mater.* **2023**, *33*, 2302033.
[4] a) S. Henke et al., *Chem. Sci.* **2018**, *9*, 1654–1660; b) Remo N. Widmer et al., *J. Am. Chem. Soc.* **2019**, *141*, 9330–9337; J. Song et al. *Angew. Chem. Int. Ed.* **2022**, *61*, e202117565.
[5] S. Ehrling et al., *Trends Chem*. **2021**, *3*, 291-304.

Radiation and temperature sensitivity of hydrophobic self-assembled monolayer coatings

Mike Moron, Susanne Dogan-Surmeier, Marc Moron, Nicola Thiering, Gordon Scholz, Christian Sternemann, Michael Paulus, and Julia Nase

Fakultät Physik/DELTA, TU Dortmund, 44221 Dortmund, Germany

Self-assembled monolayer (SAM) coatings play an important role in various fields such as microelectronics, where they are used to reduce friction in microelectromechanical devices. As high temperatures frequently occur in this area of application, thermal stability of SAM coatings is of great importance.

In this study, silicon wafers were coated with octadecyltrichlorosilane (OTS) to form a stable hydrophobic SAM. The stability of the OTS coatings against temperature and radiation was analyzed under vacuum, air, hexafluoroethane (C_2F_6), octafluoropropane (C_3F_8), decafluorobutane (C_4F_{10}) and carbon dioxide (CO_2) in a temperature range between room temperature and 319 °C. X-ray-reflectivity (XRR) measurements were performed at the beamline BL9 at DELTA using photon energies of $E_{\mathrm{ph}} = 8\,\mathrm{keV}$ and $E_{\mathrm{ph}} = 27\,\mathrm{keV}$. A picture of the experimental setup can be seen in Figure 1.

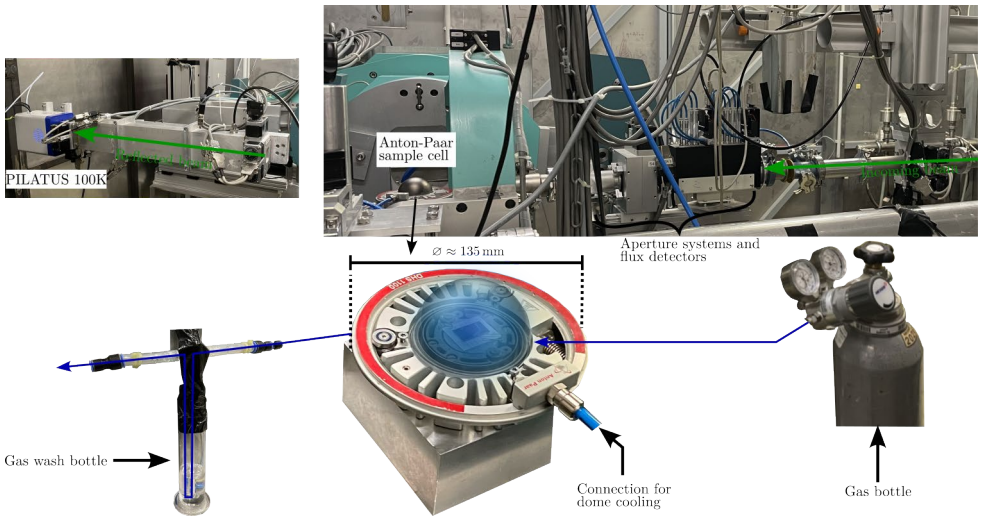

Figure 1: Picture of the experimental setup.

The OTS wafer was placed in a temperature-controlled sample environment (Anton Paar Germany GmbH, model DHS 1100) which consists of an aluminum nitride (AlN) heating plate to which a temperature control unit is connected. The temperature is measured inside the sample cell directly below the sample with a Pt-Pt10Rh thermocouple. A hemispherical graphite dome prevents contamination of the sample, ensures temperature stability, and enables measurements under vacuum ($p \approx 10^{-1}\,\mathrm{mbar}$) and different gas atmospheres up to a maximum pressure of $p = 1.3\,\mathrm{bar}$. The gas flow is regulated using a gas wash bottle. The reflected X-ray beam is recorded by a PILATUS 100K area detector (DECTRIS AG, Switzerland). Figure 2 a) shows as an example the recorded reflectitvities normalized to the Fresnel reflectivity R_F of an ideal flat silicon surface for the temperature series in vacuum at a photon energy of $E_{\mathrm{ph}} = 8\,\mathrm{keV}$. The XRR curves are shifted vertically for clarity. The vertical dashed line indicates the position of the first minimum of the reference measurement under vacuum at room temperature. The reflectivities are plotted against the wave-vector transfer $q_z = 4\pi/\lambda \sin(\alpha_i)$, where λ is the wavelength and α_i the angle of incidence of the X-ray beam. With increasing temperature, the positions of the minima shift to higher q_z values, indicating a decrease in total layer thickness. In Figure 2 b) the positions of the first minima $q_{z,fm}$ are plotted against temperature. As can be seen from the illustration, the variations of the positions with temperature can be divided into two

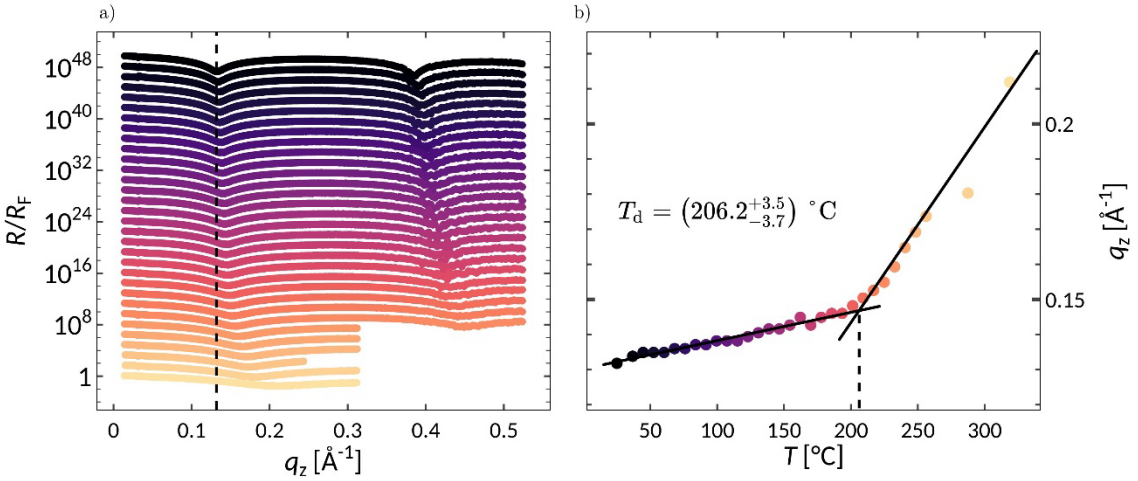

Figure 2: Reflectivities of OTS wafers under vacuum at $E_{\mathrm{ph}} = 8\,\mathrm{keV}$. b) Positions $q_{\mathrm{z,fm}}$ of the first minima of the reflectivities from a). The positions of the minima are divided into two regions for each of which a linear regression is carried out. The intersection of the two straight lines provides the temperature T_{d}.

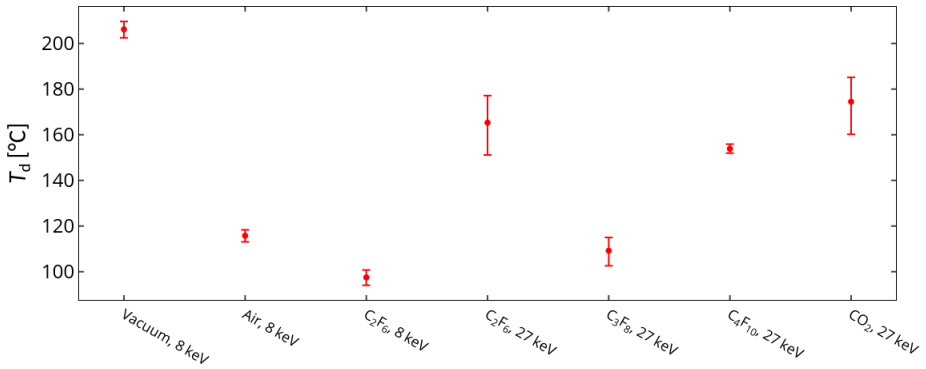

Figure 3: T_d for all investigated systems.

regions. By linear regression within the two regions, the temperature T_{d}, considered as the threshold temperature above which rapid damage to the OTS layer occurs, is obtained from the intersection of the two straight lines. For the presented system this results in $T_{\mathrm{d}} = 206.2\,°\mathrm{C}$. If this procedure is applied to all systems examined, the T_{d} values shown in Figure 3 are obtained. For the systems investigated, T_{d} varies between 97.5 °C and 206.2 °C, whereby T_{d} is highest at $E_{\mathrm{ph}} = 8\,\mathrm{keV}$ in vacuum and smallest at $E_{\mathrm{ph}} = 8\,\mathrm{keV}$ under C_2F_6 atmosphere. Except for the measurement under C_3F_8 atmosphere, the T_{d} at $E_{\mathrm{ph}} = 27\,\mathrm{keV}$ under a gas atmosphere are higher than the T_{d} obtained when using X-rays with $E_{\mathrm{ph}} = 8\,\mathrm{keV}$. This indicates that the OTS layer is more stable at higher photon energies, as less radiation dose is deposited in the OTS layer and the surrounding gas phase. The fact that T_{d} is highest for the measurement in vacuum shows that a gas phase above the OTS wafer significantly reduces the stability of the OTS layer. From this, it can be concluded that the destruction of the OTS layer is mainly caused by the formation of free radicals in the gas phase.

Acknowledgements
The authors gratefully acknowledge the DELTA machine group for providing synchrotron radiation. This work was funded by the Bundesministerium für Bildung und Forschung (Projektnummer: 05K19PEA).

Rashba type band splitting effects in 2D $(PEA)_2PbI_4$ perovskites

Supriya Ghosh[†,ǁ,#*], Bapi Pradhan[§,#], Arkamita Bandyopadhyay[π], Irina Skvortsova[^], Yiyue Zhang[§], Christian Sternemann[µ], Michael Paulus[µ], Sara Bals[^], Johan Hofkens[§,δ], Arnulf Materny [†*] and Khadga J. Karki [‡*]

[†] Jacobs University, Department of Physics and Earth Sciences, Campus Ring 1, 28759 Bremen, Germany
[ǁ]Department of Chemistry and Biochemistry, The Ohio State University, 100 West 18th Avenue, Columbus, Ohio 43210, USA
[^]Electron Microscopy for Materials Research, University of Antwerp, Groenenborgerlaan 171, 2020 Antwerp, Belgium
[µ] Fakultät Physik/DELTA, Technische Universität Dortmund,44221 Dortmund, Germany
[§]Department of Chemistry, KU Leuven, Celestijnenlaan 200F, 3001 Heverlee, Belgium
[π] Bremen Center for Computational Materials Science, University of Bremen, Bremen, Germany, 28359
[δ]Max Planck Institute for Polymer Research, Ackermannweg 10, 55128 Mainz, Germany
[‡] Guangdong Technion Israel Institute of Technology, 241 Daxue Road, Shantou, Guangdong Province 515603, P. R. China

Abstract: Strong spin-orbit coupling due to heavy atoms in a crystal or inversion symmetry breaking leads to Rashba band splitting. In spite of few recent reports on Rashba effects in 2D perovskites, the impacts of organic spacer cation on the extent of Rashba band splitting still remain to be determined. Here, using a combination of temperature dependent photoluminescence (PL) spectroscopy, density functional theory (DFT) calculations, time-resolved PL spectroscopy, and structural characterization by X-ray diffraction, we provide a comprehensive understanding of the Rashba band splitting of the 2D Ruddlesden-Popper (RP) hybrid perovskites. We demonstrate that significant structural distortions associated with polarity of organic spacer cation is responsible for the observed effect. Our investigations show that the intrinsic Rashba splitting occurs in the perovskite crystals with a highly polar organic cation, but not in the ones with lower polar cation. These findings not only provide an explanation for different type of exciton recombination processes in perovskites but also elucidate the significant impact of the nature of the organic cation on the electronic properties of 2D perovskites.

Results: The 2D nature of the material can be corroborated from the structure and morphology of the samples. To further confirm the crystal phase, synchrotron grazing incident wide angle X-ray scattering (GIWAXS) experiments were carried out. Figure 1a and 1b shows the 2D GIWAXS patterns recorded of HP (PEA) and FP (FPEA) 2D perovskites, where the out-of-plane and in-plane integration peak positions match well with the standard phase of PEA (P1, triclinic) and FPEA (P121/c1, monoclinic), see Figure 2. Out-of-plane data enables fitting the (n00) and (00n) diffraction peaks on a 2θ scale for FPEA and PEA, respectively (Figure 2). These results, analyzed using a Williamson-Hall plot, estimate the strain of the second kind (ε) (0.0059±0.005 for FPEA and 0.0041±0.005 for PEA) and the crystallite size (L) (92±10 nm for FPEA and 67±10 nm for PEA) perpendicular to the sample's surface. However, limitations in accessing broadening due to grazing incidence geometry may significantly affect the accuracy of the crystallite size estimation. Therefore, L should be regarded only as a minimum size of the flakes' crystallites in the direction perpendicular to the surface. By examining the (n00) and (00n) diffraction peaks of FPEA and PEA in the azimuthal direction and assuming isotropic tilt variation, the width of the tilt-distribution for the flakes is estimated. Specifically, this analysis suggests a tilt-distribution width of 11.6°±0.5° for PEA and 15.7°±0.5° for FPEA. This finding indicates that PEA flakes exhibit greater ordering concerning the surface normal.

Experimental detail of GIWAXS measurements: We performed grazing incidence X-ray diffraction at beamline BL9 of DELTA synchrotron radiation source (C. Krywka, C. Sternemann, M. Paulus, N. Javid, R. Winter, Ali Al-Sawalmih, Sangbong Yi, D. Raabe, M. Tolan, The small-angle and wide-angle x-ray scattering setup at beamline BL9 of DELTA, Journal of Synchrotron Radiation 14, 244 (2007).). The 2D diffraction images were measured at an incident energy of 13 keV with a beamsize of 0.05 x 1.0 mm^2 (v x h) using a MAR345 image plate detector. The angle of incidence was set to 0.25° and the setup was calibrated with a CeO_2 powder sample as standard. The 2D diffration images were converted to reciprocal space and analyzed exploiting the program package pygix/pyFAI (Kieffer, J., Valls, V., Blanc, N. & Hennig, C. New tools for calibrating diffraction setups (*J. Synchrotron Radiat.* **27**, 558–566 (2020)). The integrations were performed in the azimuthal angular range at 80°±10° and 10°±10° in order to calculate the in-plane and out-of-plane diffraction patterns.

Conclusion: We have investigated the octahedral distortions and Rashba splitting in 2D RP perovskite $(PEA)_2PbI_4$ and $(F\text{-}PEA)_2PbI_4$ by combining the temperature dependent steady state and time resolved PL spectroscopy with DFT calculations. We show that origin of lower energy PL band in $(PEA)_2PbI_4$ is due to Rashba type band splitting, a feature which is experimentally proven by demonstrating the longer PL lifetimes of the HP than FP. Furthermore, our theoretical calculation shows that structural distortions or symmetry breaking is the origin of the Rashba type band splitting effect in $(PEA)_2PbI_4$. However, presence of polar organic cation does not lead to the structural distortions or symmetry breaking in $(F\text{-}PEA)_2PbI_4$. Our work highlights that controlling the organic cation in 2D RP perovskites allows one to design stable low-dimensional hybrid perovskites with strong Rahsba effects for spintronic applications.

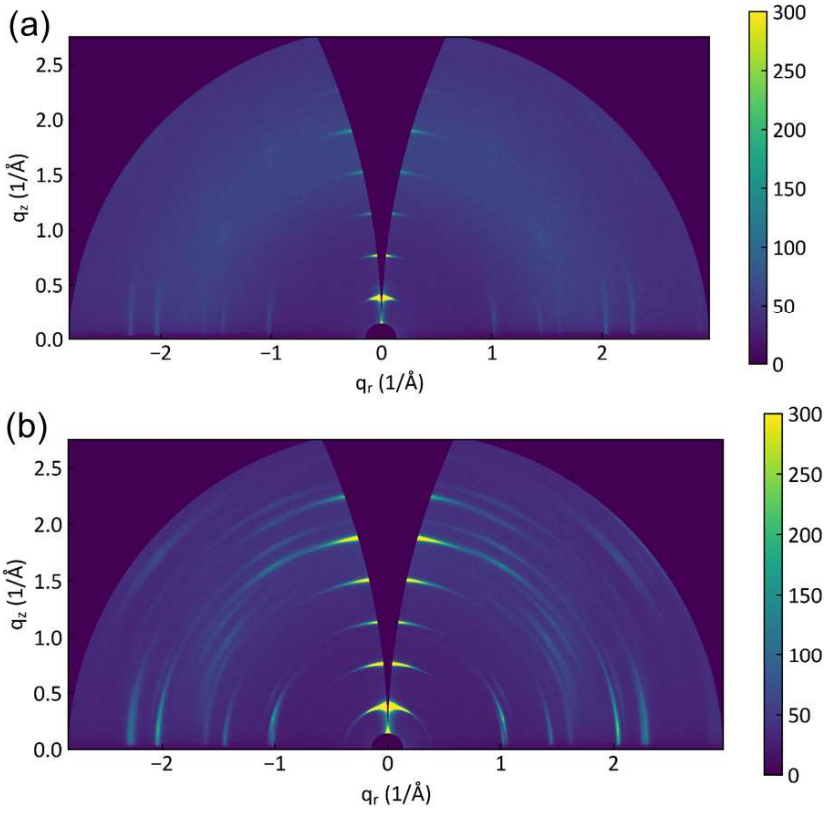

Figure 1. 2D GIWAXS scattering patterns of (a) (PEA)2PbI4 and (c,d) (F-PEA)2PbI4 measured with 13 keV X-ray energy at an incident angle of 0.25°.

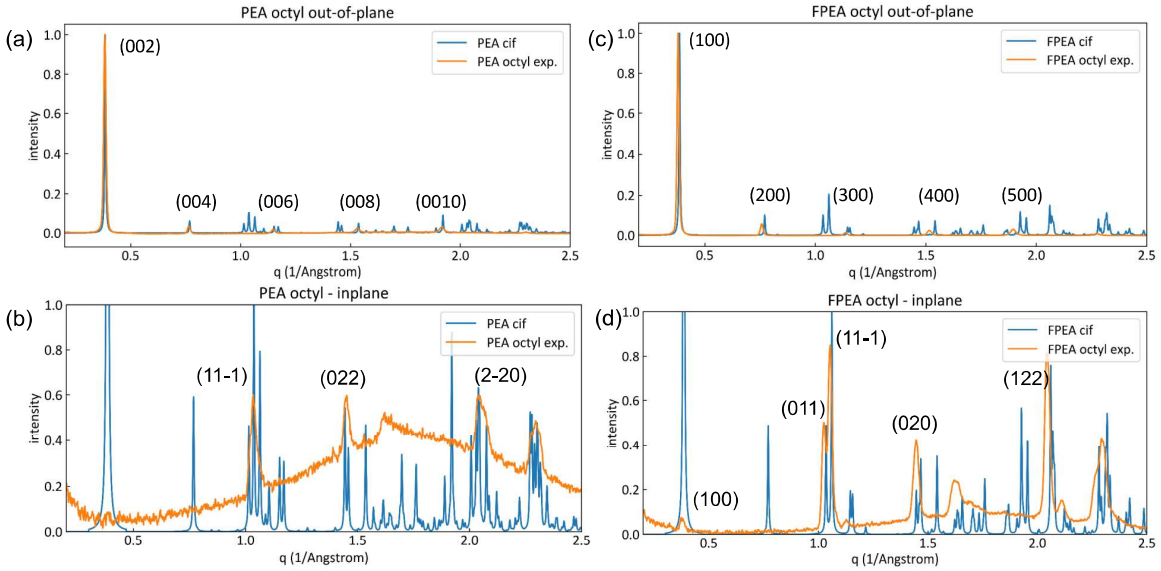

Figure 2: In plane and out-of-plane 1D line cuts of PEA (a,b) and FPEA perovskites (c,d) matched with standard CIF files.

Effect of water on the supramolecular structure of primary aliphatic amines

Michael Paulus, Christian Sternemann*

[1]Fakultät Physik/DELTA, Technische Universität Dortmund, 44221 Dortmund, Germany

*christian.sternemann@tu-dortmund.de

Primary amines are from a structural point of view similar to the linear alcohols, i.e. consisting of the same alkyl tail while the amino group NH_2 substitutes the alcohol's OH group. Like alcohols, the amines can form transient supramolecular structures via hydrogen bonding, although to a lesser extent compared to their counterparts, while offering two donor sites in contrast to the alcohols. Latter might favor branched structures in amines. Such cluster formation can be studied via the investigation of the so-called structure factor pre-peak to be observed in X-ray scattering experiments [1] and through computer simulations [2].

In this experiment we performed a study on the influence of water addition to the scattering pre-peak, and therefore to the transient cluster formation, in propylamine, amylamine and octylamine. The X-ray scattering measurements were carried out at beamline BL2 of the DELTA synchrotron radiation source using an incident photon energy of 12 keV, a bandwidth of 10^{-2}, and beam size of 0.5x0.5 mm^2. The diffraction data were collected utilizing a MAR345 image plate detector. The samples were filled into glass capillaries of 1.5 mm diameter, mounted in a Linkam temperature control sample stage and measured at 25°C. We studied amine water solutions for concentrations up to 30vol% water, conditions at which these liquids do not demix.

The diffraction patterns of amylamine/water mixtures are compared in figure 1. The structure-factor peak at a wave-vector transfer q of 14-15 nm^{-1} dominates the pattern showing increasing asymmetry to larger q with water addition owing to the contribution of the water structure factor. The structure factor peak is due to the contact of methylene/methyl groups like in the alcohols [3]. For the pure amine we observe a weak pre-peak compared to the alcohols in the q_c-range 3-5 nm^{-1} as indication of small portion of transient supramolecular associates with average size $d_c=2*\pi/q_c$ = 1.6 nm. Excitingly, the pre-peak strongly gains intensity and shifts to smaller q with addition of water. This behavior hints towards the ability of water to enhance the formation of larger clusters,

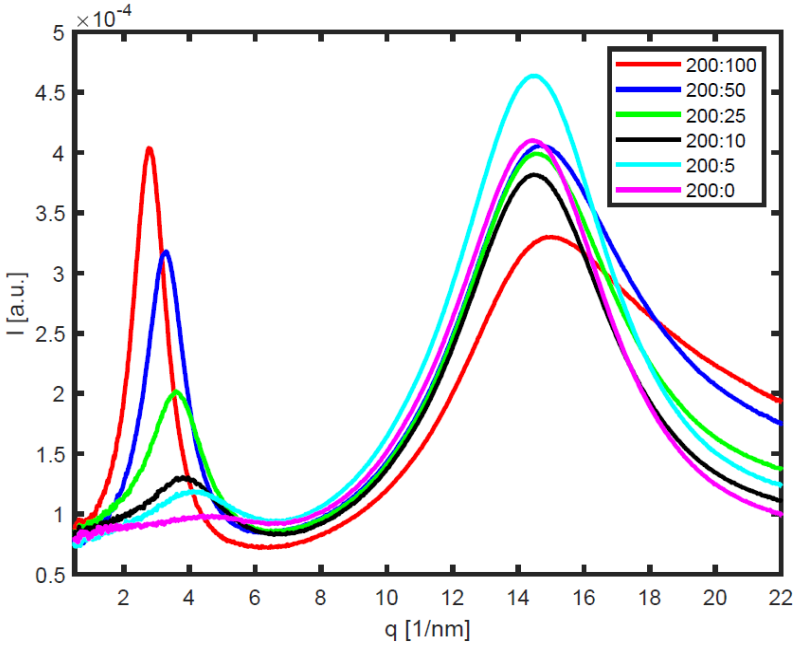

Figure 1: Diffraction patterns of various amylamine/water mixtures measured at BL2. The volume ratios between amylamine and water ranging up to 200:100, i.e. 30 vol% water (see legend). The asymmetry of the main peak is due to the contribution of the water structure factor. The pre-peak at about 3 nm^{-1} shows a peculiar dependence of water addition, i.e. shift to lower waver-vector transfer q and a remarkable intensity increase.

most probably by bridging between NH_2 groups, and increases the number of clusters formed in the mixture. Astonishingly, the pre-peaks are much stronger than that of the pure alcohol counterparts [3, 4] and even exceeds the intensity of the main peak at high water content. This behavior is likewise observed for propylamine and octylamine mixtures with water and is more pronounce for the amines having larger alkyl chains indicating the important role of the steric hindrance of the alkyl tails in the structure formation process. The details of the underlying structural processes and abundant cluster motives will be revealed in comparison with computations of the X-ray diffraction intensity based on molecular dynamics simulations and a cluster analysis using the corresponding simulation boxes. A more detailed study of this peculiar behavior of amine/water mixtures will follow. Moreover we continued our study of pure amines and complemented the temperature dependent X-ray diffraction measurements presented earlier by applying hydrostatic pressure up to 4 kbar. The evaluation of the results is ongoing.

References

[1] L. Almasy, A.I. Kuklin, M. Požar, A. Baptista, Microscopic origin of the scattering pre-peak in aqueous propylamine mixtures: X-ray and neutron experiments versus simulations, Physical Chemistry Chemical Physics 21, 9317 (2019); [2] M. Požar and A. Perera, On the micro-heterogeneous structure of neat and aqueous propylamine mixtures: A computer simulation study On the X-ray scattering pre-peak of linear mono-ols and the related microstructure from computer simulations, Journal of Molecular Liquids 227, 210 (2017); [3] M. Požar, J. Bolle, C. Sternemann, and A. Perera, On the X-ray scattering pre-peak of linear mono-ols and the related microstructure from computer simulations, Journal of Physical Chemistry B 124, 8358 (2020); [4] J. Bolle, S.P. Bierwirth, M. Požar, A. Perera, M. Paulus, P. Münzner, C. Albers, S. Dogan, M. Elbers, R. Sakrowski, G. Surmeier, R. Böhmer, M. Tolan, and C. Sternemann, Isomeric effects in structure formation and dielectric dynamics of different octanols, Physical Chemistry Chemical Physics 23, 24211 (2021).

Acknowledgments

We thank the DELTA machine group for providing synchrotron radiation and acknowledge A. Perera and M. Požar for fruitful discussions. We would like to thank the BMBF for funding via DAAD in the scope of the French-German collaboration PROCOPE 2024-2025 (Project-ID 57704875) *Analysis of the molecular coherence in the self-assembly process: experiment and theory*.

The concentration-dependent structure factor of ferritin solutions

Chang Hee Woo[1], Michelle Dargasz[2], Marvin Kowalski[2], Christian Gutt[2], Michael Paulus[1]

[1]Fakultät Physik/DELTA, TU Dortmund, 44221 Dortmund, Germany

[2]Department of Physics, University of Siegen, Emmy-Noether-Campus, Walter-Flex-Str. 3, 57072 Siegen

Ferritin is an iron-storage protein found in plants and animals. It has a hollow spherical spatial structure with an outer diameter of 13 nm. The shell consists of 24 subunits, which are either identical or at least similar. The cavity inside the protein has a diameter of 7 to 8 nm in which up to 4500 iron ions can be stored in the form of iron hydroxide/oxide. The total mass of the protein is about 900 kDa while the organic part takes 400 kDa [1]. Under neutral conditions, the net charge on the outer surface is close to zero. As proteins generally scatter X-rays rather weakly, ferritin's high iron content makes it an ideal scatterer for investigating proteins in dense sample environments. So-called crowded systems, i.e. systems in which the available space is severely restricted by a high protein concentration (self-crowding) or other macromolecules, are of particular interest here, as they come very close to the conditions within a biological cell. In this study, the structure factor of ferritin in aqueous solution was investigated as a function of concentration using small-angle X-ray scattering (SAXS). Here, the structure factor contains information about the interaction between the proteins. In a SAXS experiment, the intensity scattered by the sample is proportional to the product of the protein form factor *P(q)*, which can be determined by measuring highly diluted solutions, and the effective structure factor *S(q)*.

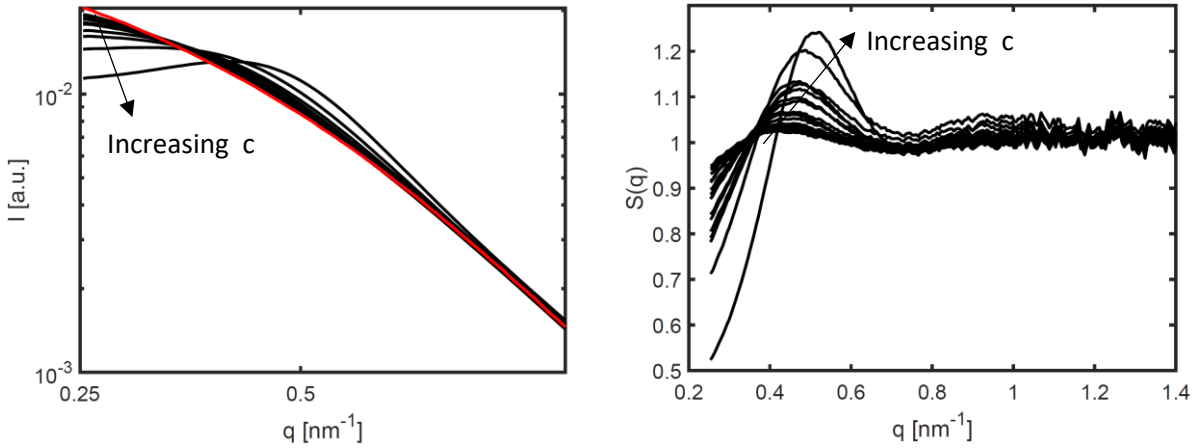

Figure 1: Left: Exemplary SAXS data of ferritin solutions with different concentrations. The form factor measurement is shown in red. As the concentration increases, a decrease in the scattering intensity at low q can be clearly seen. Right: Structure factors obtained by dividing the SAXS data of the high concentrations by the ferritin form factor. The formation of a correlation peak can be clearly seen, which shifts further towards high q with increasing concentration.

Ferritin is supplied in NaCl-containing solution (150 mM) from Sigma-Aldrich (type F4503) with a concentration of about 60 mg/ml. To increase the concentration, a few ml of the solution are placed in a centrifuge filter and centrifuged at 10000g for 15 minutes. The concentration c of the centrifuged solution is determined by heating a few 100 microliters of the solution and then weighing it. Concentrations of over 300 mg/ml can thus be achieved. The ferritin solutions were filled into borosilicate capillaries with a diameter of 1.5 mm and measured at room temperature at beamline BL2 using a photon energy of 12 keV [2]. The exposure time was 60 s per sample. To obtain the form factor, the ferritin stock solution was diluted to 6 mg/ml. To determine the

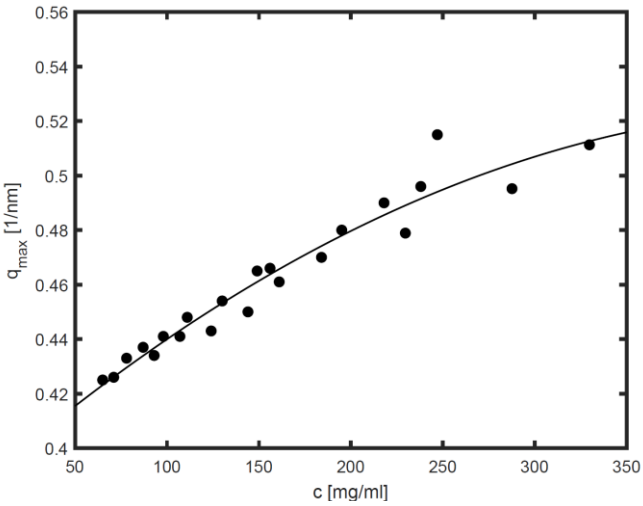

Figure 2: Position of the first maximum of the ferritin structure factor as a function of protein concentration. The line is a square fit and is for guidance only.

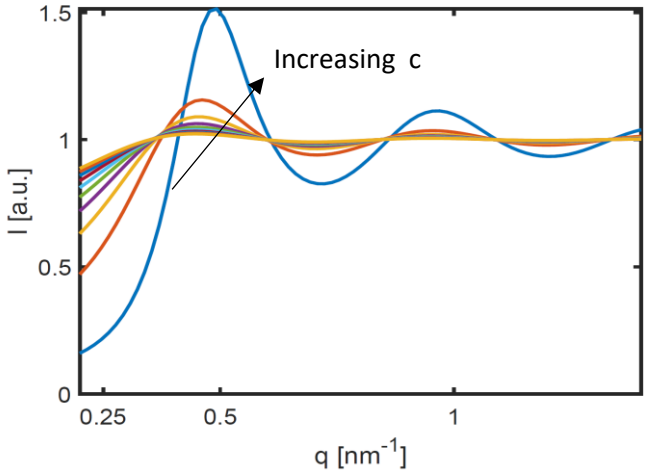

Figure 3: Simulated structure factors for a simple model consisting of hard spheres.

scattering background, which is subtracted from the SAXS data of the protein solutions, a measurement was performed on 150 mM NaCl solution. Figure 1 on the right shows examples of SAXS data measured at different concentrations and the measured form factor. It can be seen that the scattering intensity decreases with increasing concentration for small wave vector transfers q, which indicates an increasing repulsive interaction between the proteins. The right-hand side shows the structure factors resulting from dividing the data of the concentrated solutions by the ferritin form factor. The course of the structure factor again indicates a repulsive interaction potential. The increase in protein concentration causes a strong shift of the first maximum to higher *q* values. In a first step, the position of the first maximum in the structure factor was determined by a quadratic fit and plotted as a function of the protein concentration in Figure 2. This curve can now be used as a guide for determining ferritin concentrations in aqueous solutions. The condition for this, however, is that the type of interaction between the proteins does not change.

In a further step, the course of the structure factor is to be simulated with different models in order to extract information about the underlying interactions. A first attempt can be seen in figure 3, in which a model of hard spheres was used to modulate the structure factor [3].

References

[1] S. Boutet and I. K. Robinson, Precrystallization clusters of holoferritin and apoferritin at low temperature, Phys. Rev. E 75, 021913 (2007).

[2] M. Dargasz, J. Bolle, A. Faulstich, E. Schneider, M. Kowalski, C. Sternemann, J. Savelkouls, B. Murphy, and M. Paulus, X-ray scattering at beamline BL2 of DELTA: Studies of lysozyme-lysozyme interaction in heavy water and structure formation in 1-hexanol, Journal of Physics: Conference Series 2380, 012031 (2022).

[3] R. Botet, S. Kwok and B. Cabane, Percus–Yevick structure factors made simple, J. Appl. Cryst. 53, 1570-1582 (2020).

Control of molecular organization and optoelectronis properties in thin organic semiconductors by deposition parameters

Okan Yildiz[1], Shuanglong Wang[1], Zhitian Ling[1], Amanpreet Kalra[1], and Tomasz Marszalek[1,2]*

[1] Max Planck Institute for Polymer Research, Ackermannweg 10, 55128 Mainz, Germany
[2] Department of Molecular Physics, Faculty of Chemistry Lodz University of Technology, Zeromskiego 116, 90-924 Lodz (Poland)
* Email: marszalek@mpip-mainz.mpg.de

Large-area flexible, organic electronics, including light emitting diodes suffer from non-uniform opto-electrical operation between single devices related to the heterogeneity of the active layer caused by local changes in molecular organization, variability in thin layer crystallinity and repeatability of the deposition process. In order to meet these requirements, our research project is focused on the understanding and controlling the self-assemble properties and crystallization process during semiconducting film deposition. In current periodic report we investigated the photo-excited dynamics of the small semiconductor copper pthalocyanine (CuPc) in thin films, comprising two different π-stack architectures, α-CuPc and β-CuPc. In the solid state, both α-CuPc and β-CuPc morphologies exhibit mixing between Frenkel and charge-transfer excitons (Frenkel-CT mixing). Depending on the molecular organization, we find that this mixing affects the photophysical properties differently. In addition to intersytem crossing, α-CuPc exhibits symmetry-breaking charge transfer. Furthermore, it depends on the excitation wavelength. In β-CuPc, this mechanism is not observed. The differences in molecular packing and spacing in α-CuPc and β-CuPc lead to differences in electronic and vibrational coupling, and this is why the symmetry-breaking charge transfer state is only observed in the α-CuPc thin film. These results shed light on how the molecular organization mediates the balance between the competing photoexcited decay mechanisms in organic semiconductors.

Acknowledgement

This work was partially prepared as part of the „*Self-standing, flexible and solution processable organic field effect transistors for complementary inverter applications*" project that is carried out within the First Team programme of the Foundation for Polish Science co-financed by the European Union under the European Regional Development Fund (*First TEAM/2017-3/26*). The researchers involved in this projects express their gratitude to Dr. Christian Sternemann and Dr. Michael Paulus for their help in the experiments.

References

1. Esther del Pino Rosendo; Okan Yildiz; Wojciech Pisula; **Tomasz Marszalek**; Paul Blom; Charusheela Ramanan, *Physical Chemistry Chemical Physics*, **2023**, 10.1039/d2cp05240g

Characterization of crowded protein solutions for studies of protein dynamics with MHz XPCS at European XFEL

Michelle Dargasz[1], Marvin Kowalski[1], Jaqueline Savelkouls[2], Michael Paulus[2], Christian Gutt[1]

[1]Department of Physics / X-ray science, Universität Siegen, 57076 Siegen, Germany

[2]Fakultät Physik/DELTA, TU Dortmund, 44221 Dortmund, Germany

Understanding molecular processes in living cells is of great interest, not only to model and predict the dynamic properties such as intracellular transport, but also to develop future drug formulations for the pharmaceutical industry. In contrast to often studied model systems like proteins in dilute solution, molecular crowding takes place in living cells. Due to the influence of e.g., crowding agents or excluded volume effects in concentrated systems the dynamics differ from those of a dilute solution [1]. To understand processes like intra-cellular transport, phase transitions and aggregation phenomena [2] it is important to further investigate the dynamics of such systems. These collective dynamics on length and time scales of protein systems can be studied by megahertz X-ray photon correlation spectroscopy (MHz XPCS) at the beamline MID of the European XFEL. The aim of this study is to investigate the effect of molecular crowding on the diffusive dynamics of the globular protein, ferritin with different concentrations and sizes of crowding molecules in the solution. In all sample systems, the concentration of ferritin was kept constant at approximately 55 mg/ml. Polysaccharides (sucrose, ficoll and dextran) as well as polymers (polyethylene glycol) were used as crowders. Their concentration was varied between 10 wt% and 35 wt%.

In order to adjust and characterize the sample systems and thus get an impression of their structure, small-angle X-ray scattering (SAXS) was performed at beamline BL2 of the DELTA synchrotron radiation source at a photon energy of 12 keV.

The scattered intensity $I(q)$ of a SAXS experiment as a function of the scattering vector $q = {}^{4\pi}/_{\lambda} \sin({}^{\theta}/_{2})$ is given by $I(q) \sim {r_0}^2 N\, P(q)\, S_{eff}(q)$ [3] and is therefore composed of the protein form factor $P(q)$ and the effective structure factor $S_{eff}(q)$. The formfactor contains information about the spatial expansion of the particles and can be determined by measuring the scattering intensity of a diluted protein solution. For this purpose, the crowder solution was mixed with a diluted ferritin solution with a resulting ferritin concentration of around 10 mg/ml. The effective structure factor contains information about the particle-particle interactions within the solution. These interactions influence the dynamics of the particles, which is why the structure factor can provide additional information for the interpretation of the dynamics measured by a XPCS experiment. For the background subtraction and

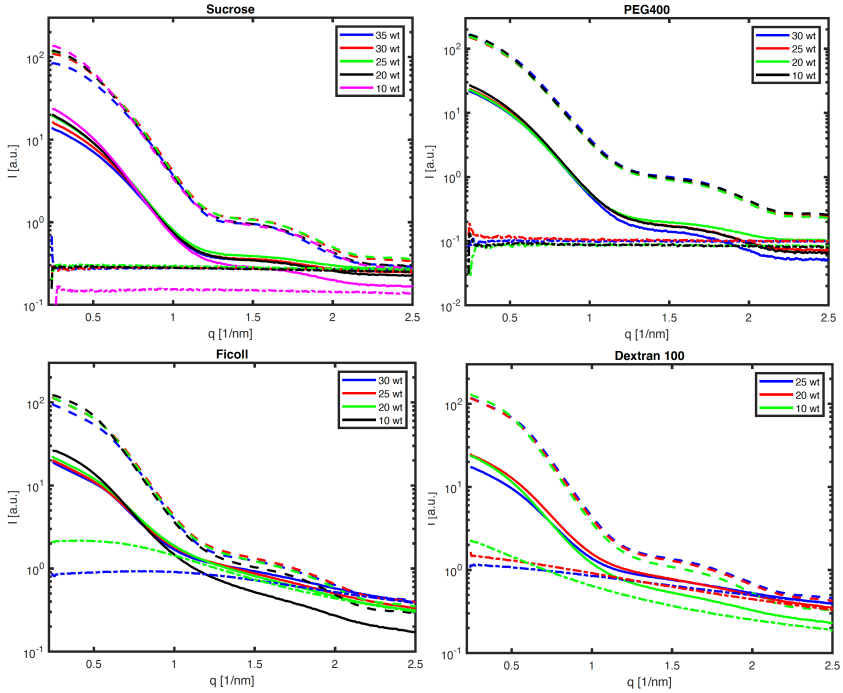

***Figure 1**: Total scattering intensity of ferritin crowder solutions (dashed lines), formfactor (solid lines) and background (dashed dotted lines) for*

to estimate the scattering contribution of the crowder solution itself, a measurement of the scattering intensity of a pure crowder solution was also performed for each concentration. The total scattering curves of the ferritin crowder solutions, the formfactor and scattering curves of the pure crowders are shown in Figure 1. All figures clearly show that the scattering contrast of the protein decreases with increasing crowder concentration. However, there is a noticeable difference between crowders of different sizes. Sucrose and PEG have a hydrodynamic radius of less than 1 nm [4][5], which makes them much smaller than the ferritin protein with a hydrodynamic radius of approx. 6 nm [6]. These small crowders have hardly any scattering contribution of their own, which can be seen in Figure 1 by the almost horizontal scattering curve of the pure crowder solutions. Apart from the decreasing scattering contrast, the shape of the entire scattering curve hardly changes. For crowders whose hydrodynamic radius is slightly higher than that of ferritin (e.g. Ficoll400 and Dextran100 with R_H~7 nm [7][8]), a clear scattering contribution from the crowder itself can be seen. This flattens out slightly with increasing crowder concentration. At low concentrations, these crowders can be described as molecules with a spherical shape that act as individual molecules. If the concentration increases, the individual molecules can entangle, resulting in a network-like structure [9]. At higher concentrations, this also has an influence on the shape of the formfactor and the total scattering intensity. In the case of Ficoll400, for example, a flattening of the scattering intensity between 0.25 nm^{-1} - 0.7 nm^{-1} can be seen.

To be able to estimate the influence of the crowder concentration on the interaction of the proteins in the solution, the next step is to determine the structure factor of the proteins. However, this is not so easy in mixtures of different molecule types. The total scattering intensity is not only influenced by the interactions between the proteins $S_{\mathrm{protein-protein}}(q)$, there are also interactions between the crowder molecules $S_{\mathrm{crowder-crowder}}(q)$ as described above and additionally interactions between the crowder molecules and the proteins $S_{\mathrm{crowder-protein}}(q)$. Both $S_{\mathrm{crowder-crowder}}(q)$ and $S_{\mathrm{crowder-protein}}(q)$ cannot be measured individually using SAXS, which is why it is not possible to subtract their scattering contribution from the total scattering intensity in order to determine the $S_{\mathrm{protein-protein}}(q)$ structure factor.

Since sucrose as a crowder does not produce a large scattering contribution of its own, an attempt was made to determine the structure factor of the sucrose ferritin solutions. This can be seen in Figure 2. The scattering contribution of the pure crowder was subtracted as a background and a diluted ferritin solution was mixed with the respective crowder solution for the formfactor measurement. The course of the structure factor indicates a strongly repulsive interaction potential. The position of the first maximum of the structure factor is between 0.43 and 0.44 nm^{-1}, regardless of the crowder concentration. This is very close to the maximum position of the structure factor of a pure ferritin solution with a similar concentration.

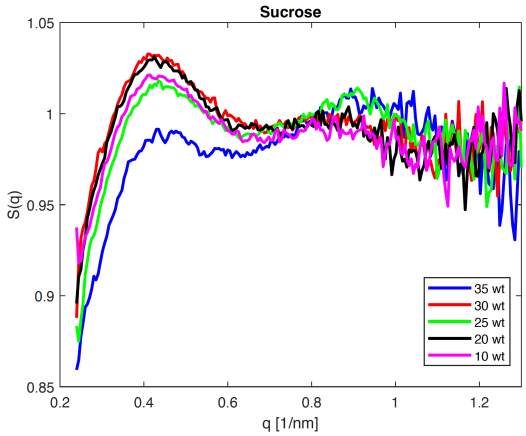

***Figure 2**: S(q) of sucrose ferritin solutions for different sucrose concentrations.*

[1] S.B. Zimmerman et al. Annu. Rev. Biophys. Biomol. Struct. 22, 27-65 (1993).
[2] M. Grimaldo et al. Q. Rev.Biophys. 52, E7 (2019)
[3] J. Als-Nielsen; D. McMorrow. Elements of Modern X-Ray Physics. 9781119998365. John Wiley und Sons, 2011
[4] X. Dong et al. Membranes. 8(2) 23 (2018)
[5] Y. Chenyakin et al. Atmos. Chem. Phys. 17, 2423–2435 (2017)
[6] W. Shatz et al. LCGC Supplements, Special Issues 37, Issue 11, 30-35 (2019)
[7] V.T. Ranganathan et al. Macromolecules 55, 9103−9112 (2022)
[8] J.K. Armstrong et al. Biophysical Journal 87, 4259-4270 (2004)
[9] K. Julius, Diss. TU Dortmund, S.140-150 (2019)

Acknowledgment: The authors kindly acknowledge DELTA for providing synchrotron radiation and for technical support.

Laser trapping assisted assembly formation of perovskites nanocrystals

Qing Qing Wang[1], Jim Jui-Kai Chen[1], Boris Louis[1], Bapi Pradhan[1], Roger Bresolí-Obach[1,2] Johan Hofkens[1],

[1] Department of Chemistry, Katholieke Universiteit Leuven, Belgium, [2] AppLightChem, Institut Químic de Sarrià, Universitat Ramon Llull, Barcelona, Catalunya, Spain

In the last decade, halide perovskite nanocrystals (NCs) have been widely studied for application in photonics and optoelectronics due to their excellent photoelectric properties[1,2,3]. More importantly, their excellent photoelectric performance can be further enhanced by orderly arranging individual NCs to form a collective array of self-assembly structure, which is known as a NC superlattice[4,5,6]. In NC superlattices, zero-dimensional perovskite NCs behave as grids and can be self-assembled into periodic lattice arrays with the assistance of solvents and surface ligands[7]. The self-assembly mode of NCs can be one-dimensional (1D) chain self-assembly, two-dimensional (2D) layered self-assembly, and three-dimensional (3D) cubic self-assembly[8]. However, these self-assembly processes require extended preparation times, often spanning hours or even days. This fact reduces the reproducibility of the methodology as the evaporation rate of the solvent also contributes to the dynamics of superlattice self-assembly[7]. The research on perovskite NC superlattices is still in its infancy. Hence, we are interested in whether we can make and control the fabrication of superlattice using laser trapping through focusing a laser beam during evaporation. Obviously, synchrotron-based X-ray diffraction is an excellent technique to compare the structure and arrangement of the submicromer-sized assembly formed using laser trapping.

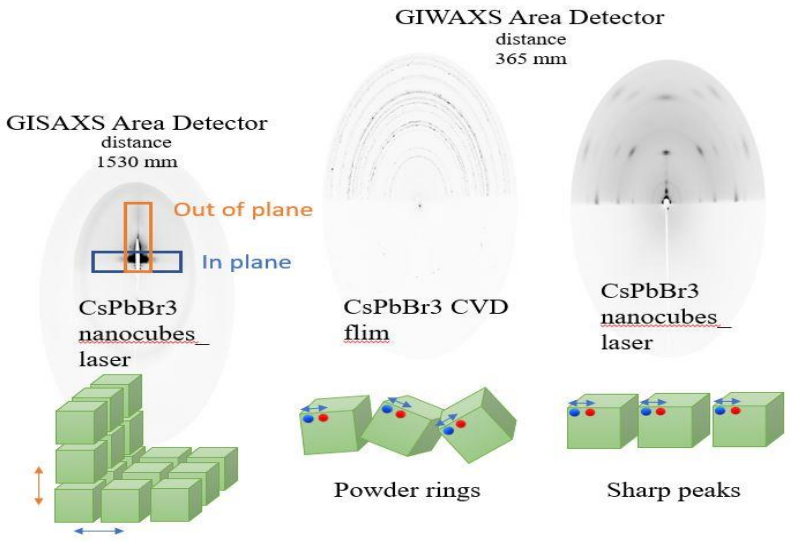

Fig1. GIWAXS (Grazing Incidence Wide Angle X-ray Scattering) and GISAXS (Grazing Incidence Small Angle X-ray Scattering) measurement.

Figures 1 show the GIWAXS (Grazing Incidence Wide Angle X-ray Scattering) and GISAXS (Grazing Incidence Small Angle X-ray Scattering) measurement performed in Beamline 9 and 2 at Delta (Dortmund Electron Accelerator) in Dortmund (Germany) during 20-24 Feb 2023. The GIWAXS analysis enabled the observation of specific point-like peaks of X-ray diffraction, indicating the alignment of nanocrystals and the formation of superlattice structures. This observation is in contrast to the random crystal orietation seen in CsPbBr3 thin films formed via chemical vapor deposition (CVD) method, where only powder rings were observed. Similarly, the GISAXS experiments also revealed the formation of a superlattice structures. By analyzing the specific peaks in the GISAXS data, the presence of the superlattice structure is confirmed.

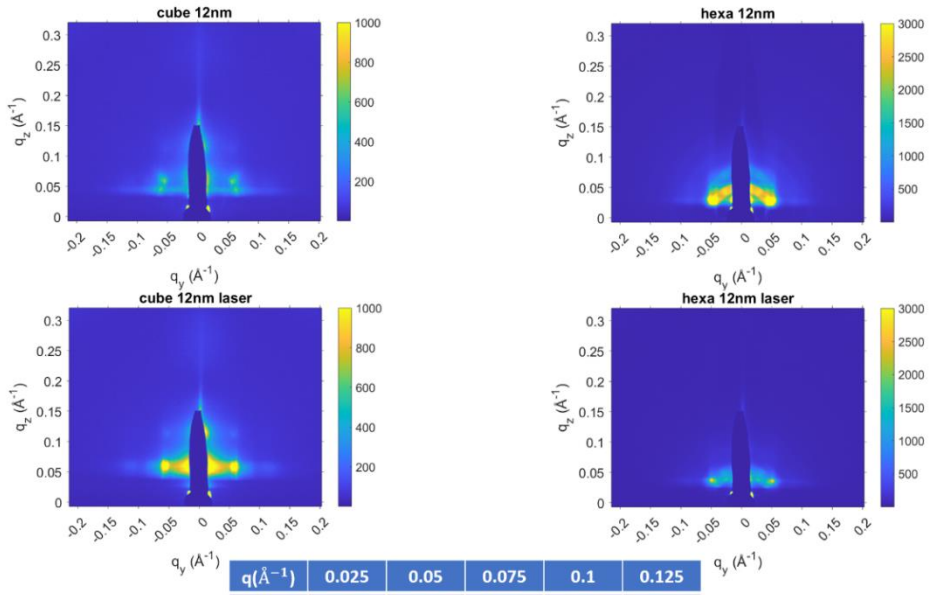

q(Å^{-1})	0.025	0.05	0.075	0.1	0.125
d (nm)	25.3	12.8	8.4	6.2	4.2

Fig2. GISAXS data obtained from of 12 nm sized cubic and hexagonal shaped $CsPbBr_3$ NC.

By examining the positions of the diffraction peaks in the GISAXS data, particularly around q~0.05 Å^{-1}, we can estimate that the distance between the crystals is approximately 12 nm, which corresponds to their size determined by HRSEM. This suggests that the NCs are closely packed within the assemblies. In the case of cubes, the GISAXS data exhibit characteristic peaks that indicate the presence of a superlattice structure. The higher intensity of the peaks observed from cubes deposited with the assistance of laser trapping demonstrates a better alignment of the superlattice, consistent with the findings from GIWAXS. This suggests that the laser trapping contributes to a more packed superlattice arrangement in the cube assemblies. For the hexagonal NCs, a mixture of randomly oriented and aligned assemblies is observed in the GISAXS data. The intensity of the hexagons deposited through spontaneous evaporation is higher, while the hexagons prepared with laser trapping show sharper peaks, indicating a tightly packed structure. Moreover, for both cubes and hexagons, by comparing the line cut profiles of the normalized peaks, it is evident that the self- assembly of NCs is highly ordered with the assistance of laser trapping, as indicated by the narrower peak widths (data not shown).

References

[1] Veldhuis, Sjoerd A., et al. "Perovskite materials for light-emitting diodes and lasers." Advanced materials 28.32 (2016): 6804-6834.; [2] Shan, Qingsong, et al. "High performance metal halide perovskite light-emitting diode: from material design to device optimization." Small 13.45 (2017): 1701770.; [3] Tan, Zhi-Kuang, et al. "Bright light-emitting diodes based on organometal halide perovskite." Nature nanotechnology 9.9 (2014): 687-692.; [4] Abécassis, Benjamin. "Three-dimensional self assembly of semiconducting colloidal nanocrystals: from fundamental forces to collective optical properties." ChemPhysChem 17.5 (2016): 618-631.; [5] Boles, Michael A., Michael Engel, and Dmitri V. Talapin. "Self-assembly of colloidal nanocrystals: From intricate structures to functional materials." Chemical reviews 116.18 (2016): 11220-11289.; [6] Kovalenko, Maksym V., and Maryna I. Bodnarchuk. "Lead halide perovskite nanocrystals: From discovery to self-assembly and applications." Chimia 71.7-8 (2017): 461-461.; [7] Jana, Atanu, et al. "Self-assembly of perovskite nanocrystals." Progress in Materials Science 129 (2022): 100975.; [8] Liu, Jiakai, et al. "Self-Assembly and Regrowth of Metal Halide Perovskite Nanocrystals for Optoelectronic Applications." Accounts of Chemical Research 55.3 (2022): 262-274.

X-ray diffraction experiments on coarse-grained niobium with lateral resolution

F. Brockner, D. Lützenkirchen-Hecht

Fk 4 – Mathematik & Naturwissenschaften, Bergische Universität Wuppertal,

Gauß-Str. 20, D-42119 Wuppertal, Germany

The interaction of intense pulsed- and CW-laser beams with metallic surfaces may lead to periodic structures on the surfaces of the irradiated materials (for reference, see e.g. [1, 2]). These laser-induced periodic surface structures (LIPSSs) have been observed on a variety of different materials, in particular dielectrics, semiconductors and metals after laser irradiation. In particular due to its energy-efficient and flexible fabrication process and the resulting sub-wavelength periodic structures, there are many potential applications in the fields of materials processing, in particular for optics and mechatronics. However, a practical challenge for the laser treatments and the development of the LIPSSs is the achievement of a homogenous and uniform surface after the procedure, because of the influence of local surface structures as e.g. in grain boundaries and different crystallographic orientations of the irradiated grains, as can be seen in Fig. 1, where a scanning electron micrograph of a laser-treated large-grain niobium sample is shown. Different periodic structures, i.e. different orientations and amplitudes of the periodic structures are observed for different grains, and in particular in the grain boundaries. If, however, large areas need to be polished homogeneously, such a variation of the surface contour may not be acceptable. Here we are interested in particular in the laser polishing of niobium, that is used in cavities for particle accelerators [3]. Laser polishing, as a dry process, may avoid the use of aggressive and toxic chemicals such as, e.g., hydrofluoric acid and may replace conventional polishing procedures such as buffered chemical polishing or electropolishing. First laser polishing experiments of Nb samples have successfully been demonstrated (see e.g. [4 - 6]), however, homogenously polishing larger areas is still a huge challenge.

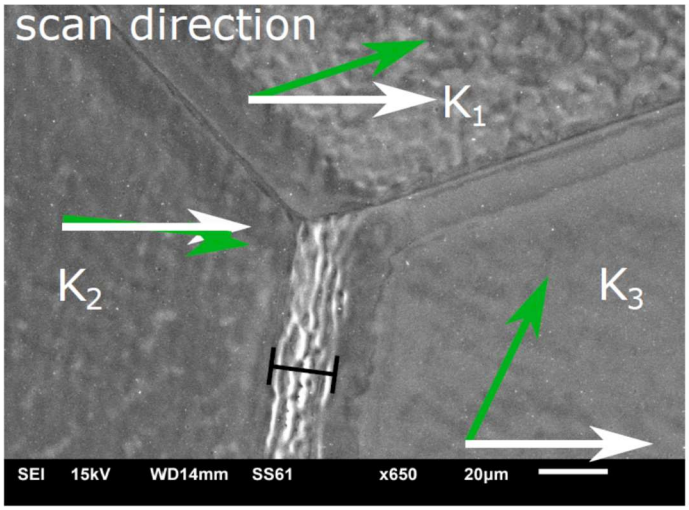

Fig. 1: Scanning electron micrograph of a coarse-grained Nb sample after a laser polishing procedure with a ns-laser in the area of the grain boundaries of three neighboring grains K1, K2 and K3. The scan direction of the laser (white arrows) as well as the orientation of the wave-like structures on the surface (green arrows) are shown. The different amplitudes of the wave-like structures and the different orientations of the wave patterns in the different grains and the grain boundaries are clearly recognized.

In order to understand the influence of the grain orientation on the laser-polishing process and the evolution of the LIPSS in more detail, knowledge about the grain orientation is thus of outmost importance. We have therefore conducted laterally resolved X-ray diffraction experiments with a small-sized beam of 0.3 mm x 0.3 mm size and a photon energy of 12.0 keV at DELTA beamline 10 [7]. The sample, polished to a mirror-like finish, was a 3 mm thick large grain sample with at least three optically visible, several mm-sized grains. The sample was mounted in a x-y-stage in the Kappa-diffractometer at beamline 10, and Θ-2Θ-diffraction patterns were obtained on a PILATUS 100 K detector (Dectris, Dübendorf, Switzerland) as a function of the localization of the X-ray beam on the sample.

Typical results are compiled in Fig. 2, where 4 different diffraction patterns are compared. The diffraction geometry was calibrated by using a polycrystalline Nb foil, so that the positions of all important Nb reflections are known and measured diffraction spots can be correctly assigned. Obviously, the measured grains have a different orientation, as only very few spots can be detected, depending on the position of the beam on the sample.

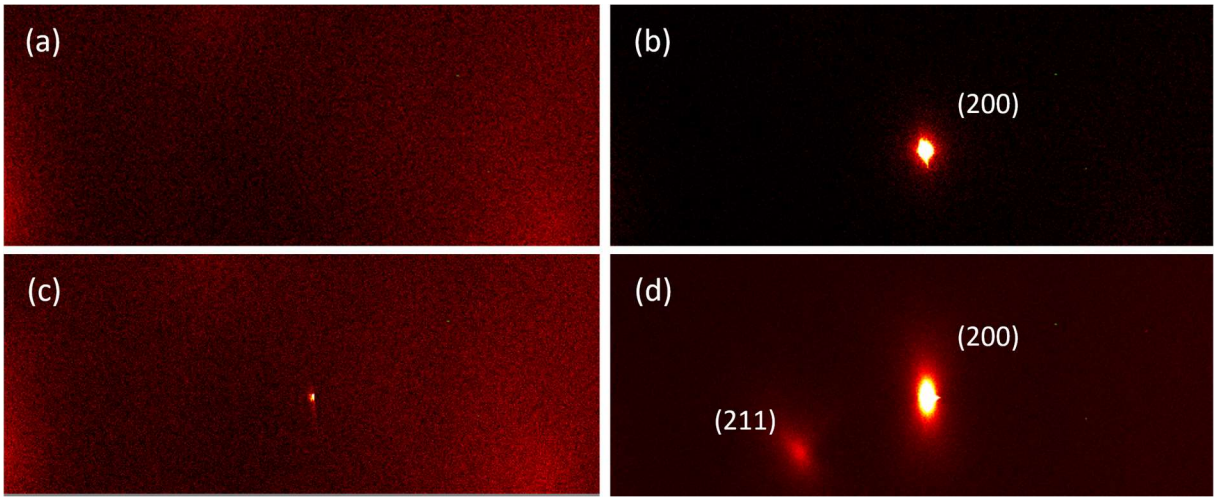

Fig. 1: Position-dependent X-ray diffraction measurements of a coarse-grained Nb sample in Θ-2Θ-geometry for different locations on the sample (a) to (d). No (a) or only very weak reflections (b), or very intense (c) or even double reflections (d) can be clearly recognized for the different locations, which indicate different crystallographic orientations of the individual grains. A comparison with a polycrystalline niobium reference sample allows the diffraction reflections to be assigned. The (110) reflex is located in the area of the right edge of the images.

Further measurements to correlate the orientation of the grains with the polishing results are, however, necessary for a final discussion. Additional spatially resolved X-ray diffraction measurements with synchrotron radiation are therefore planned, especially on surfaces that have already been laser polished.

Acknowledgements

We like to thank the DELTA machine group for the delivery of a stable and intense X-ray beam. This project was financially supported by the BMBF under project no. 05H21PXRB1 (TOSCA).

References:

[1] K. Bischoff, P. Quigley, A. Hohnholz, P. Jäschke, S. Kaierle, Procedia CIRP 94 (2020) 924.
[2] J. Huang, Y. Liu, S. Jin, Z. Wang, Y. Qi, J. Zhang, K. Wang, R. Qiu, Frontiers Phys. 10 (2022) 932284.
[3] D. Proch, P. Schmueser, W. Singer, L. Lilje, Niobium in superconducting RF cavities, Niobium Science & Technology, P. J. P. Bordignon, et al. ed., Niobium 2001 Ltd., Bridgeville, PA, 2002, pp. 187-206.
[4] V. Porshyn, P. Serbun, H. Bürger, S. Soykarci, D. Lützenkirchen-Hecht, J. Phys. Conf. Ser. 1067 (2018) 082011.
[5] V. Porshyn, P. Serbun, D. Lützenkirchen-Hecht, Phys. Rev. Acc. Beams 22 (2019) 023101.
[6] V. Porshyn, P. Rothweiler, D. Lützenkirchen-Hecht, J. Laser Appl. 32 (2020) 042009.
[7] D. Lützenkirchen-Hecht, R. Wagner, S. Szillat, et al., J. Synchrotron Rad. 21 (2014) 819

Oxidation Resistance and Nanostructure of PECVD Ti-Si-C-N Coatings

Thewes, A.[1]; Paschke, H.[2]; Brückner, T.[2]; Sternemann, C.[3]; Paulus, M.[3]; Tillmann, W.[4]; Lopes Dias, N.F.[4]; Urbanczyk, J.[4]

[1)] IOT TU Braunschweig, 44145 Dortmund, Germany

[2)] Fraunhofer Institute for Surface Engineering and Thin Films IST, Dortmund 44145, Germany

[3)] Fakultät Physik/DELTA, Technische Universität Dortmund, 44221 Dortmund, Germany

[4)] LWT TU Dortmund, 44221 Dortmund, Germany

Introduction

TiN-based coatings are often designed with a so-called nanocomposite structure, consisting of randomly oriented nanocrystalline grains (size < 10 nm) surrounded by an amorphous matrix [THE22]. Typical examples for these coatings are Ti-Si-N [VEP06], Ti-B-N [GIS94], and Ti-Si-C-N [MA07]. These nanocomposite coatings exceed hardness values of 40 GPa due to the Hall-Petch effect [VEP95]. Other authors unintentionally created amorphous films by lowering the deposition temperature (e.g. depositing at room temperature [PAR07]). The question addressed in this work is: are there more nanostructures to be found?

Method

Ti-Si-C-N coatings were deposited on single-crystalline Si-wafers via Plasma Enhanced Chemical Vapor Deposition (PECVD). The low pressure atmosphere of 200 Pa contains $TiCl_4$, $Si(CH_3)_4$, CH_4, N_2, H_2, and Ar. The chemical composition was determined via Electron Probe Microanalysis (EPMA). X-ray diffraction (XRD) measurements were performed at Beamline BL9 [KRY06] of the synchrotron light source DELTA (TU Dortmund, Dortmund, Germany) using a PILATUS 100K detector. The energy of the incident photon beam was E_0 = 27 keV and the beam size was set to 0.2 x 0.7 mm^2 (h x v). The angle of incidence was 1°. These experiments were carried out at room temperature and 950 °C.

Results and discussion

EPMA measurements revealed a chemical composition of 35.8 at.-% Ti, 8.1 at.-% Si, 41.1 at.-% C, and 12.7 at.-% N with additional 1.1 at.-% O and 1.2 at.-% Cl as residual elements from the deposition process. The authors reported an oxidation resistance of a different Ti-Si-C-N coating of at least 800 °C in their DELTA User Report 2022. This time, the authors investigated the oxidation resistance at 950 °C. The results are shown in fig. 1 (a) and (b).

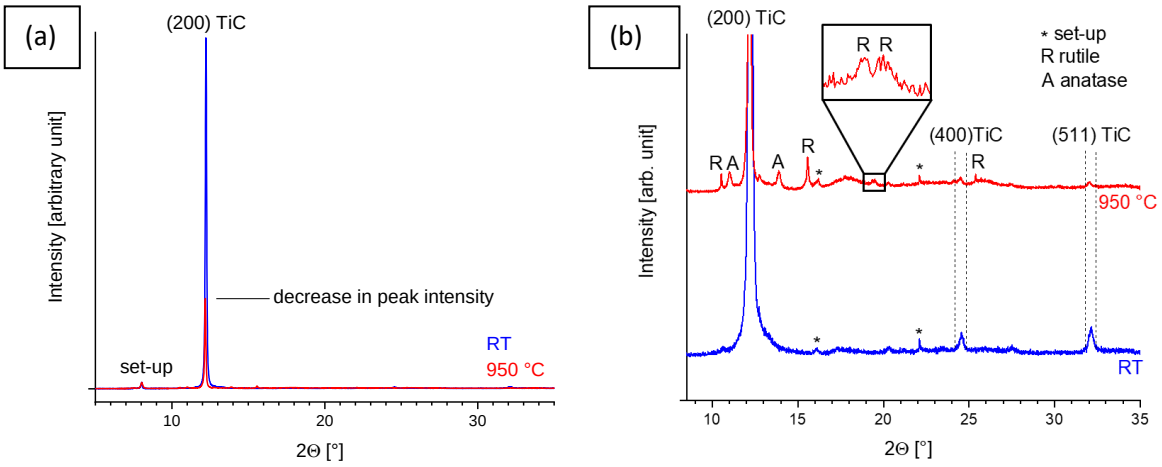

Fig. 1 *In-situ* X-ray diffraction patterns at room temperature and 950 °C (a) in an overview and (b) in a close up

In fig. 1 (a), a dominant (200) TiC reflex can be identified, which correlates with the high Ti- and C-content (35.8 and 41.1 at.-%, respectively). Regardless of the big difference in peak intensity between room temperature and 950 °C, these (200) reflexes are orders of magnitude bigger than the rest of the reflexes. The high intensity shows that there are a lot of grains oriented in the same direction. As fig. 1 (a) does neither yield any information on secondary TiC reflexes nor formation of TiO_2 reflexes at 950 °C, fig. 1 (b) shows a close up of the relevant areas. At room temperature, neither anatase nor rutile was observed, which was to be expected in the as-deposited state. Traces of (400) TiC and (511) TiC are detected, but are several orders of magnitude smaller than (200) TiC. It still shows that the crystalline structure is made of TiC and despite adequate Ti- and N-content (35.8 and 12.7 at.-%, respectively), no traces of TiN lattices were identified. At 950 °C, the same (400) TiC and (511) TiC reflexes are observed. Additionally, several anatase and rutile reflexes are identified, with many of them stronger pronounced than (400) and (511) TiC, but orders of magnitude smaller than (200) TiC. Considering the difference in peak height, only the surface-near atoms seem to be oxidized, whereas the coating underneath is intact.

Scherrer equation was used to identify the grain sizes. The calculated result for (200) TiC is 24 nm, but the margin of error increases for grains > 10 nm. Thus, it can only be estimated that the actual grain size is somewhere between 20 and 50 nm. The valuable information to be gained by Scherrer equation is, that this is no typical nanocomposite coating with a grain size of 3 to 10 nm [PAT01]. Additionally, nanocomposite coatings are known to be composed of randomly oriented grains, as they are fully mantled by an amorphous matrix and no preferred direction of growth is seen. The coating deposited in this work shows a strong texturing with (200) TiC as the preferred direction.

Conclusion

It was found, that there is a Ti-Si-C-N coating with high oxidation resistance (950 °C) beside amorphous and nanocomposite coatings. Considering the morphological zone model of Patscheider *et al.* [PAT01], the volumetric ratio of the amorphous matrix is insufficient to stop the grain growth during deposition at 10 nm, leading to unhindered grain growth and (200) TiC grain orientation. Thus, the coating is categorized as A in Patscheider's morphological zone model (compare [PAT01], Fig. 3).

Acknowledgment

We kindly acknowledge the support of the DELTA machine group and provision of synchrotron radiation beamtime. This work was supported by the German Research Foundation (DFG) within the project (grant No. 434108570).

Literature

[GIS94] Gissler, W.: Structure and properties of Ti-B-N Coatings. Surface and Coatings Technology 68/69, S. 556–563, 1994.

[KRY06] Krywka, C. et al.: The new diffractometer for surface X-ray diffraction at beamline BL9 of DELTA. Journal of synchrotron radiation Pt 1/13, S. 8–13, 2006.

[MA07] Ma, S. L. et al.: Synthesis and characterization of super hard, self-lubricating Ti–Si–C–N nanocomposite coatings. Acta Materialia 18/55, S. 6350–6355, 2007.

[PAR07] Park, I. W. et al.: Multifunctional Ti-Si-B-C-N Tribological Nanocomposite Coatings for Aerospace Applications. Materials Science Forum 539-543, S. 173–180, 2007.

[PAT01] Patscheider, J.; Zehnder, T.; Diserens, M.: Structure–performance relations in nanocomposite coatings. Surface and Coatings Technology 5/146-147, S. 201–208, 2001.

[THE22] Thewes, A. et al.: Ti-Si-B-C-N plasma enhanced chemical vapor deposition nanocomposite coatings for high temperature applications. Thin Solid Films 760, S. 139507, 2022.

[VEP06] Vepřek, S. et al.: The issue of the reproducibility of deposition of superhard nanocomposites with hardness of ≥50 GPa. Surface and Coatings Technology 12-13/200, S. 3876–3885, 2006.

[VEP95] Vepřek, S.; Reiprich, S.; Shizhi, L.: Superhard nanocrystalline composite materials: The TiN/Si 3 N 4 system. Applied Physics Letters 20/66, S. 2640–2642, 1995.

Description of the microstructural evolution during tempering of additively manufactured hot work tool steel X40CrMoV5-1

A. Röttger[1], J. Hankel[1], M Blüm[1], C. Sternemann[2]

[1]Lehrstuhl Neue Fertigungstechnologien und Werkstoffe (FUW), Bergische Universität Wuppertal, 42651 Solingen, Germany
[2]Fakultät Physik/DELTA, Technische Universität Dortmund, 44221 Dortmund, Germany

In order to reduce the costs and the production time of tools, high motivation to produce tools using additive manufacturing, designated as "Rapid Tooling", exists. In particular, the layered built-up process enables the production of complex-shaped tools with, for example, the insertion of internal cavities. These internal cavities can act as cooling channels below the tool surface, allowing optimal temperature control of the tools during operation. This optimized tool cooling increases cycle times, particularly for hot-forming tools, and thus the economic efficiency [1]. In addition to the chemical composition and the manufacturing process, the heat treatment significantly influences the microstructure and, therefore, the properties of tool steels. Conventionally, the hot work steels from the WAS2 group, considered in this investigation, are hardened and aged in the area of the secondary hardness maximum to achieve the required properties. The hardness tempering diagram of X40CrMoV5-1 steel is shown in ***Figure 1***, and the chemical composition and PBF process parameters are listed in ***Table 1***. The dotted curve represents the hardness tempering diagram of the steel X40CrMoV5-1 in cast condition (plots are taken from [2]). A hardness of 550HV10 is achieved after oil quenching from an austenitization temperature of 1050°C. In the course of a higher tempering temperature, hardness drops slightly due to the release of carbon from the supersaturated martensite and the associated transformation from the tetragonal to the cubic martensite. Further, the increase in hardness up to 580HV10 (secondary hardness regime) can be traced back to the precipitation of Mo- and V-rich secondary carbides, which increase the materials' hardness by precipitation hardening. A similar course of the hardness-tempering-diagram can be assigned to the PBF-LB/M produced, hardened, and tempered samples (samples H+A). Differences arise in the height of the secondary hardness maximum formed at a lower level.

Table 1: chemical composition of X40CrMoV5-1 steel in mass%, measured by OES

Element	C	Cr	Mo	V	Mn	Fe
Mass%	0.388	4.9	1.2	1.0	0.3	Bal.

PBF-Process Parameters used:
Power= 100W, 200°C baseplate preheating, exposure time= 110 µs, point distance = hatch distance= 30 µm

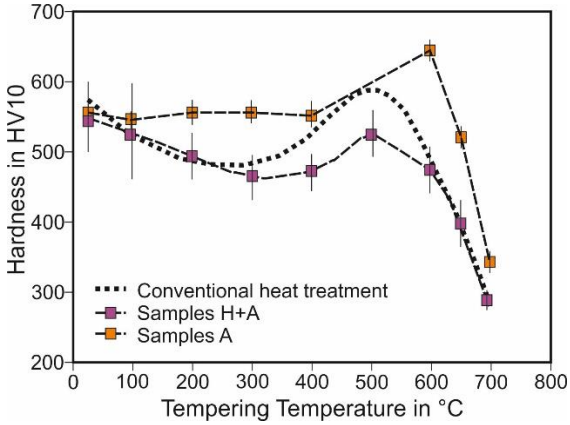

Figure 1: hardness-tempering -diagram of steel X40CrMoV5-1 in different conditions (results are taken from [2])

In comparison, the hardness of the only tempered PBF samples (samples A) is at an almost homogeneous level up to a tempering temperature of 400°C. Still, it then increases in the area of the secondary hardness maximum to higher hardness values of up to 640HV10. In addition, the secondary hardness maximum is shifted towards higher tempering temperatures. To correlate the change in the material's properties with the changes in the microstructure during tempering, diffraction experiments were carried out at BL9 at the Dortmund electron storage ring. The incident photon energy was set to 27 keV, and the beam's wavelength was 0.4592 Å. The beam size at the sample position was 0.7 x 0.05 mm^2 (h x v), and the sample was aligned so that the angle of incidence was 1°. 2D diffraction images were measured using a MAR345 image plate detector. A diffraction image of a CeO_2 reference sample

was utilized to calibrate the setup, detector–sample distance, detector tilt, and beam center. The diffractograms of the PBF-processed, quenched, and tempered diffractograms are shown in ***Figure 2***. It can be recognized that the austenite phase still remains stable up to tempering temperatures of 500°C and then transforms into the α-Fe phase. The increase in hardness in the area of the secondary hardness maximum can be mainly attributed to the precipitation of phase V_8C_7 (●), whereby the reflex intensity of the MC-phase increases from 500 to 700°C. Quantification of the resulting volume content was omitted here. In contrast, a strong reflex (see ▲-reflex at 2Θ of 14, 21, 24°) of the austenite phase is still present in sample A550, which was directly tempered after PBF-processing without further quenching step. This observation can also indirectly explain the approximately linear hardness-tempering behavior of sample A up to 400°C in ***Figure 1***. The alternating heat input causes partitioning effects. The element carbon accumulates in some austenite sub-grains by diffusion and stabilizes them. At the same time, this enrichment in carbon of some austenitic sub-grain areas causes a reduction in the C content in neighboring sub-grains. Due to the reduced C content, the martensite-start temperature locally increases, which promotes a corresponding martensitic transformation [3]. The recurring heat insertion further tempers the formed martensite in the carbon-enriched sub-domains. The hardness tempering diagrams show that the resulting hardness corresponds to a sample directly tempered at approximately 400 °C after PBF processing. In addition, the additively manufactured microstructure also has a high dislocation density, which acts as a corresponding nucleation site for the subsequent secondary carbide formation. If the samples are austenitized and quenched, the dislocation density in the samples H+A is reduced by recovery and recrystallization effects, so the secondary hardness maximum drops due to a smaller number of secondary carbides formed. Another reason for the shift in the secondary hardness maximum could be the inherently higher solution state in sample A, which is correspondingly reduced by renewed austenitization at a lower temperature. Future studies will focus on determining the local chemical composition and dislocation density to better describe the microstructure formation process during the heat treatment of additively manufactured hot-work steels. The results help to make appropriate heat treatment recommendations for technological applications or to expand the property potential of this group of steels.

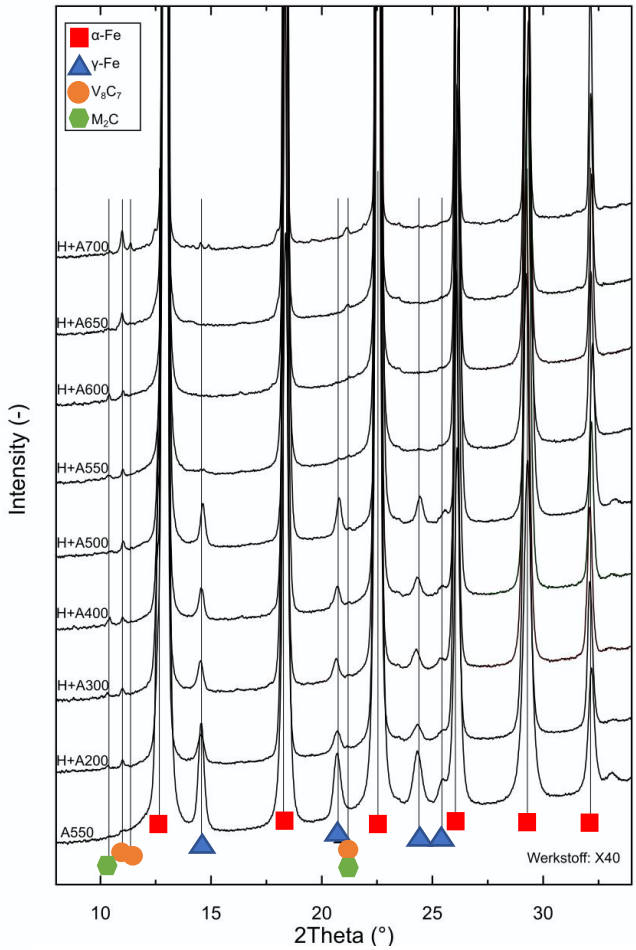

Figure 2: Diffractograms of investigated samples in different conditions

References

[1] A. Röttger, J. Boes, F. Großwendt, S. Weber: Description of a new concept for the development of adapted hot-work tool steels for laser-powder bed fusion, Additive Manufacturing, Volume 61, 2023, pp. 103292,

[2] J. Krell, A. Röttger, K. Geenen, W. Theisen: General investigations on processing tool steel X40CrMoV5-1 with selective laser melting, Journal of Materials Processing Technology, Volume 255, 2018, pp. 679-688,

[3] K. Geenen, A. Röttger, F. Feld, W. Theisen: Microstructure, mechanical, and tribological properties of M3:2 high-speed steel processed by selective laser melting, hot-isostatic pressing, and casting, Additive Manufacturing, Volume 28, 2019, Pages 585-599,

Understanding the Microstructural Formation of an Austenitic Steel during Additive Manufacturing

A. Röttger[1], J. Hankel[1], R. Ortmann[2], J. Sehrt[2], C. Sternemann[3]

1Lehrstuhl Neue Fertigungstechnologien und Werkstoffe (FUW), Bergische Universität Wuppertal, 42651 Solingen, Germany
2Lehrstuhl Hybrid Additive Manufacturing (HAM), Ruhr-Universität Bochum, 44801 Bochum, Germany
3Fakultät Physik/DELTA, Technische Universität Dortmund, 44221 Dortmund, Germany

Additive manufacturing (AM) has reached market maturity within the last two decades. Particularly when producing individual components in small batch sizes, additive manufacturing processes offer advantages over conventional melt and powder metallurgy processes in terms of production time and production costs. A material often considered for AM is the corrosion-resistant steel AISI316L (1.4404). Its frequent use can be attributed to its good corrosion properties, sufficiently high strength, and good processability by welding and AM processes. Conventionally, this steel was optimized for arc welding. The alloying elements Cr, Mo, and Ni are coordinated with one another in such a way that primary ferritic solidification of the melt occurs during welding. This primarily ferritic solidification counteracts the high sensitivity to hot cracking of austenitic steels since ferrite has a higher solubility for sulfur (S) and phosphorus (P) and a lower linear thermal expansion coefficient than the austenite phase. By binding the accompanying elements S and P, the formation of low-melting phases (FeS, Fe_3P) takes place and, thus, the formation of hot cracks can be counteracted [1]. In addition, the ferrite counteracts Ostwald ripening at elevated temperatures, so that the formation of coarse grains is suppressed during the MIM (Metal Injection Molding) production of this material.

A currently unanswered question is a statement about the microstructure that forms and the associated properties of the steel AISI316L after processing with different AM processes. With the help of this knowledge, the optimal AM process can be selected for the respective application. This study does not deal with the materials properties but focuses on measuring the ferrite volume content after processing steel AISI316L using different AM techniques. With the knowledge of the ferrite phase content formed, the alloy concept can be adjusted to the AM process (especially for PBF), or the process parameters can be adapted to counteract strong grain growth during sintering (MEX, VPP). The nomenclature, chemical composition, and the associated ferrite volume content of the specimens investigated are listed in ***Table 1***. Standard commercial systems with optimal process parameters were used for sample manufacturing (cubes with an edge length of 10 mm). Neither the systems used, nor the corresponding process parameters should be presented here in the depth that would otherwise be necessary. The chemical composition of the investigated samples was determined by optical spark emission spectrometry using a type QSG750 (OBLF GmbH, Germany).

Table 1: Chemical composition and δ-Ferrite volume fraction of the samples investigated

Sample/Element in mass%	C	Cr	Ni	Mo	Mn	N	Fe	**δ-ferrite content vol.%**
PBF-EB	0.01	17.57	12.67	2.37	0.60	0.07	bal.	0.0±0.0
PBF-LB	0.01	16.85	12.43	2.17	0.45	0.05	bal.	0.0±0.0
DED-LB	0.01	16.47	12.88	2.24	0.72	0.03	bal.	0.25±0.01
DED-Arc	0.01	17.98	12.00	2.65	1.50	0.00	bal.	2.20±0.98
MEX-TRB	0.01	16.27	10.22	2.22	0.92	0.02	bal.	4.10±0.06
VPP-LED	**0.12**	16.73	9.90	2.76	1.26	**0.22**	bal.	0.28±0.04

Nomenclature
PBF-EB= Powder Bed Fusion-Electron Beam
PBL-LB=Powder Bed Fusion-Laser Beam
DED-LB=Direct Energy Deposition-Laser Beam
DED-Arc=Direct Energy Deposition-Arc
MEX-TRB=Material Extrusion
VPP-LED= Vat photopolymerization

No ferrite phase can be detected in the microstructures of the specimens produced by PBF-LB and PBF-EB, as shown in ***Figure 1***. In the PBF-LB process, the absence of the ferrite phase can be attributed to the high solidification rate. Vittek et al. and Kelly et al. report in [2, 3] that due to the high solidification rate, the more stable ferrite formation from a formation kinetic point of view is skipped by the austenite formation due to a higher growth rate. In the PBF-EB process, the lack of ferrite formation

can be attributed to the powder bed preheating of approx. 900 °C. On the one hand, powder bed preheating reduces the high solidification rates. On the other hand, thermodynamic calculations (ThermoCalc; database TCFe12, 1 mol, atmospheric pressure; phases: austenite=fcc, ferrite=bcc, melt=liquid, Cr-rich $M_{23}C_6$=M23C6) confirm that preheating also takes place in an area where no ferrite is thermodynamically stable (see phase quantity diagram in ***Figure 1***). Thus, the ferrite previously formed during solidification is converted into the more stable austenite by annealing at 900 °C. Compared to the PBF samples, 0.25 to 2.2 vol.% ferrite could be measured in the DED samples. The higher ferrite volume content of the DED-Arc samples (2.2 Vol.-%) is due to the lower solidification rate than the laser-based DED-LB process (0.25 Vol.%). More ferrite is formed if the solidification rate decreases; thus, the microstructures of specimens produced by the sinter-based AM processes MEX-TRB and VPP-LED differ significantly in their ferrite volume content. The highest ferrite volume content in the MEX-TRB samples can be attributed to the selected sintering temperatures of approx. 1250-1350°C, where the phase ferrite is stabilized (see green lines of phase quantity diagram **Figure 1**). The VPP samples (blue lines) are also densified after compaction by solid-state sintering, similar to the MEX-TRB samples. One reason for the lower ferrite volume content can be attributed to the higher carbon and nitrogen content. Both elements strongly stabilize the phase austenite, so the stability range of the ferrite phase is shifted towards higher temperatures and the overall amount of formed ferrite is reduced.

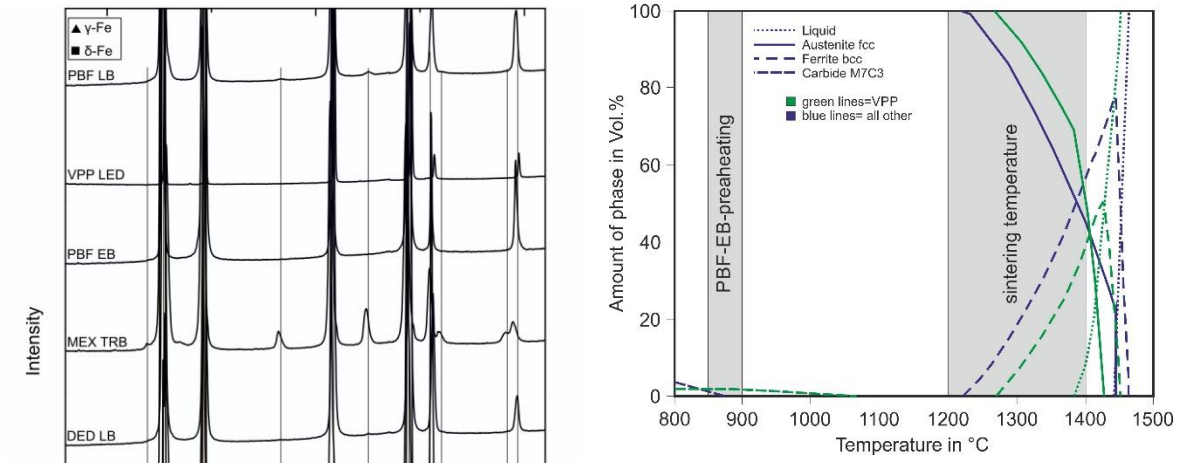

Figure 1: (left figure) Diffraction pattern of the AlSi316L steel specimens processed by different AM techniques; (top figure) Thermodynamic calculations of phase quantity diagrams for the conventional alloy of steel AISI316L (blue lines) and the VPP alloy (green lines)

References

[1] Böllinghaus, T. u. a.: *Hot Cracking Phenomena in Welds II*, 1. Aufl., Springer-Verlag, 2008, 458

[2] Vitek, J. M., Dasgupta, A. und David, S. A.: ”Microstructural modification of austenitic stainless steels by rapid solidification“,
in: *Metallurgical Transactions A* 14 (9 1983), S. 1833–1841.

[3] Kelly, T. F., Cohen, M. und Sande, J. B.: ”Rapid solidification of a droplet-processed stainless steel“, in: *Metallurgical Transactions A* 15 (5 1984), S. 819–833.

Acknowledgement

We thank Felix Großwendt from the Chair of Materials Engineering at the Ruhr University Bochum for measuring the chemical composition of the samples produced.

Entwicklung thermisch gespritzter amorphe CuNi-Schichten und NiTi-Formgedächtnisschichten

Kimberly Porscha[1], Mohamed Abdulgader[1], Ingor Baumann[1], Wolfgang Tillmann[1]
Christian Sternemann[2], Michael Paulus[2]

[1]Lehrstuhl für Werkstofftechnologie, Technische Universität Dortmund, Dortmund, Deutschland
[2]Fakultät Physik/ DELTA, Technische Universität Dortmund, Dortmund, Deutschland

**korrespondierender Autor: mohamed.abdulgader@tu-dortmund.de*

Das Lichtbogendrahtspritzen ist ein sehr wirtschaftliches Verfahren, bei welchem Draht als Spritzzusatzwerkstoff genutzt wird. Besonders durch die Verwendung preisgünstiger Ausgangswerkstoffe kann es als eine Alternative zu den bekannten Herstellungsverfahren für amorphe Schichten (mittels pulverbasierten Spritzverfahren) und Formgedächtnislegierungen (FGL) (mittels pulvermetallurgischen Verfahren) angesehen werden [KOG22], [ING22]. In einem am Lehrstuhl für Werkstofftechnologie (LWT) der TU Dortmund neuartigen Versuchsaufbau wurden mittels zwei synchron genutzten Spritzbrennern Aluminium (Al), Titan (Ti), Nickel (Ni) und Kupfer (Cu) für die Anwendung amorpher Schichten sowie geeignete NiTi-Kombinationen für FGL-Applikationen spritztechnisch hergestellt. Amorphe Metalle sowie NiTi-FGL bieten eine hohe Härte und eignen sich damit maßgebend für Verschleiß- und Korrosionsschutzbeschichtungen [HEG17]. Aus den genannten Gründen sollen daher bekannte Werkstoffkombinationen für amorphe Schichten und FGL mittels Lichtbogendrahtspritzen erzeugt werden. Ziel ist es, Informationen über den Anteil der erforderlichen Phasen und ihrer Legierungsbildung miteinander zu erhalten, um optimale glas- und formgedächtnisbildende Eigenschaften der Materialzusammensetzung und der Spritzparameter bestimmen zu können. Die Phasenanalyse der erzeugten Schichten wurde mit folgenden Parametern an der Beamline BL9 des DELTA an der Technischen Universität Dortmund durchgeführt:

- Messaufsatz: MAR345
- Wellenlänge: 0,4591 Å
- Theta: 3°
- Messzeit: 120 Sekunden

Mithilfe der Analysesoftware „Match!“ konnten die im weiteren Verlauf aufgeführten Phasen ermittelt werden. Um eine Vergleichbarkeit zwischen den im Folgenden dargestellten Phasen zu ermöglichen, wurden ausgewählte 2D-Diffraktogramme übereinander angeordnet und ihre jeweiligen Intensitäten normiert.

Ergebnisse amorphe Schichten

Das 2D-Diffraktogramm in **Abbildung 1** zeigt, dass keine größeren amorphen Phasen in der AlTiNiCu-Schicht gebildet werden konnten. Die Form der spitzen Peaks weisen auf verschiedene kristalline Strukturen hin. Bei der Probe wurde mit Primärgasdrücken von 8 bar und einem Sekundärgasdruck von 2 bar gespritzt. In der Schicht liegen Ti, Al, Ni und Cu in ungebundener Form vor. Zusätzlich sind intermetallische Verbindungen zwischen NiTi, CuNi, AlTi gebildet worden. Viele dieser Verbindungen liegen an ähnlichen zwei Theta-Winkeln wie bei den einzelnen reinen Elementen. Zusätzlich gehen Ti und Cu in der Form von TiO und Cu_2O Verbindungen mit Sauerstoff ein. Diese entsprechen separaten Peaks, können aber auch überlagernd an anderen Peaks entdeckt werden. Generell können viele der Peaks in den höheren zwei Theta-Winkelbereichen entweder Ti und Al oder Ni und Cu und deren Verbindungen zugeordnet werden. Demgegenüber können die Peaks mit den höchsten Intensitäten im Bereich um 13° mehreren Elementen zugeordnet werden. Die Elemente gehen nur teilweise eine Verbindung untereinander ein, daher bildet sich keine homogene Schicht aus.

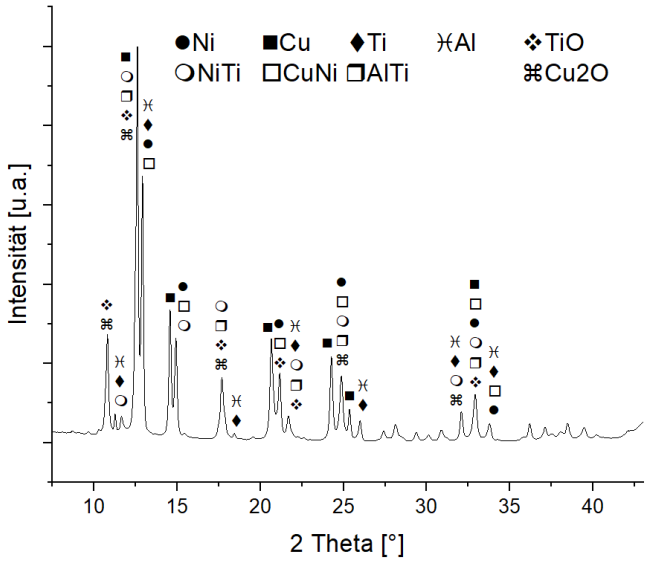

Abbildung 1: Schicht erzeugt durch Lichtbogenspritzen mit vier verschiedenen Spritzzusatzwerkstoffen (Ti, Al, Ni und Cu) und unter Verwendung von Sekundärgas.

Ergebnisse NiTi-FGL

Eine Charakteristik des Lichtbogendrahtspritzprozesses ist das nicht-achsensymmetrische Aufschmelzen der Elektrodenspitzen, das für die Partikelerzeugung verantwortlich ist [HUS07]. Vor allem bei zwei unterschiedlichen Drahtwerkstoffen wird daher empfohlen, dass das Material mit einem höheren Schmelzpunkt als Anode und das Material mit einem niedrigeren Schmelzpunkt als Kathode verwendet werden sollte [WAT02]. Außerdem zeigen Untersuchungen, dass insbesondere Ti bei höheren Temperaturen zu einer erhöhten Affinität zu Sauerstoff und Stickstoff neigt [CHE22]. Daher wurden für die folgenden 2D-Diffraktogramme Titan als Anode (Schmelzpunkt 1668°C) [CHE22] und Nickel

(Schmelzpunkt 1455 °C) [HOL95] ausgewählt. Aufgrund des hohen Reaktionsvermögens von Ti wurden die dargestellten Spritzversuche unter Argonatmosphäre als Inertgas durchgeführt. Um den Einfluss der Verfahrgeschwindigkeit der Spritzpistole auf die Schicht zu untersuchen, wurde diese variiert. Wie Fehler! Verweisquelle konnte nicht gefunden werden.entnommen werden kann, hat eine unterschiedliche Verfahrgeschwindigkeit von 18.000 mm/s, 36.000 mm/s und 72.000 mm/s keinen wesentlichen Einfluss auf die Phasenbildung in der NiTi-Beschichtung, weshalb die Zuordnung der jeweiligen Phasen lediglich im oberen Diffraktogramm erfolgt. Neben den signifikanten Peaks von reinem Ni und reinem Ti können übergreifende NiTi-Phasen festgestellt werden.

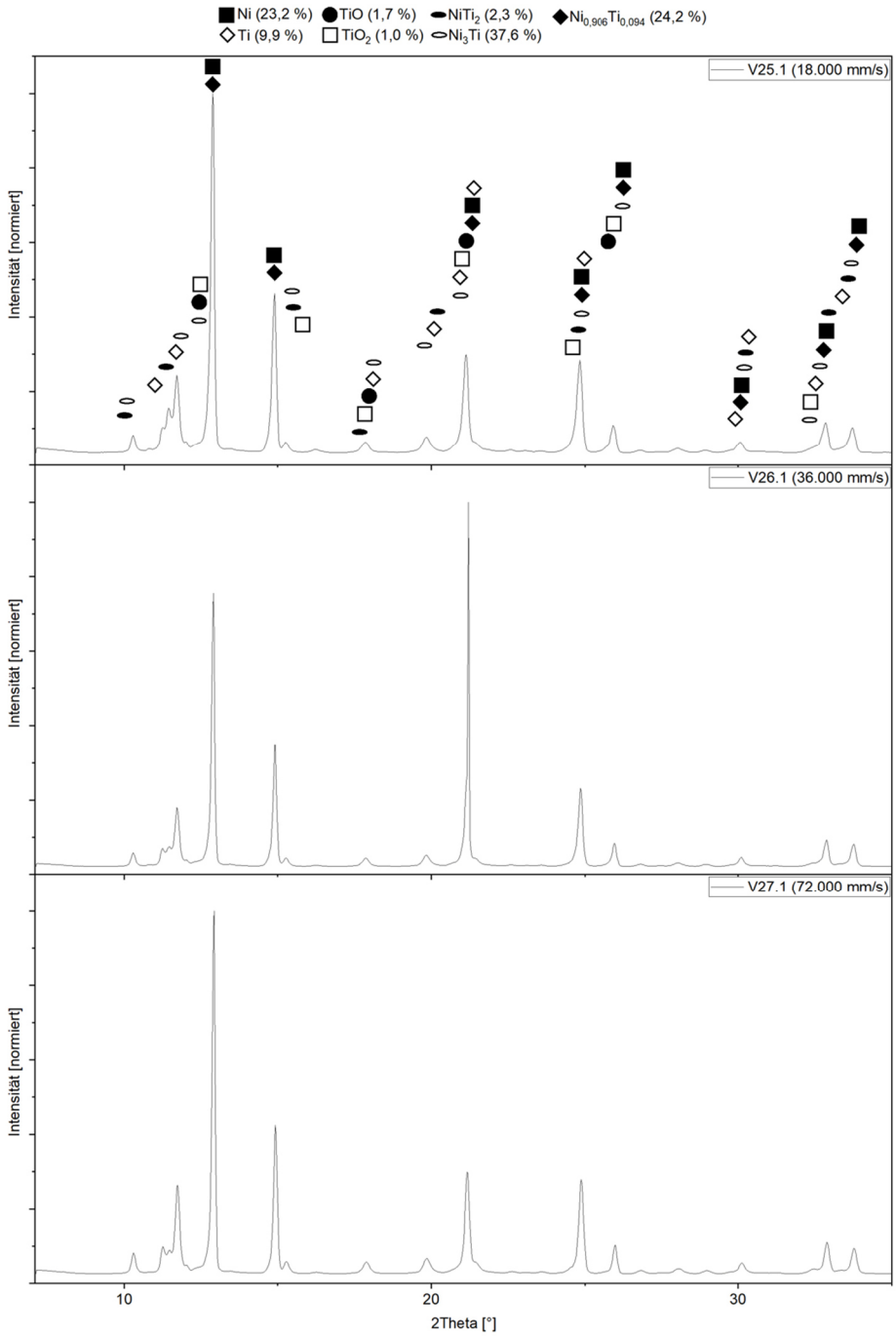

Abbildung 2: Einfluss der Variation der Verfahrgeschwindigkeit der Spritzpistole auf die Bildung von NiTi-Phasen beim Lichtbogendrahtspritzen.

Die Ursache der erhöhten Intensität bei ungefähr 22° bei der Probe V26.1 ist bislang ungeklärt und bedarf weiteren Untersuchungen. Trotz einer Argonatmosphäre konnten geringe Anteile von Titanoxiden in der Beschichtung festgestellt werden. Formgedächtnislegierungen liegen nur in bestimmten Legierungszusammensetzungen vor. Bei einer NiTi-FGL liegt dabei der Atomprozentsatz von Ti bei annähernd 50 % [KUM22]. Dieses Verhältnis konnte bislang nicht in den untersuchten Beschichtungen festgestellt werden. Nachgelagerte REM-Untersuchungen zeigen jedoch einen übergreifenden Anteil an Ti von 48 Gew.-% (dunkle Lamellen) und 52 Gew.-% an Ni (helle Lamellen) im Beschichtungssystem, die durch geeignete Nachbehandlung in Näherung zu einer Ni0,507Ti0,493-FGL führen könnte (siehe
Abbildung 3) [HOR91].

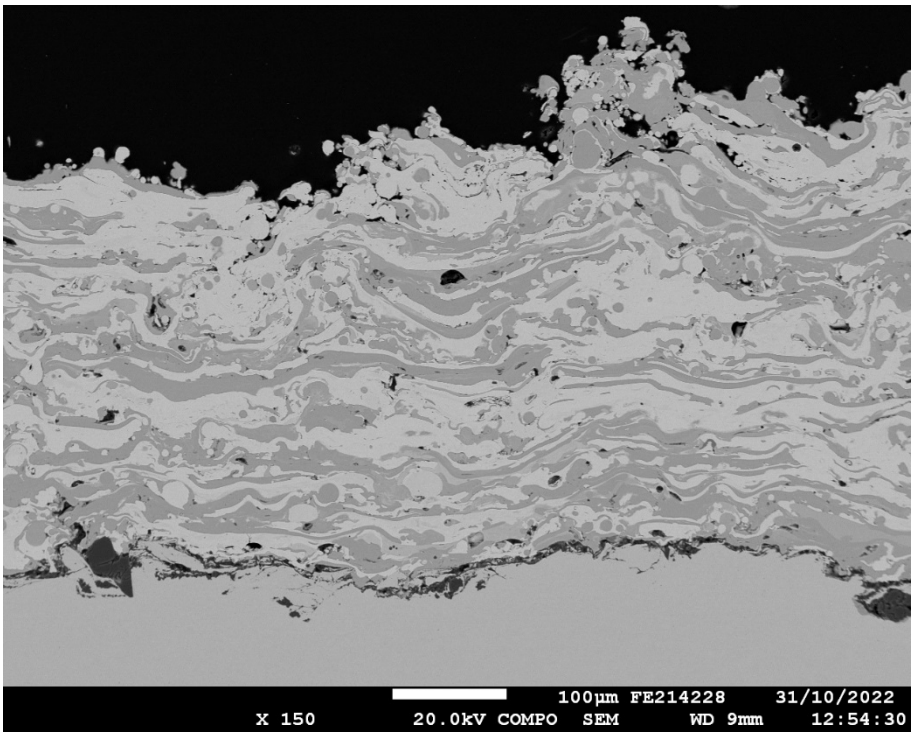

Abbildung 3: REM-Aufnahme einer NiTi-Schicht im Compo Modus.

Danksagung

Die Ergebnisse werden im Rahmen von zwei Masterarbeiten benötigt, die als Voruntersuchungen für (DFG-)Anträge dienen. Die Autoren danken dem DELTA der TU Dortmund für die Nutzung der Beamline 9 und für die wissenschaftliche Unterstützung bei den Phasenanalysen.

Literaturverzeichnis

[CHE22] Chemie.de: Titan (Element), in: Chemie.de, https://www.chemie.de/lexikon/Titan_%28Element%29.html (2022).

[HEG17] Hegels, D.: Optimierung thermischer Verhältnisse bei der Bahnplanung für das

thermische Spritzen mit Industrierobotern, Dissertation, Dortmund, 2017.

[HOL95] Holleman-Wiberg: *Lehrbuch der Anorganischen Chemie*, Verlag de Gruyter, Berlin, 101. Auflage, (1995), ISBN 3-11-012641-9.

[HOR91] Hornbogen, E.: *Legierungen mit Formgedächtnis,* Westdeutscher Verlag. N388, (1991), ISBN 3-531-08388-0

[HUS07] Hussary, N. A.; Heberlein, J.: *Effect of System Parameters on Metal Breakup and Particle Formation in the Wire Arc Spray Process,* Journal of Thermal Spray Technology. 16 (2007), S. 140–152.

[ING22] Maaß, B., Kortmann, A., Großmann, C.: *Formgedächtnis-Technik,* in: Anwenderkurs der Firma Ingpuls GmbH (2022).

[KOG22] Koga, G. Y.; Bolfarini, C.; Kiminami, C. S. et al.: *An Overview of Thermally Sprayed Fe-Cr-Nb-B Metallic Glass Coatings: From the Alloy Development to the Coating's Performance Against Corrosion and Wear,* Journal of Thermal Spray Technology, 4 (2022), S. 923–955.

[KUM22] Kumar Patel, S., Roshan, R.: *NiTi superalloys*, in: Nickel-Titanium Smart Hybrid Materials, Elsevier Inc., (2022), S. 105-121.

[WAT02] Watanabe, T.; Sato, T.; Nezu, A.: *Electrode phenomena investigation of wire arc spraying for preparation of Ti-Al intermetallic compounds,* Thin Solid Films. 407 (2002), S. 98–103.

X-ray diffraction on pre-oxidized copper powders for laser-based powder bed fusion

E. Schneider[1], J.F. Hankel[2], R. Ortmann[3], M. Paulus[1], A. Röttger[2], J.T. Sehrt[3], C. Sternemann[1]

[1]Fakultät Physik/DELTA, Technische Universität Dortmund, 44221 Dortmund, Germany
[2]Lehrstuhl Neue Fertigungstechnologien und Werkstoffe (FUW), Bergische Universität Wuppertal, 42651 Solingen, Germany
[3]Lehrstuhl Hybrid Additive Manufacturing (HAM), Ruhr-Universität Bochum, 44801 Bochum, Germany

The powder bed fusion of metals using a laser beam for additive manufacturing (AM) of components has achieved market maturity. This technology enables the production of e.g. aerospace components using Inconel 718 [1], medical devices using Ti6Al4V [2], or the manufacture of tools using marble steel [3]. The layer-by-layer AM process presents advantages over casting, shaping, and subtractive manufacturing methods for machining complex parts with internal cavities. Ongoing research strives to expand this process to encompass a greater range of metals and alloys. However, employing copper in these processes poses challenges due to its high thermal conductivity and reflectivity to the commonly used 1064 or 1070 nm wavelength infrared lasers. Efforts are being made to direct the oxidization of copper powders in order to optimize them for use in AM [4, 5] and reduce recovered powders for reuse [6]. The variables potentially impacting the process include particle shape, atmosphere, time, and temperature. X-ray diffraction provides a method to characterize such powders ex-situ and in operando on an atomic structural level.

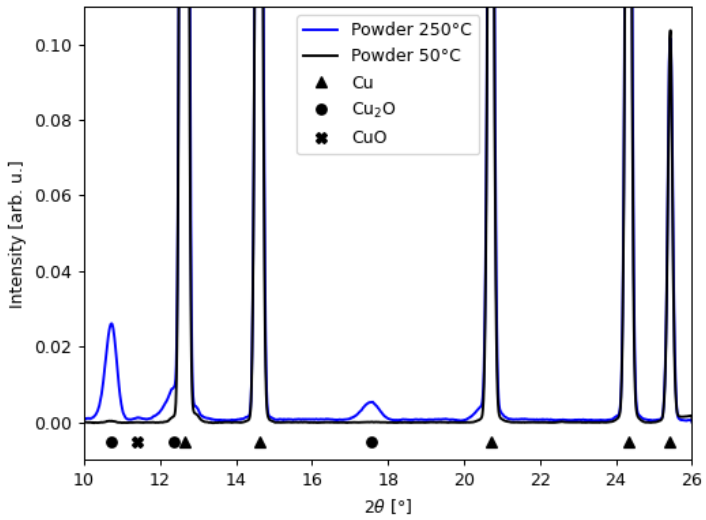

Figure 1: Diffraction patterns of a native Cu powder and a powder pre-oxidized at 250 °C in air for one hour.

Pure Cu-powder has been atomized from pure Cu wire (grade CW008A, Haecker Metall, Germany) using an atomizer ATOlab (3Dlab, Poland). Afterwards, the powder particles were sieved to obtain a particle size distribution between 20 µm – 63 µm. To enhance comprehension of the pre-oxidation process, samples of the powder were annealed in a muffle furnace in air to study the effect of temperature and time on the samples' oxide content and type of oxide formed, i.e. Cu_2O and CuO. The oxidized powder samples were enclosed in capillaries and mounted on the sample rotation unit for powder diffraction at beamline BL9 of the DELTA synchrotron radiation source. The X-rays had an energy of 27 keV and the beam size was 1 x 1 mm^2. The scattered intensity was detected with a MAR345 image plate detector. Figure 1 compares the diffraction patters of the native Cu powder and the one annealed for 30 minutes at 250°C. Latter confirms that Cu_2O and a smaller amount of CuO have formed. A Rietveld refinement using the program package MATCH! [7] revealed the composition of the respective samples. The results of this analysis is presented in Figure 2. Up to 100°C no formation of oxides was observed. From 150°C on, the amount of Cu_2O gradually increased while the first signatures of the CuO

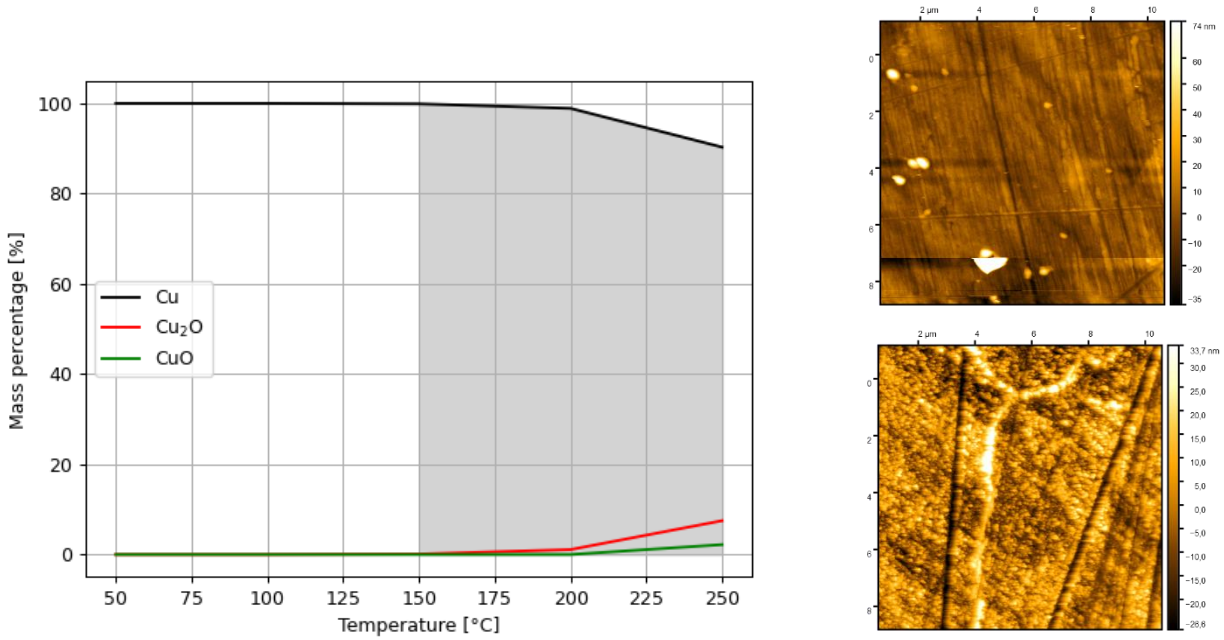

Figure 2: Amount of Cu_2O and CuO determined from the diffraction patterns using the program package MATCH! (left). Atomic force microscopy images of Cu-plates annealed at similar conditions than the powders indicating surface oxidation (right).

phase appeared at 250°C. Consequently, directed Cu_2O formation requires annealing temperatures below 205 °C. A detailed analysis of the powder characteristics is ongoing. Furthermore, we measured selected oxidized Cu plates for comparison with the oxidized powders (not shown here) and characterized them by atomic force microscopy (see Figure 2 for selected examples). Based on these results, dedicated ex-situ and in-situ oxidation and reduction experiments are foreseen to produce powders for optimized AM applications.

References

[1] X. Wang, et al: Review on powder-bed laser additive manufacturing of Inconel 718 parts, Proceedings of the Institution of Mechanical Engineers, Part B: J. of Eng. Manuf., 231 (2016) 11, S. 1890-1903.

[2] E. Mahmoud, et al: Optimization of SLM process parameters for Ti6Al4V medical implants, Rapid Prototyping Journal, 25 (2019) 3, pp. 433-447.

[3] J. Pieklo, A. Garbacz-Klempka: Verwendung von Maraging-Stahl 1.2709 für die Herstellung von Teilen von Druckgussgeräten mit konformem Kühlsystem, Materials, 13 (2020) 23, S. 5533.

[4] R.N. Gu, P. Chen, Y.H. Zhou, H. Wang, X.C. Yan, K.S. Wong, M. Yan, Intentional Oxidation and Laser Remelting of Highly Reflective Pure Cu for Its High-Quality Additive Manufacturing, Advanced Engineering Materials, 25 (2023) 5, 2101138.

[5] S.D. Jadhav, J. Vleugels, J.-P. Kruth, J. Van Humbeeck, K. Vanmeensel, Mechanical and electrical properties of selective laser-melted parts produced from surface-oxidized copper powder, 2 (2020) 2, e94.

[6] J.Y. Kim, J.A. Rodriguez, J.C. Hanson, A.I. Frenkel, and P.L. Lee, Reduction of CuO and Cu_2O with H_2: H mbedding and Kinetic Effects in the Formation of Suboxides, J. Am. Chem. Soc., 125 (2003), S. 10684-10692

[7] Match! - Phase Analysis using Powder Diffraction, Version 3.10, Crystal Impact - Dr. H. Putz & Dr. K. Brandenburg GbR, Kreuzherrenstr. 102, 53227 Bonn, Germany, https://www.crystalimpact.de/match.

Acknowledgments

We thank the DELTA team for providing synchrotron radiation. This work was supported by the DFG via projects STE 1079/9-1, RO 4523/9-1, and SE 2935/6-1.

A study on the phase evolution in HVOF sprayed coatings using WC-CoCr feedstock with different spray parameters

Mark Dennis Kensy[1], Justin Kopp[1], Michael Paulus[2], Christian Sternemann[2]
Ingor Baumann[1], Wolfgang Tillmann[1]

[1]Institute of Materials Engineering, TU Dortmund University, Germany
44227 Dortmund, Leonhard-Euler-Straße 2
[2]Fakultät Physik / DELTA, TU Dortmund University, Germany
44221 Dortmund
*corresponding author: dennis.kensy@tu-dortmund.de

High-Velocity Oxy-Fuel (HVOF) is an advanced thermal spray process that employs a supersonic jet of oxygen and fuel gas mixture to propel fine powder particles onto a substrate. In this process, the powder particles are heated to high temperatures, resulting in a rapid melting and solidification upon impact. The high velocity and kinetic energy of the particles during HVOF spraying lead to coatings with exceptional density, adhesion, and low porosity. The phase transformation during HVOF spraying is a critical aspect of the process, as it greatly influences the final microstructure and properties of the coatings. In this research, we investigated the interrelationships between the spray parameters and the phase evolution of the coatings. In the context of HVOF, agglomerated and sintered WC-CoCr feedstock with a particle size distribution in the range of -45 +15 µm and a primary carbide size of 2.5 µm was utilized. Cylindrical specimens of 42CrMo4 steel, measuring 30 mm in diameter and 6 mm in thickness, were used as substrate material. Prior to the coating deposition, the substrate surfaces were grit-blasted with corundum and cleaned in an ultrasonic ethanol bath. The HVOF spraying system JP5000/8000 HP/HVOF was used to conduct the spraying experiments. To achieve this, we carried out 27 experiments in which we systematically varied the spraying parameters and investigated their effects on phase development. The boundaries of the CCD experimental design were established at the following values:

- Oxygen-Level OL [l/min]: 779 – 944
- Kerosine-Level KL [l/h]: 21 – 25
- Stand-off distance [mm]: 300 – 400

The phase composition of both the WC-CoCr feedstock materials and the WC-CoCr coatings produced by HVOF spraying was determined via X-ray diffraction (XRD) analysis conducted at Beamline BL9 of DELTA, utilizing an image plate detector,

MAR345. In these experiments, the photon energy was set to E = 20 keV, and the incident angle was ω = 5°. To calibrate the experimental setup, a LaB6 reference measurement was conducted. The phase analysis was carried out using the Match! software package by CRYSTAL IMPACT, Germany, utilizing the crystallographic open database [1]. With regards to the diffractograms of the WC-CoCr feedstock materials (86% WC, 10% Co, and 4% Cr), distinct Bragg reflections corresponding to hexagonal WC, cubic Co_3W_3C, and cubic Co or Cr were observed (**Figure 1**). The presence of Co_3W_3C in the starting powder is ascribed to the manufacturing process. These phases are difficult to distinguish due to their closely coordinated lattice parameters.

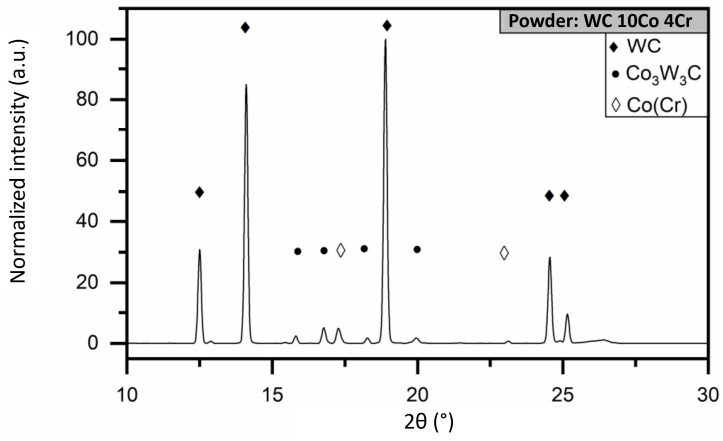

Figure 1: XRD patterns obtained from the WC-CoCr feedstock.

The XRD patterns obtained from the WC-CoCr coating in **Figure 2**. demonstrate that WC is the predominant phase. However, after a normalization of the peaks (based on the largest WC peak at Θ = 19°), the WC peaks are generally less pronounced in the coating's microstructure compared to the powder. The presence of crystalline eta-carbides (Co_3W_3C) is usually observed in small quantities. Furthermore, the coatings exhibit the presence of W_2C and W phases, which are not initially present in the powder. To facilitate the comparability of phase intensities, the integrals of specific material peaks are calculated:

- **WC:** 12.16° to 12.75°
- **W_2C:** 14.85° to 15.33°
- **Co_3W_3C:** 16.46° to 17.04°
- **W:** 22.44° to 22.80°

W_2C is an effect of decarburization of WC in the flame during spraying. An increased intensity of W_2C results in less intensity of WC. A correlation between W_2C intensity and the spray distance reveals that higher spray distances lead to greater W_2C intensity, indicating longer dwell times and enhanced decarburization of the powder at greater spray distances.

The formation of elemental tungsten (W) results from further decarburization. However, the amount of this phase in the coating is very low and decreases with higher intensity of the WC peaks. Also with increasing spray distance the intensity of W raises, too. Co_3W_3C was already a phase of the powder. Their intensity in the coating is smaller than that of the powder. Therefore, Co_3W_3C seems to dissolve during spraying. In comparison to WC a small inversely proportional correlation is found.

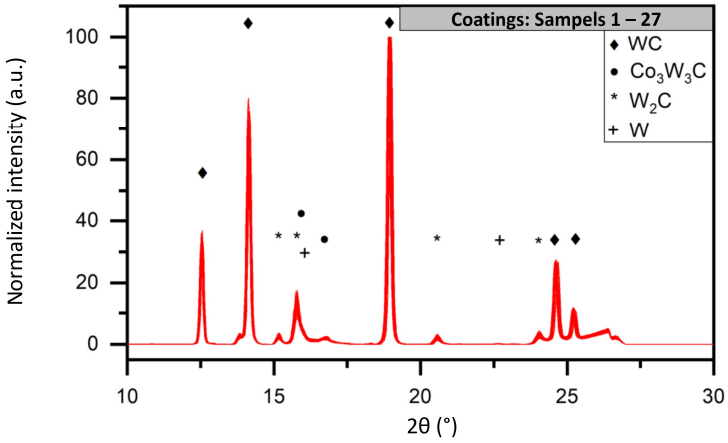

Figure 2: XRD patterns obtained from the WC-CoCr sprayed coatings.

By using a larger spray distance, the Co_3W_3C phase increases. Surprisingly, no significant difference in the intensity of Co_3W_3C is found between small and medium spray distances. This suggests that the quantity of Co_3W_3C has a quadratic correlation with respect to the spray distance. One possible explanation is that Co_3W_3C was already present in the starting powder, and a thermodynamic equilibrium is achieved during spraying. This suggests that the quantity of Co_3W_3C has a quadratic correlation with respect to the spray distance. One possible explanation is that Co_3W_3C was already present in the starting powder, and a thermodynamic equilibrium is achieved during spraying [2].

Acknowledgements

The authors gratefully acknowledge the DELTA machine group for providing synchrotron radiation and their support at BL9.

References

[1] A. Vaitkus, A. Merkys, S. Gražulis, Validation of the Crystallography Open Database using the Crystallographic Information Framework, J. Appl. Crystallogr. 54(2), 2021, 661–672.

[2] H.L. de Villiers Lovelock, Powder/Processing/Structure Relationships in WC-Co Thermal Spray Coatings: A Review of the Published Literature, Journal of Thermal Spray Technology Volume 7(3) 1998, p. 357–373.

Thermal spraying and phase analysis of quasicrystalline Al-Cu-Fe coatings

Ingor Baumann[1], Torben Olaf Kasperek[1], Jonas Zajaczkowski[1], Wolfgang Tillmann[1]
Christian Sternemann[2], Michael Paulus[2], Marko Sipura[3], Nenad Piljic[4]

[1]Institute of Materials Engineering, TU Dortmund University, Dortmund, Germany
[2]Faculty of physics/ DELTA, TU Dortmund University, Dortmund, Germany
[3]MD Global Trading GmbH, Bad Wimsbach, Austria
[4]DANEN TRADE GmbH, Salzburg, Austria

**corresponding author: ingor.baumann@tu-dortmund.de*

Quasicrystalline materials (QCM) were discovered in the early 1980s and are therefore a comparatively young group of materials. QCM are usually ternary alloys with aluminum, zinc, cadmium or titanium as the main constituent. Several studies have been conducted to determine the unique combination of physical and mechanical properties of these materials, such as high hardness, low coefficients of friction, low thermal and electrical conductivity as well as non-stick properties. To functionalize surfaces of tools and components with QCM, thermal spray processes can be used in a very efficient way. However, QCM are very complex alloys with the individual elements having also very different properties (such as density and melting point for example). In addition, they are very brittle and partially metastable. This complicates their processing by means of thermal spraying. Because of their interesting properties, QCM have been the focus of various research works. The particular heat and current transport properties make QCM ideal for use in solar absorbers. Due to their unique atomic structure, QCMs are also suitable for storing gases such as hydrogen. The low surface energy, which leads to non-stick properties, was investigated for use in frying pans and airplane shells as an alternative to thermally susceptible PTFE. However, the fundamental relationships between the structure and the resulting properties of QCM are not yet fully understood. Thanks to new manufacturing processes, the previously very expensive feedstock material is now available at affordable prices and in appropriate quantities (for instance to be used for thermal spraying), which has further increased the industry's interest in this material class.

The structure of quasicrystals exhibits a particular (five-, eight-, ten- or twelvefold) symmetry that fundamentally differs from crystalline materials. While atoms or molecules in crystalline materials are arranged in a periodic structure that repeats in each of the three spatial directions as an identical pattern, the elementary building blocks in QCM are arranged in an ordered but aperiodic structure. Studies using XRD analysis revealed a unique pattern with sharp diffraction points that exhibit the typical icosahedral or decagonal structure. Other studies showed that there is a relationship between quasicrystals and the Penrose tiling pattern. Many QCM materials have already been discovered. They are

generally classified into two groups: Stable and metastable quasicrystals. Among them, metastable Al-Cu-Fe alloys with striking pentagonal facets, following an icosahedral symmetry, are mostly interesting and most-studied due to their favorable properties at low costs.

Thermal spraying of such material was performed in this study and the phase evolution was scrutinized by means of synchrotron radiation as part of a master's thesis, which serves as a preliminary examination for a (DFG) proposal. The main objective was to study the possibilities of a coating deposition on mild steel by means Cold Gas Spraying (CGS), High Velocity Oxy-Fuel flame spraying (HVOF) and Plasma Spraying (PS), which required the search for suitable spraying parameters for each spray process. Since there are already a few studies in the literature on PS of the material, the focus was placed on HVOF and CGS. However, PS was performed for comparison. During the spray experiments, the fraction of QC phases in the coatings was projected to be maximized and their influence on the microstructure as well as on the tribo-mechanical properties was investigated. Various parameter studies (OFAT and DOE) were carried out. In addition, the influence of heat treatment to increase the QC phase fraction was additionally studied. During all experiments, the phase evolution in the powder (using a capillary) and the coatings was analyzed in six shifts with synchrotron radiation at Beamline 9 (DELTA, TU Dortmund University). **Figure 1** illustrates the experimental setup for both analyses. The following methods and parameters were chosen for the diffraction experiments:

- Detector: Mar345
- Photon energy in eV: 27,000 eV
- Wavelength in Å 0.4592009259259259
- Angle: 1, 3, 5°
- Measuring time powder: 10 seconds (in capillary)
- Measuring time coating: 60 - 120 seconds

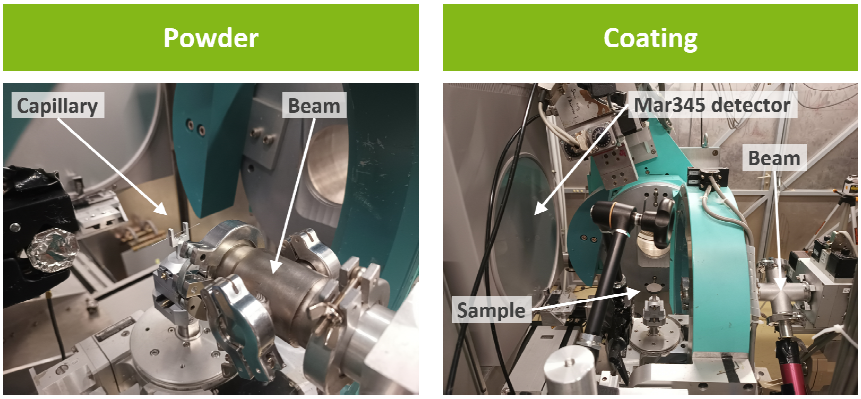

Figure 1: Experimental setup of the diffraction experiments for the powder and the coating on Beamline 9 (DELTA, TU Dortmund University).

Due to the special symmetry of the QC powders and coatings, a direct determination and assignment of the phases by means of a typical phase analysis for crystalline materials was

not possible. In the latter, it is assumed that the crystal is completely built up by an periodical arrangement of elementary cells which, by displacements, fills the entire crystal without gaps. However, this is not possible for a quasicrystal with fivefold symmetry (Al-Cu-Fe) because the atoms are not arranged periodically. The evaluation of the diffraction peaks was therefore carried out with the help of literature. The diffraction patterns of the works of Pillaca et al. [1], Fleury et al. [2] and Sordelet et al. [3] were used, since these researchers were able to prove that the peaks are quasicrystals by determining Miller's indices. **Figure 2** illustrates the diffraction patterns with the determined peaks of the employed QC powder composed of Al = 45.42 at.-%, Cu = 32.90 at.-% and Fe = 21.68 at.-%. The orange star symbolizes the quasicrystalline fractions determined from the literature comparison and the green triangle indicates the AlFe solid solution phase. The powders were found to contain a high proportion of quasicrystalline phases. By combining XRD, EDS, WDS and differential thermal analyses (DTA) with CALPHAD simulations, the following well-known, but also other non-stoichiometric QC phases could be identified: Al_7Cu_2Fe, $Al_{65}Cu_{20}Fe_{15}$, $Al_{65}Cu_{22}Fe_{13}$, $Al_{65}Cu_{23}Fe_{12}$, $Al_{62}Cu_{25}Fe_{13}$, $Al_{76.5}Cu_{5.5}Fe_{18}$, $Al_{68.5}Cu_{20.25}Fe_{11.25}$.

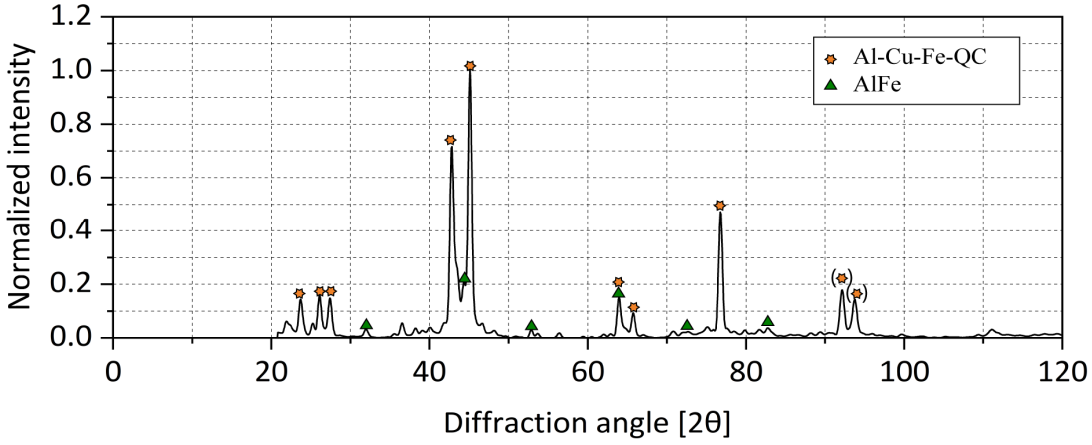

Figure 2: Diffraction patterns with the determined peaks of the employed Al-Cu-Fe QC powder.

Figure 3 shows the results of the CALPHAD simulation. As demonstrated here, the highest icosahedral QC phase content is present in the microstructure from 380 - 700°C. At higher temperatures (700 – 833°C), diffusion processes initially occur and BCC-B2 solid solutions are formed. Starting at a temperature of 830°C, a liquid phase is formed. Their amount increases up to a temperature of 1200°C, at which the entire material is in a molten state. Based on these findings, coating experiments were carried out by means of the three mentioned spray processes. However, cold gas spraying of QC powders was not successful. Despite the use of maximum thermos-kinetic process parameter settings (T = 1,100°C and p = 50 bar), only an insufficient coating application could be realized. The reason for this is the brittleness of the QCM, which leads to poor deformability and thus to rebounding of the spray particles after impact on the substrate. In contrast, coating by HVOF and PS processes could be realized successfully.

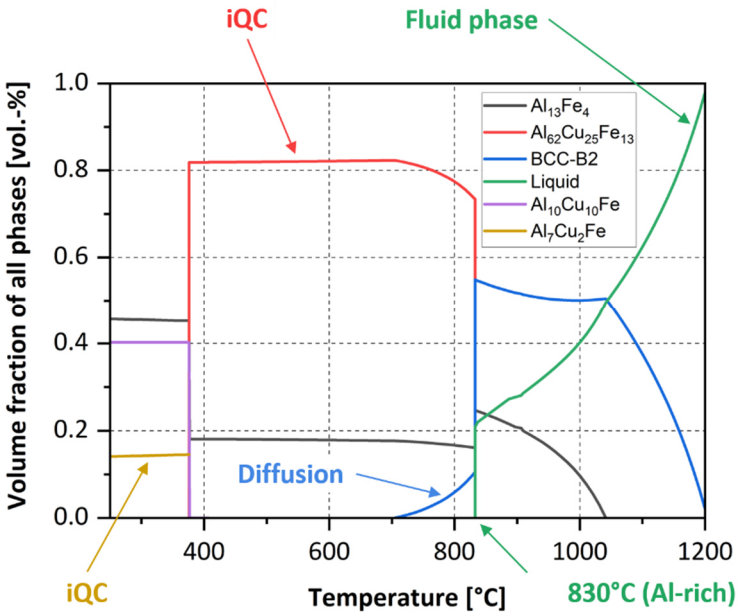

Figure 3: CALPHAD simulation of the Al-Cu-Fe QCM.

Their microstructures at two different magnifications are shown in **Figure 4**. The coating properties are promising for both the PS and HVOF spraying, as a high microhardness of > 650 HV0.3 was observed for the HVOF coatings and > 734 HV0.05 for the PS coatings. The coating thickness and deposition efficiency were also found to be adequate for both coating processes (PS: 51 – 73 %, HVOF: 17 – 45 %).

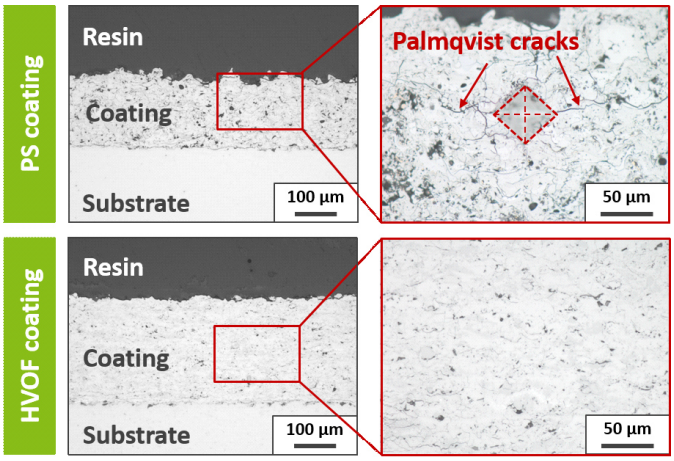

Figure 4: Microstructure of the PS- and HVOF sprayed Al-Cu-Fe coatings.

It was found that the microstructure of the HVOF coated samples was generally better than that of the PS samples in terms of roughness, porosity level and the general morphological homogeneity. However, different problems encountered during coating with both processes. With HVOF, it was difficult to achieve a stable process condition, as both the barrel and the injection nozzles gradually became heavily clogged. As a result, the process was interrupted after several passes of the gun over the substrate and the coating procedure

remained incomplete. Finally, both parts of the gun must be thoroughly cleaned or replaced. The PS coatings in turn exhibited a great number of cracks, pores insufficiently melted areas and some growth defects. This led to reduced cohesive strength and increased surface roughness. Indentations to determine the fracture toughness lead to strong Palmqvist crack development, as can be seen in Figure 4 for the microstructure of the PS coatings. These coatings need to be optimized in further coating experiments. However, a higher deposition efficiency could be realized with PS (51 – 73 %) compared to HVOF (17 – 45 %).

Figure 5 shows the diffraction patterns of the HVOF and PS sprayed Al-Cu-Fe QC coatings compared to the starting powders. The diffraction chart of the coatings contains all components that are also present in the one of the QC powder. The Al-Cu-Fe QC peaks are symbolized by an orange star, the AlFe solid solution by a green triangle and the iron phase by a red square.

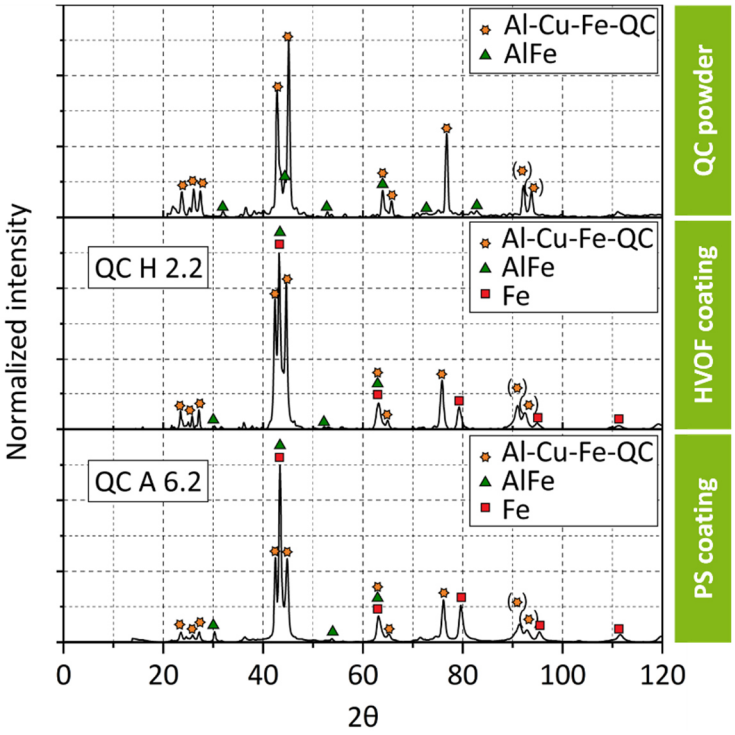

Figure 5: Diffraction charts for the Al-Cu-Fe QC powder as well as for the PS- and HVOF sprayed Al-Cu-Fe QC coatings.

All recorded main peaks (for the powder, the PS- and the HVOF sprayed coatings) are located at the same position. Free-standing iron peaks are found at $2\vartheta = 80°$, 95° and 113° and iron peaks superimposed with some other phases at $2\vartheta = 43°$ and 63°. The highest peak in all samples is the iron / AlFe peak at $2\vartheta = 43°$. The second highest peaks are the QC ones at $2\vartheta = 42°$ and 44.5°, respectively. It can be seen, that the relative intensity of the iron and AlFe peaks increases with decreasing QC peak intensities. While the AlFe phases did not vary greatly within the respective experiments for PS and HVOF spraying and in comparison to the powder, the QC phases showed differences in the intensities for the two coating processes. The highest intensities were found in the HVOF coatings. The analysis of

the results of this work has shown that there is no significant dependence of the microhardness and toughness on the QC phase ratio. This is in contrast to the works of other researchers who have observed an increase in microhardness with the increase in QC phase fraction (Lepeshev et al. [4], Fleury et al. [2]). However, it could be found, that with HVOF spraying the QC phase ratio can be improved by 50 % when the lambda-value is reduced form $\lambda = 1.25$ to $\lambda = 1.05$ and the kerosene flows from 24 to 18 l/h. Apparently, lower process temperatures during HVOF spraying seem to have a positive effect on the retention of QC phases. In plasma spraying, however, no clear correlation was observed between the process parameter settings and the QC phase amount.

After the coating development and phase analyses the sliding wear behavior of the PS and HVOF sprayed coatings with highest QC phase ratio was evaluated using a ball-on-disc test with a Ø 6 mm 100Cr6 ball as a counter body 15,000 cycles, a load of 10 N and a sliding velocity of v = 0.4 m/s. The friction coefficients and debris formation in the wear track of PS and HVOF coatings are shown in **Figure 6**. The PS and HVOF coatings achieved moderate friction coefficients with μ(PS) = 0.45 and μ(HVOF) = 0.51. Literature values of 0.15 - 0.1 could not be proven. During the sliding wear test, oxygen-rich debris and tribo-films with traces of chromium could be determined in the wear zone. For this reason, there were partial fluctuations in the coefficients of friction.

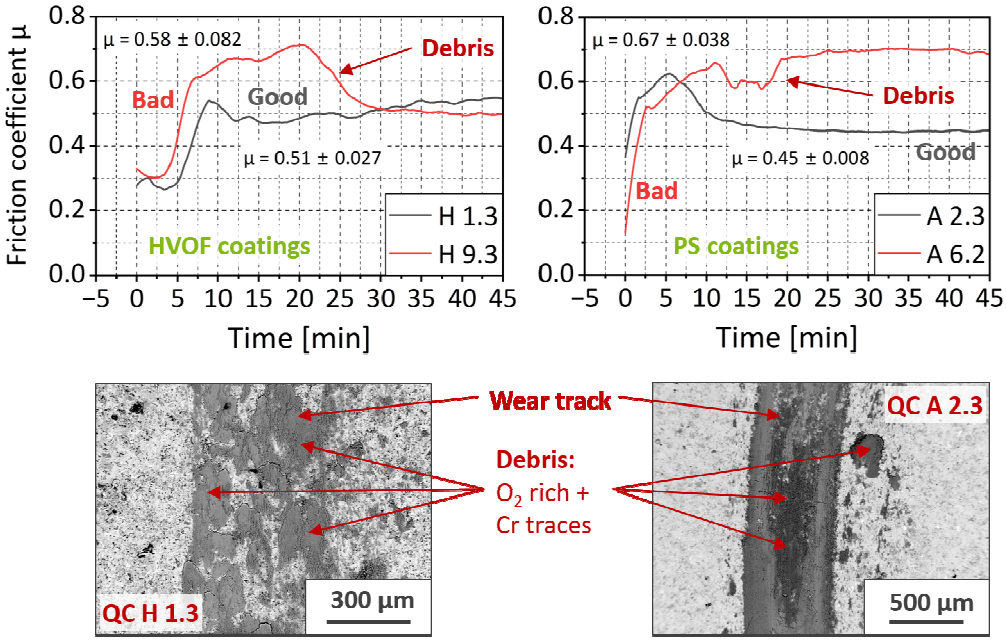

Figure 6: Friction coefficients and debris formation in the wear track of PS and HVOF coatings.

With total values ranging from $6.9 \cdot 10^{-5}$ to $0.0473 \cdot 10^{-5}$ mm^3/N · m, all sprayed QC coatings achieved very good sliding wear performance. The sliding wear coefficient of the PS coatings ($0{,}0473 \cdot 10^{-5}$ mm^3/N · m) was significantly better than the one for the HVOF coatings ($2{,}4 \cdot 10^{-5}$ mm^3/N · m). By applying a heat treatment at 650°C for one hour in a tube furnace in argon atmosphere (with heating rate of 800 K/h) and a subsequent cooling in ambient air,

the QC phase fraction in the HVOF coatings could be increased by a factor of 1.3. This had a positive influence on the wear resistance to sliding wear (around 4.7 times higher wear resistance), but did not lead to an improvement in the coefficient of friction. However, the reasons for the better sliding wear behavior of the PS coatings compared to HVOF on the one hand and the improvement in the sliding wear behavior of the HVOF coatings after heat treatment on the other hand have not yet been clarified and require further investigation.

The conducted experiments in this study have shown, that it is possible to produce Al-Cu-Fe QC coatings by means of PS and HVOF processes with good / moderate microstructure. Corresponding spray parameters were determined for both processes within this study. In contrast, cold gas spraying of this material was not successful due to the high brittleness and low deformability of the material. The PS and HVOF coatings showed a high microhardness for purely metallic coatings and thus a very good tribological resistance to frictional wear which is better than HSS steel but lower than WC-12Co coatings, which are typically used for wear protection. However, the fracture toughness of the microstructure is low due to the brittleness of the ternary Al-Cu-Fe alloy. Good deposition efficiencies were also achieved with both spraying processes. The QC Al-Cu-Fe is a highly complex system that still offers and requires further research work regarding thermal spraying.

Acknowledgements

The authors would like to thank the DELTA of TU Dortmund University for the use of Beamline 9 and for the scientific support during the phase analyses.

Literature

[1] M. Pillaca Quispe, C. V. Landauro, M. Z. Pinto Vergara, J. Quispe-Marcatoma, C. Rojas-Ayala, V. A. Peña-Rodríguez, E. Baggio-Saitovitch: „Influence of high energy milling on the microstructure and magnetic properties of the Al–Cu–Fe phases: the case of the i-Al 64 Cu 23 Fe 13 quasicrystalline and the ω-Al 70 Cu 20 Fe 10 crystalline phases", RSC Advances", 2016.

[2] E. Fleury, S. Lee, W. Kim, D. Kim: „Effects of air plasma spraying parameters on the Al–Cu–Fe quasicrystalline coating layer", Journal of Non-Crystalline Solids", 2000.

[3] D. J. Sordelet, M. F. Besser, J. L. Logsdon: „Abrasive wear behavior of Al–Cu–Fe quasicrystalline composite coatings", Materials Science and Engineering: A", 1998.

[4] A. A. Lepeshev, O. A. Bayukov, E. A. Rozhkova, I. V. Karpov, A. V. Ushakov, L. Y. Fedorov: „Modification of the phase composition and structure of the quasicrystalline Al-Cu-Fe alloy prepared by plasma spraying", Physics of the Solid State", 2015.

An X-ray diffraction study on AlCrVY(O)N thin films for high-temperature applications

Eric Schneider[1], Finn Ontrup[2], Jaqueline Savelkouls[1], Gordon Scholz[1]
Kevin Lehninger[1], Christian Sternemann[1], Michael Paulus[1], Nelson Filipe Lopes Dias[2]
Wolfgang Tillmann[2]

[1]Fakultät Physik/DELTA, TU Dortmund University, 44221 Dortmund, Germany
[2]Fakultät Maschinenbau, Institute of Materials Engineering, TU Dortmund University, 44221 Dortmund, Germany

In production engineering, major efforts are made to optimize tool coatings for applications exposed to elevated process temperatures. A specific focus lies especially on dry machining or machining with minimum quantity lubrication. Thus, depending on the material and tool design such as the shape of the cutting edge, temperatures between 300 °C and 1000 °C can occur during turning operations [1]. In order to enable machining of high-strength materials, the high-temperature properties of the tool coatings need to be tailored according to the application. The addition of vanadium to AlCrN favours the formation of so-called Magneli phases to reduce the friction at high temperatures [2], whereas a small amount of yttrium improves the oxidation resistance [3]. A novel approach is to introduce oxygen into the AlCrVYN deposition process to tailor the oxide state of the thin films. The aim of this project is to obtain a fundamental understanding of the dependence between deposition parameters, coating structure, and oxidation behavior.

For the X-ray diffraction (XRD) studies, different AlCrN, AlCrVYN, AlCrVYON samples were deposited on WC-Co substrates by direct-current magnetron sputtering (dcMS), high power impulse magnetron sputtering (HiPIMS) and a hybrid dcMS/HiPIMS process. In this regard, the O2 gas flow rate was varied from 0 to 20 sccm in the deposition process. During the XRD measurements, the coated WC-Co substrates were stepwise heated, between 25 °C and 1000 °C. The annealing of the samples takes place in an external tube furnace. At beamline BL9 at DELTA we used a photon energy of 27 keV and a beam size of 1.5 x 0.1 mm^2 (h x v). The scattered intensity was detected by a MAR345 image plate detector.

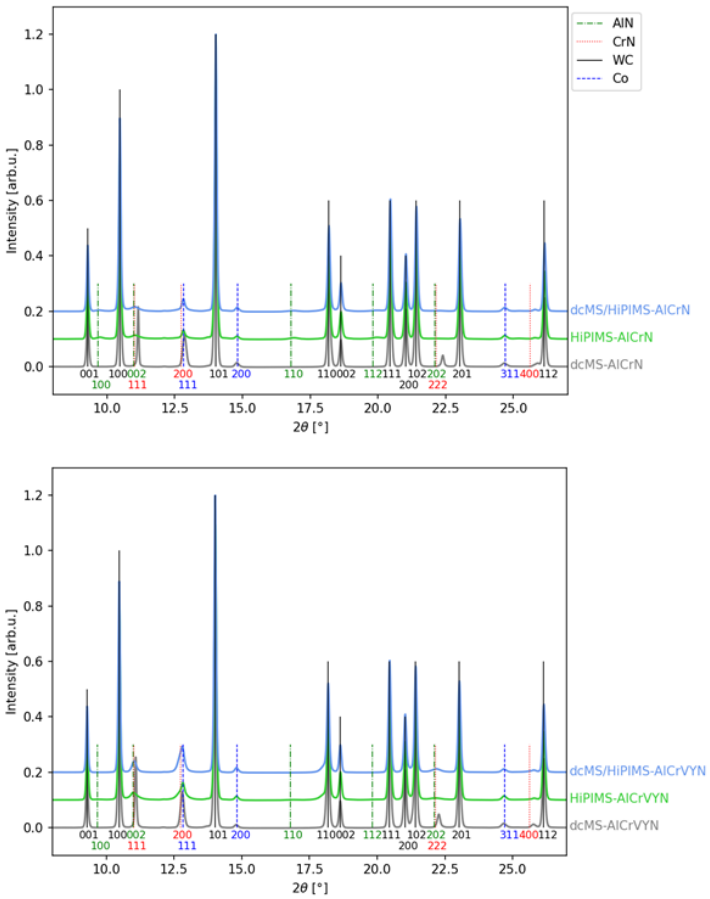

Figure 1: XRD patterns of the AlCrN and AlCrVYN thin films deposited by either dcMS, HiPIMS, or hybrid dcMS/HiPIMS measured at a photon energy of 27 keV at an angle of incidence of 4°.

The diffraction patterns of the different AlCrN and AlCrVYN thin films are shown in Figure 1. The vertical lines indicate positions for the identification of cubic CrN-like structures [4], hexagonal AlN-like structures [5], and the WC-Co substrate. Due to the low thickness of the thin films, the WC [6] Bragg reflections of the WC-Co substrate are clearly visible in all diffractograms. In addition, reflections can be attributed to hexagonal Co [7]. All diffraction patterns show reflections of fcc-CrN and, it becomes evident that the HiPIMS-AlCrN and dcMS/HiPIMS-AlCrN

thin films show an additional hcp-AlN phase. The Bragg reflections of the measured data shift slightly to higher scattering angles, which is indicative of a smaller unit cell compared to the reference. This shift can be explained by the addition of Al, which has a smaller atomic radius than Cr [8].

Initial analysis of the AlCrVYON samples (data not shown) suggest another phase in addition to the compounds assigned in Figure 1. These reflections can be attributed to chromium heminitride (Cr_2N). Cr_2N is used in the samples as a binder between substrate and coating to improve adhesion.

Besides the influence of the deposition parameters on the structure of the thin films, their oxidation behavior was also investigated. Between 800 °C and 850 °C, the oxidation of the thin films sets in for all AlCrVYN samples. By adding oxygen, the oxidation temperature is reduced in some cases to 700 °C.

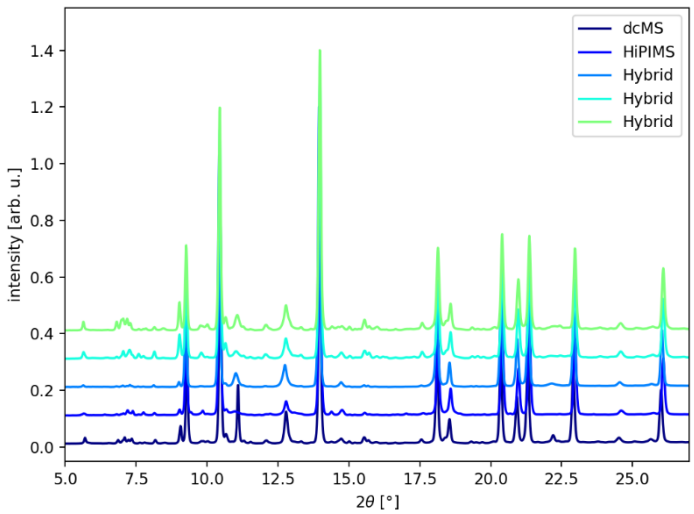

Figure 2: Comparison of the oxidation process of the AlCrVYN samples after ex-situ heating to 900°C.

For a detailed study of the oxidation process, the samples were compared after *ex situ* heating to 900 °C (see figure 2). In comparison to the unheated samples, the heated ones show significantly more Bragg reflections, which can be attributed to the oxidation process. The large number of oxide phases potentially being present in the layer complicates a phase analysis. For this reason, complementary X-ray absorption measurements were carried out at BL10 of DELTA to better constrain the appearance, assignment and quantification of oxides in the samples and, thereby, gain an understanding of oxide formation depending on the structural properties of this thin film systems.

References

[1] K.-M. Li, S.Y. Liang, Modeling of Cutting Temperature in Near Dry Machining, J. Manuf. Sci. Eng. 128 (2006) 416–424.

[2] W. Tillmann, D. Kokalj, D. Stangier, M. Paulus, C. Sternemann, M. Tolan, Investigation on the oxidation behavior of AlCrVxN thin films by means of synchrotron radiation and influence on the high temperature friction, Applied Surface Science, Volume 427, Part B, 2018, Pages 511-521.

[3] F. Rovere, P.H. Mayrhofer, A. Reinholdt, J. Mayer, J.M. Schneider, (2008): The effect of yttrium incorporation on the oxidation resistance of Cr–Al–N coatings. In: Surface and Coatings Technology 202, Issue 24, S. 5870-5875,

[4] R. Wyckoff, Second edition. Interscience Publishers, New York, New Yorkrocksalt structure, Crystal Structures 1963 (1963) 85–237.

[5] K. Miwa, A. Fukumoto, First-principles calculation of the structural, electronic, and vibrational properties of gallium nitride and aluminum nitride, Physical review. B, Condensed matter 48 (1993) 7897–7902.

[6] J. Leciejewicz, A note on the structure of tungsten carbide, Acta Cryst 14 (1961) 200.

[7] L. Marick, Variation of Resistance and Structure of Cobalt with Temperature and a Discussion of Its Photoelectric Emission, Phys. Rev. 49 (1936) 831–837.

[8] A.E. Reiter, V.H. Derflinger, B. Hanselmann, T. Bachmann, B. Sartory, Investigation of the properties of Al1−xCrxN coatings prepared by cathodic arc evaporation, Surface and Coatings Technology, Volume 200(2005), Issue 7,S. 2114-2122.

Acknowledgments

The authors gratefully acknowledge the financial support of the Deutsche Forschungsgemeinschaft (DFG, German Research Foundation, Germany) within the project 448604890 (TI 343/190-1, TO 169/21-1) and INST 212/330-1, project number 619186.

Thermal stability of expanded austenite generated by low-temperature plasma nitriding

Brückner,T.[1]; Paschke, H.[1]; Thewes, A.[2]; Sternemann, C.[3]; Paulus, M.[3]

[1] Fraunhofer Institute for Surface Engineering and Thin Films IST, 44145 Dortmund, Germany
[2] IOT TU Braunschweig, 44145 Dortmund, Germany
[3] Fakultät Physik/DELTA, Technische Universität Dortmund, 44221 Dortmund, Germany

Introduction

Austenitic stainless steels are designed to offer good corrosion properties. In contrast their wear resistance is quite poor. To use austenitic stainless steels in tribocorrosive environments, it is necessary to increase the wear resistance without decreasing the corrosion properties. An efficient way to achieve this is low-temperature plasma nitriding (LT-PN). In this case surface hardening is realized by interstitially solved nitrogen atoms. Due to the low treatment temperature of less than 450°C the chromium stays solved in the matrix and does not form chromium nitrides, which would decrease the corrosion resistance.
In some use cases the temperature stability of the formed surface layer of the austenitic steel can play a significant role as well and even an increase of temperature for a short time may cause a lasting change in the surface layers properties leading to a loss of both surface hardness and corrosion resistance. To get information about the thermal stability, x-ray diffraction (XRD) investigations at austenitic steel were carried out at DELTA.

Experimental

The steel used for the described investigations was an specially produced austenitic steel (CN0.85). The chemical composition is shown in table 1. LT-PN was carried out for 16 h at 380°C with a H_2:N_2-ratio of 80:20. Prior to nitriding, a plasma fine cleaning step was carried out for 2 h to remove the passivation layer.

Table 1: Chemical composition of the austenitic steel in wt-%

	C	Cr	Mn	Mo	Ni	V	Si	N	Fe
CN0.85	0.26	18.25	17.85	0.05	0.15	0.08	0.25	0.59	balance

XRD measurements were performed at beamline BL9 of the synchrotron light source DELTA (TU Dortmund, Dortmund, Germany) [Kryw06]. A MAR345-detector was used to measure diffraction patterns and the energy of the incident photon beam was 27 keV with a beamsize of 1.0 x 0.2 mm² (h x v). Prior to heating the sample, a measurement at room temperature was carried out. The sample was then heated up until a temperature of 350°C was reached for the first measurement. Based on that, the following measurements were carried out stepwise every 50°C until a temperature of 900°C was reached. Measurements were carried out in both air and vacuum.

Results and Discussion

Selected XRD-patterns of measurements in air are shown in figure 1 a). The XRD-pattern at room temperature shows the presence of expanded austenite. This is recognizable by the shifted peaks of the γ-phase. A phenomenon already described by other authors [Foss06] due to the interstitially solved nitrogen-atoms stretching the lattice. The expanded austenite is stable up to 450°C. As soon as a temperature of 500°C is reached, significant Bragg reflections of CrN are detected. Further heating leads to shifting of γ_N-peaks to γ Bragg reflections. Probably because the solved nitrogen is forming CrN. When the temperature is increased even further, Cr_2O_3-peaks occur while CrN-peaks decrease. XRD-patterns for heating in vacuum are shown in figure 1 b). In contrast to the measurements in air, in this case the peaks indicating the formation of CrN appear later. At 500°C there are only minor peaks visible for CrN. Strong Bragg reflections appear when a temperature of 600°C is reached. In addition, no pronounced Cr_2O_3-peaks

are observed at 900°C. The absence of Cr_2O_3-peaks is due to the missing oxygen under vacuum conditions. The difference in the temperature of CrN-formation may be a hint for nitrogen diffusing out of the sample under vacuum conditions due to a lower nitrogen-partial-pressure than under atmospheric conditions. As a result, less nitrogen is available to form nitrides. Another explanation may be found in a different heating time for both setups. Due to measurement conditions, the total heating time for the measurements under vacuum took longer, which in turn may effect the formation of the detected phases. All in all the measuring cycle in vaccum took about 15 Minutes longer than in air.

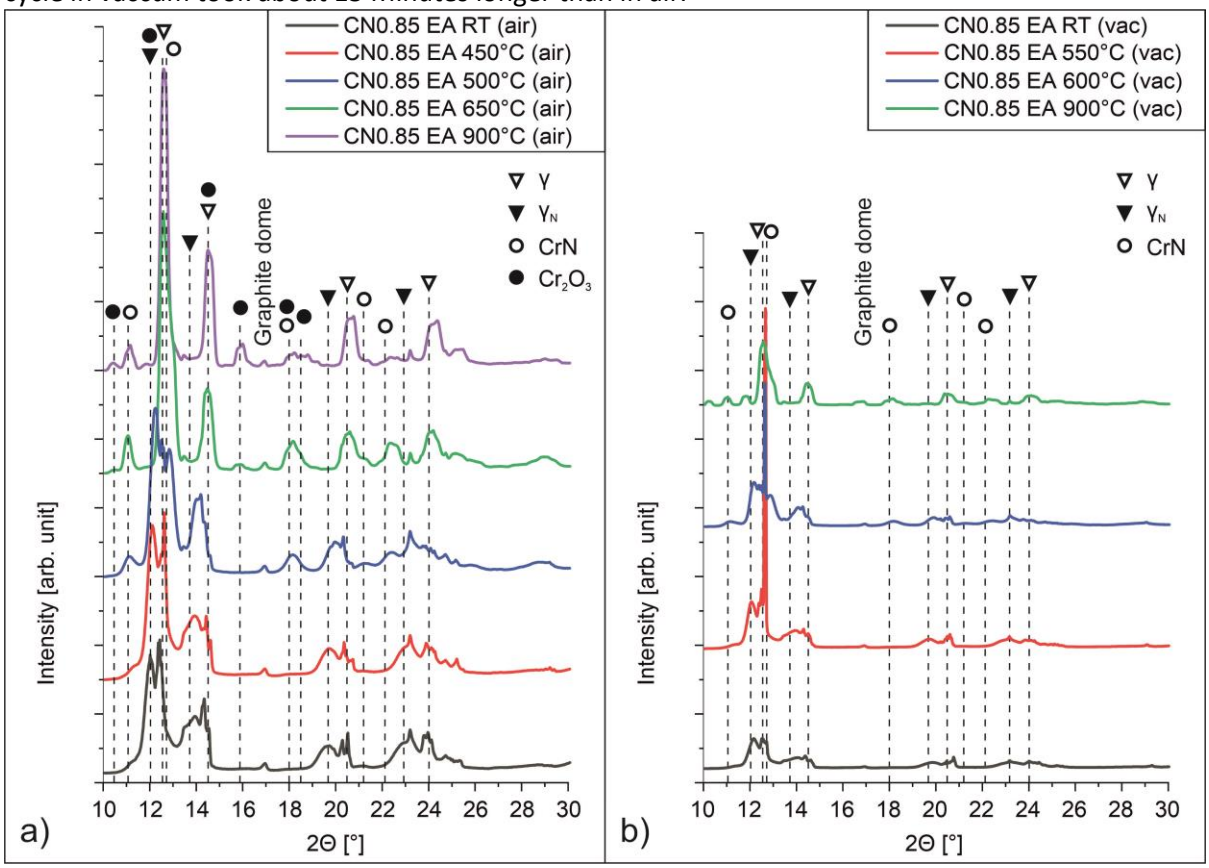

Figure 1: a) XRD-results of expanded austenite measured in air atmosphere at different temperature b) XRD-results of expanded austenite measured under vacuum conditions at different temperature

Conclusions

It was clearly shown that the expanded austenite is stable only up to a certain temperature. This is true both in air and vacuum, although the measured temperature at which phase dissolution occurs is different. However, this does not have to be due to the environmental conditions, as time also plays a role at this point. To determine the exact relationship between time and temperature, further studies are necessary.

Acknowledgment

We kindly acknowledge the support of the DELTA machine group providing synchrotron radiation. The performed measurements contribute helpful insights to the project „Energieeffizienz durch Standzeiterhöhung von Lagern unter tribokorrosiven Betriebsbedingungen – BMWK POSEIDON II“ within the subproject of the Fraunhofer IST (FKZ 03ET1477D) „Randschichtmodifikation des Grundmateriales, Duplexbehandlungen“. We are thankful to the BMWK for the given financial support.

Literature

[Kryw06] Krywka, C.; Paulus, M.; Sternemann, C.; Volmer, M.; Remhof, A.; Nowak, G.; Nefedov, A.; Pöter, B.; Spiegel, M.; Tolan, M.: The new diffractometer for surface X ray diffraction at beamline BL9 of DELTA, Journal of Synchrotron Radiation 13 p. 8-13 (2006)

[Foss06] Fossati, A.; Borgioli, F.; Galvanetto, E.; Bacci, T.: Glow-discharge nitriding of AISI 316L austenitic stainless steel: influence of treatment time. Surface & Coatings Technology 200 p. 3511 – 3517 (2006)

In-situ GIXRD study of Aluminium doped Lithium Lanthanum Zirconium Oxide (LLZO) garnet solid electrolytes

Sundeep Vema[1], Farheen N. Sayed[1], Supreeth Nagendran[1], Christian Sternemann[2], Michael Paulus[2] and Clare P. Grey[1]

[1]Department of Chemistry, University of Cambridge, Cambridge CB2 1EW, United Kingdom
[2]Fakultat Physik/DELTA, TU Dortmund, 44221 Dortmund, Germany

Doped LLZO ($Al_{0.36}Li_{5.92}La_3Zr_2O_{12}$) solid electrolyte (SE) based solid-state batteries can enable high energy storage devices due to their compatibility with Li metal anode and high voltage cathodes, offer greater thermal and electrochemical stability than current state of the art liquid electrolyte-based Li-ion batteries. Doped LLZO is known to react with trace amount of moisture and carbon dioxide in the atmosphere. This results in the exchange of Li^+ in lattice with H^+ to form H-LLZO (Protonated LLZO) and lithium hydroxide and lithium carbonates on the surface[1,2]. This leads to lattice contraction and a change of symmetry from $Ia\bar{3}d$ to $I\bar{4}3d$. The resulting inhomogeneous surface layers have very low Li-ion conductivity and thus increase the interfacial resistance when paired with Li metal anode. This leads to non-uniform current distribution at the interface which deteriorates its electrochemical performance. It is known that the surface can be regenerated by heating the sample at temperatures above 400 °C[3,4], but the exact mechanism of surface layer decomposition under different gas environments is not well understood. It has also been reported that regeneration of H-LLZO ($Li_{7-x}H_xLa_3Zr_2O_{12} + xLiOH \rightarrow Li_7La_3Zr_2O_{12} + xH_2O$), is a heterogeneous process wherein upon heating the surface regenerates quickly compared to layers just beneath. Synchrotron XRD on powders showed decomposition of LLZO to pyrochlore (La_2Zr_2O7) at temperatures above 650 °C[5]. Since the pyrochlore formation starts at the surface of powders and pellets, the initiation of such decomposition reaction cannot be well captured by powder XRD, surface sensitive techniques such as GIXRD are needed.

We studied the decomposition of surface layers (Lithium hydroxide and Lithium carbonate) on air-exposed pellets by heating samples under different gas environments (argon, vacuum, flowing air and static air) from RT to 800 °C and by collecting GIXRD patterns at 0.1°, 0.2° and 0.5° incident angles (14 keV). Our study revealed that heating under all environments except static air up to 500 °C resulted in complete regeneration of sample surfaces by decomposition of surface layers but heating above 500 °C resulted in irreversible decomposition to form pyrochlores under argon and flowing air but not under vacuum. Static air was found to be a non-ideal environment to heat samples as pyrochlore formation and complete disappearance of LLZO peaks were observed at comparatively lower temperatures. By combining these observations with *in-situ* near ambient pressure – XPS measurements, we were able to show that the best and safest environment to regenerate an air-exposed LLZO sample is by heating to 500 °C under oxidising conditions (O_2 partial pressure > 1 mbar). Upon subjecting the samples to these conditions, we were able to assemble Li-LLZO-Li symmetric cells with < 10 Ωcm^2 interface resistances[6].

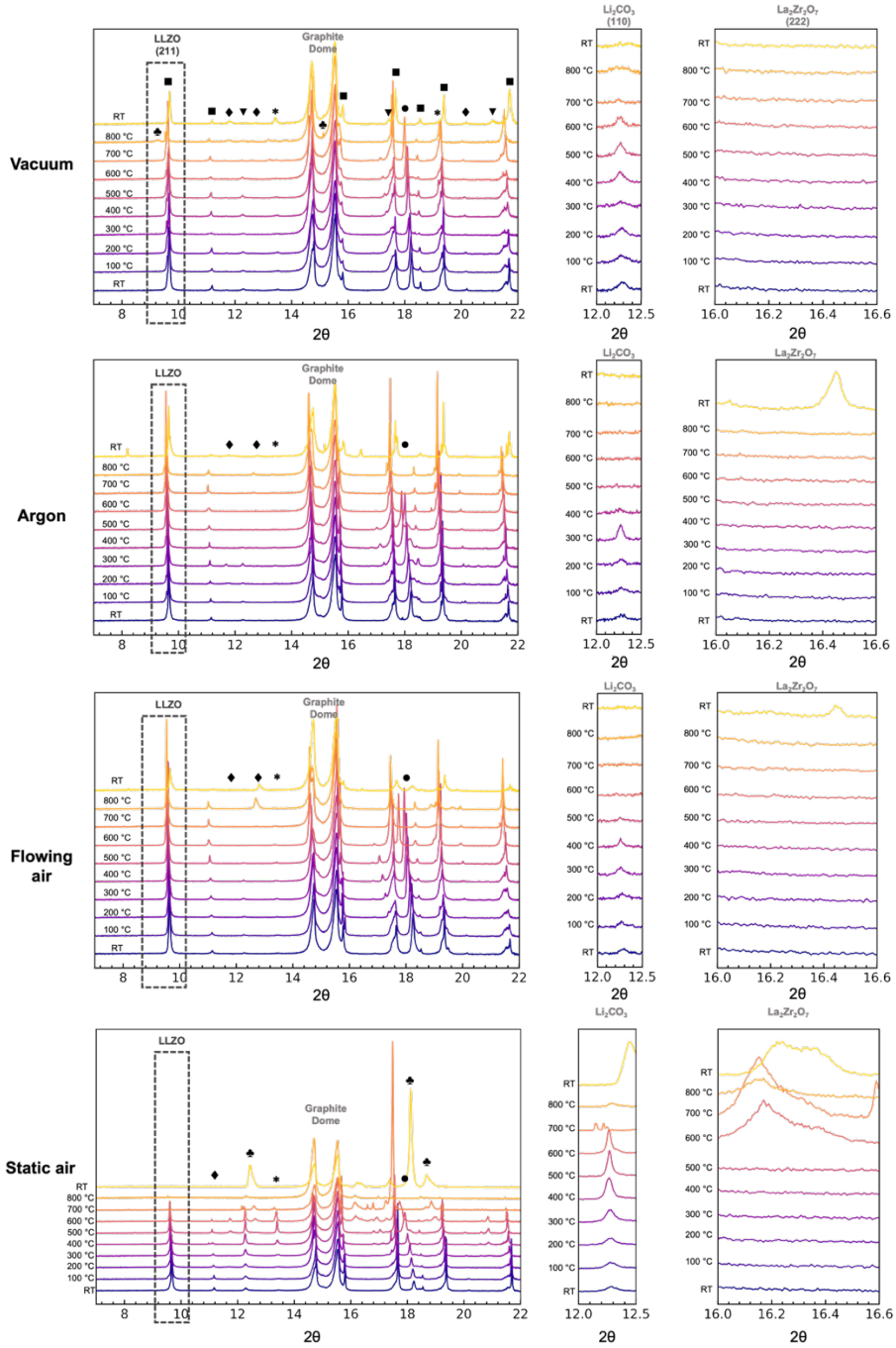

Figure 1: GIXRD (14 keV) patterns of Al-LLZO samples heated under different environments (0.1° incidence). The grey dotted-line box and ■ represents LLZO reflections, ♦ represents Li_2ZrO_3, ⬢ represents $LaAlO_3$, ● represents LiOH and ▼ represents Li_2CO_3. The peaks represented by ♣ in the vacuum case at 800 °C could not be indexed to any known compound, these peaks disappear upon cooling down to RT.

References:

1 A. Sharafi, S. Yu, M. Naguib, M. Lee, C. Ma, H. M. Meyer, J. Nanda, M. Chi, D. J. Siegel and J. Sakamoto, *J Mater Chem A Mater*, 2017, **5**, 13475–13487.

2 L. Cheng, M. Liu, A. Mehta, H. Xin, F. Lin, K. Persson, G. Chen, E. J. Crumlin and M. Doeff, *ACS Appl Energy Mater*, 2018, **1**, 7244–7252.

3 A. Sharafi, E. Kazyak, A. L. Davis, S. Yu, T. Thompson, D. J. Siegel, N. P. Dasgupta and J. Sakamoto, *Chemistry of Materials*, 2017, **29**, 7961–7968.

4 R. H. Brugge, F. M. Pesci, A. Cavallaro, C. Sole, M. A. Isaacs, G. Kerherve, R. S. Weatherup and A. Aguadero, *J Mater Chem A Mater*, 2020, **8**, 14265–14276.

5 J. Cai, B. Polzin, L. Fan, L. Yin, Y. Liang, X. Li, Q. Liu, S. E. Trask, Y. Liu, Y. Ren, X. Meng and Z. Chen, *Mater Today Energy*, 2021, **20**, 100669

6 S. Vema, F. N. Sayed, S. Nagendran, B. Karagoz, C. Sternemann, M. Paulus, G. Held and C. P. Grey, *ACS Energy Lett*, 2023, **8**, 3476–3484.

Investigating the structure evolution of $FePO_4$ during competitive (de)intercalation of Na and Li via *operando* X-ray diffraction

Andreas Kuhlmann[1], Marten Huck[1], Emil J. Skrentny[1], Christian Sternemann[2], Hans-Georg Steinrück[1]

[1]Department of Chemistry, Paderborn University, 33098 Paderborn, Germany

[2]Fakultät Physik/DELTA, TU Dortmund University, 44221 Dortmund, Germany

Electrochemical desalination methods are a promising technology due to their high energy efficiency. Recently, electrochemical desalination was expanded towards utilizing faradaic (intercalation and conversion) electrodes, which is promising at high salinities; the corresponding devices are denoted “desalination batteries” (DBs). Towards practical implementation, we need to understand the fundamental physics and chemistry underlying their performance and degradation[1].

Our aim was to reveal the mechanisms of ion (de)intercalation and storage in iron phosphate-based electrodes at the atomic scale. These phenomena are encoded in the variation of unit cell parameters during galvanostatic cycling (GC) and therefore measurable using *operando* X-ray diffraction (XRD).

We investigated $FePO_4$ as cathode active materials in pure aqueous LiCl and NaCl solutions, as well as in mixed solutions. The active materials were coated as slurry onto carbon cloth and placed into a pouch cell with an activated carbon cloth counter electrode, AgCl reference and glass fiber separator. Using a 3D printed stage setup (Fig. 1), a batch of three cells could be cycled and measured. XRD measurements were performed at beamline BL9 of DELTA using 27 keV incident photon energy and utilizing a MAR345 image plate scanner. In GC, a constant current (mA) was applied, determined by the C-rate C/N, where C is the theoretical capacity (mAh/g) multiplied by the mass (g) of the material, and N the duration of (dis)charge (h) to reach the theoretical capacity.

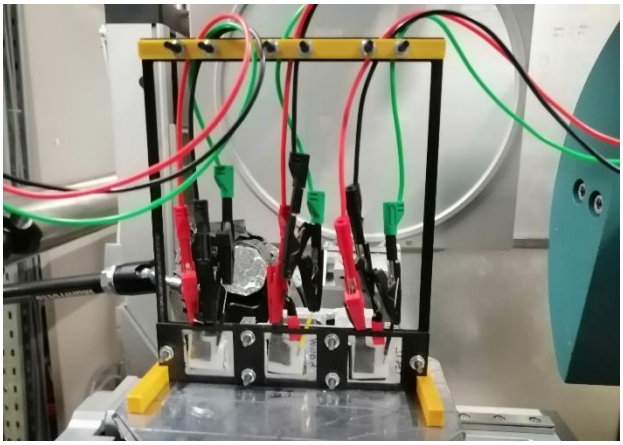

Figure 1: Setup for operando *synchrotron XRD experiments at BL9. The pouch cells are cycled galvanostatically at different C-rates.*

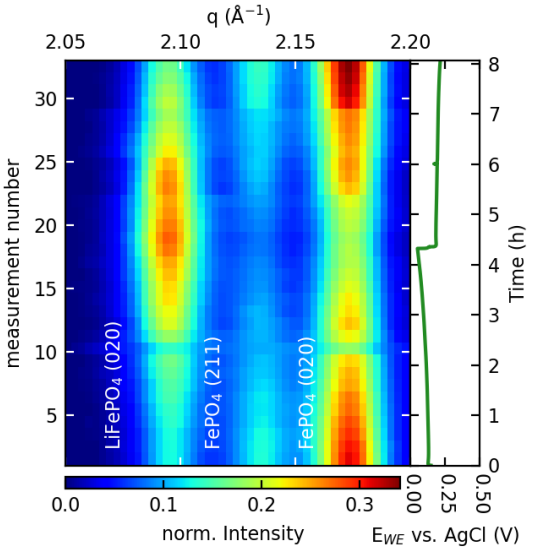

Figure 2: Galvanostatic cycling and operando *synchrotron XRD of $FePO_4$ (C/10) in 1 M LiCl. Potential limits -0.05 to 0.50 V.*

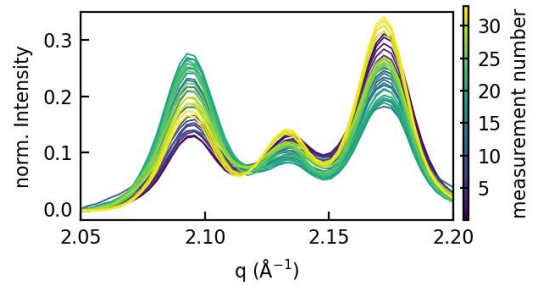

Figure 3: Operando synchrotron XRD result between 2.05 and 2.20 Å^{-1} of $FePO_4$ during galvanostatic cycling in 1 M LiCl at C/10.

The (de)intercalation of Li^+ for $FePO_4$ in 1 M LiCl at C/10 is tracked well by the $LiFePO_4$ (020), $FePO_4$ (211), and (020) Bragg reflections (Fig. 2). The behavior shows similarities to that in organic electrolytes[2]. The process is dominated by the typical phase separation with a two-phase coexistence of $LiFePO_4$ and $FePO_4$, both having the olivine phase. Lower contribution of phases with intermediate composition is seen by the "intensity bridges" at ca. 2.150 $Å^{-1}$ with intensity evolution during GC, and at 2.115 $Å^{-1}$ (Fig. 3). These bridges do not reach the base line, implying that Li contents close to 0 and 100% are not reached during this experiment.

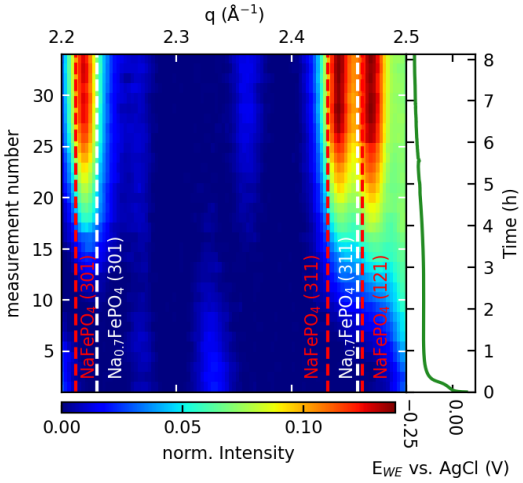

Figure 4: Galvanostatic cycling and operando *synchrotron XRD of $FePO_4$ (C/8) in 1 M NaCl. Potential limits -0.30 to 0.60 V.*

The intercalation of Na^+ for $FePO_4$ causes a gradual increase of reflections corresponding to $Na_{0.7}FePO_4$, and $NaFePO_4$[3] (Fig. 4). After 3 h, the potential plateau decreases from -0.16 V to -0.21 V. The slow kinetics and intermediate $Na_{0.7}FePO_4$ structure compared to Li^+ intercalation could be attributed to the higher ionic radius of Na^+[3-4], and a higher diffusion barrier in $FePO_4$[5]. Besides, a possible disturbance is the oxygen reduction reaction (ORR) below -0.20 V vs. AgCl which could contribute parasitic capacity, and dominate the electrochemical reaction[6].

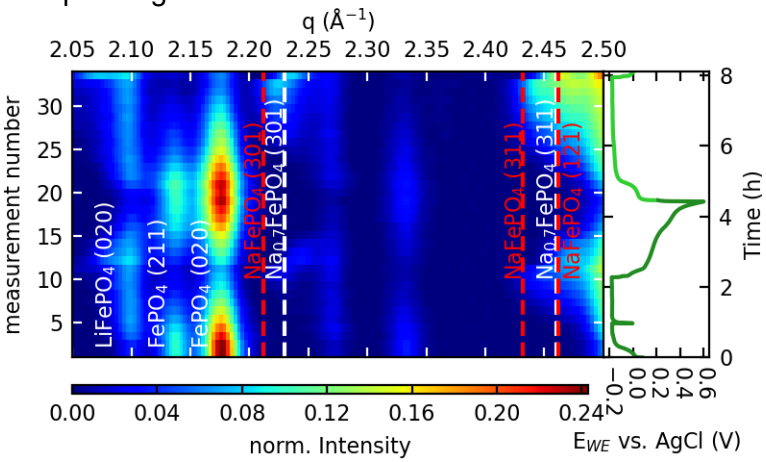

Figure 5: Galvanostatic cycling and operando *synchrotron XRD of $FePO_4$ (C/5) in NaCl/LiCl solution (Na^+/Li^+ 100:1, 1 M NaCl). Potential limits -0.20 to 0.60 V. During the intercalation step, the experiment was set to the next setpoint manually to prevent the risk of excessive ORR.*

Finally, GC in a mixed 100:1 NaCl/LiCl solution shows two plateaus each for deintercalation, and intercalation (Fig. 5). The intercalation starts with a short plateau at 0.03 V attributed to Li^+ intercalation. Then, the potential approaches -0.18 V. Based on $Na_{0.7}FePO_4$ (311), and $NaFePO_4$ (311) and (121), it is attributed to Na^+ intercalation. We observe evidence for phase transformation of $Na_{0.7}FePO_4$ to $NaFePO_4$. The initial intercalation of Li^+ could promote Na^+ intercalation by lowering the volume mismatch between $FePO_4$, and $Na_{0.7}FePO_4/NaFePO_4$[4]. During Na^+ intercalation, the intensity of Li^+ does not change. This suggests that its intercalation is suppressed. We tentatively speculate that this is caused by the Na^+/Li^+ ratio. The deintercalation process is *vice versa*. At 2.7 - 2.8 h and 8.0 - 8.1 h, it is striking that the intensity of $LiFePO_4$ (020) is increasing before the expected decrease. We propose that there is an intriguing short time frame during Na^+ deintercalation in which the potential is in the region of Li^+ intercalation causing this observation.

References

[1] Li et al., *Adv. Sci.* **7**, 2002213 (2020). **[2]** Hess et al., *Nat. Commun.* **6**, 8169 (2015). **[3]** Moreau et al., *Chem. Mater.* **22**, 4126-4128 (2010). **[4]** Fang et al., *ACS Appl. Mater. Interfaces* **7**, 17977-17984 (2015). **[5]** Ong et al., *Energy Environ. Sci.* **4** (2011). **[6]** Liu et al., *Joule* **4**, 1459-1469 (2020).

Studying cathode dynamics during the (de)intercalation of cations in manganese oxide-based electrodes for water desalination using *operando* X-ray diffraction

Marten Huck[1], Andreas Kuhlmann[1], Emil J. Skrentny[1], Christian Sternemann[2], Hans-Georg Steinrück[1]

[1]Department of Chemistry, Paderborn University, 33098 Paderborn, Germany

[2]Fakultät Physik/DELTA, TU Dortmund, 44221 Dortmund, Germany

During a time of critical water scarcity, desalination offers a solution to make seawater usable. One innovative and particularly energy-efficient electrochemistry-based approach are desalination batteries (DBs), which are capable of storing and recovering energy through chemical bonds[1]. Despite their potential for seawater desalination, DBs encounter electrode stability challenges akin to aqueous batteries. The complications associated with complex electrolyte solutions created by the use of seawater underscore the need to decipher the physics and chemistry underlying the performance and degradation of DBs.

Our goal was to reveal the mechanisms of (de)intercalation and storage of ions in manganese oxide-based electrodes at the atomic scale. These phenomena are encoded in the variation of unit cell parameters during galvanostatic cycling (GC) and are therefore uniquely accessible using operando X-ray diffraction (XRD).

We investigated $LiMn_2O_4$ and $Na_{0.44}MnO_2$ as cathode active materials in pure aqueous LiCl and NaCl solutions, as well as in mixed solutions. The active materials were coated as slurry onto carbon cloth and placed into a pouch cell with an activated carbon cloth counter electrode, AgCl reference and glass fiber separator. Using a 3D printed stage setup (see Report [A. Kuhlmann]), a batch of three cells was cycled and measured. XRD measurements were performed at beamline BL9 of DELTA with 27 keV incident energy using a MAR345 image plate scanner. In GC, a constant current (mA) was applied, determined by the C-rate C/N, where C is the theoretical capacity (in mAh/g) multiplied by the mass (g) of the material, and N the duration of (dis)charge (h).

Fig. 1 presents results achieved with $LiMn_2O_4$ in LiCl and $Na_{0.44}MnO_2$ in NaCl. Both

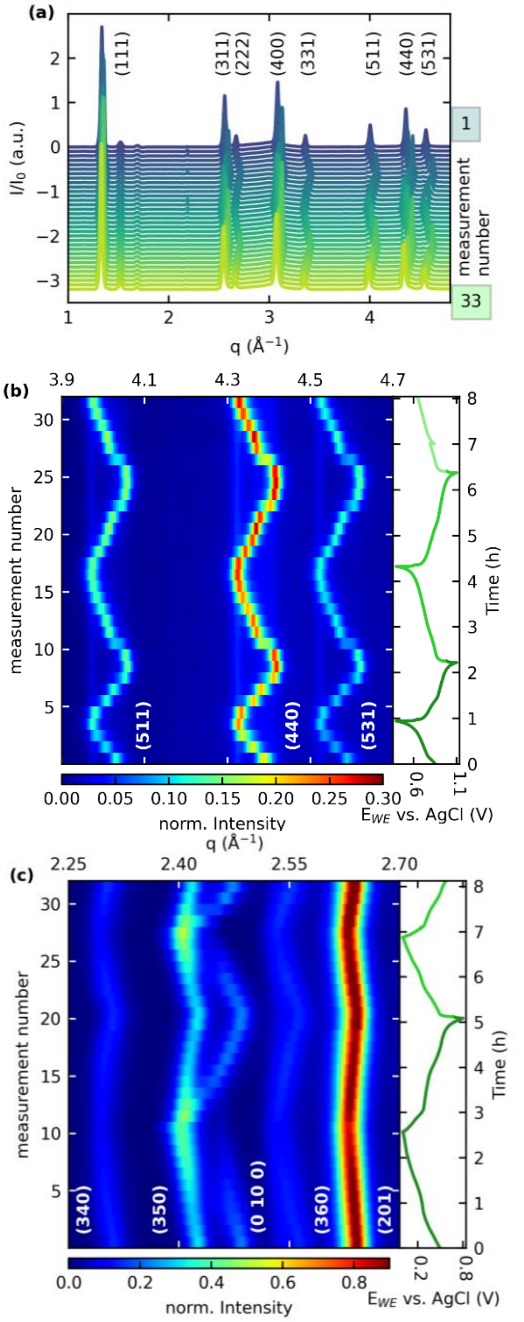

Figure 1: Galvanostatic cycling and operando synchrotron XRD data for $LiMn_2O_4$ in 1M LiCl ((a): waterfall plot of 33 measurements taken at 15-minute intervals; (b): data from graph (a) in a 2D plot) and (c) for $Na_{0.44}MnO_2$ in 1M NaCl (2D), both at C/4.

materials exhibit the reversible shift in peak position characteristic for manganese oxides. When applying a negative current to the cathode, Li^+ or Na^+ intercalate into the manganese oxide and cause the Mn–O bonds to elongate, which leads to a gradual increase in lattice cell volume. The increased (or decreased, in case of deintercalation) lattice parameters are reflected in the d-spacing, thereby causing the peak shift. A continuous shift suggests a solid-solution reaction.

$LiMn_2O_4$ (Fig. 1b) shows the formation of three main "phases" during (de-)intercalation, namely $Li_1Mn_2O_4$, $Li_{0.5}Mn_2O_4$ and $Li_{0.015}Mn_2O_4$ (λ-MnO_2)[2]. This phase transition is accompanied by two potential plateaus visible in the GC data. Both $LiMn_2O_4$ and λ-MnO_2 represent the $Fd3m$ space group, while $Li_{0.5}Mn_2O_4$ is suggested to be part of a subgroup of $\mathrm{Fd3m}$ with lower symmetry, $F\bar{4}3m$.[3] Additionally, a remaining $Li_1Mn_2O_4$ phase can be seen for all peaks (e.g., (440)), suggesting an incomplete deintercalation due to parts of the cathode not actively involved in the deintercalation process.

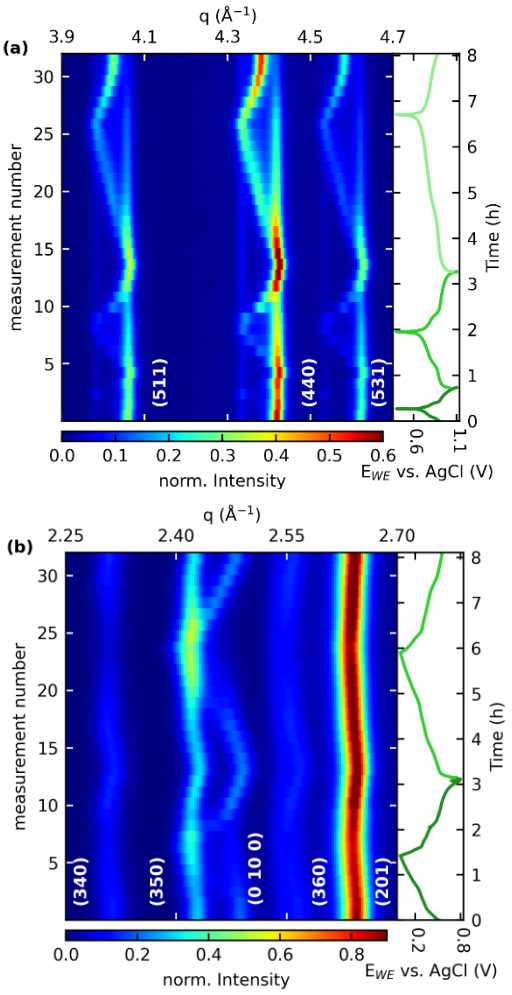

Figure 2: Galvanostatic cycling and operando synchrotron XRD data for (a) $LiMn_2O_4$ (C/3, C/6, C/10) and (b) for $Na_{0.44}MnO_2$, (C/4) both in 1M 1:1 LiCl:NaCl

In mixed solution systems such as 1 M 1:1 LiCl:NaCl (Fig. 2a), the electrode shows decreased capacity and incomplete intercalation, likely due to a depletion of Li^+. This is supported by findings in solutions with 1:100 LiCl:NaCl. At the same time, no intercalation of Na^+ into the $LiMn_2O_4$ spinel structure could be detected via the emergence of a new additional $Na_xMn_{2-x}O_4$ phase, suggesting high selectivity towards Li^+ over Na^+.

$Na_{0.44}MnO_2$ (Fig. 1c) does not show the formation of superstructures or (sub) space groups apart from its orthorhombic lattice cell and $Pbam$ space group, which could be due to the (de-)intercalation phases being structurally very close.[4] It does however present a clear shift of diffraction peaks, including the splitting of (350) into (350) and (0 10 0) between $Na_{0.44}MnO_2$ and $Na_{0.20}MnO_2$[4].

In mixed solutions (Fig. 2b), no additional Li-rich phase could be detected via a new peak emerging, suggesting a high selectivity towards Na^+ over Li^+. This selectivity could help to decrease Na content in Li-rich waters, whereas $LiMn_2O_4$ is promising to extract Li^+ efficiently.

References

[1] Li et al., *Adv. Sci. (Weinh)* **7**, 2002213 (2020).
[2] Slautin et al., *Batteries* **4** (2018).
[3] Julien, Massot, *Mater. Sci. Eng. B* **97**, 217-230 (2003).
[4] Sauvage et al., *Inorg. Chem.* **46**, 3289-3294 (2007).

Hard X-ray spectroscopy

EXAFS investigations of CoPt alloys loaded on nitrogen-doped carbon and nitrogen-doped carbon with CoN_x

K. Yuan[a], Y. Chen[a], B. Wu[a], F. Braun[b], L. Voss[b], T. Trompeter[b], D. Lützenkirchen-Hecht[b]

[a] *College of Chemistry and Chemical Engineering/Institute of Polymers and Energy Chemistry (IPEC), Nanchang University, Nanchang, 330031, China*

[b] *Faculty of Mathematics and Natural Sciences-Physics Department, University of Wuppertal, Gauss-Str. 20, D-42119 Wuppertal, Germany*

Nowadays, bulk platinum catalysts have outstanding catalytic activity for catalyzing the conversion from O_2 to H_2O (oxygen reduction reaction, ORR) in proton exchange membrane fuel cells (PEMFCs, see e.g. [1]). However the huge costs associated with the use of Pt have severely constrained the evolution and hindered the practical application of Pt-based PEMFCs [2]. Accordingly, different strategies have been followed to reduce the amount of the used Pt, e.g. by developing Pt-based single atom catalysts [3] or by employing Pt-alloy nanomaterials with reduced content [4, 5] but improved ORR activity.

Here, we prepared two supported PtCo-alloy nanoparticle catalysts on nitrogen-doped carbon (sample PtCo@N-C) and nitrogen-doped carbon with Co-Nx (sample PtCo@Co-N-C), with varied neighboring dopants. We have performed EXAFS experiments at the Pt L3-edge and the Co K-edge in order to investigate the local coordination environment around Pt and Co, respectively. For the synthesis of the PtCo@N-C sample, ZIF-8 MOFs assembled on the surface of MnO_2 nanoflowers were heated to a temperature of 1000 °C in a tube furnace under N_2 flow and etched with 2M HCl to obtain the nitrogen-doped carbon, that was impregnated with Pt and Co to obtain the PtCo@N-C precursor. For PtCo@Co-N-C, ZnCo MOFs assembled on the surface of MnO_2 nanoflowers were heated in a tube furnace as above, and etched subsequently to obtain a nitrogen-doped carbon with Co-Nx sites (CoNC carrier). Similar to the PtCo@N-C preparation, this carrier was wet-impregnated with Co and Pt to obtain the second precursor. Both precursors were then treated with H_2/N_2 flow at 700 °C to form PtCo alloys loaded on the N-C carrier and the Co-N-C carrier, respectively. The synthesized CoPt-alloy catalysts materials were further subjected to an acid wash with 0.5 M HCl, dried in vacuum, and finally annealed in a H_2/N_2 flow at 200 °C.

EXAFS investigations have been performed at the DELTA materials science beamline 10, using a Si(111) channel-cut monochromator and ionization chambers as detectors for the incidence and transmitted intensities [6]. The powder samples were filled into PVC sample holders in order to obtain a homogeneous sample with sufficient absorption at the Co K-edge (7709 eV) and the Pt L_3-edge (11564 eV), respectively.

In Fig. 1, the results of the EXAFS measurements at the Co K-edge are compiled. Compared to the Co metal foil, substantially smaller EXAFS oscillations were observed for the PtCo@N-C and PtCo@Co-N-C samples, well in agreement with the presence of small nanoparticles. Furthermore, the Co K-edge data of the PtCo@Co-N-C sample shows clear indications that a large portion of the Co was bound to nitrogen in the N-C-carrier (peak at about 1.5 Å in the FT), and only a smaller peak related to Co-Co and Co-Pt neighbors at 2.3 Å. In contrast, the magnitude of the FT of the PtCo@N-C sample only reveals signals related to Co-Co and Co-Pt neighbors, and in agreement with this, the overall amplitude of the k^2-weighted EXAFS fine structures $k^2*\chi(k)$ reveals a substantially increased amplitude (insert of Fig. 1).

In Fig. 2, the results of the EXAFS measurements at the Pt L_3-edge are displayed. Again, the amplitude of the Pt metal foil EXAFS fine structure oscillations is larger compared to that of the nanoparticle alloys. In qualitative agreement with the measurements at the Co K-edge, the EXAFS of the PtCo@Co-N-C sample resembles that of the Pt metal foil, since a substantial amount of the cobalt

contained in this sample is bond to the N-C-carrier, i.e., the remaining Pt is mostly bond to Pt and not to Co. Well in agreement with this qualitative analysis, the FT and the $k^2*\chi(k)$ for the PtCo@-N-C sample show substantial differences, due to the presence of many Co-Pt bonds at different distances, most prominent in the range of ca. 4 Å to about 6 Å.

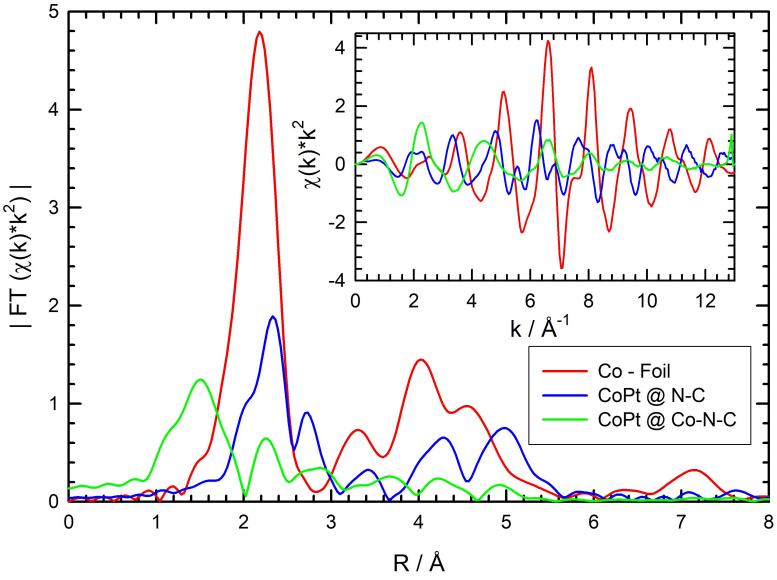

Fig. 1: Comparison of the magnitude of the Fourier-transform of the k^2-weighted EXAFS fine structure oscillations $|FT(k^2*\chi(k)|$ for a Co metal foil, PtCo@N-C and PtCo@Co-N-C samples at the Co K-edge. In the insert, the k^2-weighted EXAFS fine structure oscillations $\chi(k)*k^2$ are presented for the three samples.

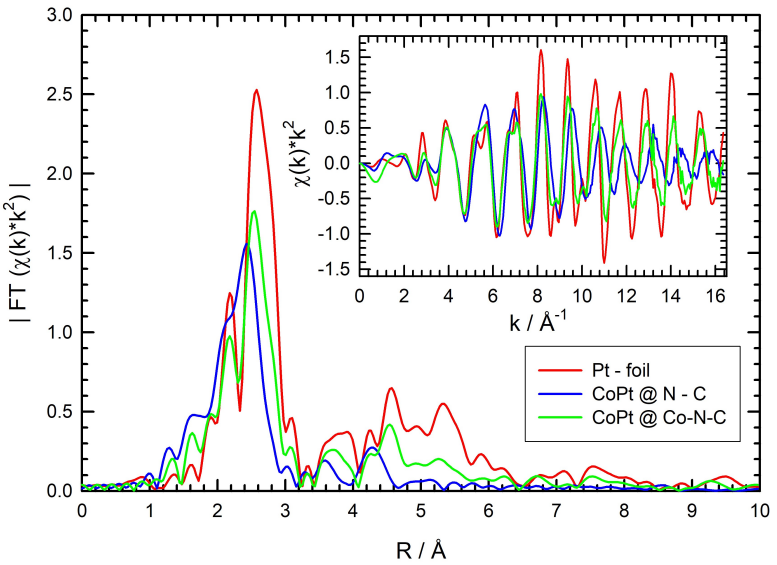

Fig. 2: Comparison of the magnitude of the Fourier-transform of the k^2-weighted EXAFS fine structure oscillations $|FT(k^2*\chi(k)|$ for a Pt metal foil, PtCo@N-C and PtCo@Co-N-C samples at the Pt L_3-edge. In the insert, the k^2-weighted EXAFS fine structure oscillations $\chi(k)*k^2$ are presented for the three samples.

A more quantitative analysis of the EXAFS measurements is currently under way and will be published in a forthcoming publication.

Acknowledgements

We gratefully acknowledge the DELTA machine group for providing synchrotron radiation reliably.

References

[1] S. Zaman, L. Huang, A. I. Douka, H. Yang, B. You, B. Y. Xia, *Angew. Chem. Int. Ed. 60 (*2021) 17832.
[2] Y. Sun, S. Polani, F. Luo, S. Ott, P. Strasser, F. Dionigi, Nat. Commun. 12 (2021) 5984.
[3] J. Zhao, C. Fu, K. Ye, Z. Liang, F. Jiang, S. Shen, X. Zhao, L. Ma, Z. Shadike, X. Wang, J. Zhang, K. Jiang, Nature Commun. 13 (2022) 685.
[4] S.L.A. Bueno, H.M. Ashberry, I. Shafei, S.E. Skrabalak, Accounts Chem. Res. 54 (2021) 1662.
[5] B Wu, J. Xiao, L. Li, T. Hu, M. Qiu, D. Lützenkirchen-Hecht, K. Yuan, Y. Chen, CCS Chem 5 (2023) 2545.
[6] D. Lützenkirchen-Hecht, R. Wagner, S. Szillat, et al., J. Synchrotron Rad. 21 (2014) 819.

X-ray absorption studies of metal foils at room and cryogenic temperatures for DAPHNE4NFDI

S. Paripsa[(a)], C. Schlesiger[(b)], B. Kanngiesser[(b)], A. Gaur[(c)], J.-D. Grunwaldt[(c)], D. Lützenkirchen-Hecht[(a)]

[(a)]Fakultät für Mathematik und Naturwissenschaften, Bergische Universität Wuppertal, Gaußstraße 20, 42119 Wuppertal

[(b)]Institut für Optik und Atomare Physik, TU Berlin, Hardenbergstr. 36, 10623 Berlin

[(c)]Karlsruher Institut für Technologie (KIT), Institut für Technische Chemie und Polymerchemie, Engesserstr. 20, 76131 Karlsruhe.

The DAPHNE4NFDI (**DA**ta from **PH**oton and **N**eutron **E**xperiments for NFDI) consortium is dedicated to enhancing research with photons and neutrons at large-scale facilities, aiming to make experiment data FAIR, that is **F**indable, **A**ccessible, **I**nteroperable and **R**eusable, thus increasing scientific efficiency and knowledge extraction. More information is given in [1].

Within DAPHNE4NFDI, an important pilot project was to develop a reference database in the field of X-ray absorption spectroscopy with a planned inclusion of X-ray emission spectroscopy and related techniques. For the developed database initial steps are including data from metal foils measured at room temperature (RT). We are now expanding our database with data from measurements at cryogenic temperatures, to enhance its research applicability. Contributions from the wider scientific community are welcome to further augment the database's scope and depth. For further details please see http://xafsdb.ddns.net/ and ref. [2].

In the present contribution, we have performed X-ray absorption fine structure measurements on pure reference foils, focusing on the K and L absorption edges, in addition to similar studies on compounds, with detailed information provided in Table 1.

Table 1: XAFS measurement details for pure reference foils and compounds.

Element	Edge(s)	Temperature
Fe	K	RT, 77 K
Ni	K	RT, 77 K
Co	K	RT, 77 K
Ta	L_1, L_2, L_3	77 K
Alloy: $Fe_{40}Ni_{40}B_{20}$	Fe-K, Ni-K	77 K
Alloy: $Fe_{41.5}Ni_{40}P_{14}B_6$	Fe-K, Ni-K	77 K

The variety of metal foil measurements as references were specifically aimed at starting to fill our database with a wide range of data collected under different experimental conditions, such as temperature variations and beamline characteristics. This effort is crucial in order to establish a versatile foundation for the database. All experiments were carried out at the DELTA beamline 10 [3], utilising a Si(111) channel-cut monochromator, with a 100% N_2 –filled ionisation chamber I_0 and a 80% N_2, 20% Ar- filled ionisation chamber I_1. Each reference sample was encased in Kapton tape and stuffed between two thin rectangular holders with a sufficiently large rectangular cut-out, while each alloy foil was directly placed into the sample holder. EXAFS data were recorded at RT and in a liquid nitrogen bath cryostat at 77K.

The Fourier-transform magnitude of the k^2-weighted EXAFS of Fe, represented as $|\chi(R)|Å^{-3}$ is shown in Fig. 1 (right). Examination of the FT EXAFS spectra displays distinct structural characteristics of Fe. The first peak at around 2.2 Å represents the Fe-Fe nearest neighbour interactions and indicates backscattering effects as well as interference patterns that are characteristic of the sample's metallic iron lattice. This is seen in both the RT (red) and the 77K measurement (blue). At 77K, the following peaks at around 3.6 Å, 4.5 Å and 5.4 Å, corresponding to farther atomic interactions, are more pronounced. The increased sharpness and intensity of these peaks in the 77 K spectrum compared to RT reflect a reduction in thermal vibrations and dynamic disorder within the lattice, as the lower temperature enhances the constructive

interference. The sharper definition at 77 K suggests a lower Debye-Waller factor, confirming less atomic displacement and a more ordered state. Similar results were obtained for a Ni metal foil at the Ni K-edge and a Co metal foil at the Co K-edge at a temperature of 77 K (see Fig. 2 left, resp. right).

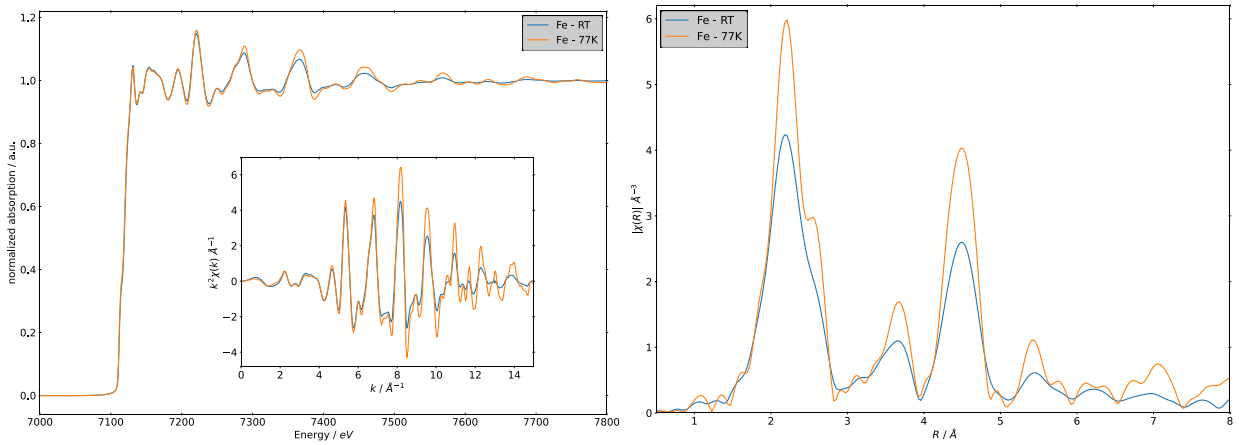

Figure 1: (left) Raw EXAFS spectra obtained from an iron metal foil at the Fe K-edge for RT in blue and at 77 K in orange. Inset: extracted EXAFS fine structures $\chi(k)*k^2$. (right) Magnitude of the Fourier transform of the k^2-weighted EXAFS fine structure $|\chi(R)|$Å^{-3} for an iron metal foil at the Fe K-edge (k-range for the FT: 2.396 Å^{-1} ≤ k ≤ 16.406 Å^{-1}).

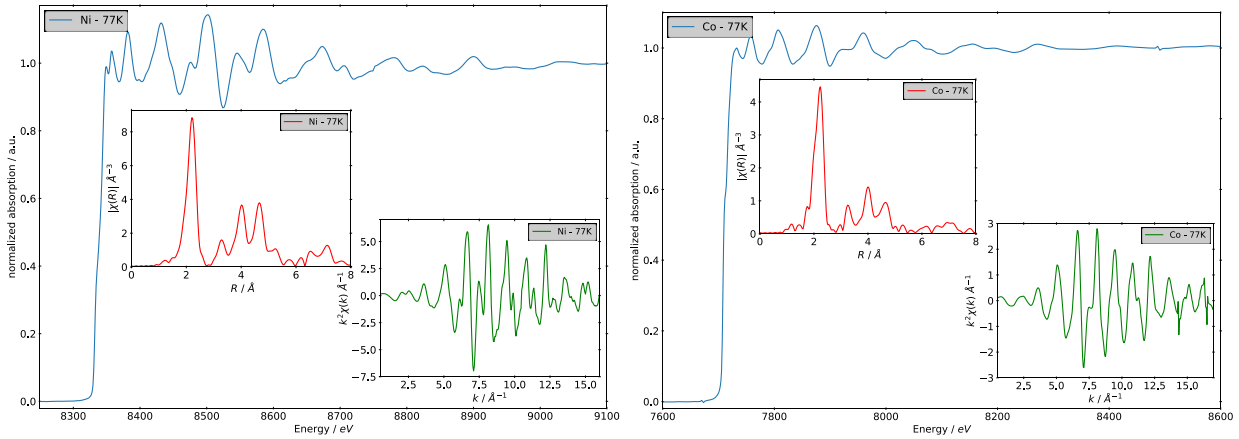

Figure 2: (left) EXAFS spectrum of a Ni metal foil at 77 K measured at the Ni K-edge. In the insets, the extracted EXAFS fine structures ($\chi(k)*k^2$, green) and the magnitude of the Fourier transform of the k^2-weighted EXAFS fine structure ($|\chi(R)|$Å^{-3}, red) are shown (k-range for the FT: 1.852 Å^{-1} ≤ k ≤ 19.374 Å^{-1}). (right) EXAFS spectrum of a Co metal foil at 77 K measured at the Co K-edge. Insets: extracted EXAFS fine structures ($\chi(k)*k^2$, green) and the magnitude of the Fourier transform of the k^3-weighted EXAFS fine structure ($|\chi(R)|$Å^{-3}, red) are shown (k-range for the FT: 2.723 Å^{-1} ≤ k ≤ 20.265 Å^{-1}).

Acknowledgement

We gratefully acknowledge the DELTA machine group for providing synchrotron radiation reliably. This work is supported by the consortium DAPHNE4NFDI in the context of the work of the NFDI e.V. The consortium is funded by the DFG - project number 460248799.

References:

[1] A. Barty et al., Zenodo, DAPHNE4NFDI - Consortium Proposal, June, 2023, doi: https://doi.org/10.5281/zenodo.8040606

[2] A. Gaur, S. Paripsa et al., Zenodo, Metadata Fields and Quality Criteria - XAS Reference Database under DAPHNE4NFDI, October, 2023, doi: https://zenodo.org/records/8412918

[3] D. Lützenkirchen-Hecht, R. Wagner, S. Szillat, et al., J. Synchrotron Rad. 21 (2014) 819.

An X-ray absorption near-edge structure study on AlCrVYN thin films

Eric Schneider[1], Finn Ontrup[2], Jaqueline Savelkouls[1], Nicola Thiering[1], Christian Sternemann[1], Michael Paulus[1], Nelson Filipe Lopes Dias[2], Ralph Wagner[3], Dirk Lützenkirchen-Hecht[3], Wolfgang Tillmann[2]

[1]Fakultät Physik/DELTA, TU Dortmund University, 44221 Dortmund, Germany
[2]Fakultät Maschinenbau, Institute of Materials Engineering, TU Dortmund University, 44221 Dortmund, Germany
[3]Fakultät für Mathematik und Naturwissenschaften, Fachgruppe Physik, University of Wuppertal, 42119 Wuppertal, Germany

The temperature-dependent investigation of complex thin-film systems such as AlCrVYN often leads to the formation of different oxides, which are difficult to separate from each other by X-ray diffraction. It is therefore advisable to use a further complementary method which helps to constrain the number of possible phases formed. The aim of this X-ray absorption study is to obtain a fundamental understanding of the oxidation behavior of AlCrVYN coatings during temperature treatment of thin films produced with varying deposition parameters.

For the X-ray absorption near-edge structure (XANES) studies, AlCrVYN thin films were grown by direct current magnetron sputtering (dcMS), high power impulse magnetron sputtering (HiPIMS) and a hybrid dcMS/HiPIMS process. We studied coated WC-Co substrates that were stepwise heated *ex situ*, between 25 °C and 1000 °C. Figure 1 shows the XANES setup used at beamline BL10 at DELTA [1]. The XANES measurements were performed in fluorescence detection mode at the vanadium K-edge (5465 eV) using a grazing angle of 3°, to identify vanadium to be present in different oxidations states. In this setup we used a beam size of 0.2 x 8.0 mm^2 (*v* x *h*).

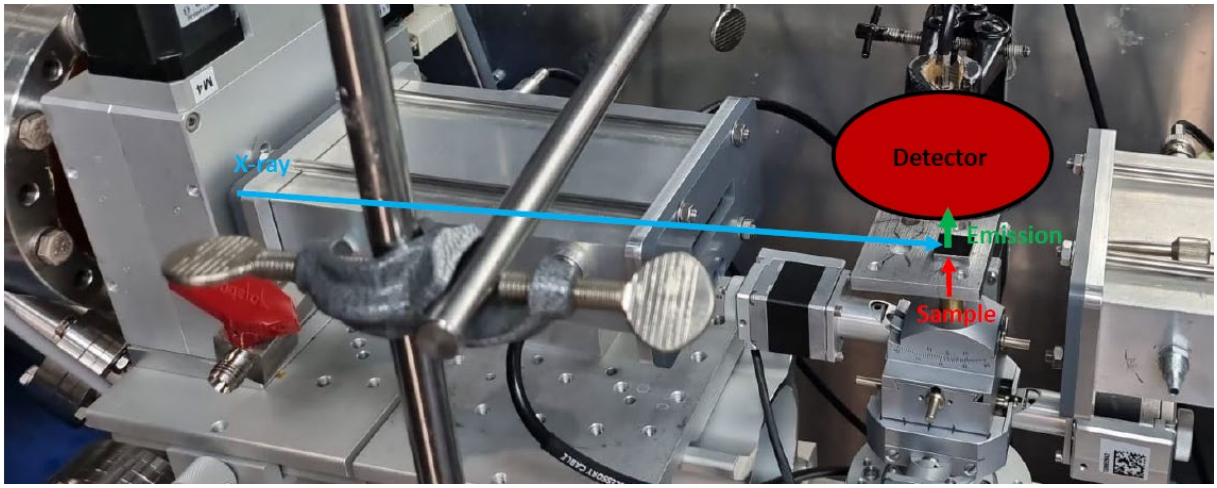

Figure 1: XANES flourescence detection setup at beamline BL10. During the measurements, the sample is aligned to an grazing angle of 3°. Measurements were taken in a range of incident energy from 5405 eV to 5685 eV to detect the vanadium K-edge.

Via the analysis of the pre-edge peaks of the XANES vanadium K-edge spectra, the formation of vanadium oxides in thin films is investigated. Similar to iron oxides, the pre-edge area and main-edge position provide information about the oxidation state of vanadium [2, 3]. Figure 2 shows the vanadium K-edge of all samples produced with dcMS, HiPIMS and hybrid dcMS/HiPIMS processes measured at room temperature (left) and after heating to 875°C (right). By comparing the pre-edge features of the samples with the pre-edges of the references, i.e. vanadium oxides of different oxidation state ranging from 0 to 5, the average oxidation state of the film was be determined.

In Figure 2, left, the occurrence of the pre-peak indicates that all samples already contain a certain amount of oxides in their initial state, while the samples react differently with oxygen at elevated temperatures (Figure 2, right).

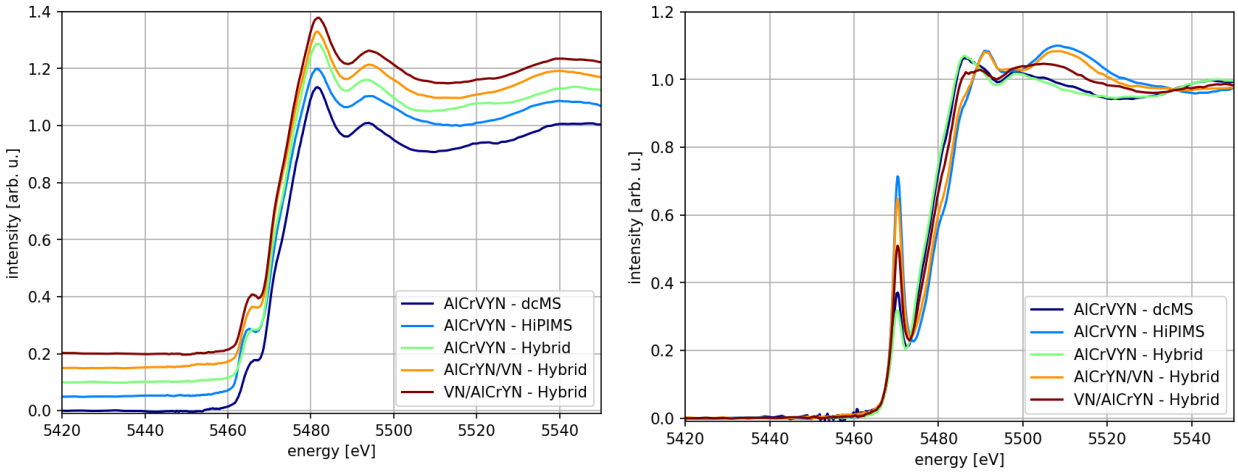

Figure 2: XANES spectra at the vanadium K-edge of all samples at room temperature (left) and after annealing at 875°C

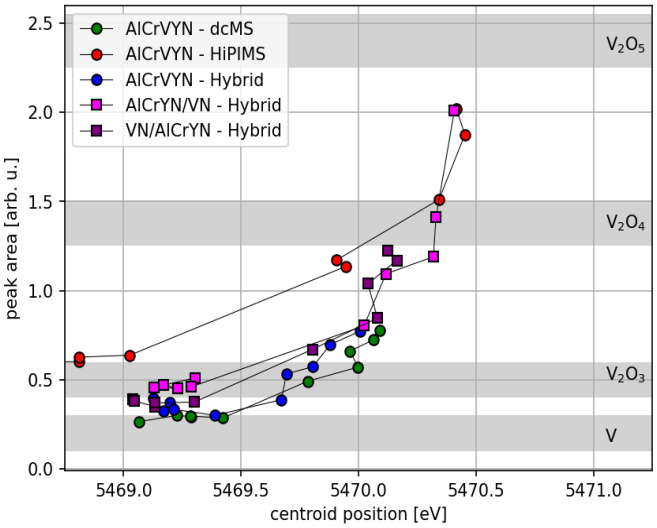

Figure 3: Comparison of the temperature dependent oxidation behavior of all samples based on the position and area of the pre-edge. The temperatures to which the samples were exposed increase from left to right. The grey areas indicate the pre-edge behavior of reference samples.

An overview of the oxidation behavior of the different samples can be found in Figure 3. Here, the area of the pre-peak is shown as a function of the position of the vanadium K-absorption edge and compared with reference data off different vanadium oxides. All samples show an increase in oxidation number with increasing temperature during annealing, resulting in different average oxidation states after annealing.

References

[1] D. Lützenkirchen-Hecht, R. Wagner, S. Szillat, A.K. Hüsecken, K. Istomin, U. Pietsch, R. Frahm, The multi-purpose hard X-ray beamline BL10 at the DELTA storage ring, Journal of Synchrotron Radiation, Volume 21, 2004, Pages 819-26.

[2] M. Wilke, G. M. Partzsch, R. Bernhardt, D. Lattard, Determination of the iron oxidation state in basaltic glasses using XANES at the K-edge, Chemical Geology, Volume 213, Issues 1–3, 2004, Pages 71-87

[3] W. Tillmann, L. Hagen, D. Kokalj, M. Paulus, M.Tolan, Temperature-induced formation of lubricous oxides in vanadium containing iron-based arc sprayed coatings, 2018

Acknowledgments

We thank the DELTA team for providing synchrotron radiation. This work was supported by the DFG via TO 169/21-1 and TI 343/190-1.

EXAFS investigations of high-entropy-alloy nanoparticles on nitrogen-doped carbon

T. Trompeter[a], X. Tang[b], K. Yuan[b], Y. Chen[b], D. Lützenkirchen-Hecht[a]

[a] *Faculty of Mathematics and Natural Sciences-Physics Department, University of Wuppertal, Gauss-Str. 20, D-42119 Wuppertal, Germany*

[b] *College of Chemistry and Chemical Engineering/Institute of Polymers and Energy Chemistry (IPEC), Nanchang University, Nanchang, 330031, China*

The definition of a high-entropy alloy (HEA) refers to alloys that are composed of five or more elemental compounds, and a concentration between 5 and 35 atomic percent of each of the contributing elements [1, 2]. Based on the mixed configuration entropy S, which is given by

$$S = - R \Sigma x_i \ln (x_i), \qquad eq. (1)$$

with R the molar gas constant, and the x_i representing the molar fraction of each element (i) in the alloy, the entropy of a HEA is substantially increased compared to that of pure metals and intermetallic compounds [3, 4]. The increase of the mixed configuration entropy appears to be beneficial for the formation of a thermodynamically stable single-phase solid solution, and suppresses the appearance of a more fragile intermetallic compound. By inclusion of different metallic elements with different radii with a random site occupation, local lattice distortions, i.e. deviations from the elemental bond distances, are generated [5]. Assuming the presence of five elements and an equimolar concentration of all elements, equation (1) reduces to $S = R \ln (5) \approx 1.5 R$; i.e. an alloy can be considered as a high-entropy alloy if $S \geq 1.5R$ [1, 2]. HEAs have attracted attention due to their unique physico-chemical properties, that are interesting for different applications. Furthermore, by tuning the metallic component, the properties of the HEA can be influenced to a large degree. As a prominent example, HEAs are able to regulate the geometric as well as the electronic structures substantially, and may serve as a platform to construct catalysts with tailored properties [6]. In the present contribution, we have therefore investigated MnCoNiCuZn high-entropy alloys on nitrogen-doped carbon as potential candidate for catalytical applications. The HEA was synthesized by mixing and ball-milling appropriate amounts of carbon black, zeolite ZIF-8, manganese-, cobalt-, nickel- and copper-nitrate. The obtained material was subsequently centrifugated, washed with de-ionized water and freeze dried. Finally, the powder was pyrolyzed under N_2-atmosphere at 800 °C. According to an ICP-OES analysis, the prepared HEA had an elemental contribution of 29.6 % Mn, 37.8 % Co, 13.0 % Ni, 7.5 % Cu and 12.1 % Zn, resulting in a mixed configuration entropy $S \approx 1.44$ R, so that the prepared material can be considered as a HEA.

The EXAFS investigations at the Mn (6539 eV), Co (7709 eV), Ni (8333 eV), Cu (8979 eV) and Zn (9659 eV) K-edges have been conducted at the DELTA wiggler beamline 10 using a Si(111) monochromator and ionization chambers as detectors for the incident and transmitted X-ray intensities [7]. The powder sample was gently pressed into a circular spacer to obtain a sample thickness with suited absorption for the experiments. According to the raw data, the edge jumps at the five investigated edges are 0.28 for Mn, 0.61 for Co, 0.32 for Ni, 0.30 for Cu and 0.33 for Zn, leading to slightly different concentrations of 15.9 (Mn), 26.8 (Co), 15.2 (Ni), 16.7 (Cu) and 25.4 (Zn) in comparison to the results of the ICP-OES, and a mixed configuration entropy $S \approx 1.58$ R, supporting the inter-pretation of a HEA material. In Fig. 1, the magnitude of the Fourier-Transform of the k^3-weighted EXAFS fine structures $|FT (\chi(k)*k^3)|$ measured at the different edges are compared. In Fig. 1(a), the $|FT (\chi(k)*k^3)|$ of the HEA at the Co, Ni and Cu edge are compared to the FT of a nickel reference foil. As can be seen, there are small differences in the position of the nearest neighbor peak, and in peaks related to higher bond distances, also in comparison to the Ni metal reference foil, reflecting the local lattice distortions in the HEA material. Furthermore also the peak amplitudes are different.

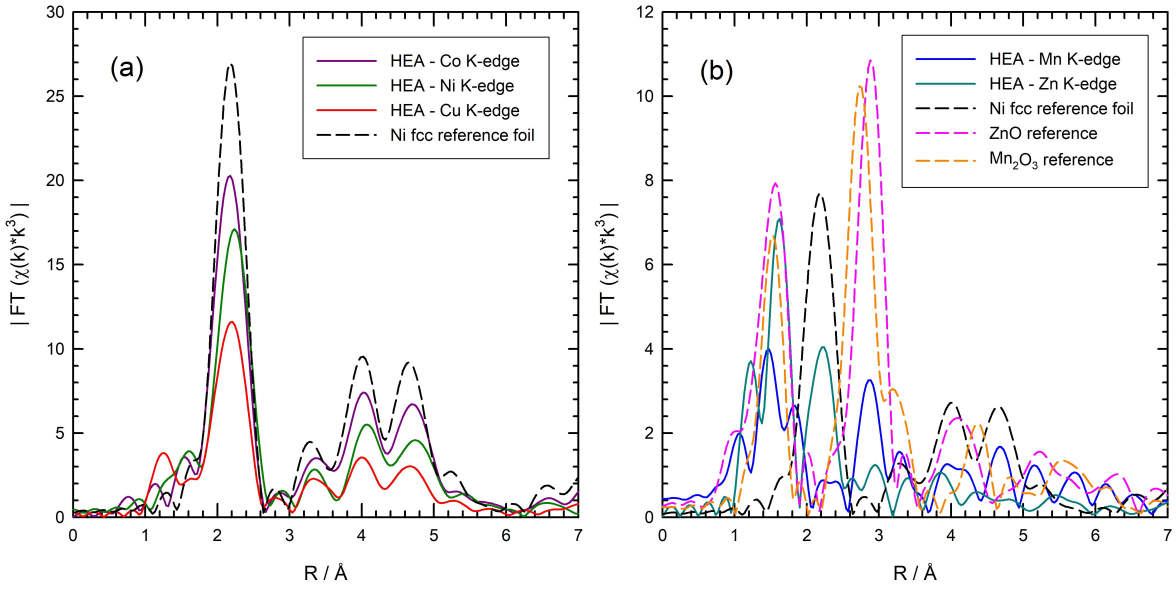

Fig. 1: Magnitude of the Fourier-Transform of the k^3-weighted EXAFS fine structure oscillations $|FT(\chi(k)*k^3)|$ from the high-entropy alloy. (a) Co, Ni and Cu K-edge. For comparison, the FT of a Ni metal reference foil is also shown. (b) Mn and Zn K-edge data of the HEA in comparison to the FT of the Ni metal reference foil, and ZnO and Mn_2O_3 oxide reference materials.

For the Mn and Zn K-edge data, distinct differences to the metal references are found in the FT-transformed data of the HEA (Fig. 1(b)). Here, peaks at smaller bond distances are found for Mn and Zn, close to the bond distances expected for Mn_2O_3 and ZnO, the data of which are plotted in Fig. 1(b) for comparison. While an intense Zn-Zn-scattering peak is found for the HEA at the Zn K-edge, only weak metal contributions are detectable in the Mn K-edge spectrum of the HEA. We thus may conclude that the less noble metals Mn and Zn of the HEA are substantially oxidized, while Co, Ni and Cu are present in purely metallic state. A more detailed analysis of the obtained data for this HEA as well as for additional high entropy alloys with different elemental compositions is currently under way.

Acknowledgements

We gratefully acknowledge the DELTA machine group for providing synchrotron radiation reliably.

References

[1] D.B. Miracle, O.N.A. Senkov, Acta Mater. 122 (2017) 448.
[2] W. Zhang, P.K. Liaw, Y. Zhang, Sci. China Mater. 61 (2018) 2.
[3] J.W. Yeh, S.K. Chen, S.J. Lin, et al., Adv. Eng. Mater. 6 (2004) 299.
[4] E.P. George, D. Raabe, R.O. Ritchie, Nat. Rev. Mater. 4 (2019) 515.
[5] J.W. Yeh, Ann. Chim. Sci. Mater. 31 (2006) 633.
[6] Y. Xin, S. Li, Y. Qian, et al., ACS Catalysis 10 (2020) 11280.
[7] D. Lützenkirchen-Hecht, R. Wagner, S. Szillat, et al., J. Synchrotron Rad. 21 (2014) 819.

Time-resolved EXAFS investigations of Zn corrosion in KOH

D. Lützenkirchen-Hecht, L. Voss, C. Schneider

Faculty of Mathematics and Natural Sciences-Physics Department, University of Wuppertal, Gauss-Str. 20, D-42119 Wuppertal, Germany

In the past decades, rechargeable Zn-based batteries have gained increasing interest due to their low cost, use of earth-abundant materials, their inherent safety and also due to their electrochemical performance, making them an interesting alternative in comparison to Li-ion batteries. However, the development of Zn-batteries is not as developed as the Li-technology, because of e.g. the lower operation voltage, the instability of cathode materials and the dissolution of the Zn-working electrode. Reviews about Zn-based batteries can be found e.g. in Ref. [1] and [2]. In the context of corrosion, it is important to note that Zn may form oxides and hydroxides at its surface during battery operation, and soluble Zn-species are released during discharge [3-5]. In this context, structural investigations of the Zn-species released into the electrolyte are important in order to further understand the operation and in particular the possible corrosion of the batteries.

We have therefore performed in-situ EXAFS investigations during the anodic polarization of Zn metal sheets in alkaline KOH solutions of different concentration. As sketched in the insert of Fig. 1, the X-ray beam passes through the electrolyte in a distance of typically 0.2 – 0.3 mm to the metal working electrode, and both transmission as well as fluorescence mode EXAFS were detected. The experiments were performed at the Zn K-edge (9659 eV) at DELTA beamline 10 [6], employing the recently commissioned continuous energy-scanning (quick-scanning) EXAFS mode [7]. While gas-filled ionization chambers were used for the measurement of incident and transmitted intensities, a large area passivated implanted planar silicon (PIPS) detector (55 mm diameter) placed close to the electrochemical cell was employed for the detection of the emitted fluorescence radiation. For the electrochemical measurements, a three-electrode compartment consisting of the Zn-working electrode (99.999 %, Mateck, Germany), a Pt-wire as counter electrode and an Ag/AgCl reference electrode (3M KCl, U = 0.2 V vs. standard hydrogen electrode, SHE) were employed. The cell consists of a PTFE-frame glued to the working electrode, and two large-area Kapton (polyimide) windows for the incident and transmitted X-ray beam. The cell, with an X-ray beam path of 5 mm and a KOH electrolyte volume of about 0.5 cm^3, was open to the air and all measurements were conducted at room temperature. Electrochemical polarization were carried out with a SimPot 300 potentiostat (M. Schramm, University of Düsseldorf, Germany). The active corrosion of the Zn was initiated by an increasing anodic current, and thus Zn is dissolved and accumulates in the electrolyte volume above the corroded metal surface. For the experiments conducted here, both potentiostatic as well as galvanostatic polarizations with different potentials and current densities were applied.

Selected spectra obtained during the galvanostatic oxidation of the Zn electrode in a 0.2M KOH solution with a current density of 2 mA/cm^2 are displayed in Fig. 1. Here every 10^{th} scan is displayed, i.e. in total more than 80 spectra were recorded during the experiment. First of all the results show that the increase of the zinc-concentration in the electrolyte above the electrode can be followed with time resolved fluorescence mode EXAFS (33 s / spectrum). Clear indications for Zn present in the solution are detectable after a few minutes of polarization. Keeping in mind that the concentration of Zn is usually in the order of 10^{-3} Mol/l corresponding to about 20 ppm only, the data quality appears reasonable.

From the geometry of the experiment, i.e. a path length of 5 mm, the tabulated total mass attenuation cross sections below and above the Zn K-edge (i.e., 33.8 cm^2/g and 251.9 cm^2/g, see Ref. [8]), the atomic concentration (6.57×10^{22} $atoms/cm^3$) and mass density (7.133 g/cm^3) of Zn-metal, the concentration of the Zn in the solution (c) can be calculated to $c \approx \Delta\mu(c) / 7.13$ l/mol, when $\Delta\mu(c)$ is the change of the absorption measured in the transmission mode EXAFS spectra (not shown here). For details of the calculation, please refer to ref. [9]. Following this scheme, a 1 millimolar Zn solution

would lead to an edge height of about Δμ(c) ≈ 0.007, which is obtained after about 5 minutes of polarization with 2 mA/cm^2.

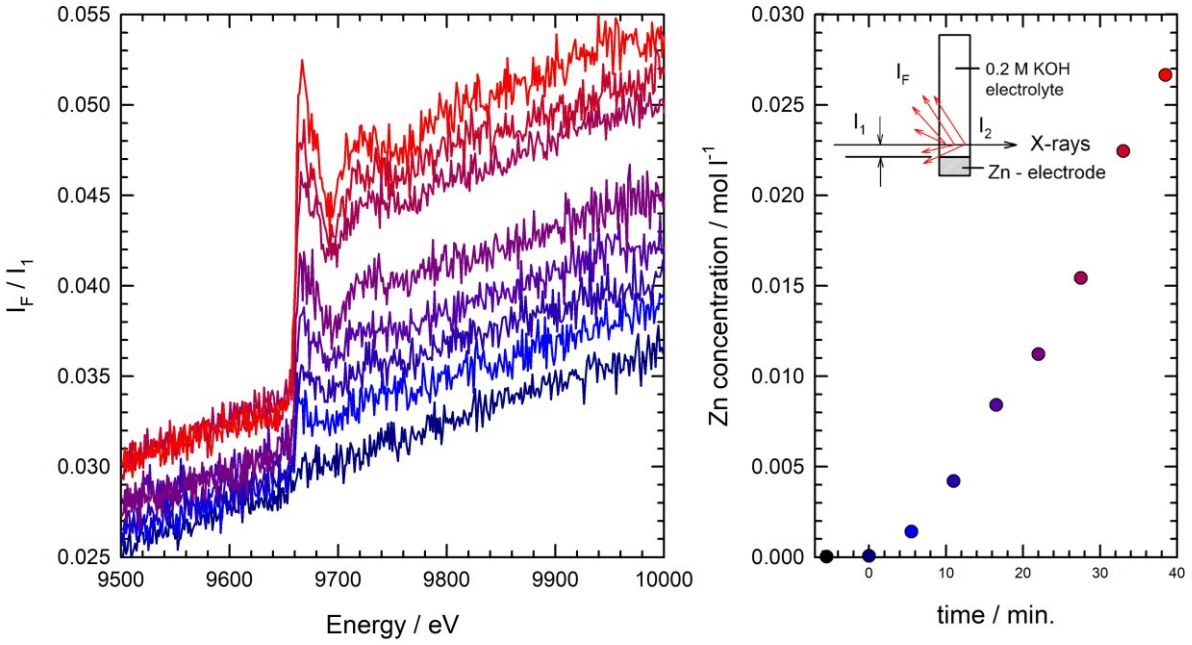

Fig. 1: (Left panel) Temporal evolution of in-situ fluorescence QEXAFS experiments (33 s/scan) at the Zn K-edge during the electrochemical corrosion of Zn in alkaline KOH (0.2M solution). The X-ray beam passes the electrochemical cell parallel to the corroded metal surface in a distance of ca. 0.2 mm as schematically shown in the insert in the right figure. The concentration of the Zn in solution was calculated from the absorption jump at the edge (Δμ) measured in transmission mode (right panel).

A first qualitative evaluation of the data confirmed the presence of a zinc aquo-complex in the alkaline solution. The comparison with spectra of solid zinc oxide (ZnO), hydroxide $Zn(OH)_2$ and Zn^{2+}-complexes in aqueous solutions clearly confirm these initial conclusions. Moreover, a simple increase of the anodic current level during galvanostatic polarization does not lead to an increased level of Zn in the solution, but in contrast to an enhanced oxygen evolution, and thus, the details of the processes are subject of future investigations.

Acknowledgements

We gratefully acknowledge the DELTA machine group for providing synchrotron radiation reliably. The experiments were financially support by the German Federal Ministry of Education and Research (BMBF) under project no. 05K19PXA and 05K22PXA.

References

[1] W. Shang, W. Yu, Y. Liu, et al., Energy Storage Mater. 31 (2020) 44.
[2] C. Han, W. Li, H.K. Liu, et al., Nano Energy 74 (2020) 104880.
[3] J.F. Parker, C.N. Chervin, I.R. Pala, et al., Science 356 (2017) 415.
[4] C. Cachet, B. Saidani, R. Wiart, J. Electrochem. Soc. 138 (1991) 678.
[5] S. Thomas, I.S. Cole, M. Sridhar, et al., Electrochim. Acta 97 (2013) 192.
[6] D. Lützenkirchen-Hecht, R. Wagner, S. Szillat, et al., J. Synchrotron Rad. 21 (2014) 819.
[7] D. Lützenkirchen-Hecht, S. Paripsa, L. Voss, F. Braun, F. Eckelt, DELTA Annual Report (2023), page 23.
[8] M.J. Berger, J.H. Hubbell, S.M. Seltzer, et al., XCOM: Photon Cross Sections Database, NIST Standard Reference Database 8 (XGAM) https://www.nist.gov/pml/xcom-photon-cross-sections-database
[9] D. Lützenkirchen-Hecht, R. Frahm, J. Phys. Chem. B 105 (2001) 9988.

Grazing incidence EXAFS investigations of thin gold films with time resolution

L. Voss, F. Braun, D. Lützenkirchen-Hecht

Faculty of Mathematics and Natural Sciences-Physics Department, University of Wuppertal, Gauss-Str. 20, D-42119 Wuppertal, Germany

Grazing incidence X-ray absorption spectroscopy allows surface sensitive EXAFS experiments [1, 2]: Due to a penetration depth in the order of some few nm, the information captured in the reflected X-rays and the excited X-ray fluorescence radiation originate from the near surface region only. Accordingly, grazing incidence EXAFS measurements are frequently used to study surface phenomena such as adsorption [3, 4], oxidation and corrosion [5, 6] or thin film growth phenomena [7]. Furthermore, a variation of the incidence angle (Θ) allows depth profiling on layer materials [8, 9]. Experiments usually take about 30 minutes for each individual EXAFS scan, depending on e.g. the concentration of the absorber element and the dimensions of the sample. However, many interesting samples undergo temporal changes, e.g. during catalysis, gaseous or aqueous corrosion, film growth etc., and thus, dynamic measurements are highly demanded. Here, time-resolved, quick-scanning EXAFS is an interesting opportunity: Instead of measuring the spectrum on a point-by-point basis with typical integration times of about one second and more, the data are obtained on-the-fly, while the monochromator is scanned continuously [10]. By a combination of the quick-scanning EXAFS technique and the grazing incidence geometry, thus, surface sensitive experiments may be conducted to follow dynamical processes [11, 12].

Here, we have used quick-scanning EXAFS in grazing incidence geometry to investigate thin gold films on float glass substrates at DELTA beamline 10 [13]. As described in this report [14], quick scanning EXAFS has been implemented at this beamline, enabling EXAFS scans over a scan range of about 1000 eV and more within less than 30 s of acquisition time. Employing the macro-programming techniques feasible in the SPEC beamline control software, several EXAFS scans for various different incidence angles were measured automatically. Here, we have employed N_2- and Ar-filled ionization chambers for the measurement of the incident and the reflected intensities, and a large area passivated implanted planar silicon (PIPS) detector for the excited fluorescence radiation, respectively. The experiments were carried out at the Gold L_3-edge (11919 eV), with a measurement time of 30-60 s for each scan covering the energy range from 11700 eV to 12500 eV. The experimental data were normalized to the intensity of the direct beam, so that a reflectivity is obtained for each energy. In Fig. 1, reflection and fluorescence mode EXAFS spectra obtained within 48 s each for different incidence angles are depicted. As can be seen, both the reflectivity as well as the fluorescence EXAFS data quality is suited for a detailed analysis, i.e. meaningful structural information about the investigated thin film sample may be obtained.

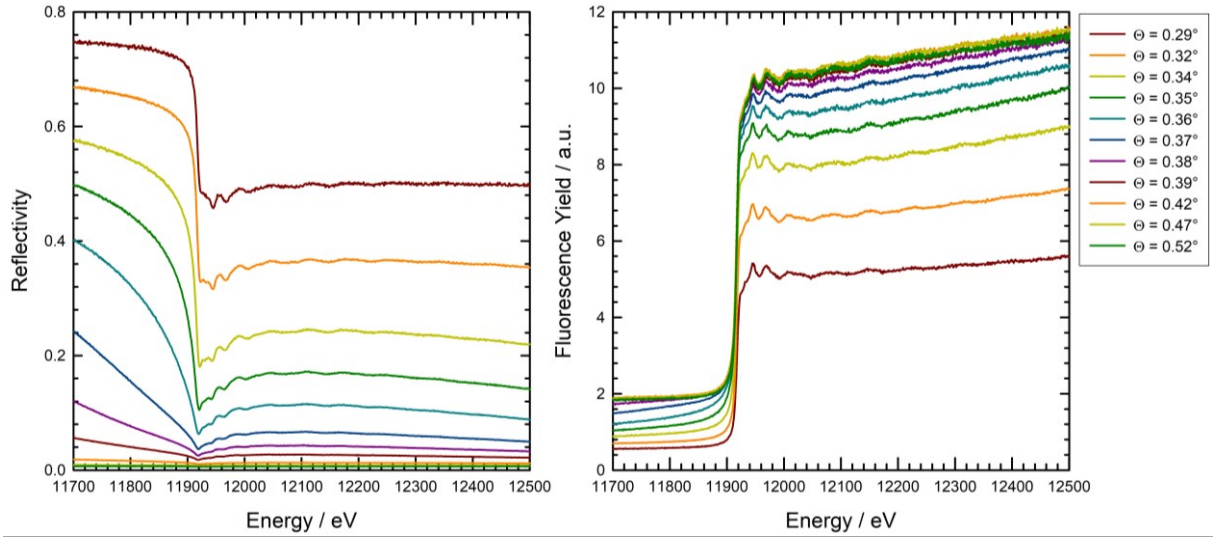

Fig. 1: Continuous Quick-Scanning EXAFS measurements of a thin Gold film at the Au L_3-edge in the grazing incidence geometry for different incidence angles as indicated. Both the reflected intensities as well as the fluorescence yield measured with a large area PIPS-diode were acquired with a total time of less than 50 s for each spectrum.

As mentioned above, automated scans acquired consecutively employing different incidence angles appears feasible for a very effective use of the beamtime for static samples. In addition, routines for the automatic alignment of the sample in the beam are available, so that several samples may be investigated allowing better data statistics. Furthermore, in-situ and time-resolved investigations of thin film processes such as sputtering [7, 12] and electrodeposition [15, 16] as well as anodic oxidation [8] will be conducted in the near future. In addition, heat treatments of thin layers [17] may be followed with appropriate time resolution in the future.

Acknowledgements

We gratefully acknowledge the DELTA machine group for providing synchrotron radiation reliably. The experiments were financially support by the German Federal Ministry of Education and Research (BMBF) under project no. 05K19PXA.

References

[1] S.M. Heald, Rev. Sci. Instrum. 63 (1992) 873.
[2] S.M. Heald, E. Keller, E.A. Stern, Phys. Lett. A 103 (1984) 155.
[3] M. A. Denecke, J. Rothe, K. Dardenne, et al., Phys. Chem. Chem. Phys. 5 (2003)939
[4] F.R. Thornley, N.T. Barrettt, G.N. Greaves, et al., J . Phys. C: Solid State Phys. 19 (1986) L563.
[5] D. Gajdek, P.A.T. Olsson, S. Blomberg, et al., J. Phys. Chem. C 126 (2022) 3411.
[6] D. Lützenkirchen-Hecht, R. Frahm, Physica B 357 (2005) 213.
[7] F. Braun, F. Eckelt, L. Voss, et al., Rad. Phys. Chem. 204 (2023) 110707.
[8] P. Keil, D. Lützenkirchen-Hecht, J. Synchrotron Rad. 16 (2009) 443.
[9] N.M. Souza-Neto, A.Y. Ramos, H.C.N. Tolentino, et al., J. Appl. Cryst. 42 (2009) 1158.
[10] R. Frahm, Nucl. Instrum. Methods Phys. Res. A 270 (1988) 578.
[11] D. Hecht, R. Frahm, H.-H. Strehblow, J. Phys. Chem. 100 (1996) 10831
[12] K. Bruder, P. Keil, D. Lützenkirchen-Hecht, R. Frahm, Physica Scripta T115 (2005) 963.
[13] D. Lützenkirchen-Hecht, R. Wagner, S. Szillat, et al., J. Synchrotron Rad. 21 (2014) 819.
[14] D. Lützenkirchen-Hecht, S. Paripsa, L. Voss, F. Braun, F. Eckelt, DELTA Annual Report (2023), page 23.
[15] D. Hamulić, I. Milošev, D. Lützenkirchen-Hecht, Thin Sol. Films 667 (2018) 11
[16] D. Lützenkirchen-Hecht, D. Hamulić, R. Wagner, I. Milošev, Rad. Phys. Chem. 175 (2020) 108113
[17] D. Lützenkirchen-Hecht, K. Maadour, R. Wagner, R. Frahm, DELTA Annual Report (2015), p. 89.

X-ray emission spectroscopy study of the spin transition in an amine-functionalized porous coordination polymer

V. Rubio-Giménez,[1] C. Albers,[2] C. Bartual-Murgui,[1] M. Romero-Ángel,[1] S. Tatay,[1] C. Martí-Gastaldo,[1] R. Sakrowski,[2] G. Scholz,[2] N. Thiering,[2] M. Paulus,[2] C. Sternemann[2] and J.A. Real[1]

[1]Instituto de Ciencia Molecular, Universitat de València, Catedrático José Beltrán 2, 46980 Paterna, Spain.
[2]Fakultät Physik / DELTA, Technische Universität Dortmund, Maria-Goeppert-Mayer-Str. 2, D-44227 Dortmund, Germany.

Porous coordination polymers (PCPs) with amine functionalities can be applied to selective gas separation from gas mixtures or used in sensing applications.[1] The PCPs can include iron which is capable to undergo a spin crossover transition from high spin (HS) to low spin (LS) iron with decreasing temperature.[2] At a given temperature, the spin switching effect can be induced by the presence of guest molecules in the pores of the material.[3,4]

Hofmann-type coordination polymers (HCPs) are a class of material that show such spin crossover. [5,6] They are composed of layers of alternating octahedral Fe^{II} and square planar Pt^{II} centers connected via cyanide groups while the Fe^{II} ions are coordinated to two additional pillaring ligands and such can form 2D or 3D structures. In this study we investigated a mixed ligand 3D HCP with an amine functionalized axial ligand that shows a peculiar dependence of the spin transition on CO_2 pressure, i.e. the incorporation of CO_2 molecules into the structure directly alters the spin transition temperature as observed via SQUID magnetometry. We applied X-ray emission spectroscopy (XES) in order to determine the spin state of iron *in situ* by variation of temperature using vacuum and CO_2 atmosphere.

The XES measurements of the iron's $K\beta_{1,3}$ emission (7025-7075 eV) were performed at beamline BL2 utilizing a von Hamos spectrometer with white beam excitation. The powder sample was loaded into a glass capillary with 1.5 mm diameter and secured with wool to enable pumping and venting of the sample volume. The sample itself was mounted in a Linkam temperature stage that allowed to apply vacuum or controlled gas pressure via regulation valves and differential pumping. Before the measurements, the sample was activated at 127 °C. The emission spectra taken under vacuum are presented in Figure 1 (left) together with the differences to the HS-state reference measured at 127 °C. The changes in spectral shape clearly indicate a HS to LS transition with decreasing temperature. In order to evaluate the spin state change in more detail we used both IAD (integrated absolute difference) and M1 (center of mass of the main fluorescence line) analysis.[7] The results are presented in Figure 2 (left). The observed spin state change is well in line with the observations from SQUID magnetometry measurements and show a clear hysteresis of the spin transition when the temperature is lowered and again increased.

Next, the sample was exposed to a CO_2 atmosphere at a pressure of 0.6 bar. In this case, the measurements were limited to a -65 °C to avoid freezing of CO_2. Down to this temperature, we could not observe a full HS to LS transition (see Figures 1 and 2 (right)). However, a change in spin state for about 25% of the Fe^{II} atoms contained in the sample can be observed which sets in at higher temperature and is almost complete above -50 °C compared to vacuum conditions. This observation confirms the influence of the gas on the onset of the spin transition, but likewise hints to sample damage due to radiation. Hence, in the next step we activated the same sample at 150 °C under vacuum conditions and measured emission spectra at -85 °C to -125 °C. The sample showed no spin transition at these conditions, which we trace back to severe radiation damage of the sample by radical formation under CO_2 atmosphere induced by white beam exposure. Thus, the study under CO_2 atmosphere

requires a different experimental setup in which high energy excitation with monochromatic X-rays is combined with scanning the sample during the measurements to avoid radiation damage.

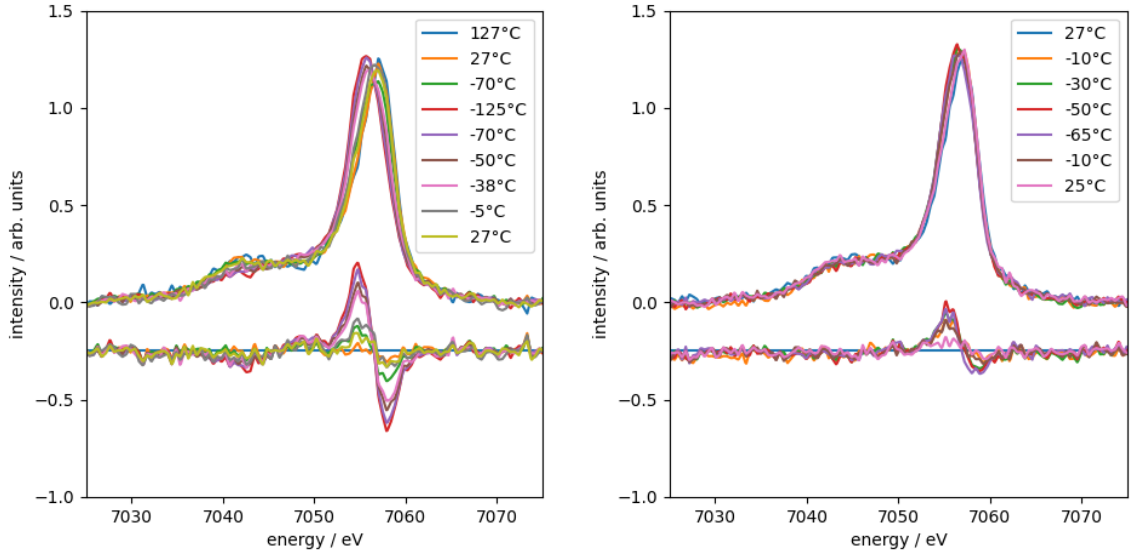

Figure 1. XES Fe $K\beta_{1,3}$ emission measurements performed at BL2 on a 3D HCP powder sample in vacuum (left) and at 0.6 bar CO_2 atmosphere (right). Below the XES spectra, the differences to the reference spectra, i.e. the spectrum measured at 127 °C and the spectrum measured at 27 °C for the vacuum and CO_2 run, respectively, are shown, which have been used for IAD analysis.

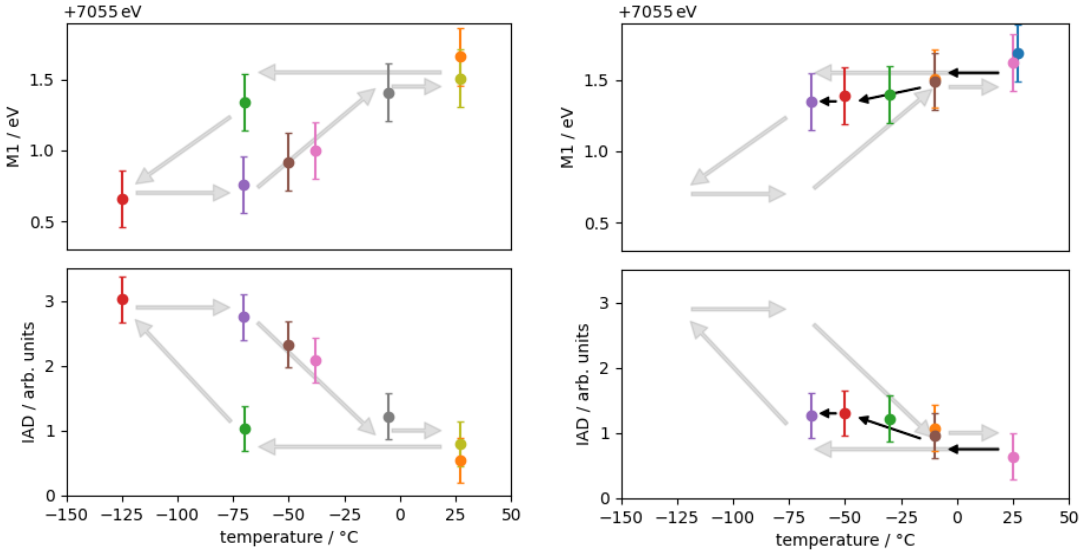

Figure 2. Integrated absolute difference (IAD, bottom) and M1 values (top) calculated for the spectra shown in Figure 1 in vacuum (left) and for CO_2 atmosphere (right). The arrows serve as guide to the eye for the temperature dependence of the HS to LS transition.

[1] A. J. Emerson, A. Chahine, S. R. Batten, D. R. Turner, *Coord. Chem. Rev.* **2018**, *365*, 1–22.
[2] J. A. Real, A. B. Gaspar, V. Niel, M. C. Muñoz, *Coord. Chem. Rev.* **2003**, *236*, 121–141.
[3] J. A. Real, A. B. Gaspar, M. C. Munoz, *Dalton Trans.* **2005**, *0*, 2062–2079.
[4] E. Coronado, G. Minguez Espallargas, *Chem. Soc. Rev.* **2013**, *42*, 1525–1539.
[5] M. C. Muñoz, J. A. Real, *Coord. Chem. Rev.* **2011**, *255*, 2068–2093.
[6] K. Otsubo, T. Haraguchi, H. Kitagawa, *Coord. Chem. Rev.* **2017**, *346*, 123–138.
[7] C. Albers, R. Sakrowski, N. Thiering, L. Libon, G. Spiekermann, J.M. Kaa, H. Gretarsson, M. Sundermann, M. Tolan, M. Wilke and C. Sternemann, *J. Anal. At. Spectrom.* **2023**, *38*, 1097–1107.

High temperature corrosion properties of novel FeCrNi-Mn multi principal-element alloys (MPEAs)

Yasemin Yesilcicek [a], Annika Wetzel [a], Salbin Sediqi [a], Katrin Böttcher [a], Dirk Lützenkirchen-Hecht [b], Ozlem Ozcan [a]

[a] *Federal Institute for Materials Research and Testing, Berlin, Germany*
[b] *Faculty 4 - Physics Department, Bergische Universität Wuppertal, Wuppertal, Germany*

The systematic exploration of new alloy compositions is imperative for the advancement of new material development. A smart strategy for exploring new chemical compositions in phase diagrams involves the creation of gradient alloys via the application of diffusion-controlled synthesis [1, 2]. This approach serves as an efficient means for swiftly identifying prospective material combinations and single-phase alloy chemistries.

This study focusses on the exploration of quaternary multi-principle-element alloys (MPEAs) utilizing diffusion multiples. A diffusion system was established by combining an equimolar ternary alloy (FeCrNi) with Mn. ThermoCalc simulations were employed to ascertain suitable temperature ranges for formation of single-phase alloys. Depending on the diffusion constants of the selected metals, diffusion times were adjusted to obtain diffusion zones with a depth of greater than 50 µm. Microstructural and compositional data were acquired through scanning electron microscopy (SEM) and energy dispersive X-ray spectroscopy (EDX), and these were correlated with local mechanical properties assessed via nanoindentation. Our findings reveal that ThermoCalc simulations exhibit commendable predictive accuracy for crystallographic phases. However, particularly in the Mn-FeCrNi system, the emergence of Cr-rich secondary phases was observed, resulting in Cr-depletion within the matrix near these secondary phases. Three compositions were selected from the diffusion couples (Fig. 1), Cr-rich precipitations (Precipitation), the matrix surrounding the precipitations (Matrix) and the Diffusion zone and casted as bulk alloys using arc melting for further analysis.

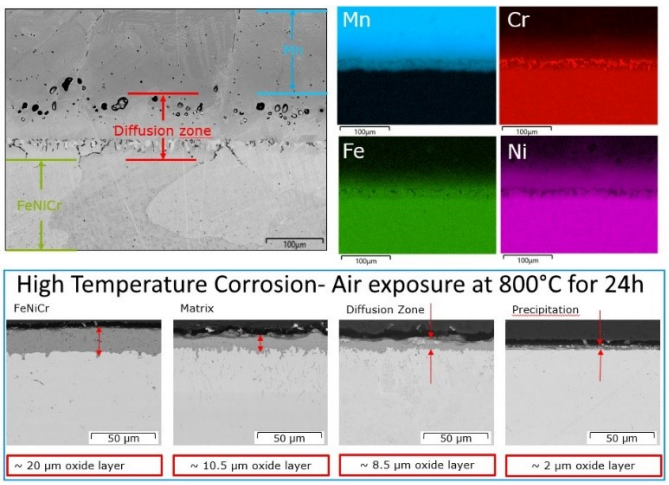

Figure 1. SEM and EDX images of the gradient zone of the diffusion couple (top) and SEM images of the cross-sections of FrCrNi MPEA, and the MPEAs casted with the compositions of the Precipitation phase, Matrix region and Diffusion zone after exposure to air at 800° C for 24 h (bottom).

The FeCrNi MPEA base alloy and casted Precipitation, Matrix and Diffusion Zone samples were exposed to oxidative thermal treatment in air at 800°C for 24 h. Ex situ XANES experiments at the Fe, Ni, Mn and Cr K-edges have been performed to elucidate the changes in oxide chemistry of the MPEAs. The experiments were conducted at DELTA Beamline 10 using a channel cut Si (111) monochromator and gas-filled ionization chambers as detectors and a large area fluorescence detector. The samples were placed parallel to the x-ray beam and positioned with a transmission detector. The angle for the measurements was determined by analyzing the reflectance spectra. Fluorescence spectra were collected on as-prepared and aged MPEA alloy surfaces at different incidence angles.

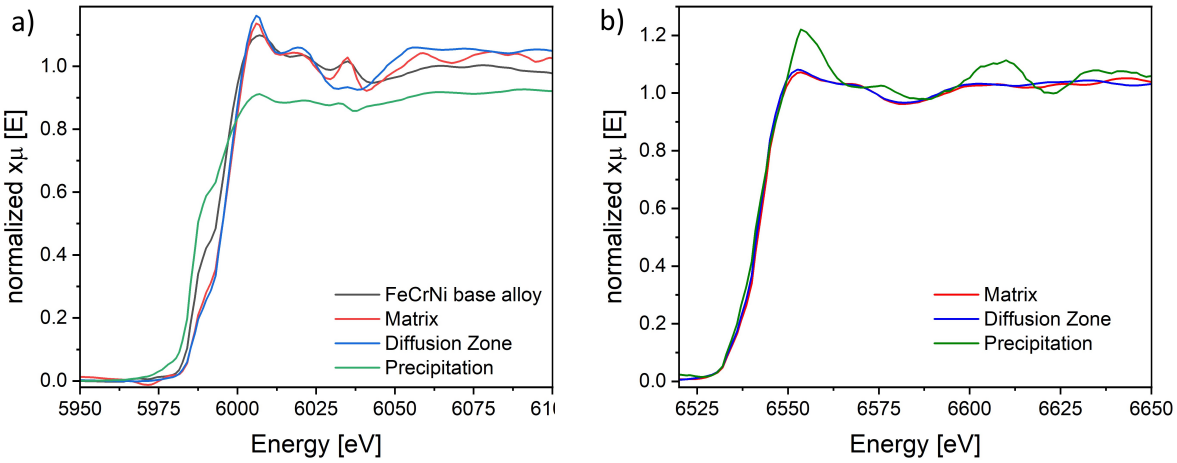

Figure 2. Normalized XANES Spectra collected on FeCrNi MPEA, Matrix, Diffusion zone and precipitation samples after oxidation treatment at 800°C for 24 h collected at 10° incidence angle at a) Cr and b) Mn K-Edge.

Normalized XANES spectra collected on FeCrNi MPEA, Matrix, Diffusion zone and precipitation samples at Cr and Mn K-Edge are presented in Figure 2 a and b, respectively. The spectra acquired on alloys casted with the matrix and diffusion zone compositions have shown a similar behavior with comparable metallic and oxidic contributions for both Cr and Mn after the oxidation treatment. The base alloy had higher metallic Cr contribution than the matrix and diffusion zone alloys. The XANES spectra of the precipitation phase had the highest metallic Cr signal and a strongest Mn-oxide whiteline of all investigated samples.

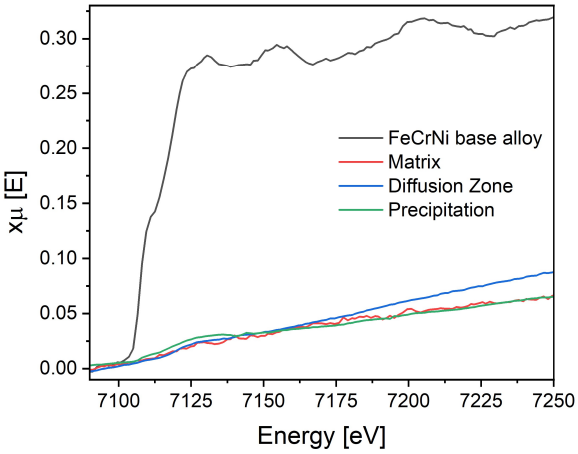

Figure 3. XANES Spectra collected on FeCrNi MPEA, Matrix, Diffusion zone and precipitation after oxidation treatment at 800°C for 24 h collected at 10° incidence angle at Fe K-Edge.

The non-normalized XANES spectra collected on FeCrNi MPEA, Matrix, Diffusion zone and precipitation samples at Fe K-Edge are presented in Figure 3. On all Mn containing alloys, a clear suppression of the Fe absorption edge was observed. Similar behavior was observed also at the spectra collected at the Ni K-edge (not shown here). Considering the SEM analysis of the cross-section specimens after the oxidation treatment, this behavior can be explained with the different oxide film chemistries prevailing in the presence of Mn in the alloy. The high-temperature grown oxide film on the FeCrNi base alloy is composed of Cr, Fe and Ni oxides, whereas on Mn-containing alloys, Cr and Mn oxides dominate the oxide film chemistry.

In the upcoming beamtimes, longer high-temperature corrosion experiments will be performed to test whether the suppression of oxide growth observed with Mn-containing alloy chemistries can be retained over longer exposure times. Moreover, different atmospheres containing water vapor and CO_2 will be tested.

Acknowledgement

We gratefully acknowledge the DELTA machine group for providing synchrotron radiation reliably.

References

1. Springer, H. and D. Raabe, Rapid alloy prototyping: Compositional and thermo-mechanical high throughput bulk combinatorial design of structural materials based on the example of 30Mn–1.2 C–xAl triplex steels. Acta Materialia, 2012. 60(12): p. 4950-4959.
2. Li, Z., et al., Combinatorial metallurgical synthesis and processing of high-entropy alloys. Journal of Materials Research, 2018. 33(19): p. 3156-3169.

XANES/EXAFS investigation of Fe and Co K edges in metallic glass FeCoSiB

N. Hayen[1,3], M. Mewes[1], P. Jordt[1,3], L. Petersdorf[1,3], S. Hövelmann[1,3],
M. Paulus[2], C. Sternemann[2], D. Lützenkirchen-Hecht[4], B. M. Murphy[1,3]

[1]Institut für Experimentelle und Angewandte Physik, Christian-Albrechts-Universität zu Kiel, Leibnizstraße 19, 24118 Kiel, Germany
[2]Fakultät Physik/DELTA, Technische Universität Dortmund, Maria-Goeppert-Mayer-Str. 2, 44227 Dortmund, Germany
[3]Ruprecht Haensel Laboratory, Christian-Albrechts-Universität zu Kiel, 24118 Kiel, Germany
[4]Bergische Universität Wuppertal, Gaußstraße 20, 42119 Wuppertal, Germany

The SFB 1261 project aims to fabricate highly sensitive magnetic field sensors for biomedical applications. Metallic glasses are particularly promising materials for these sensors, with the preferred candidate in SFB 1261 being $(Fe_{0.9}Co_{0.1})_{78}Si_{12}B_{10}$ (FeCoSiB), featuring high magnetostriction and favourable soft magnetic behaviour [1]. In addition, we had the opportunity to investigate an alternative material as well, namely $Fe_{70.4}Ga_{17.6}B_{12}$ (FeGaB). Our study is focused on the investigation of the local short-range order around iron and cobalt atoms within these compounds, complementing our experiments on the medium- and long-range structural order. The central goal of this investigation is to observe changes to this order *in situ* with varying temperature, as degradation of the material's magnetic quality was observed after exposure to typical annealing conditions in a production environment [2].

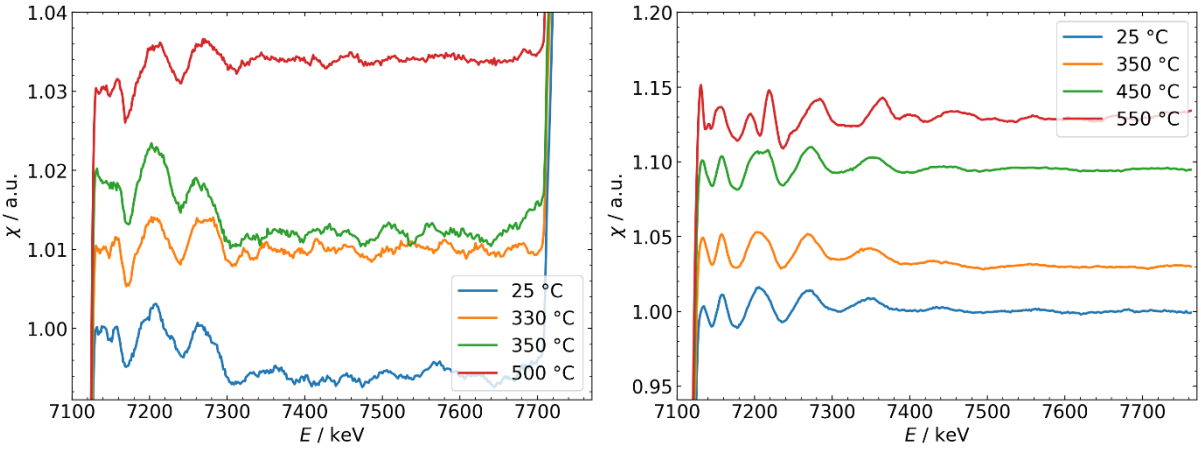

Figure 1: EXAFS curves of the Fe K edge taken at selected temperatures for FeCoSiB (left) and FeGaB (right). FeCoSiB shows very weak fine structure oscillations and high noise level. There is also no notable change in the pattern even when verifiably passing the crystallization point of 450°C. On the other hand, FeGaB showed much more pronounced oscillations and a clear phase transition at around 500°C.

For this experiment EXAFS measurements were conducted at beamline BL10 of the DELTA synchrotron radiation source. The Anton-Paar cell setup available at the beamline was used as the environment for *in situ* heating up to 550°C maximum under vacuum of approximately 1 mbar. The metallic glass samples were prepared as 5µm thick films deposited on 10mm x 10mm Fused Silica substrates. Samples were angled to match the beam footprint and ensure full illumination of the available volume, and the intensity of the incoming beam and the fluorescence from the sample were measured. For the annealing procedures the samples were heated to the target temperature and held there for 15 minutes before cooling back to room temperature. EXAFS measurements were taken once room temperature was reached, after we observed that data taken at high temperatures was affected detrimentally by strong thermal broadening.

Both for FeCoSiB and FeGaB data sets for temperatures ranging from room temperature to 550°C with 20°C steps were acquired. Some selected examples for the Fe K edge are displayed in Figure 1, with an obvious contrast between the very noisy results from FeCoSiB and the much more well-defined EXAFS response from FeGaB. Since both experiments were conducted under the same conditions, the cause for the poorer data quality is assumed to be somehow intrinsic to FeCoSiB. As an increase in counting statistics did not affect the noise level significantly, indicating that there is some other source. The FeCoSiB curves include the Co K edge which was also measured, but since it is an order of magnitude weaker there were no EXAFS oscillations visible at all. The phase transition of FeCoSiB expected at 450°C did not produce any significant effect in the data. In contrast, FeGaB gave good EXFAS signal and showed a phase transition at 500°C. Therefore, we focused our efforts in analysis on this sample.

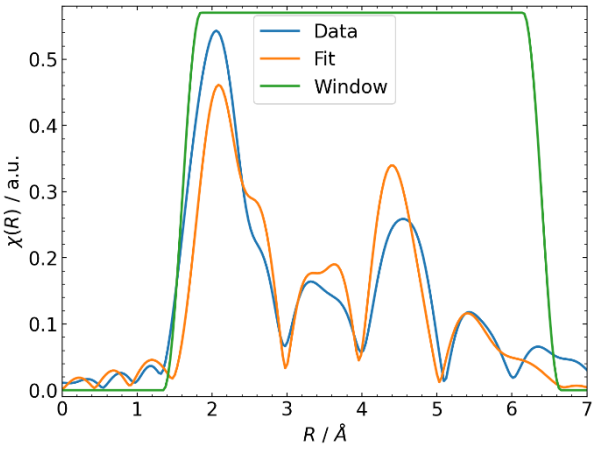

Figure 2: Fit of a FeGaB EXAFS result after the phase transition (550°C) with a model composed of α-Fe and Fe_3Ga. The model is dominated by contributions from α-Fe, as is to be expected with over 70% Fe content. Fe3Ga was chosen as a plausible candidate for the component containing Ga, but it is yet to be verified that this phase is actually the one forming here.

Data extraction and analysis was performed with the Demeter tools, which allow the conversion of the data to real space distributions that can be fitted to theoretical calculations. Figure 2 shows one example for the FeGaB data after the phase transition, fitted to a mixture of α-Fe and Fe_3Ga. This is the best model we were able to produce thus far; the limiting factor is the number of independent model parameters available for the given data resolution.

In summary, we measured EXAFS spectra to investigate the metallic glasses FeCoSiB and FeGaB under *in situ* conditions. The two systems gave very different results: While the EXAFS signal from FeGaB was good and could be described with a model composed of α-Fe and Fe_3Ga, FeCoSiB displayed a very weak response. For future experiments on FeCoSiB we plan to measure the absorption of FeCoSiB instead of fluorescence.

References

[1] V. Hrkac, E. Lage, G. Köppel, J. Strobel, J. McCord, E. Quandt, D. Meyners, and L. Kienle, Amorphous FeCoSiB for exchange bias coupled and decoupled magnetoelectric multilayer systems: Real-structure and magnetic properties, J. Appl. Phys. 116, 134302 (2014). (https://doi.org/10.1063/1.4896662)

[2] C. T. Koops, S. B. Hrkac, M. Abes, P. Jordt, J. Stettner, A. Petraru, H. Kohlstedt, V. Hrkac, N. Wolff, L. Kienle, O. H. Seeck, G. Nisbet, O. M. Magnussen, and B. M. Murphy, Elastic Coupling at Epitaxial Multiferroic Interfaces: in situ X-ray Studies of Electric Field Induced Strain, IFMBE, volume 77 (2019). (https://doi.org/10.1007/978-3-030-31866-6_38)

Acknowledgements

We would like to thank the DELTA team for both their support and for providing us access to synchrotron radiation. We acknowledge funding of this project by the DFG via project A6 in SFB 1261 „ Biomagnetic Sensing “.

Development of multi-principal alloy nanoparticles for electrocatalysis applications using pulsed laser ablation in liquids

Salbin Sediqi [a], Yasemin Yesilcicek [a], Annika Wetzel [a], Katrin Böttcher [a], Dirk Lützenkirchen-Hecht [b], Ozlem Ozcan [a]

[a] *Federal Institute for Materials Research and Testing, Berlin, Germany*
[b] *Faculty 4 - Physics Department, Bergische Universität Wuppertal, Wuppertal, Germany*

Nanoparticle electrocatalysts composed of multi-principal element alloys (MPEAs) hold promise as a cost-efficient and effective substitute for noble metal electrocatalysts. The complex chemical composition and high configurational entropy inherent in MPEAs offer advantages for tailoring catalytic activity, product selectivity, and enhanced stability in challenging reaction environments. Bimetallic catalyst systems incorporating copper (Cu) have already demonstrated a notable enhancement in catalytic efficiency when compared to monometallic systems.[1] Consequently, the objective of this project is to design nanoparticle electrocatalysts based on Cu-containing MPEAs for the carbon dioxide reduction reaction.

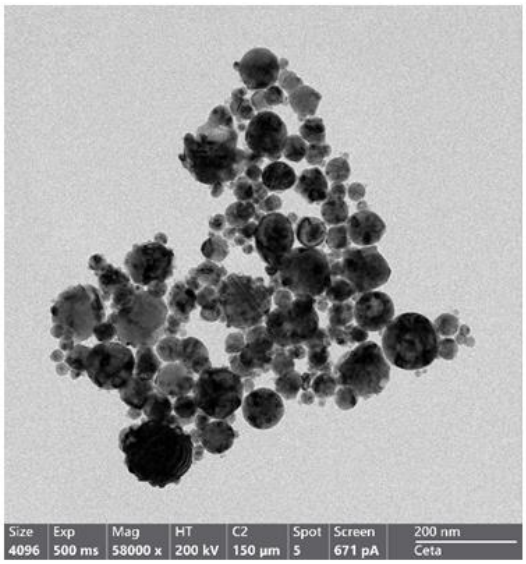

Figure 1. TEM image of the CuZnNi nanoparticles synthesized by means of ultra-short-pulse laser ablation from a Cu target in an aqueous solution containing Zn and Ni ions.

In this project, we explore the electrocatalytic potential of noble metal-free nanoparticles (NPs) derived from multi-principal element alloys (MPEAs) for the electrocatalytic reduction of CO_2 [2]. Utilizing a one-step pulsed laser ablation in liquids (PLALs) method with metal cation additives in the ablation medium, we aim to synthesize alloy nanoparticles using a single metal target. The particle morphology was investigated by means of transmission electron microscopy (TEM) and energy-dispersive X-ray (EDX) mapping. Due to the small particle size and core-shell type composition, EDX measurements were not able to provide a reliable quantification of the chemical composition. Furthermore, the understanding of the local oxidation states during the electroreduction experiments requires the use on an in situ / in operando approach.

The aim of the measurements performed in this beamtime was to assess the success of the alloying concept using a single metal target and cation additives in the ablation environment.

Moreover, we focused on testing the sample build-up for upcoming measurements with the in situ electrochemical cell and to determine the optimal nanoparticle loading on the ITO electrode for an adequate signal quality. For the test experiments at BL10, the cell previously developed for microbially influenced corrosion (MIC) studies was used [3, 4]. In the cell assembly, the ITO-coated PET foil carrying the nanoparticle/Nafion® composite film faces the electrolyte and acts as the window for the incident beam and backscattered fluorescence detection.

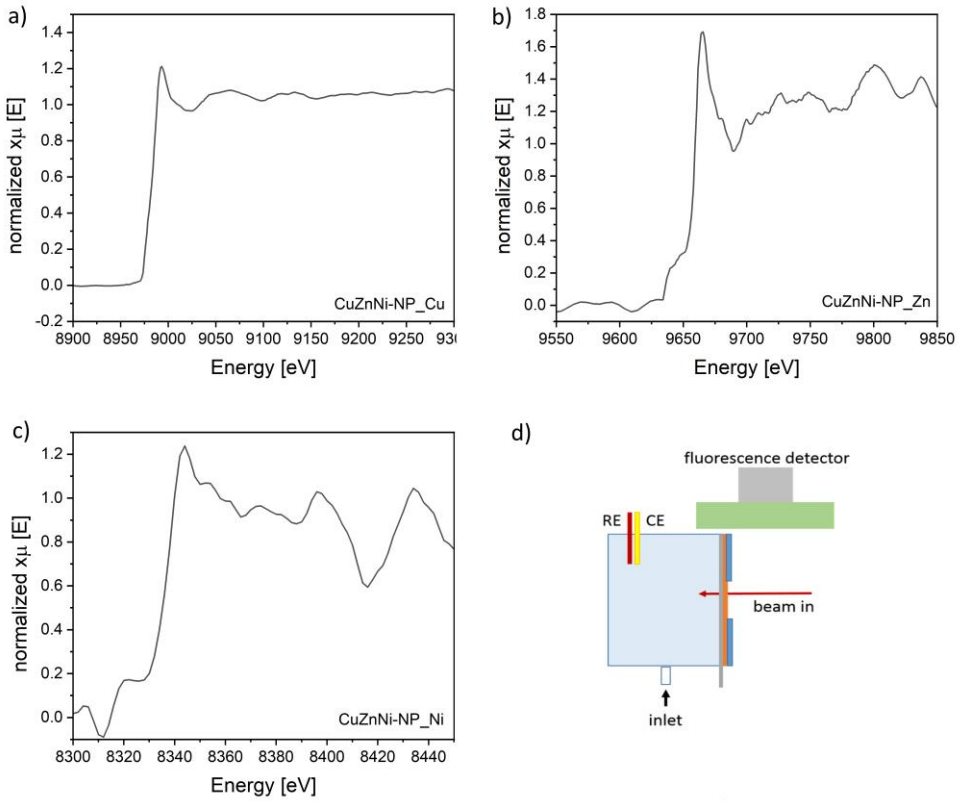

Figure 2. Normalized XANES spectra collected on CuZnNi nanoparticle loaded Nafion® membrane film at a) Cu, b) Zn and c) Ni K-Edge with d) the sketch of the measurement cell

Ablation experiments were performed on Cu targets in the presence of Zn and Ni cations in the ablation medium, as well as with Ni target and Cu and Zn as additives. The normalized XANES spectra of the nanoparticle/Nafion® composite catalyst films prepared with the Cu target are presented in Figure 2. It was observed that the target material, in this case Cu, dominates the alloy composition and has a high metallic character. Zn and Ni spectra indicate that those two metals are mostly present in form of oxidic species. Moreover, non-normalized XANES spectra (not shown here) reveal that the Zn content is at least three-times higher than Ni content. The XANES analysis supports the EDX results hinting on a core-shell type nanoparticle with the incorporation of the cations in the ablation medium in the oxidic shell. Last but not least, with the results of this beamtime, optimal procedure for the sample preparation and film thickness were determined for the in situ experiments planned for upcoming beamtimes.

Acknowledgement
We gratefully acknowledge the DELTA machine group for providing synchrotron radiation reliably.

References

[1] C.G. Morales-Guio, E.R. Cave, S.A. Nitopi, J.T. Feaster, L. Wang, K.P. Kuhl, A. Jackson, N.C. Johnson, D.N. Abram, T. Hatsukade, C. Hahn, T.F. Jaramillo, Improved CO2 reduction activity towards C2+ alcohols on a tandem gold on copper electrocatalyst, Nature Catalysis 1(10) (2018) 764-771.
[2] H.P. Blanes, P. Ghiasi, J. Sandkühler, Y. Yesilcicek, S. Pentzien, A. Conradi, C. Prinz, D. Al-Sabbagh, A.F. Thünemann, O. Ozcan, J. Witt, High CO2 reduction activity on AlCrCoCuFeNi multi-principal element alloy nanoparticle electrocatalysts prepared by means of pulsed laser ablation, J Mater Res Technol 24 (2023) 9434-9440.
[3] N. Wurzler, J.D. Schutter, R. Wagner, M. Dimper, D. Lützenkirchen-Hecht, O. Ozcan, Trained to corrode: Cultivation in the presence of Fe(III) increases the electrochemical activity of iron reducing bacteria - An in situ electrochemical XANES study, Electrochem. Commun. 112 (2020) 106673.
[4] N. Wurzler, J.D. Schutter, R. Wagner, M. Dimper, D. Lutzenkirchen-Hecht, O. Ozcan, Abundance of Fe(III) during cultivation affects the microbiologically influenced corrosion (MIC) behaviour of iron reducing bacteria Shewanella putrefaciens, Corros. Sci. 174 (2020).

Notes

Notes